

NASA CR-159595
SSS-R-79-3904

(NASA-CR-159595) EXTENSION, VALIDATION AND
APPLICATION OF THE NASCAP CODE Final
Report, 9 Sep. 1977 - 11 Jan. 1979 (Systems
Science and Software) - 326 p HC A15/MF A01

N79-27397

Unclas

CSCL 09C G3/33 27935



EXTENSION, VALIDATION AND APPLICATION OF THE NASCAP CODE

I. Katz, J.J. Cassidy, M.J. Mandell,
G.W. Schnuelle, P.G. Steen, D.E. Parks,
M. Rotenberg and J.H. Alexander

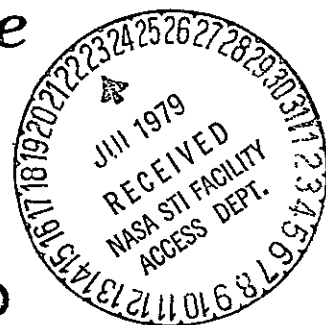
Systems, Science & Software

Prepared For

NATIONAL AERONAUTICS AND
SPACE ADMINISTRATION

NASA Lewis Research Center

Contract NAS3 - 21050



1. Report No NASA CR-159595		2. Government Accession No.		3. Recipient's Catalog No.	
4. Title and Subtitle EXTENSION, VALIDATION AND APPLICATION OF THE NASCAP CODE				5. Report Date January 1979	
				6. Performing Organization Code	
7. Author(s) I. Katz, J. J. Cassidy, M. J. Mandell, G. W. Schnuelle, P. G. Steen, D. E. Parks, M. Rotenberg, and J. H. Alexander				8. Performing Organization Report No. SSS-R-79-3904	
9. Performing Organization Name and Address Systems, Science and Software P. O. Box 1620 La Jolla, California 92038				10. Work Unit No. YOS 7278	
				11. Contract or Grant No. NAS3-21050	
12. Sponsoring Agency Name and Address National Aeronautics and Space Administration Lewis Research Center Cleveland, Ohio 44135				13. Type of Report and Period Covered Contractor Report 9/1977 - 1/1979	
				14. Sponsoring Agency Code 6124	
15. Supplementary Notes					
16. Abstract <p>The NASCAP code dynamically simulates the charging of an object in a specified plasma environment. It is fully three-dimensional, and it can solve complex problems in a few hours of computer time or less. The current contract called for extension, validation, and application of NASCAP.</p> <p>Numerous extensions were made in the code. They fall into three categories: a greater range of definable objects, a more sophisticated computational model, and simplified code structure and usage. The bulk of this report documents these extensions.</p> <p>An important validation of NASCAP was performed using a new two-dimensional computer code (TWOD). Also, an interactive code (MATCHG) was written to compare material parameter inputs with charging results.</p> <p>The first major application of NASCAP was performed on the SCATHA satellite. A detailed shadowing study and a charging calculation were completed. NASCAP was installed at the Air Force Geophysics Laboratory, where researchers plan to use it to interpret SCATHA data.</p>					
17. Key Words (Suggested by Author(s)) NASCAP, Spacecraft Charging, Photo-sheath, SCATHA, Computer Simulation			18. Distribution Statement Publicly Available		
19. Security Classif. (of this report) Unclassified		20. Security Classif. (of this page) Unclassified		21. No. of Pages 333	
				22. Price*	

* For sale by the National Technical Information Service, Springfield, Virginia 22161

TABLE OF CONTENTS

	Page
SUMMARY	1
1. INTRODUCTION	3
2. NASCAP CAPABILITIES	6
3. INPUT	44
4. POTENTIAL SOLVER	45
4.1 ELEMENT BY ELEMENT COPRODUCT	45
4.2 SCALED CONJUGATE GRADIENT	46
5. LONGTIMESTEP OPTION — SUBROUTINE LIMCEL	49
5.1 NEED FOR THE LIMCEL ROUTINE	49
5.2 AN IMPLICIT CHARGING TREATMENT	50
5.3 OVERALL STRUCTURE OF THE LIMCEL ANALYSIS	51
5.4 PRELIMINARY PHASE: LUMPED CIRCUIT MODEL	54
5.5 EXPLICIT PHASE	58
5.6 PRELIMINARY CHARGING ANALYSIS	59
5.7 DETERMINATION OF TRIAL POTENTIALS FOR FIXED NODES	60
5.8 FLUX DERIVATIVE DETERMINATION	62
5.9 FINAL CHARGING ANALYSIS	63
5.10 DECREASE IN EFFECTIVE PHOTOCURRENTS . . .	65
6. BOOMS	88
6.1 BOOM DEFINITION	88
6.2 RESTRICTIONS ON BOOMS	89
6.3 BOOM CELL FLUX SUMMARY	90
7. SUBDIVISION	91
7.1 RESULTS	91
7.2 CELLS AND ELTS	95
7.3 FACES AND EDGES	96
7.4 SDINPU — OBJECT DEFINITION	98

TABLE OF CONTENTS (Continued)

	Page
7.5 RESTRICTIONS	100
7.6 SDLIST	110
7.7 RESIDUALS AND SUBDIVISION	111
7.8 STORAGE	115
7.9 INTERNAL REPRESENTATION	116
7.10 SIGNIFICANT SUBDIVISION CONSTANTS	120
7.11 SIGNIFICANT SUBDIVISION ARRAYS	121
7.12 SUBDIVISION SUBROUTINE SUMMARIES	123
7.13 CODE STRUCTURE	137
8. PARTICLE DETECTORS	143
8.1 SPECIFICATION OF DETECTOR ORIENTATION.	145
8.2 THE DETECTOR COORDINATE SYSTEM	149
8.3 CALCULATION OF ENERGY FLUX AT A CELL SURFACE	150
8.4 DETECTOR ENERGY FLUX DENSITY MEASURE- MENT	154
8.5 NASCAP PARTICLE DETECTOR ACTIVATION	159
8.6 NASCAP DETECTOR SCRATCH FILES	161
8.7 DETECTOR KEYWORD INPUT FILE.	162
8.8 DESCRIPTION OF DETECTOR PARAMETER OPTIONS BY KEYWORD	163
8.8.1 General Detector Definition Parameters	163
8.8.2 Detector Aperture Definition Parameters	163
8.8.3 Independent Variables and Fixed Parameters	164
8.8.4 Plot Scaling Options	165
8.8.5 Reverse Trajectory Particle Tracking	166
8.8.6 Specification of Environment for Detectors	166

TABLE OF CONTENTS (Continued)

	Page
9. PARTICLE EMITTERS	167
9.1 LOW DENSITY PARTICLE EMITTERS: GENERAL DESCRIPTION	167
9.2 SPECIFICATION OF EMITTER BEAM ORIENTATION	169
9.3 PARTICLE EMITTER BEAM CURRENT REPRESENTATION	170
9.4 DISCRETE PARTICLE EMISSION ANGLES AND ENERGIES	171
9.4.1 Uniform Angular Current Density Dependence	171
9.4.2 Cosine θ Angular Current Density Dependence	172
9.4.3 Gaussian Energy Current Density Dependence	172
9.4.4 Rational Energy Current Density Dependence	174
9.5 NASCAP PARTICLE EMITTER ACTIVATION . . .	175
9.6 NASCAP EMITTER SCRATCH FILES	176
9.7 EMITTER KEYWORD FILE PREPARATION	177
9.8 DESCRIPTION OF EMITTER PARAMETER OPTIONS BY KEYWORD	178
9.8.1 Emitter Dependent Parameters . .	178
9.8.2 Emitter Independent Parameters .	182
9.9 KEYWORD CARD PROCESSING ERRORS	184
9.10 SPECIAL RESTRICTIONS	184
9.11 ADDITIONAL OPERATION NOTES	185
10. AMBIENT CHARGE DENSITY	186
10.1 RESULTS	189

TABLE OF CONTENTS (Continued)

	Page
11. SURFACE CONDUCTIVITY	201
11.1 EFFECTS OF BULK AND SURFACE CONDUCTIVITY OF THE POTENTIAL DEVELOPED BY DIELECTRICS EXPOSED TO ELECTRON BEAMS	202
11.2 SURFACE CONDUCTIVITY	218
12. DISCHARGE, PATCH, SPACE CHARGE DENSITY PLOTS .	220
12.1 THREE FURTHER MODIFICATIONS	220
12.2 NASCAP DISCHARGE ANALYSIS	220
12.3 PATCH SURFACES	224
12.4 SPACE CHARGE DENSITY	224
13. SHADOWING CALCULATIONS	228
13.1 CODES AND DATA FILES	228
13.2 REMAPPING AT NASA-LERC	230
13.3 DESCRIPTION OF PROGRAM RUNSTREAM INPUT	232
13.4 OBJECT DEFINITION FILES	236
13.5 RUNSTREAMS	237
14. MATCHG -- A MATERIAL CHARGING CODE	241
14.1 INTRODUCTION	241
14.2 USE OF THE CODE	242
14.3 SAMPLE RUNS	245
15. CDC 6600 CONVERSION	255
15.1 MACHINE INDEPENDENT SUBROUTINES	255
15.2 MACHINE DEPENDENT SUBROUTINES	256
15.3 LOAD AND EXECUTE	257
16. SCATHA CHARGING ANALYSIS	258

TABLE OF CONTENTS (Continued)

	Page
17. TWOD — TWO DIMENSIONAL SPACECRAFT CHARGING	
COMPUTER CODE	289
17.1 INTRODUCTION	289
17.2 CODE STRUCTURE	290
17.3 EFFECTIVE PHOTOSHEATH CONDUCTIVITY . .	293
17.4 EXAMPLE: ISOTROPIC FLUX	297
17.5 COMPARISON OF TWOD AND NASCAP	299
18. THIN PLATES	308
18.1 THIN PLATE EXAMPLES	308
18.2 DEFINITION OF THIN PLATES	313
REFERENCES	315

LIST OF FIGURES

Figure No.		Page
5.1	Block diagram of LONGTIMESTEP option. .	53
5.2	Lumped-circuit model of spacecraft constructed by NASCAP and used for LONGTIMESTEP option	55
5.3	Surface node list (PTLIST) entry format	57
5.4	Flow chart of Final Charging Analysis portion of subroutine LIMCEL	64
7.1	Plate with two fixed conductors; Y = 8.00	92
7.2	Potentials at subdivided points, 1 cm above surface; Z = 8.5, Y = 7.99 . .	93
7.3	No subdivided points, bilinear inter- polation potentials; Z = 8.5, Y = 7.99.	94
7.4	Extra nodes on subdivided cell	96
7.5	Surface cell list (JSURF) entry format	118
7.6	Element table codes and orientation codes	119
10.1	Potential contours around a 2 m aluminum cube, including the effect of ambient charge density	190
10.2	Potential contours around a 2 m aluminum cube, including the effect of ambient charge density	191
10.3	Potential contours around a 2 m aluminum cube, including the effect of ambient charge density	192
10.4	Capacitance of a 1 m aluminum cube versus Debye length	193
12.1	Discharge printout - grounded aluminum cube.	222

LIST OF FIGURES (Continued)

Figure No.		Page
12.2	Discharge printout — floating aluminum cube	223
12.3	Space charge density contours about small SCATHA model, uncharged in severe substorm	226
12.4	Space charge density contours about small SCATHA model charged to -675 volts	227
13.1	Generation of shadow program tape	229
13.2	Runstream used to generate shadowing table for ML12-6 aperture	238
17.1	Block diagram of TWOD code	291
17.2	Conductivity in photoelectron sheath	294
17.3a	Potential profile outside uniformly sunlit sphere	298
17.3b	Space charge density profile outside uniformly sunlit sphere	298
17.4	Equilibrium potential contours from TWOD code	300
17.5	Photosheath density from TWOD code	301
17.6	Potential contours (two grids) from NASCAP code	303
17.7	Photosheath density for inner grid from NASCAP "SHEATH" routine	304
17.8	Equilibrium surface potential versus angle for a cylinder sunlit from one side	305
17.9	Potential versus radial distance for a cylinder sunlit from one side, in direction of incident sunlight	306
18.1	Conducting parallel plates in a grounded tank	309

LIST OF FIGURES (Continued)

Figure No.		Page
18.2	Conducting paddle satellite in a test tank	310
18.3	A differentially charged dielectric covered plate in sunlight	311
18.4	Guard ring parallel plate capacitor . .	312

LIST OF TABLES

Table No.		Page
8.1	Cell Coordinate System Rotation With Respect to Satellite System . . .	147

SUMMARY

The NASCAP code dynamically simulates the charging of an object in a specified plasma environment. It is fully three-dimensional, and it can solve complex problems in a few hours of computer time or less. The current contract called for extension, validation, and application of NASCAP.

Numerous extensions were made in the code. They fall into three categories: a greater range of definable objects, a more sophisticated computational model, and simplified code structure and usage. The bulk of this report documents these extensions.

An important validation of NASCAP was performed using a new two-dimensional computer code (TWOD). Also, an interactive code (MATCHG) was written to compare material parameter inputs with charging results.

The first major application of NASCAP was performed on the SCATHA satellite. A detailed shadowing study and a charging calculation were completed. NASCAP was installed at the Air Force Geophysics Laboratory, where researchers plan to use it to interpret SCATHA data.

1. INTRODUCTION

This is the final report on work performed by Systems, Science and Software on Contract NAS3-21050, "Extension, Validation and Application of the NASCAP Code". The work was performed between September 9, 1977 and January 11, 1979.

Most of the material contained in this final report was originally produced for monthly progress reports. Some detailed documentation has been added, and some papers produced separately have been included. Additional documents produced under this contract include a revised NASCAP User's Manual (SSS-R-78-3739 (DRAFT), NASA CR-159417), and a SCATHA Experiment Shadowing Study (SSS-R-78-3658 (DRAFT)). Other documents of interest regarding NASCAP are:

"Three-Dimensional Dynamic Study of Electrostatic Charging in Materials", Interim Report, SSS-R-78-3124.

"A Three-Dimensional Dynamic Study of Electrostatic Charging in Materials", NASA CR-135256.

"NASCAP User's Manual", NASA CR-135259.

The above publications show the development of NASCAP and give background information which is not included in this report or in the NASCAP User's Manual. A summary of current NASCAP capabilities is provided in Chapter 2.

While the first version of NASCAP, developed under Contract NAS3-20119, was largely successful, it was apparent that many shortcomings had to be overcome to make NASCAP a truly useful engineering and scientific tool. These shortcomings fell into the general categories of (1) reliability and ease of use; (2) generality, particularly of object definition; and (3) facilities for study of scientific experiments and other charging-related phenomena.

PRECEDING PAGE BLANK NOT FILMED

PRECEDING PAGE BLANK NOT FILMED

The use of NASCAP was made simpler and more flexible through expanded use of keyword input and user-specified program logic. These changes are described briefly in Chapter 3, and more fully in the NASCAP User's Manual (CR-159417). The NASCAP potential solver was simplified and made more reliable by implementation of element-by-element residual summation and a Scaled-Conjugate-Gradient iterative scheme. The advantages of these techniques are discussed in Chapter 4. The most difficult problem solved during this contract period was the failure of NASCAP's explicit timestepping procedure. The LONGTIMESTEP feature (Chapter 5) was developed to guarantee reasonable results even when the various physical processes had widely disparate time constants.

NASCAP object definition was extended in several ways. Thin booms (Chapter 6) extending beyond the inner mesh were incorporated to facilitate modeling of satellites having long appendages. Thin plates (Chapter 18) now provide improved modeling of large solar panels. Cell subdivision (Chapter 7) was implemented to improve resolution of an object surface. Also, the "patch" building blocks (Chapter 12) were added to simplify definition of objects having complex surface patterns.

Code generality was further enhanced by taking account of two additional physical processes. Space charge due to the ambient plasma (Chapter 10) may be included in a Debye screening approximation. In case of materials having substantial surface conductivity (Chapter 11), the effects of this property can be evaluated.

In addition to improving the simplicity, reliability, and generality of the charging simulation, facilities were added to study the consequences of charging. The DETECTOR feature (Chapter 8) allows detailed study of particles incident upon a surface cell. The related EMITTER feature

STUDY OF THE CONSEQUENCES OF CHARGING

(Chapter 9) may be used to study the consequences of charged particle emitters. A discharge analysis (Chapter 12) may be used to detect discharge sites and predict the effects of these discharges on spacecraft potential. The SHEATH option (Chapter 12) invokes a first-order calculation of the space charge density due to emitted low-energy electrons.

Four further code development tasks were performed under this contract. Chapter 14 describes the conversion of NASCAP for a CDC 6600 computer, and its installation at Air Force Geophysics Laboratory. Chapter 13 describes the interactive MATCHG code. MATCHG treats backscatter and secondary emission from materials in a manner identical to NASCAP, and is intended for preliminary assessment of material properties. A preliminary version of a two-dimensional (R- θ) spacecraft charging code capable of accurately predicting currents and space charge in the photosheath was developed for the purpose of comparison with NASCAP. Chapter 17 describes this code and the results of its NASCAP comparison. Finally, the HIDCEL routines were developed into a fast, highly accurate shadowing code (Chapter 13) used to produce the SCATHA Experiment Shadowing Study.

Another major effort undertaken for this contract was development of a model of the SCATHA spacecraft for use in NASCAP and performance of a SCATHA charging study. The SCATHA application is described in Chapter 16.

At the close of the contract period, NASCAP was deemed to be in a form suitable for general distribution. A workshop was held at NASA/Lewis Research Center, December 12-14, 1978, attended by representatives of government and industry. This workshop was designed to introduce the attendees to NASCAP's methods and capabilities, and provide them with hands-on experience in its use. NASCAP is being made available through COSMIC.

2. NASCAP CAPABILITIES

Chapter 2 of this report is a verbatim reproduction of a paper given at the USAF/NASA Spacecraft Charging Technology Conference, 31 October 1978. This paper gives a good summary of the form of NASCAP as it exists at the end of the contract year.

THE CAPABILITIES OF THE NASA CHARGING ANALYZER PROGRAM*

I. Katz, J. J. Cassidy, M. J. Mandell,
G. W. Schnuelle, P. G. Steen
Systems, Science and Software
J. C. Roche
NASA-Lewis Research Center

ABSTRACT

Desirable features in a spacecraft modeling code are enumerated. The NASCAP (NASA Charging Analyzer Program) is discussed in terms of its approach to the problem. Samples of problem setup and output are provided which demonstrate the ease with which the program can be used. A simple but interesting case of spacecraft charging is examined and other applications are discussed.

1. INTRODUCTION

The basic concerns of a computer spacecraft model can be broken down into five areas.

1. Features of the spacecraft itself.
2. Features of the environment.
3. The spacecraft-environment interaction.
4. Man-hours to set up and computer time to run a calculation.
5. A way to verify the model.

In modeling the spacecraft itself, the point is to get in as much detail as can reasonably be included. This will vary depending on the type of model being used. The features desired^[1] are first, some geometrical detail, such as the basic shape of the spacecraft body and any protrusions such as booms and antennae. Second, one would want to include which parts of the surface are bare conductor and which are dielectric coated. Third, it would be nice to have some

* This work supported by the National Aeronautics and Space Administration, Lewis Research Center, under Contract NAS3-21050.

representation of the electrical circuitry connecting parts of the spacecraft surface.

It is also important to decide what approximations go into the environment surrounding the spacecraft. The most basic decision is how to model the ambient plasma. Can you include the region far from the spacecraft, and get a detailed look at the region close in? Can you specify normal and extreme conditions? Does the plasma change in time? Other aspects of the environment that are of concern are the sun, the plasma sheath, and particle trajectories.

The spacecraft-environment interaction is mainly a matter of particle currents to and from the spacecraft surface. The important charging currents are

1. Incident electrons
2. Photocurrent
3. Incident protons
4. Secondary electrons from electron impact
5. Secondary electrons from proton impact
6. Electron backscatter

These processes vary around the spacecraft surface, depending on local potential, surface material, and solar illumination. An ideal model would take all this local information into consideration when calculating particle fluxes.

Computer time for spacecraft modeling can be prohibitive. A model that is general ends up solving a series of equations with hundreds or thousands of variables. An exact solution is enormously expensive, and it may be hard to get convergence from an iterative solution. Much care must be put into this aspect of the problem, lest an otherwise elegant modeling program start to impersonate an infinite loop.

The most expensive way to verify a modeling program is to build a spacecraft like the model and send it up. Other, more reasonable techniques, are to model ground experiments,

to check answers for reasonableness, and to test the program on known problems.

2. NASCAP APPROACH

As we have seen, the physics which must be examined in order to model spacecraft charging presents a problem of formidable dimensions. It would be impractical to develop a computer code that was state of the art in every aspect of the problem. By placing restrictions on the class of problems to be examined we have been able to construct the NASA Charging Analyzer Program which provides useful information in those cases of most practical interest. It is most applicable to the high voltage charging caused by magnetospheric substorms.

Our approach has been to limit the range of ambient environments to those whose Debye lengths, λ_D , are large compared to object dimensions. For magnetospheric substorms this is definitely true.

$$\theta_e \sim 10,000 \text{ eV}$$

$$n_e \sim 1 \text{ cm}^{-3}$$

$$\lambda_D \sim 0.7 \text{ km}$$

Only for the very largest conceivable spacecraft are object dimensions comparable to Debye lengths. For finite Debye lengths we have included ambient plasma screening approximations, albeit of modest applicability.

Overall, we have modeled all aspects of the problem except electromagnetic wave propagation. Our idea has been to use the best available analytical theories wherever possible and to minimize the brute force number crunching. By doing this we have been able to combine good treatments of ambient environment, sheath, complex object, and electrical and particle interactions into a single code. This is done by using known physics and developing approximate models where necessary.

For example, NASCAP contains analytical approximations to electron backscatter as a function of electron energy and angle. While not as accurate as Monte Carlo transport results, these formulations do give reasonable yield estimates and can be evaluated quickly at hundreds of surface locations each time-step. Thus we obtain reasonable estimates in reasonable amounts of time as opposed to best estimates regardless of cost. This philosophy permeates the code. Where quasi-analytical models were necessary but unavailable, we have developed them.

The procedure followed in the code is to approximate the spacecraft in a 3-D Cartesian grid. Free space around the satellite is provided by nesting grids within grids where each grid has a linear dimension twice that of the grid it surrounds. There can be an arbitrary number of these nested grids. However, the more grids, the longer the computer time per calculation (see Figure 1).

All parts of the spacecraft must remain in the innermost grid, except for booms which can extend into several grids. The object itself is composed of an assembly of cubes, sliced cubes, plane surfaces, and skinny cylinders, as shown in Figure 2. Each surface can be of an independently specified material, with up to 15 different materials permitted (Figure 3). Certain classes of surfaces may be subdivided for higher resolution.

Object definition is by far the most complicated aspect of using a three-dimensional computer code. To make the program easy to use, NASCAP provides an extremely simple object definition language. Complex three-dimensional spacecraft can be described with a minimum of effort. The satellite shown in Figure 4 is a good example. The central structure is octagonal with a gold circumference and aluminum top and bottom surfaces. The two planar sheets represent solar cells with kapton covering the back surface. They are attached to the main body with kapton coated cylinders. This object was defined using 31 brief

lines of input (Figure 5). The simple object definition commands are fully explained in the NASCAP User's Manual.^[2]

Once the object definition is complete, the program alternately calculates charge accumulations on surfaces, and potentials caused by these charges. Due to the variety of time-scales in the system, the algorithm used to advance the charge distribution in time is extremely complex, so complex that it uses a couple thousand element self-generated capacitor model as its own internal estimator.

NASCAP produces a variety of printed and graphical output. The fundamental idea is to help the user follow the progress of the calculation (Figures 6-14).

The first graphic output is a two-dimensional view of the spacecraft with surface cells shaded to show the material types. Each surface cell is individually classified by material, with up to 15 different material types allowed.

Next is a three-dimensional perspective view of the spacecraft without hidden line removal. This is helpful in tracking down object definition problems. It is followed by a view from the same perspective with surface cells outlined. In this surface cell plot, hidden lines are removed. The user gets a quick and accurate feeling for the defined object. The routine that generates these plots also calculates exposed surface areas for determining photoelectron emission.

These plots are generated at object definition time, before the actual satellite charging begins. The major outputs of the charging calculation are the flux breakdown printout and potential contours.

The flux breakdown printout shows, for any surface cell(s), the charging currents operating on that cell. Each individual surface cell requires a separate calculation. By requesting flux breakdown printouts, the user can closely follow the charging process at any point on the surface.

Contour plots are an efficient way to show what's happening to the electrostatic potential both near the spacecraft and far away. The user can look at the potential contour plots generated every time cycle and get a good feeling for global changes in the spacecraft sheath.

NASCAP detector routines plot flux density versus energy of particles reaching the detectors. Detectors can be placed, at the user's discretion, on any surface cell.

The emitter routines plot trajectories of particles emitted at various energies. These trajectories, along with potential contour plots, give a very good idea of fields surrounding the spacecraft or test tank object.

Finally, if local electric field stresses exceed some user specified threshold value, a message is printed and the code redistributes charge as if a discharge had occurred.

3. VALIDITY OF THE MODEL

With a model as broad in scope and as complex (over 400 subroutines) as NASCAP, the immediate question is "How do you know that it gets reasonable answers?" So that we have confidence in NASCAP results, testing and comparing to analytical results has been a major part of the development program. The accuracy of the various components have been examined in configurations simple enough to determine their inherent accuracy.

Since the capacitance of simple objects such as spheres, cubes and cylinders are known quite well, we have used these to determine how well the potential routines work. For all cases the NASCAP results were within 10 percent of analytical predictions, and for objects of more than a zone resolution and for booms of radius much less than the grid spacing, the NASCAP results were accurate to a few percent. The electric fields in space were of corresponding accuracy near the satellite and increasing accuracy away from the vehicle. The accuracy of the

potentials are limited only by the ability of the finite element interpolation functions to represent the true solution. For complex objects, the NASCAP code uses the same algorithms and the accuracy should be comparable. Since NASCAP automatically takes into account mutual capacitances, it is a vast improvement over hand generated capacitor models for complex spacecraft.

NASCAP assumes that charge is accumulated on, as opposed to deposited within, dielectrics. Bulk conduction is included. We have performed detailed one-dimensional calculations of charge transport within dielectrics, and have found this to be a reasonable approximation for electrons of a few to tens of kilovolts in all but the thinnest of dielectrics. It is also an approximation that can easily be modified in the future if the need arises.

The charging currents are the algebraic sum of incident fluxes and backscattered, secondary, and photoemitted electrons. For spherical test cases we have compared NASCAP reverse trajectory currents with spherical probe formulas.^[3] Depending on the number of trajectories sampled the results were in reasonable agreement, the largest errors due to the differences between numerical and analytical integrals over angle of the backscatter and secondary emission formulas. Thus the two basic requirements of a charging calculation, the potential and charge accumulation, are performed well by NASCAP.

The NASCAP material interaction models have been developed from literature results. Their predictions are being compared with laboratory experiments and are the subject of another paper. It should be pointed out, however, that NASCAP accepts parameters for these models as input and that the models themselves are contained in very short, easily replaceable subroutines. Consequently, modifications and improvements in the formulations can be made very simply if needed.

The particle trajectory algorithms are second order accurate in particle timesteps insuring good conservation of

energy and magnetic moment. Orbits are followed beyond the outermost grid boundaries by using an extrapolation of the monopole potential. This allows long excursions of emitted particles to see if they return to the spacecraft.

The algorithm employed to integrate charging currents over a timestep is quite complex to ensure physical results. Rather than describe the technique in detail, we present a calculation which illustrates how it works.

A simple example, which nevertheless displays some of NASCAP's usefulness as a model, is the case of a spherical object in sunlight. Since the photocurrent is larger than the incident electron current, a capacitor-current balance model would lead one to the conclusion that a sunlit surface will remain at a positive potential relative to the surrounding plasma. However, the NASCAP charging current integration routines recognize that space charge limiting prevents photoelectrons and secondary electrons from supporting a potential barrier of more than a few volts. This feature, combined with the multidimensional aspects of the potential leads to a very different equilibrium, one with the illuminated surfaces a kilovolt negative.

We ran NASCAP for the case of a teflon coated sphere in sunlight. The environment for this case is an isotropic, Maxwellian plasma with a temperature of 20 keV and a density $n_e = n_i = 1 \text{ cm}^{-3}$. Sunlight was incident on one side of the sphere (Figure 15).

Figures 16-22 show the time development of the electrostatic field. (The satellite-sun line lies in the plane of these figures. Dark and sunlit cells are differentiated by shading.) For the first ~ 0.1 second the sphere charged uniformly. Over the next few seconds, the negative charge accumulated by the shaded surfaces began to dominate the electrostatic field, causing a saddle point to appear in front of a sunlit surface. At about 10 seconds the potential at the saddle point

became negative. The sunlit surface maintained a potential a few volts positive relative to the saddle point. Final steady state is reached with the sunlit surface at -1.0 kV and the shaded surface at -3.6 kV.

The final steady state potentials were reached at time $t \approx 10^4$ sec. This involved some 30 timesteps, and used total computer time of about one-half hour. Thus in a reasonable amount of computer time NASCAP can provide good physical insight into charging phenomena, insight which is unobtainable using simpler computer models.

4. APPLICATIONS OF NASCAP

NASCAP is designed primarily to give engineering estimates of spacecraft potentials during magnetospheric substorms. It also can provide detailed particle spectra for a given environment and spacecraft potential configuration in order to aid in interpreting results of scientific experiments. As of this time the applications of NASCAP have been limited to the comparison with laboratory material charging test results and to the generation of models of a few scientific spacecraft. Comparisons have been done to validate the material properties portion of the code.

One application of NASCAP which is of engineering importance is the study of active charging control. The operation of onboard charged particle beams has been proposed as a means of minimizing the effects of ambient environment spacecraft charging. NASCAP features an emitter algorithm that models the trajectories and charge transfer effects of such beams. For example, we have placed a one kilovolt, one milliampere electron emitter on a satellite precharged to -2.5 kV. The potentials on spacecraft ground and on an insulated surface as a function of time are shown on Figure 23. Notice that the insulator will differentially charge to a substantial negative potential. Sample particle trajectory plots during the charging

phase are shown in Figure 24. By modeling such systems NASCAP can estimate their utility and point out any severe design problems, so that actual flight experiments have the best chance for success.

An important problem, particularly in the future, is the interactions of large space structures. While not specifically designed for this application, the finite Debye length sheath treatment in the NASCAP code will combine with the reverse trajectory particle flux routines to give good estimates of space charge limited charge collection. The present algorithm employs linear Debye shielding (Figures 25-26). In the future, models of the ambient plasma sheath more relevant to dense collisionless plasmas, will be implemented. The object definition routines can already handle objects of large size by decreasing the object resolution (Figure 27).

The most ambitious application to date is the generation of the SCATHA model. This model utilizes the full capabilities of the code. The model and some preliminary calculations are the subject of another paper.

REFERENCES

1. Whipple, E., "Proceedings of the Spacecraft Charging Technology Conference," 24 February 1977, p. 889.
2. Cassidy, J. J., "NASCAP User's Manual - 1978," (DRAFT) NASA CR-159417, 1978.
3. Katz, I., D. E. Parks, M. J. Mandell, J. M. Harvey, D. H. Brownell, Jr., S. S. Wang and M. Rotenberg, "A Three Dimensional Dynamic Study of Electrostatic Charging in Materials," NASA CR-135256, August 1977.

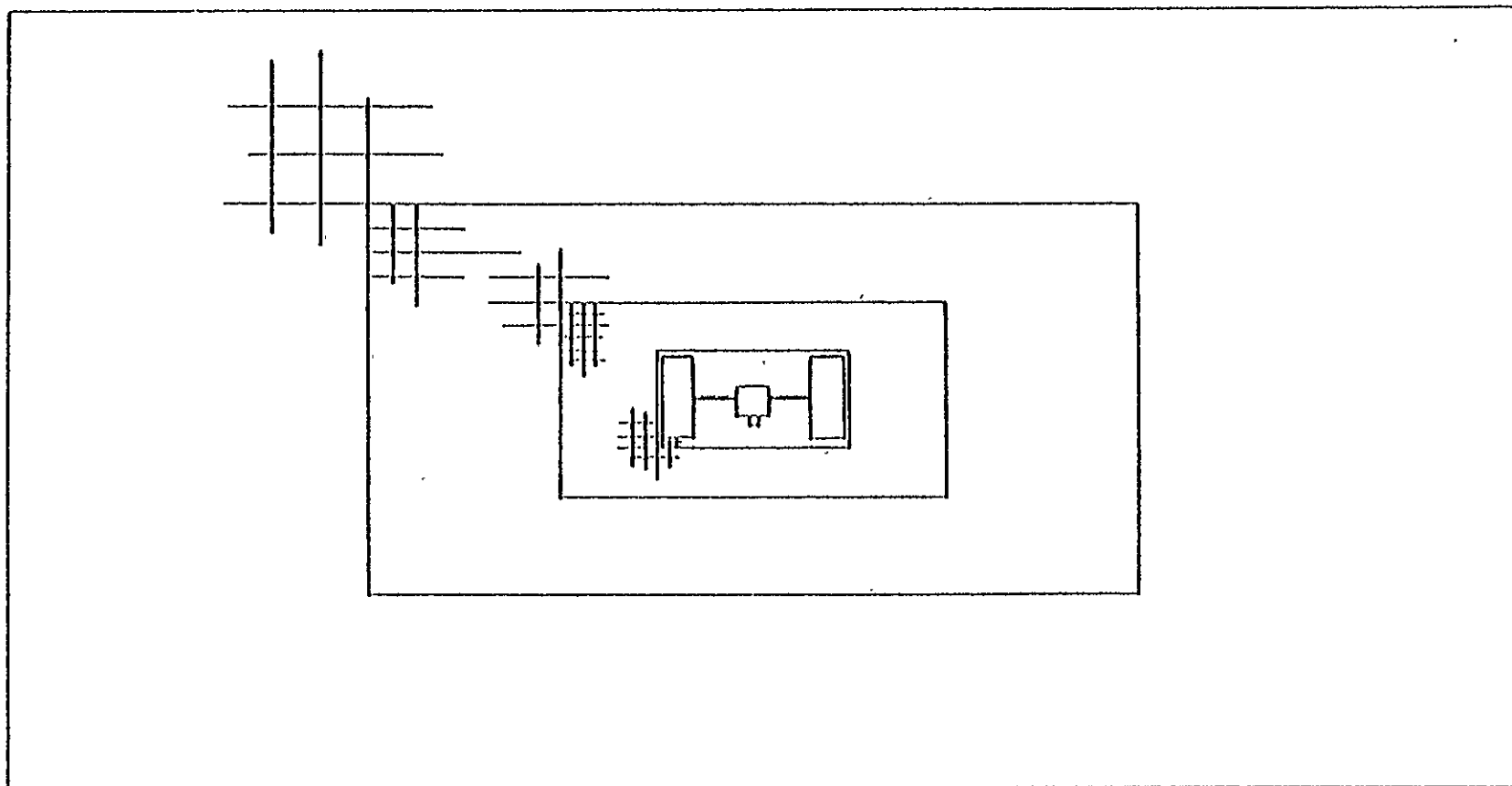


Figure 1. A two-dimensional view of the first four nested meshes. Each succeeding mesh increases the volume of calculation space by a factor of eight. Calculation time is roughly linear with the number of meshes.

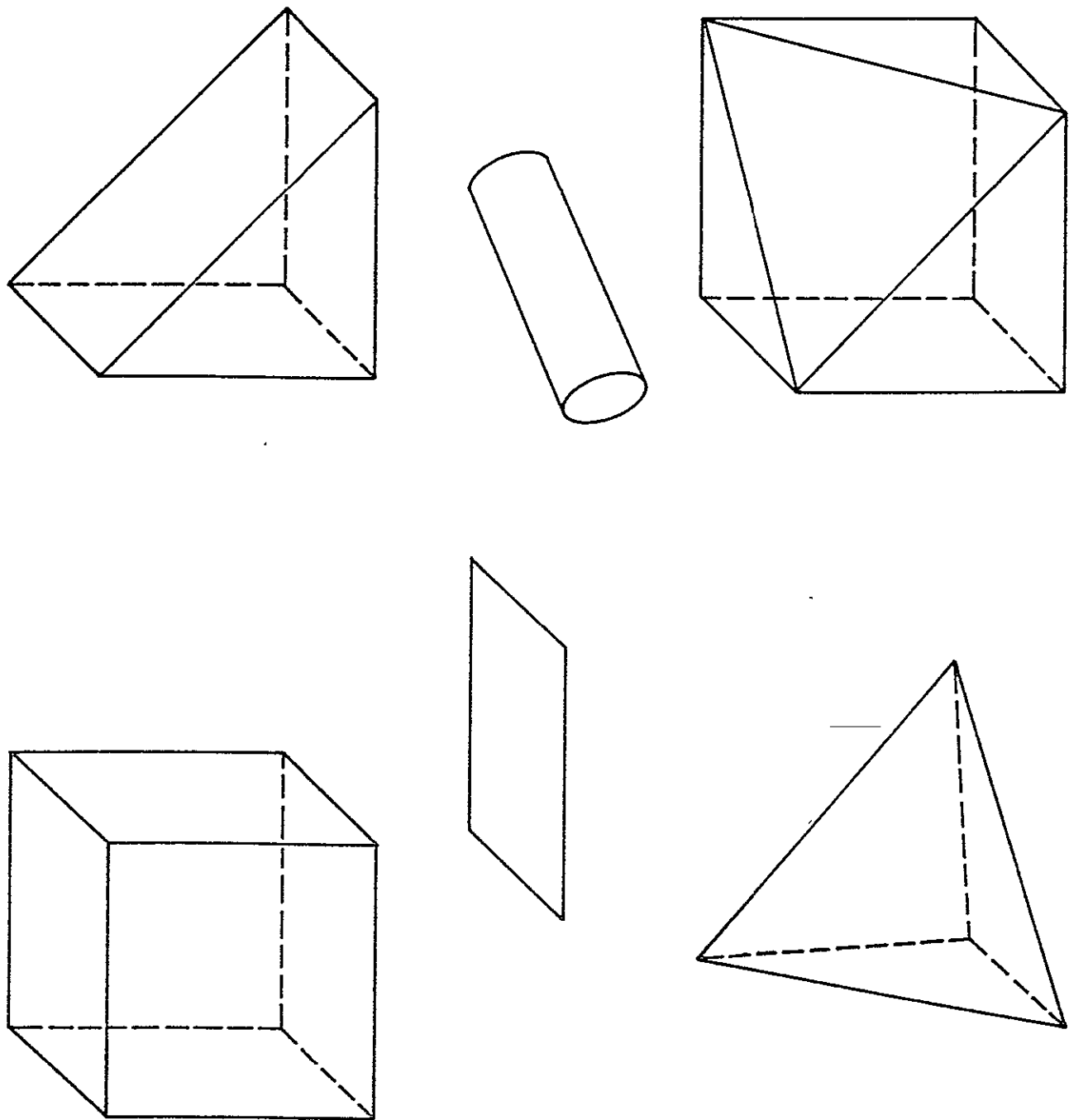


Figure 2. NASCAP can simulate virtually any object that can be built from these fundamental shapes - cube, three types of sliced cube, planar square, and thin cylinder.

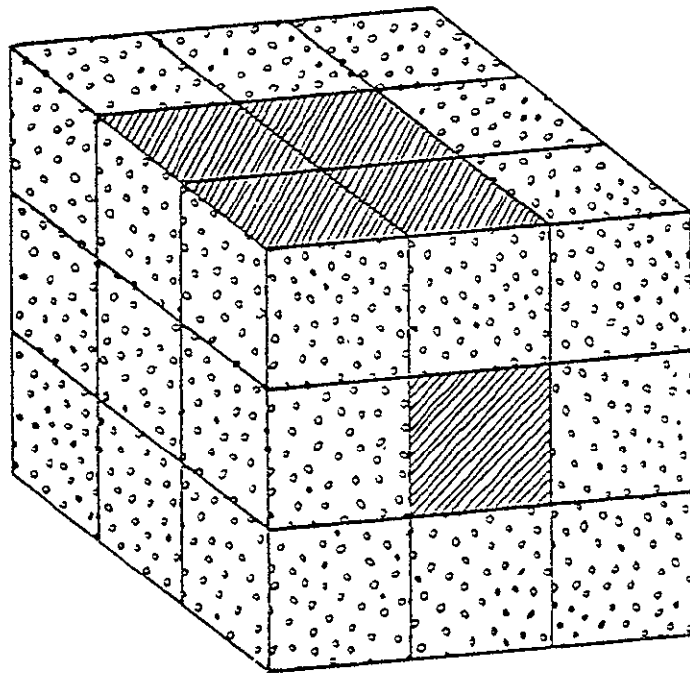


Figure 3. The spacecraft surface is made up of as many as 1200 surface cells. Each cell is assigned a material type and an underlying conductor. The surface cell may represent either bare conductor or dielectric layer.

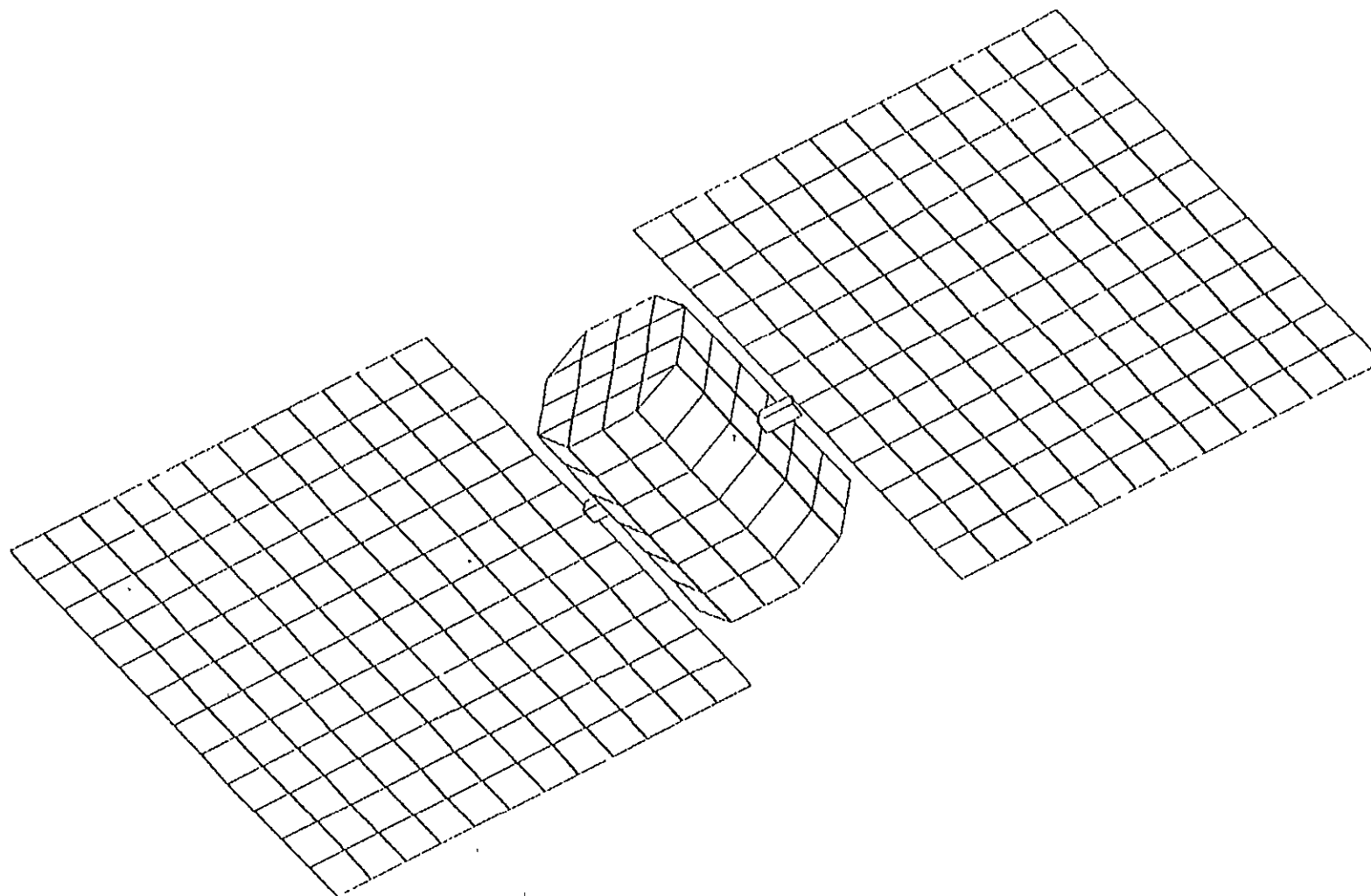


Figure 4. Paddle satellite. A geometrically complex object with four types of surface material.

```

[MATERIAL PROPERTIES DEFINITIONS]

OCTAGON
  AXIS      -3      0      0      3      0      0
  WIDTH      4
  SIDE       2
  SURFACE    -      ALUMINUM
  SURFACE    C      GOLD
  SURFACE    +      ALUMINUM
  ENDOBJ
  [ PLATE
  | CORNER      -6      0      -15
  | DELTAS      12      0      12
  | TOP        +Y      SIO2
  | BOTTOM      -Y      KAPTON
  | ENDOBJ
  ]
  PLATE
  CORNER      -6      0      3
  DELTAS      12      0      12
  TOP        +Y      SIO2
  BOTTOM      -Y      KAPTON
  ENDOBJ
  BOOM
  AXIS      0      0      2      1      0      0      3      1
  RADIUS    0.2
  SURFACE    KAPTON
  ENDOBJ
  BOOM
  AXIS      0      0      -2      1      0      0      -3      1
  RADIUS    0.2
  SURFACE    KAPTON
  ENDOBJ
  ENDSAT

```

Figure 5. Object definition. The object in the preceding figure (paddle satellite) is defined by these commands.

SURFACE CELL MATERIAL COMPOSITION AS VIEWED FROM THE POSITIVE X DIRECTION

FOR X VALUES BETWEEN 1 AND 17

MATERIAL LEGEND

1	
GOLD	
2	
SOLAR	
5	
VELONC	
7	
BLACKC	
8	
KAPTON	
10	
TEFLON	
11	
INDOX	
12	
YGOLDC	
13	
ALUMI	
14	
BOONAT	
15	
ML12	

ORIGINAL PAGE IS
OF POOR QUALITY

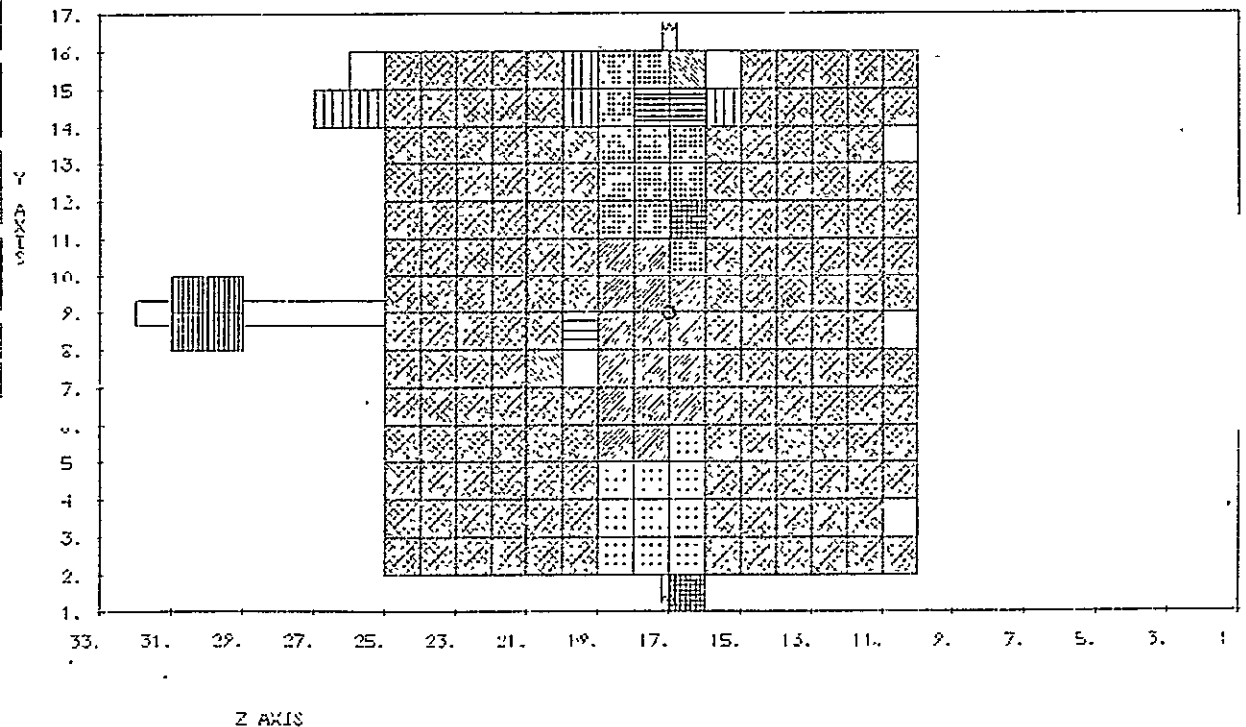


Figure 6. Satelllite illustration plots show the material composition of each surface cell.

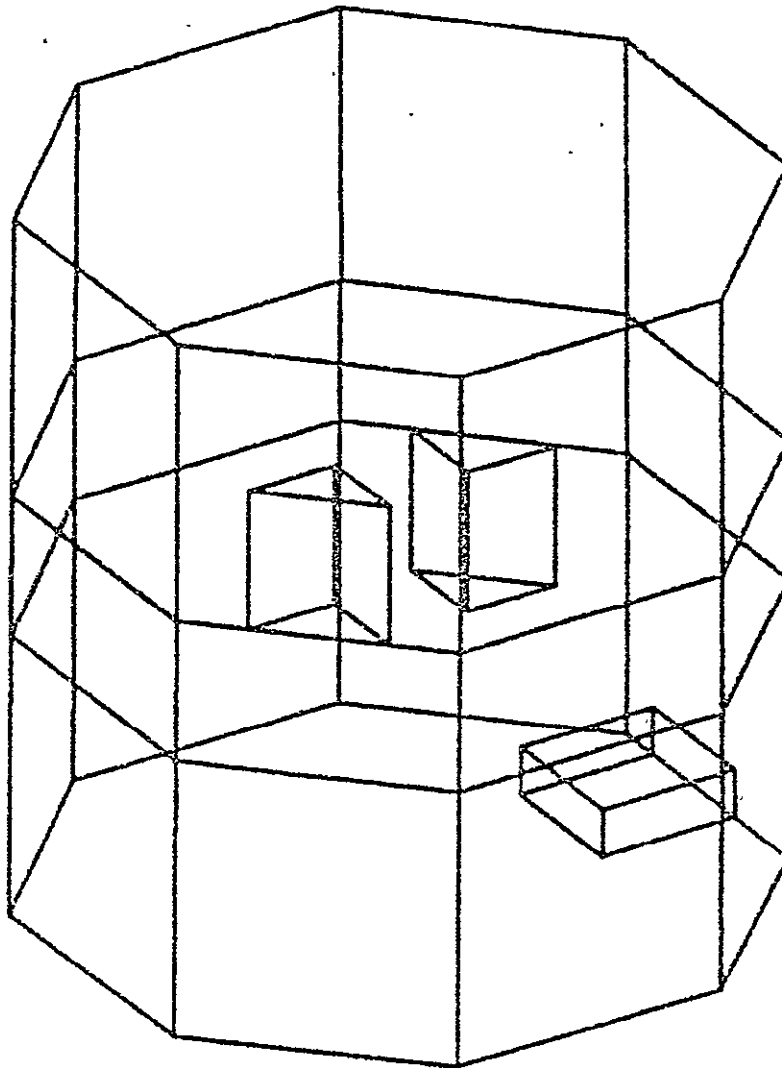


Figure 7. Object structural plots give a perspective view without hidden line removal.

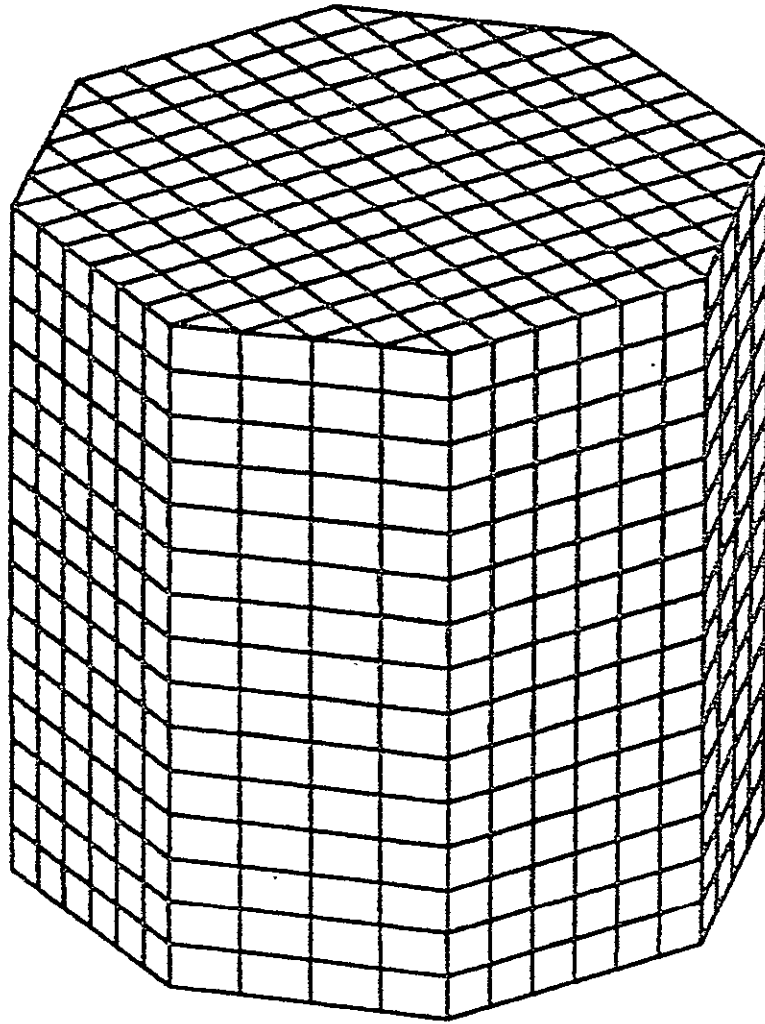


Figure 8. Surface cell hidden line plots give a clear idea of overall spacecraft structure.

SURFACE CELL NO. 15

CODE = 011112100702

LOCATION = 9 10 8

NORMAL = 0 1 -1

MATERIAL = TEFLON

POTENTIAL = -1.096+01 VOLTS

FIELD = 7.665-3 VOLTS/METER

FLUXES IN A/M**2

INCIDENT ELECTRONS 3.16-06

RESULTING BACKSCATTER 8.60-07

RESULTING SECONDARIES 1.32-06

INCIDENT PROTONS 7.39-08

RESULTING SECONDARIES 7.17-07

PHOTOCURRENT 0.00

- - - - -

NET FLUX -1.96-07

Figure 9. A breakdown of charging currents can be requested for any surface cell. This information is given at each timestep.

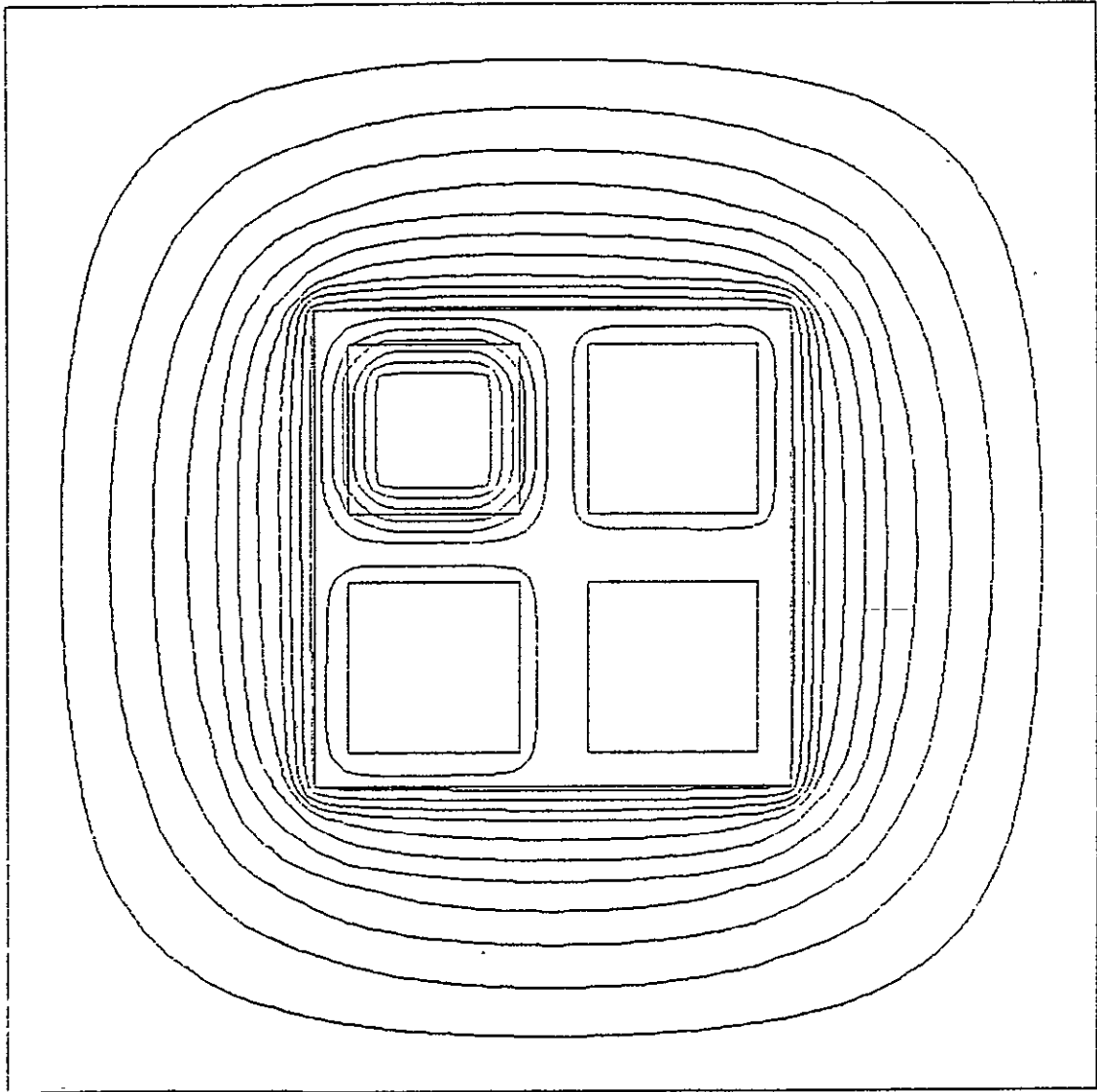


Figure 10. Two-dimensional potential contour plots give a clear picture of electrostatic potential at each timestep.

ORIGINAL PAGE IS
OF POOR QUALITY

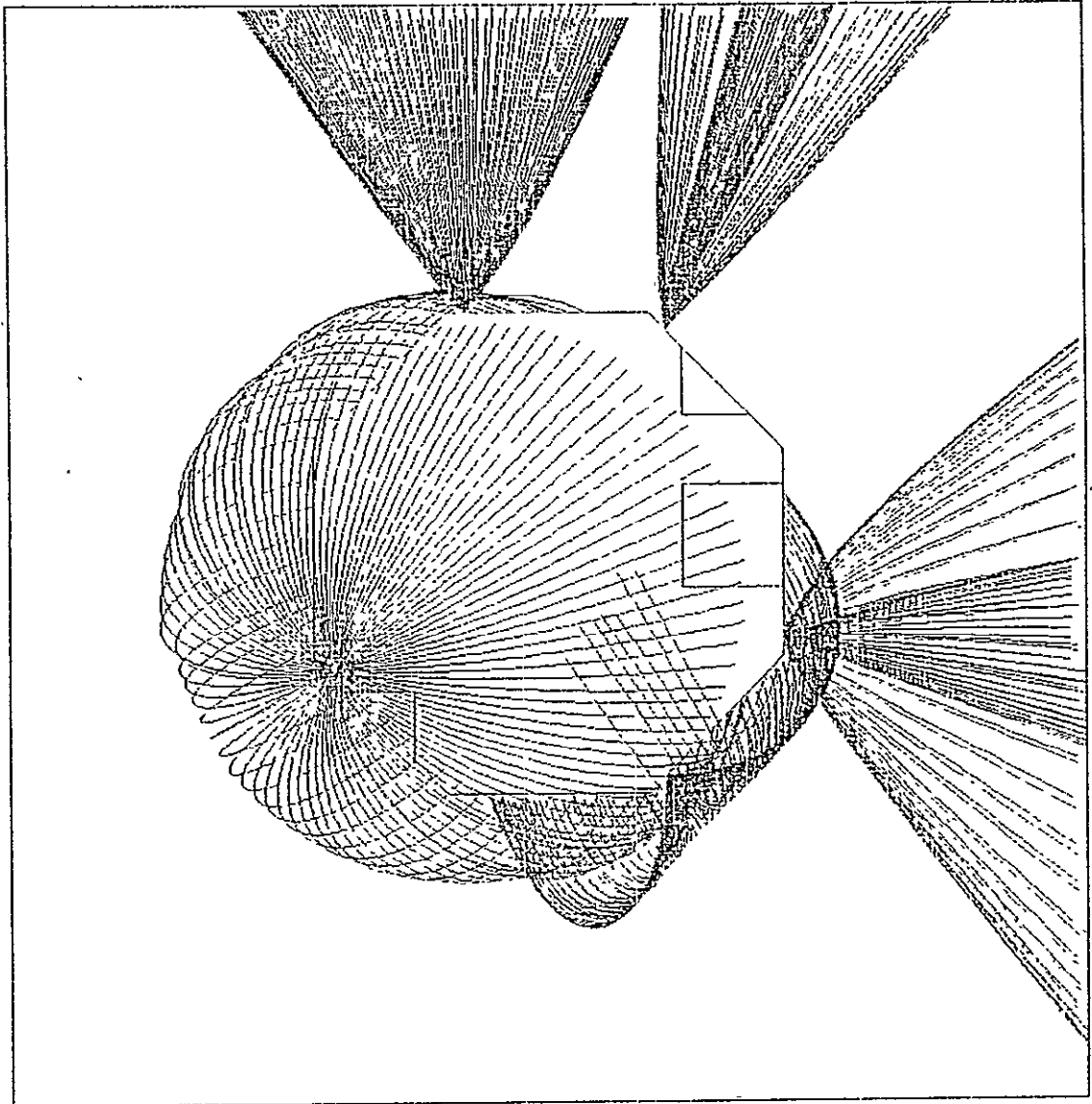


Figure 11. Particle emitters can be specified at any surface cell. This plot shows particles from five emitters for various angles of emission.

ORIGINAL PAGE IS
OF POOR QUALITY

ENERGY FLUX IN EV/CM²-SEC-CP-EV AT CYCLE 1 MEASURED BY
DETECTOR LOCATED AT CELL NUMBER 0 (INTERPOLATED AT 5 POINTS)
PROTON FLUX (HEAVY) SCALED BY 1.00E-3 ELECTRON FLUX (LIGHT) UNSCALED.

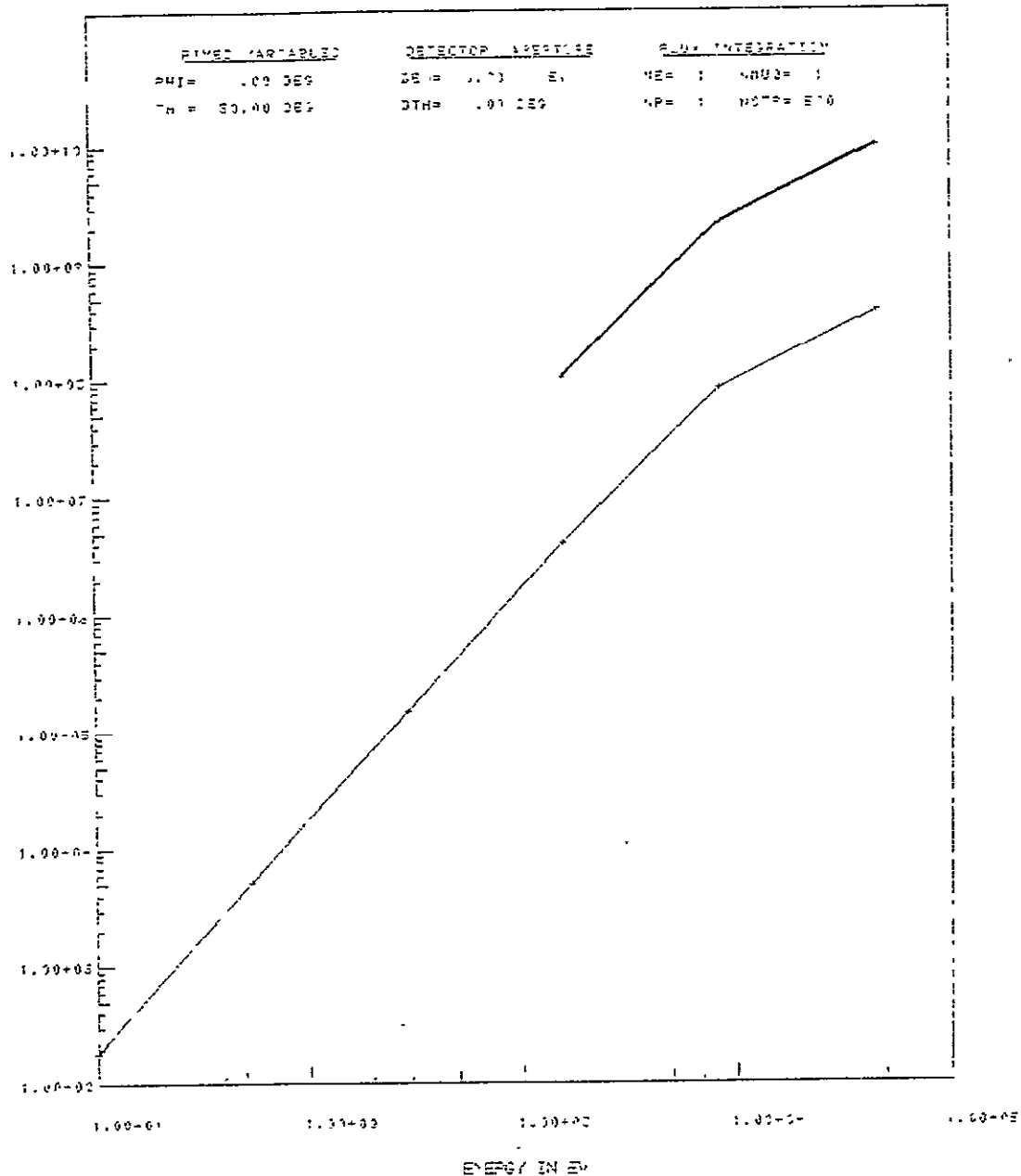


Figure 12. Particle detector plots show energy versus flux density. Detectors can also be located at any surface cell.

ORIGINAL PAGE IS
OF POOR QUALITY

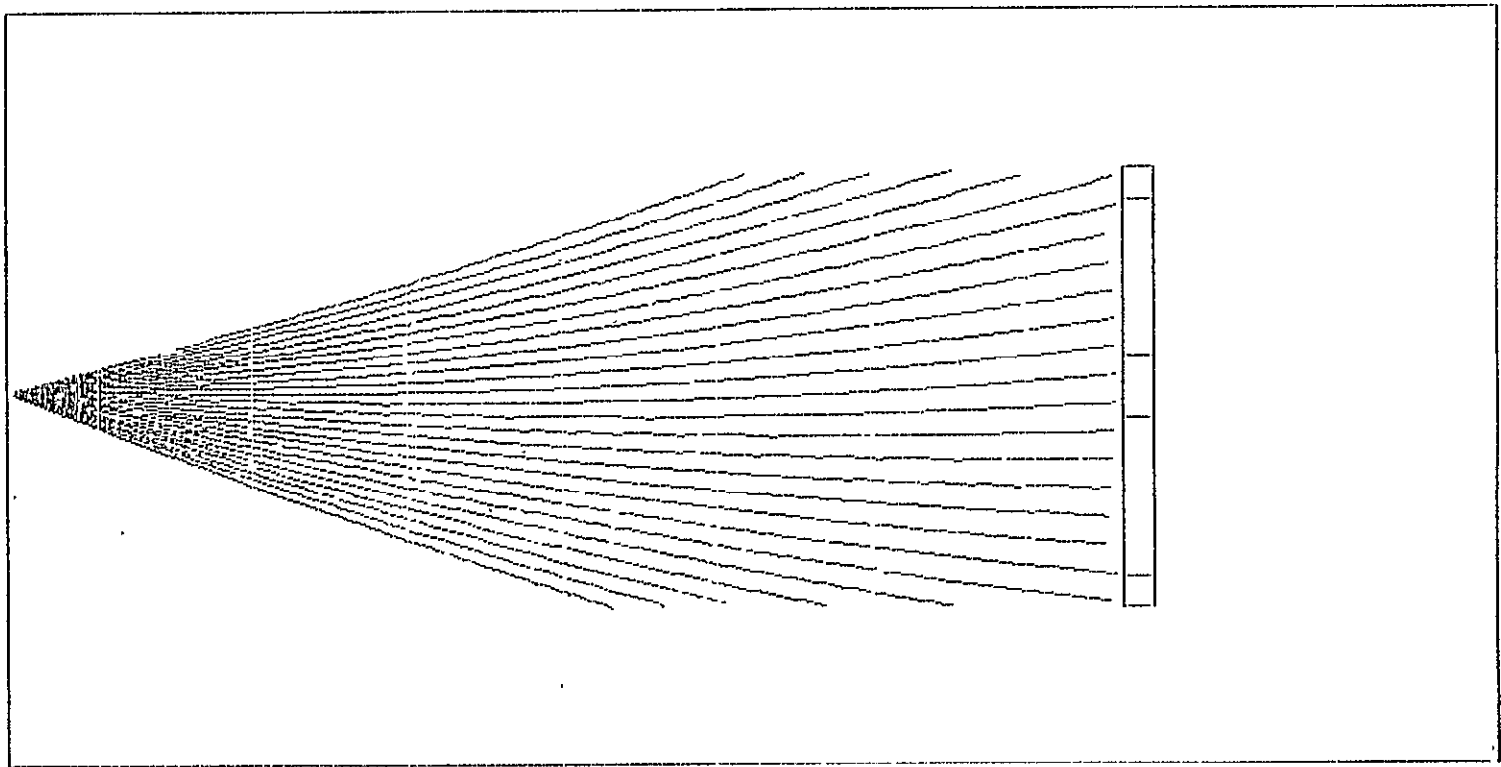


Figure 13. Graphic output for the test tank case includes trajectories of electrons from the source to the object.

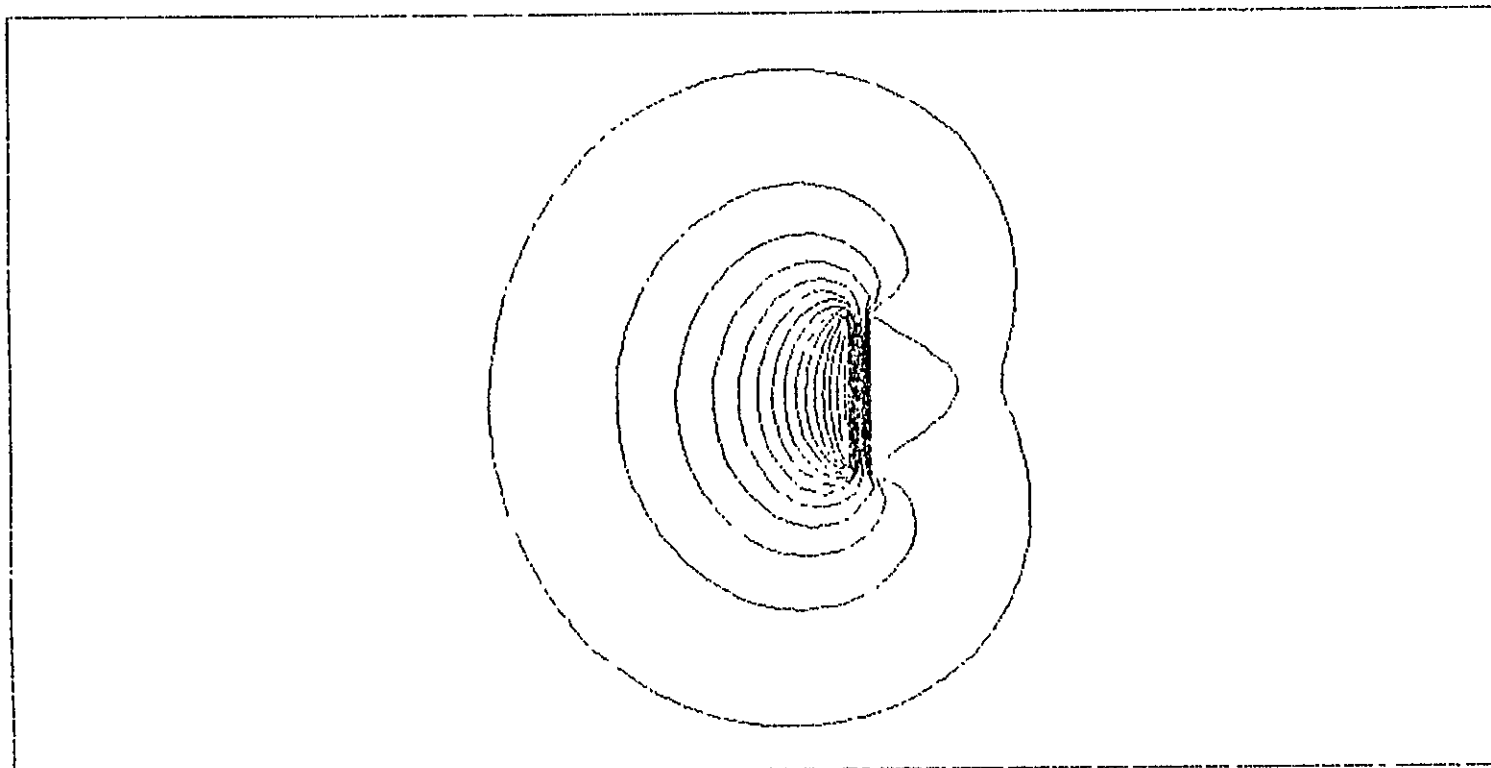


Figure 14. Potential contours around a fully charged teflon covered grounded plate in a ground test tank. An electron beam is coming from the left. Notice the fully formed potential saddle point to the right of the plate.

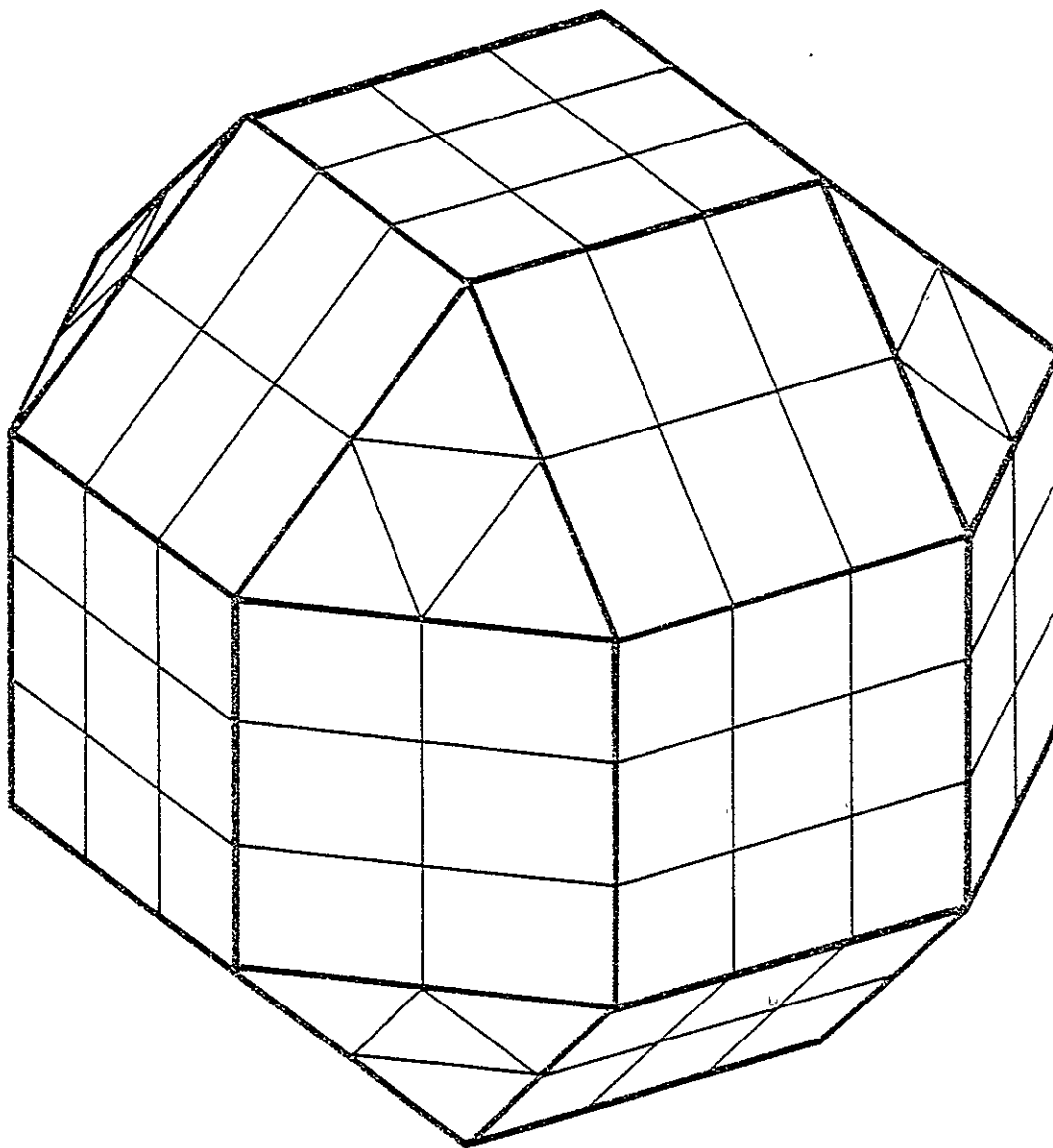


Figure 15. A NASCAP sphere — modeled as a twenty-six faceted object. This one is 3 meters in diameter with 158 surface cells and 144 surface nodes.

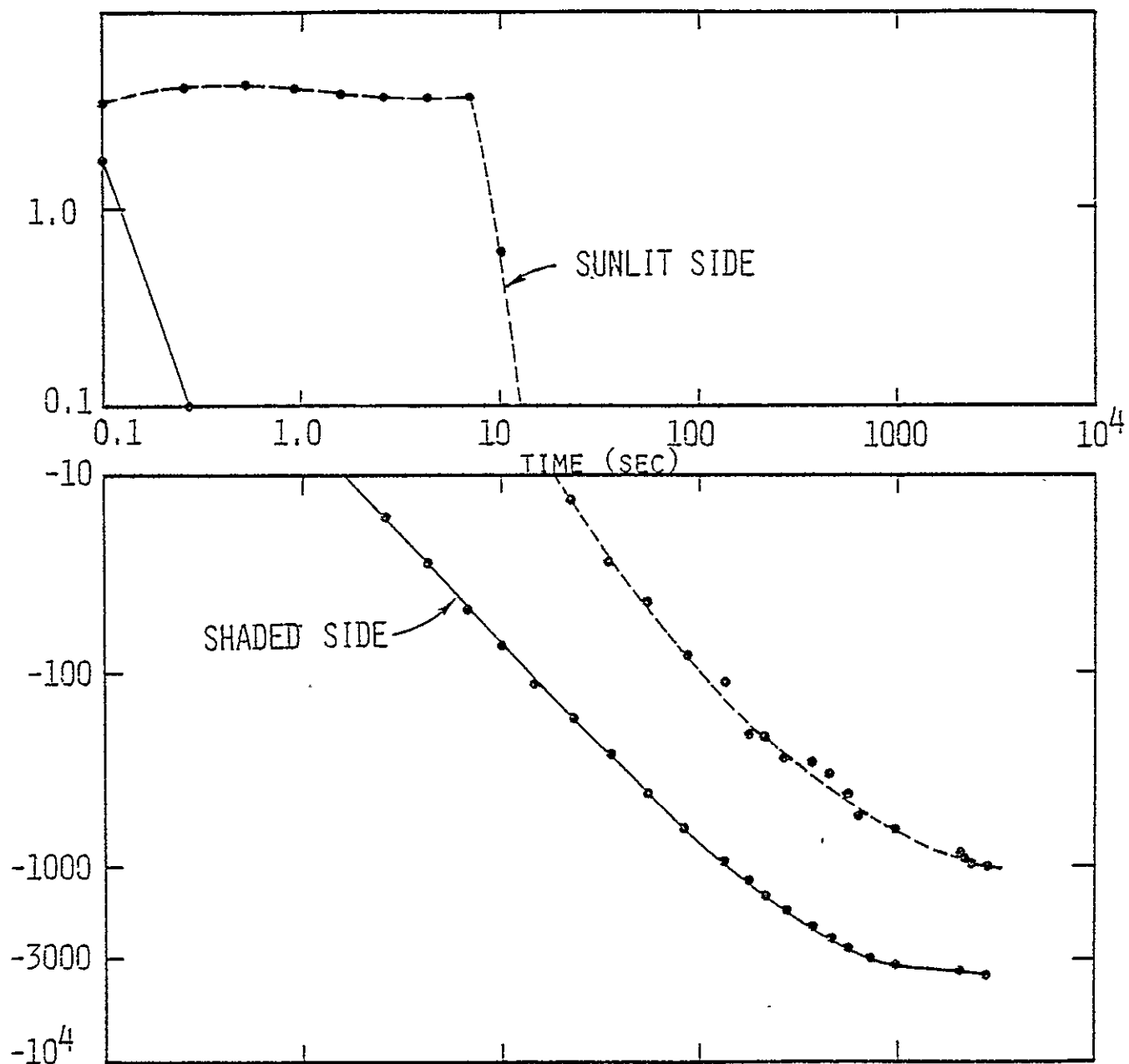


Figure 16. Potentials on shadowed and solar illuminated surfaces of a teflon sphere in a plasma ($N_e = 10^6/\text{m}^3$, $\theta = 20 \text{ keV}$).

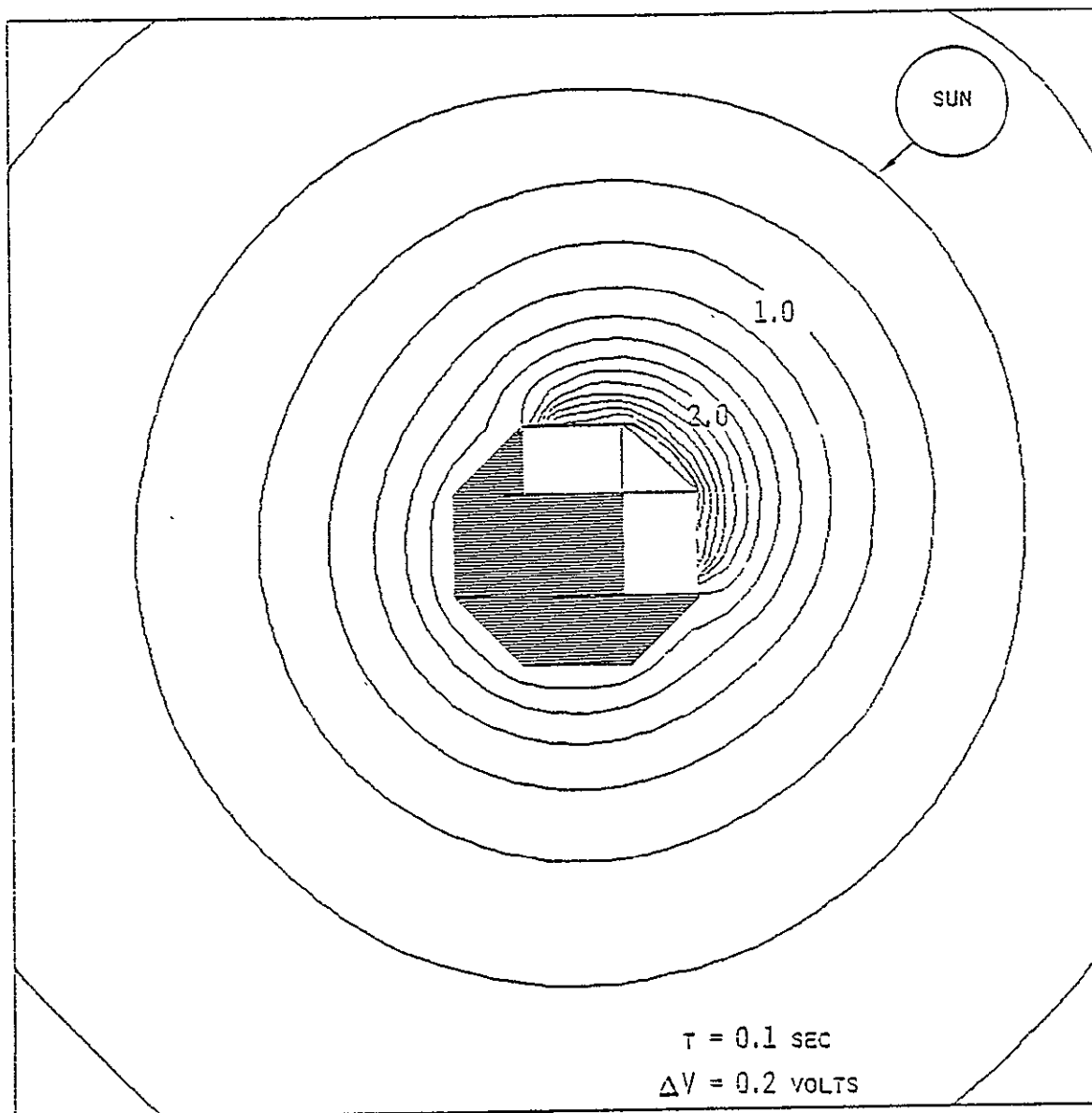


Figure 17. Potential contours about a sunlit sphere early in time.

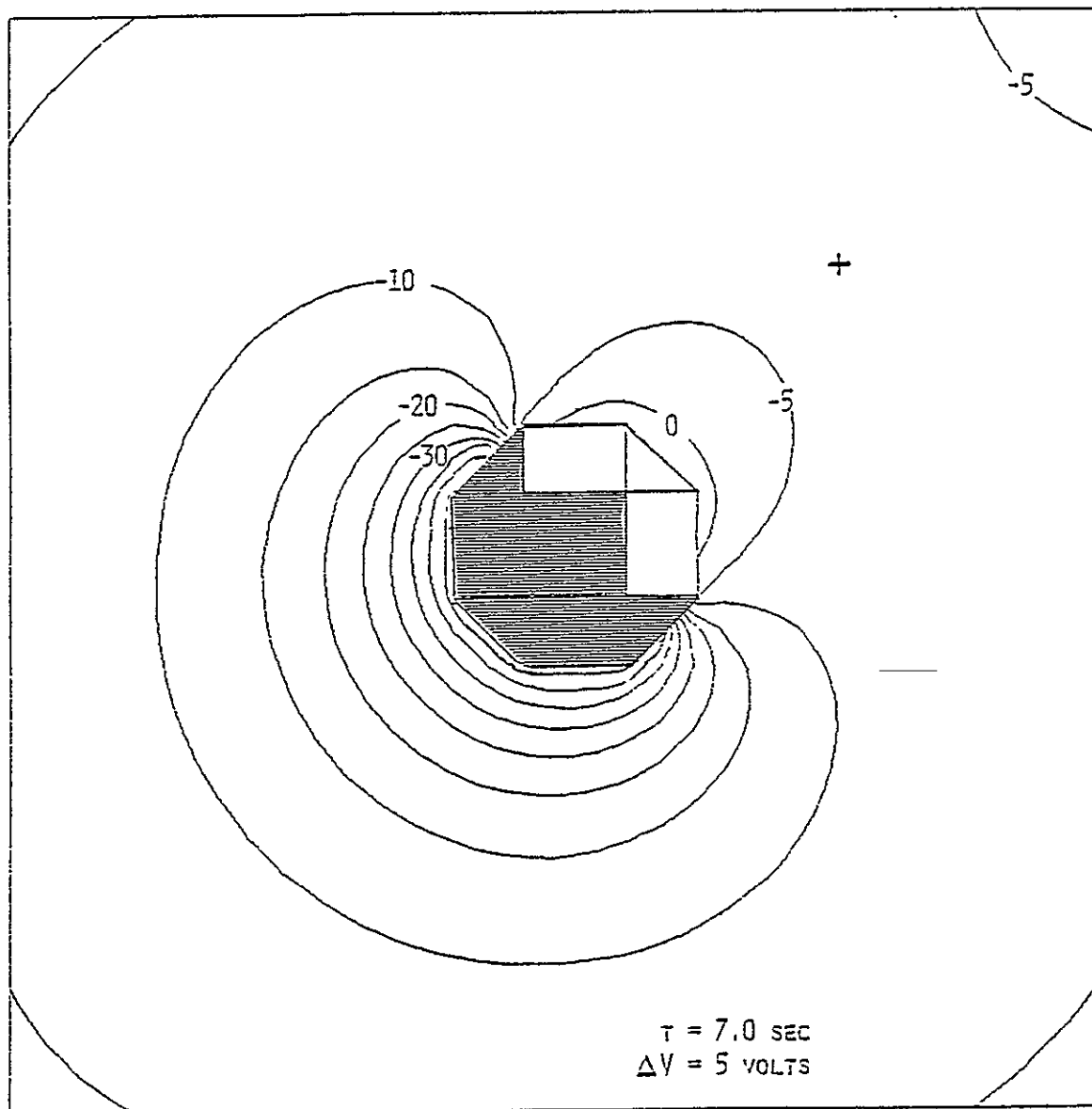


Figure 18. Potential contours around sunlit sphere showing early appearance of saddle point (x) at -5.6 volts.

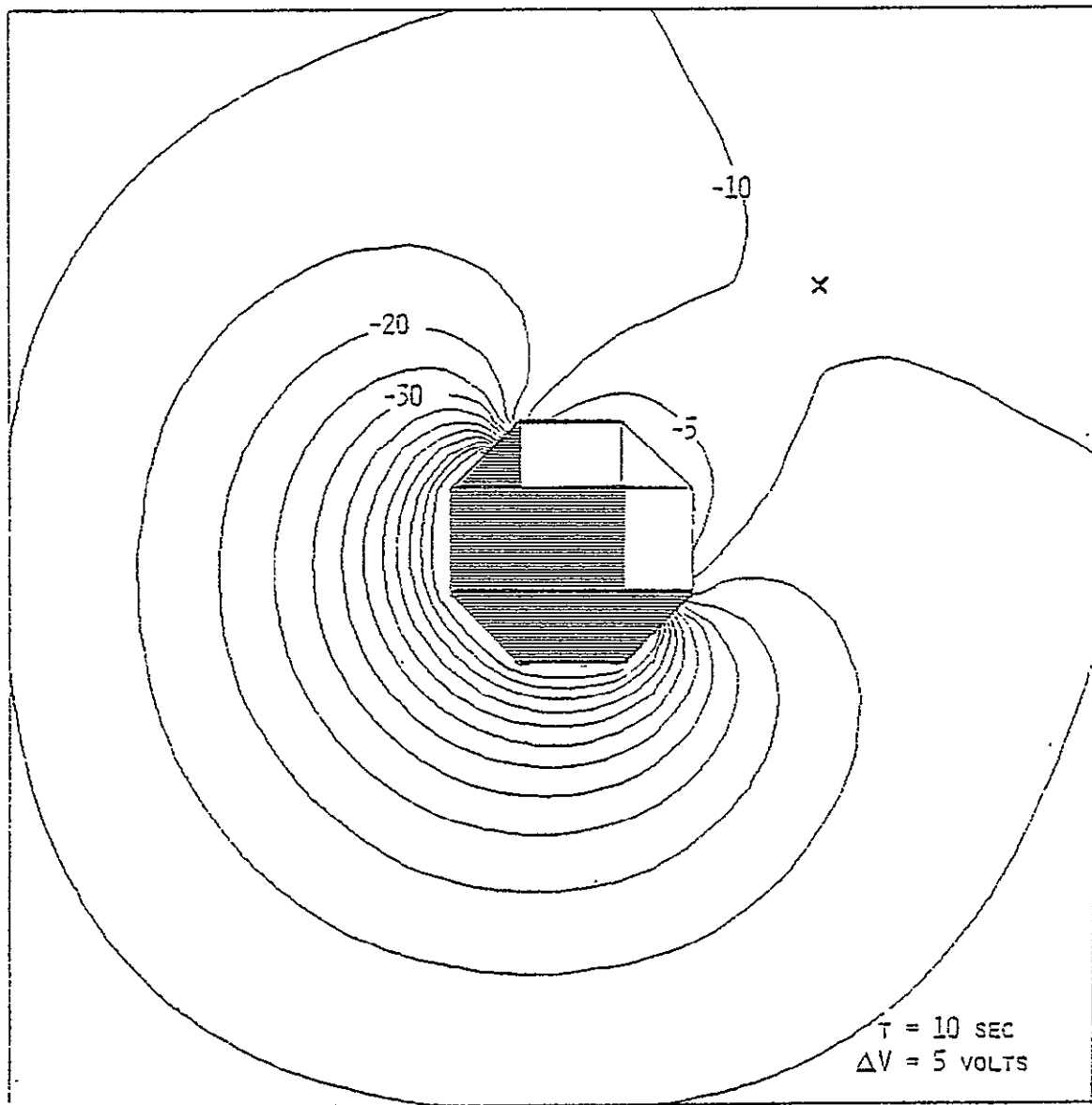


Figure 19. Potential contours around sunlit sphere showing fully formed saddle point at approximately -8 volts.

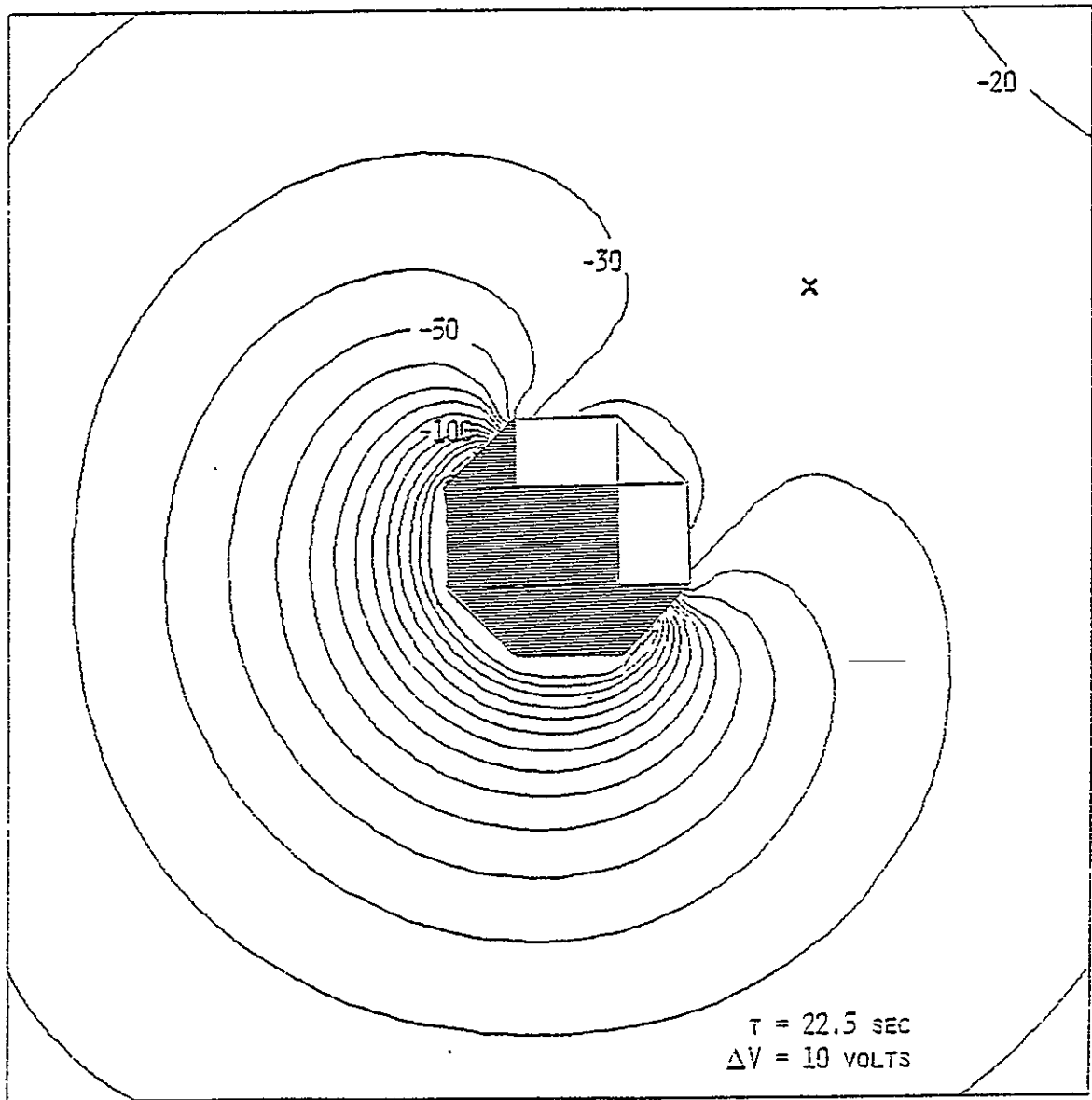


Figure 20. Potential contours about sunlit sphere showing saddle point at approximately -25 volts.

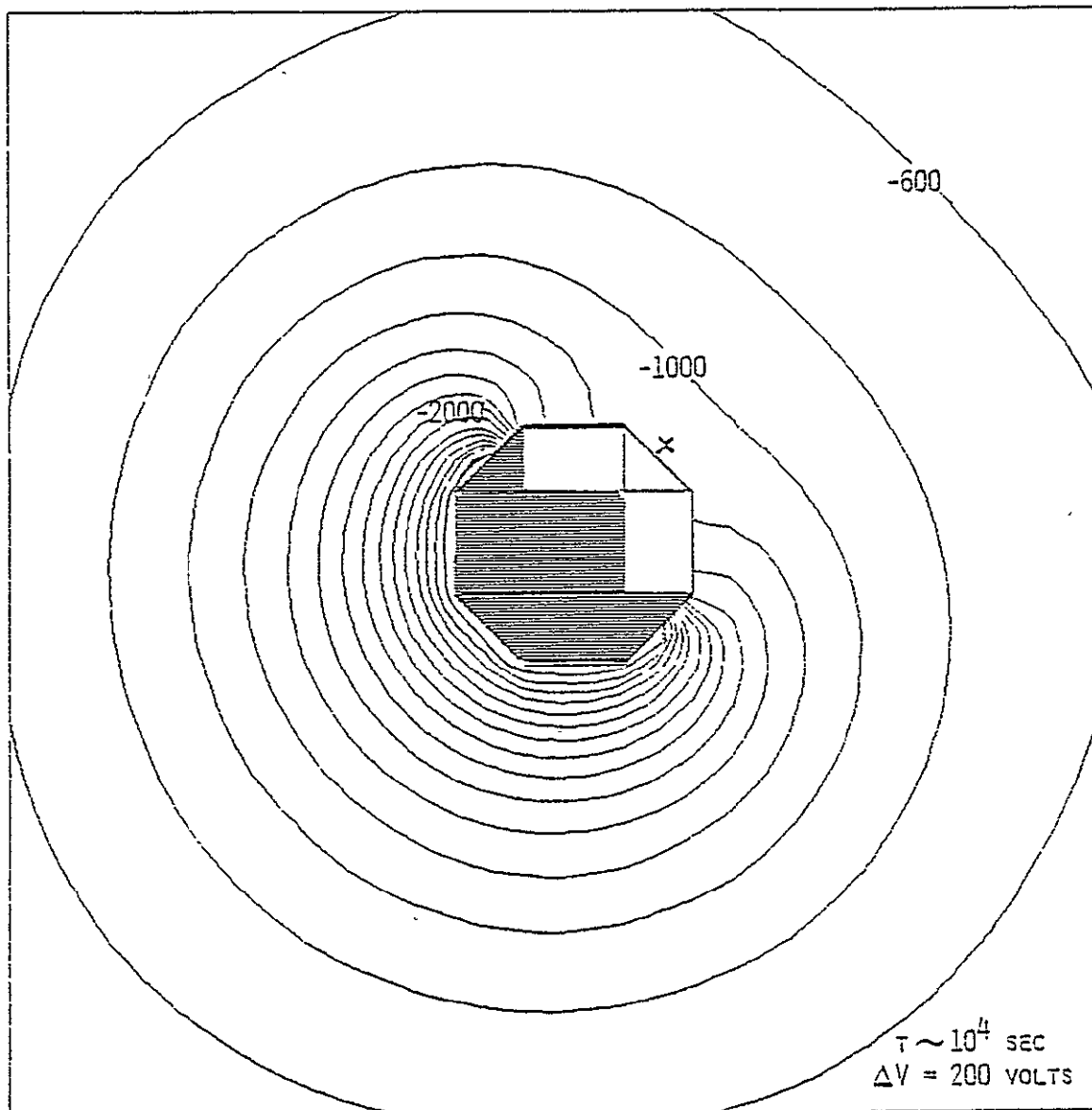


Figure 21. Steady state potential contours about sunlit sphere.

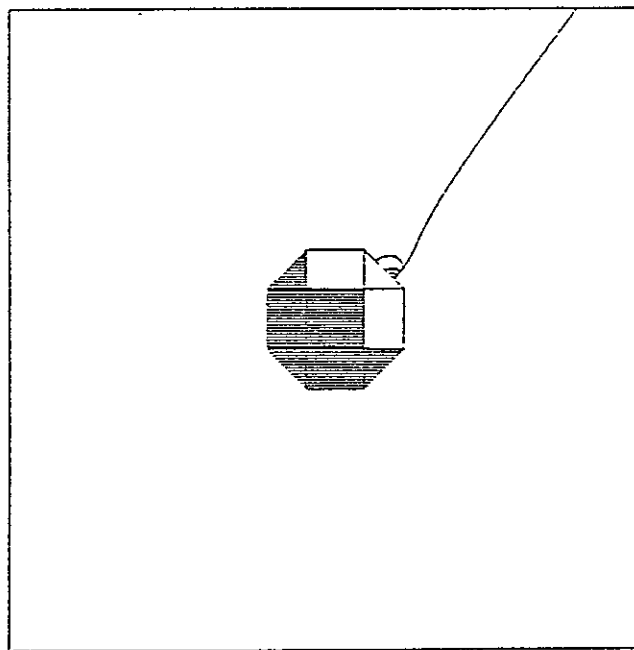
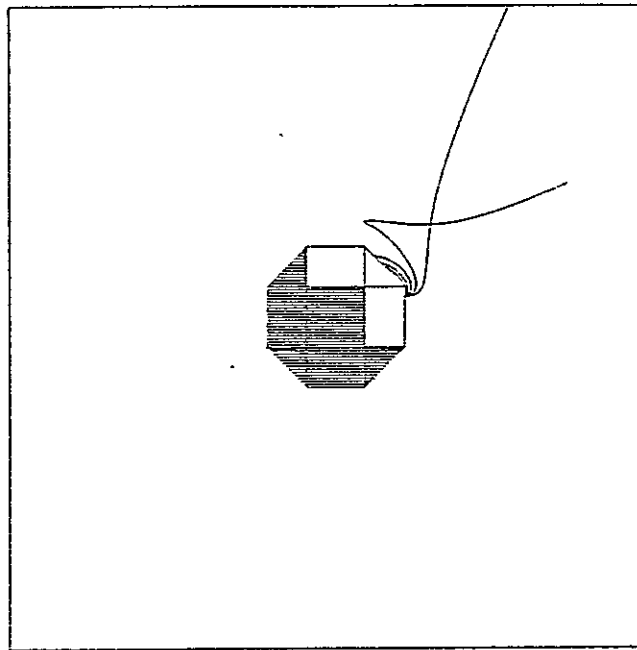


Figure 22. Trajectories of electrons emitted at various energies from fully charged sunlit sphere.

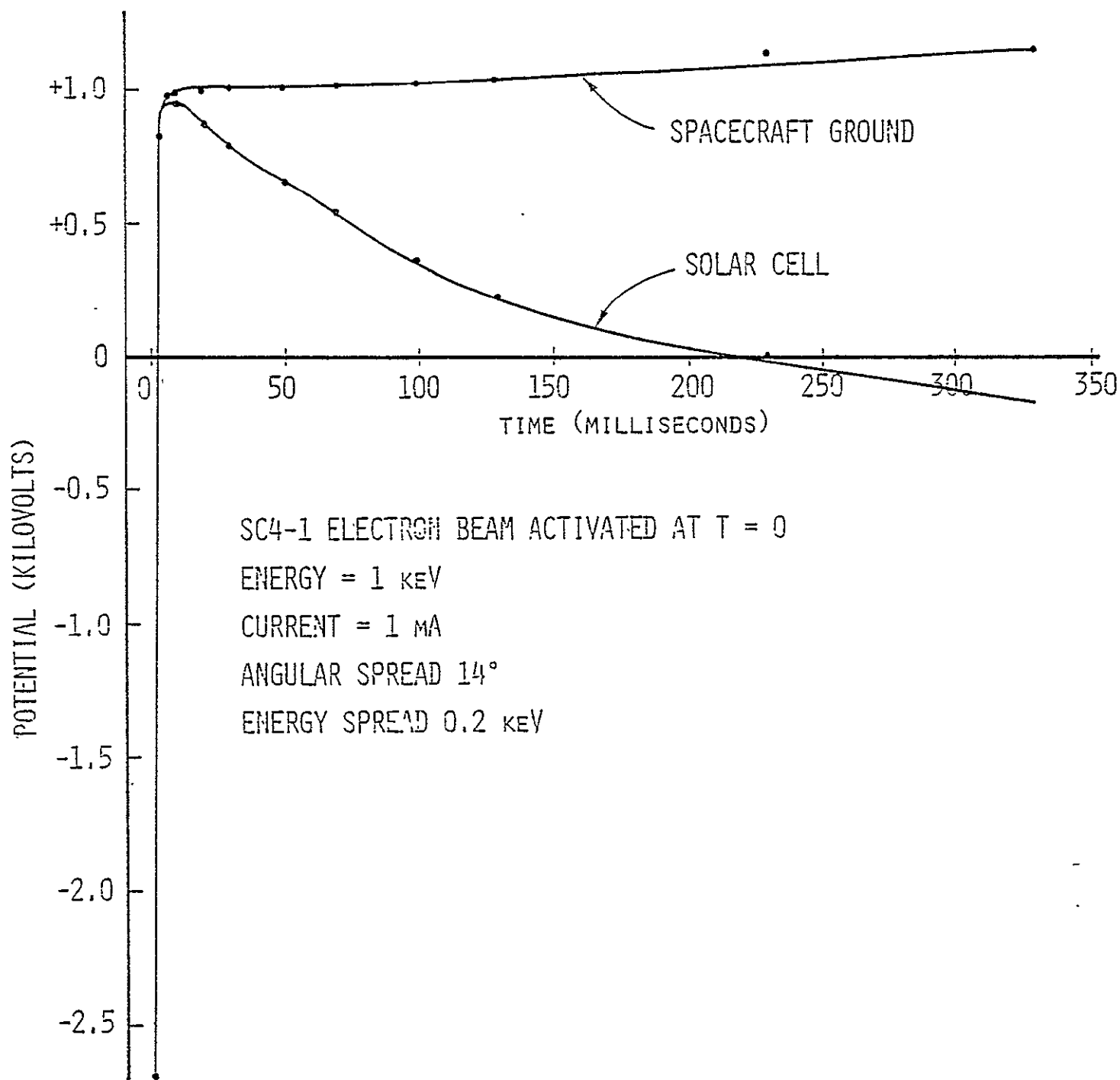


Figure 23. Active control simulation. A 1 mA particle emitter is activated with beam energy of 1 keV. The spacecraft goes from a negative 2.5 kV potential to positive 1.0 kV. Spacecraft ground remains at about that level while a solar cell on the surface falls back to a negative potential. *

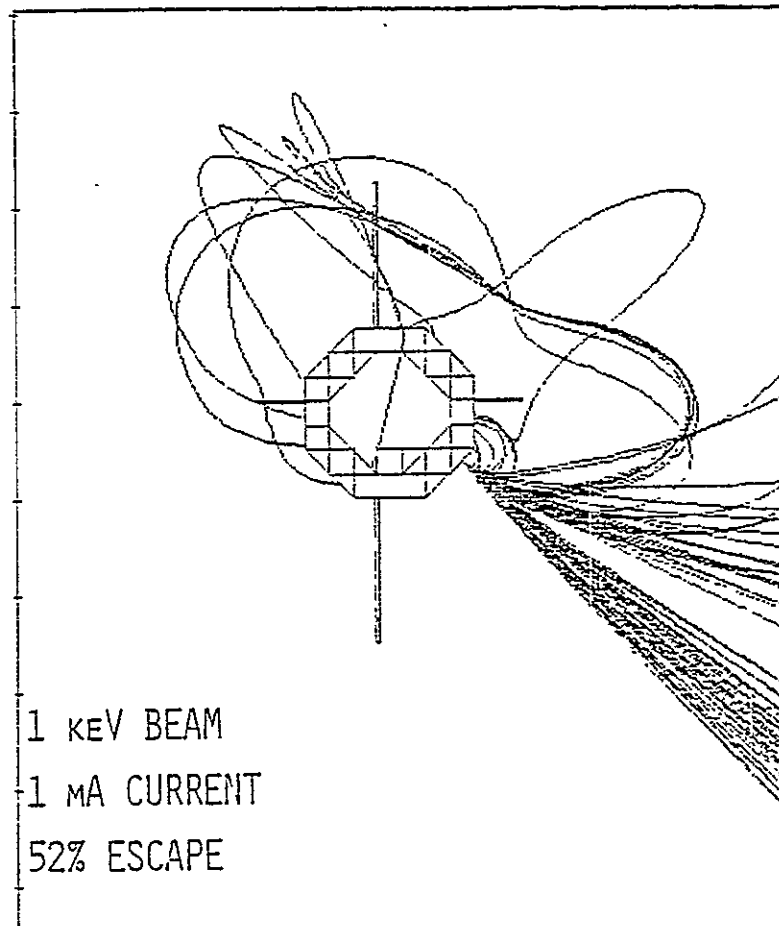


Figure 24. Particle emitter trajectory plot. Some of the emitted particles escape the spacecraft vicinity, while others return to various points on the surface.

*

ORIGINAL PAGE IS
OF POOR QUALITY

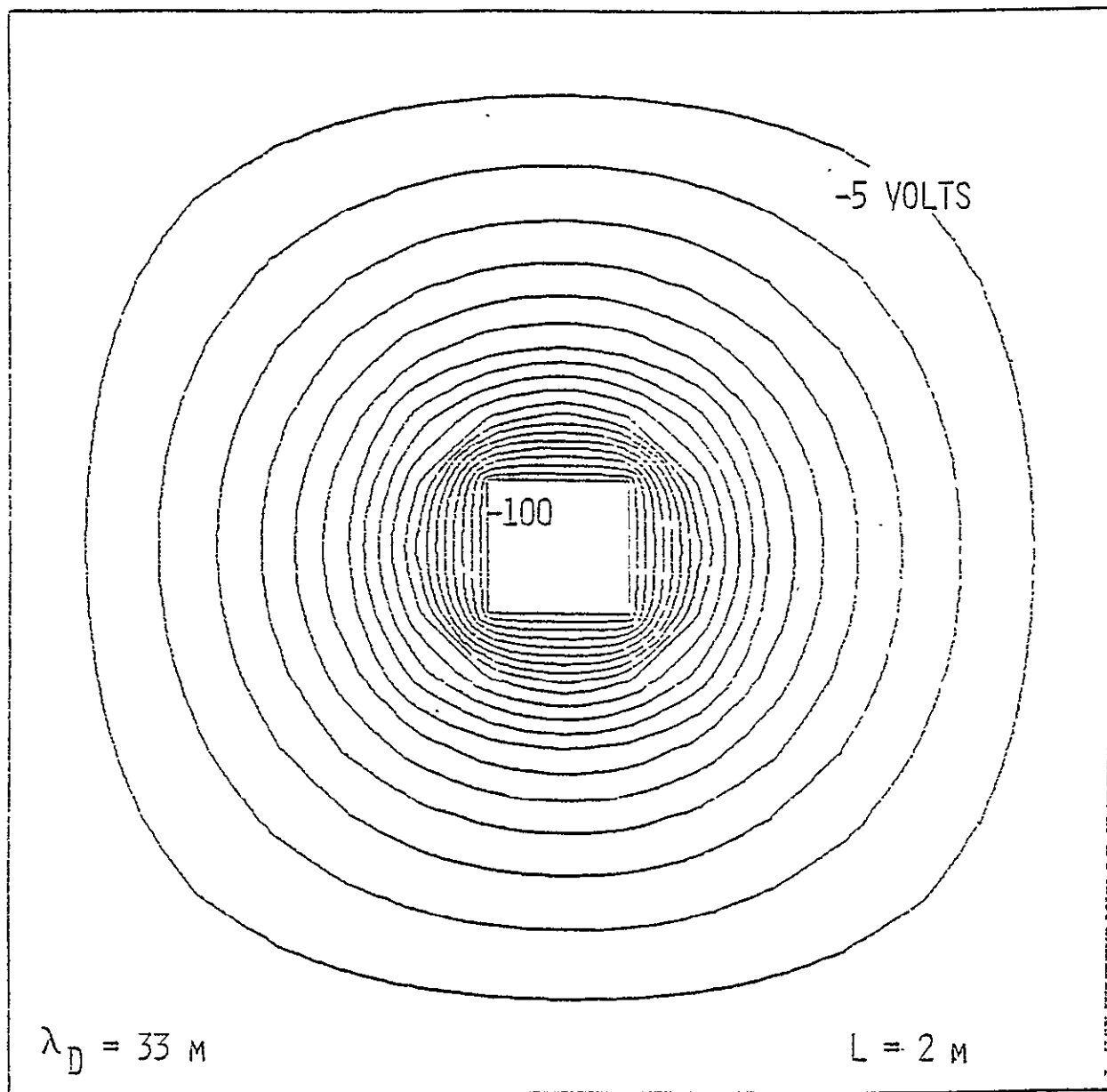


Figure 25. An approximate screening expression is employed to show shielding effects. Shown is a two meter cube charged to -100 V, in a plasma with Debye length of 33 meters.

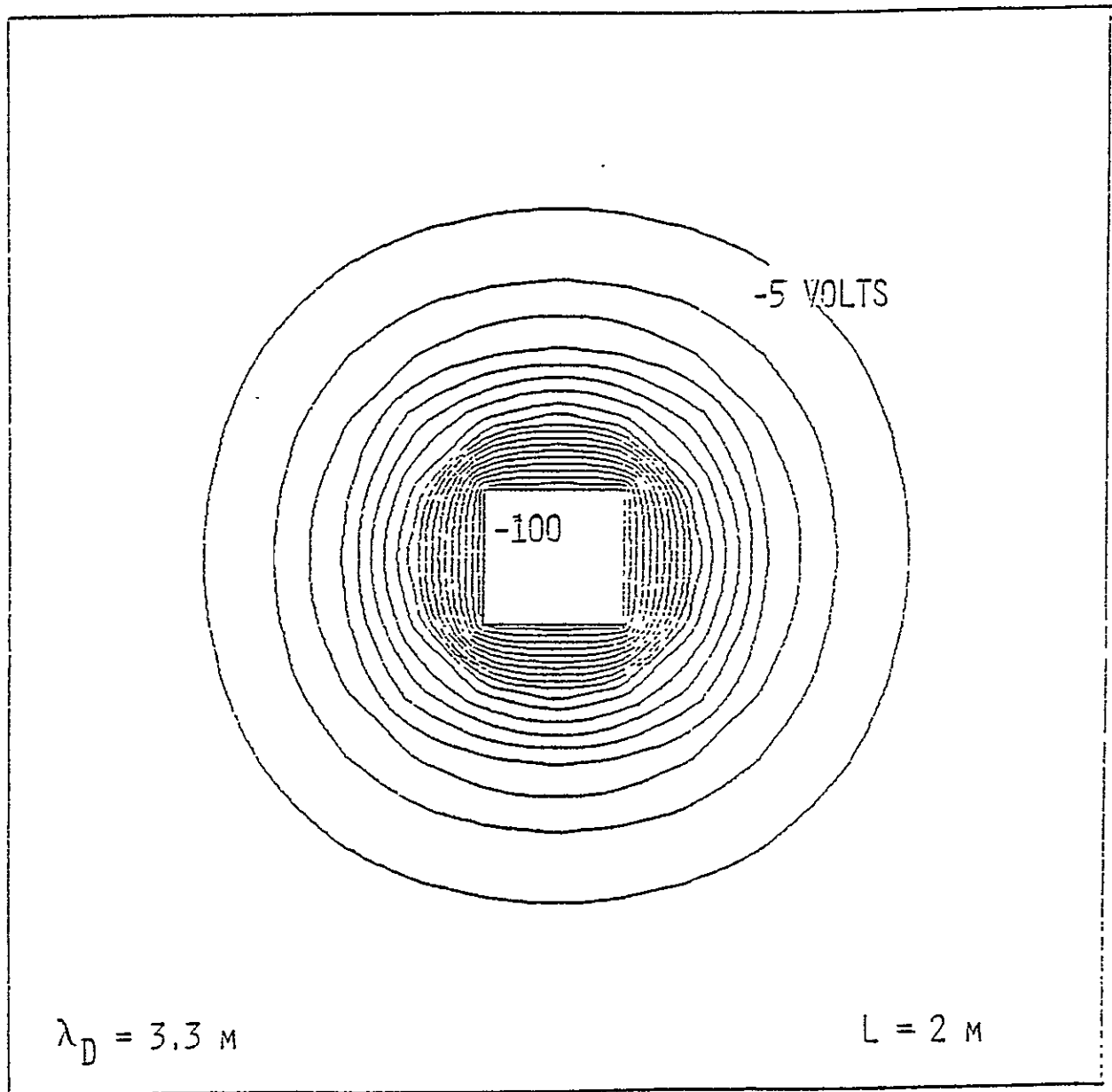


Figure 26. Here the same cube is charged once again to -100 V. This plasma has Debye length of 3.3 meters. The denser plasma leads to more significant shielding, and the potential falloff is steeper near the cube.

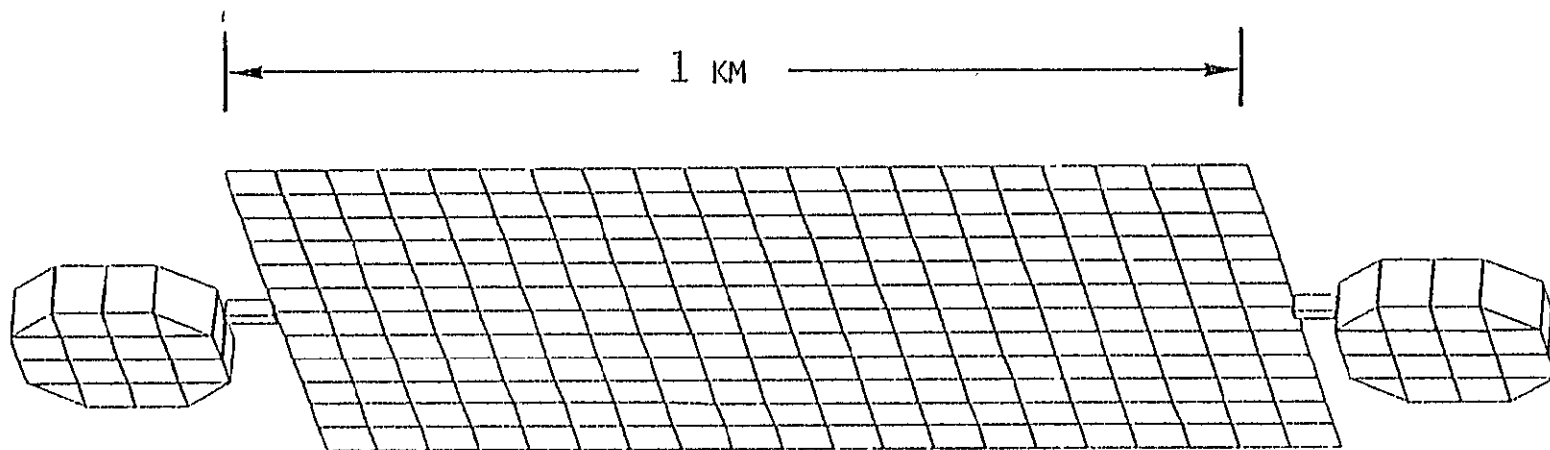


Figure 27. Solar power space station model.

3. INPUT

In March of 1978 the NASCAP input routines were substantially rewritten, resulting in greatly simplified running procedures. The changes were, first, modular program control, and second, default keyword values.

The total input required from a typical NASCAP user is first, a set of command words, and second, a set of three input files which describe the object, the environment, and the user-selected program options.

The command words allow modular program control. The user can perform object definition or not, or ask for a shadowing calculation or not, before any charging analysis is performed. User options can be changed between charging timesteps. The control word names and their functions are given in the NASCAP User's Manual (DRAFT).^[1]

The files used to describe the object and the environment remain essentially unchanged. The user options file is new. All of the program control options which used to be included in the NASCAP runstream are now in the options file. These are quantities like file numbers, graphics and printed output control, length of timesteps, and size of computational grid. Default values are supplied for all of these options. Options not specified assume the default values. This improvement has greatly simplified NASCAP use. Options and defaults are listed in the NASCAP User's Manual (DRAFT).^[1]

4. POTENTIAL SOLVER

Two major changes were made in the NASCAP potential solver. The first was to calculate the coproduct Au in terms of the volume elements rather than in terms of the nodal points. As a result, coding for "special elements" is greatly simplified. Boom-type elements and other new types can more easily be included. The second change improved the Poisson solver routines. The old conjugate gradient technique has been replaced by a scaled conjugate gradient technique. The new method takes approximately the same amount of computer time per iteration, but converges in far fewer iterations.

4.1 ELEMENT BY ELEMENT COPRODUCT

The element oriented coproduct (residual) calculation required major restructuring of many routines in the TRILIN section of the code. It was accomplished in the following manner.

The major task was to form the residuals for each potential value from volume or surface "stiffness matrices" operating on the potentials, as opposed to combining the element stiffness matrices together into a giant matrix. The advantage is that the local matrix bandwidth is reduced greatly. Additionally, NASCAP's I/O time has been greatly reduced, with only a modest increase in CPU time.

Algebraically, NASCAP now generates the residual vector \tilde{r} by the product

$$\tilde{r} = A\phi ,$$

where

$$A = \sum_{\text{elements } \{j\}} U_j ,$$

U_j being the stiffness matrix for element j . U_j connects only the nodal points that bound element j , and for a simple element is a symmetric 8×8 matrix. A is a sparse matrix with typically 27 nonzero entries in each row. Since only the residual vector \tilde{r} is used in the conjugate gradient potential solver, we need not store A but rather form the residual vector from element residuals, \tilde{r}_j .

$$\tilde{r} = \sum_j \tilde{r}_j$$

$$\tilde{r}_j = U_j \phi$$

Algebraically, the two techniques are identical

$$\tilde{r} = \sum_j \tilde{r}_j = \sum_j (U_j \phi) = \left(\sum_j U_j \right) \phi = A \phi .$$

But operationally within NASCAP, the formation of residuals element by element greatly simplifies the coding necessary to treat booms, struts, thin plates and surface subdivision.

4.2 SCALED CONJUGATE GRADIENT

The changes necessary to implement the scaled conjugate gradient method were mainly in the POTENT (subset of TRILIN) section of the code. This method improves convergence tremendously in cases of large zone size and very thin dielectric skins. It is accomplished by scaling the large coproduct

matrix so all diagonal elements are of order unity. We describe below three conjugate gradient methods for the solution of linear equations $Mx = y$: (1) the original NASCAP method; (2) a scaled method; and (3) a simple computational method equivalent to (2). Method (3) is used in the present version of NASCAP.

Method 1: The Ordinary Conjugate Gradient Method.^[2]

Define $r^0 = y - Mx^0$; $p^0 = r^0$

Then

$$\begin{aligned} a^i &= (r^i, r^i) / (p^i, M p^i) \\ x^{i+1} &= x^i + a^i p^i \\ r^{i+1} &= r^i - a^i M p^i \\ b^i &= (r^{i+1}, r^{i+1}) / (r^i, r^i) \\ p^{i+1} &= r^{i+1} + b^i p^i \end{aligned}$$

Method 2: The Scaled Problem.

Define matrix D : $D_{ij} = |M_{ij}|^{-1/2} \delta_{ij}$

Then solve (DMD) $(D^{-1}x) = Dy$

Define $r_s^0 = Dr^0$, $p_s^0 = r_s^0$, $M_s = DMD$

Then

$$\begin{aligned} a_s^i &= (r_s^i, r_s^i) / (p_s^i, M_s p_s^i) \\ (D^{-1}x)^{i+1} &= (D^{-1}x)^i + a_s^i p_s^i \\ r_s^{i+1} &= r_s^i - a_s^i M_s p_s^i \\ b_s^i &= (r_s^{i+1}, r_s^{i+1}) / (r_s^i, r_s^i) \\ p_s^{i+1} &= r_s^{i+1} + b_s^i p_s^i \end{aligned}$$

Finally,

$$x^n = D(D^{-1}x)^n$$

Method 3: Code Formulation

It is possible (and desirable) for computational purposes to formulate (2) in a manner which does not require the calculation of D or M_s .

Define $p_c^i = Dp_s^i$ and $r_c^i = D^{-1}r_s^i$. Then (2) can be written as

$$r_c^0 = y - Mx^0, \quad p_c^0 = D^2 r_c^0$$

Then

$$a_s^i = (D^2 r_c^i, r_c^i) / (p_c^i, M p_c^i)$$

$$x^{i+1} = x^i + a_s^i p_c^i$$

$$r_c^{i+1} = r_c^i - a_s^i M p_c^i$$

$$b_s^i = (D^2 r_c^{i+1}, r_c^{i+1}) / (D^2 r_c^i, r_c^i)$$

$$p_c^{i+1} = D^2 r_c^{i+1} + b_s^i p_c^i$$

Notice that in this code formulation the solution vector x and the matrix M need never be explicitly scaled.

5. LONGTIMESTEP OPTION - SUBROUTINE LIMCEL

During the past several months the analysis performed by the LIMCEL routine, invoked by specifying the LONGTIMESTEP option, has become a cornerstone of the NASCAP modeling effort. Through this analysis the applicability of NASCAP has been extended to physical regimes where we had not previously dared to attempt calculations; such as differential charging in sunlight and active control by high current emitters. In this chapter we discuss the need for the LIMCEL routine and the logic used in it, as well as some of the physical principles upon which the logic is based and some of the mathematics used to apply it.

5.1 NEED FOR THE LIMCEL ROUTINE

At the end of our first contract year a serious shortcoming of NASCAP was apparent: NASCAP could not satisfactorily simulate charging of an object initially dominated by emission of low-energy secondary- or photo-electrons. Other problems were also seen from time to time, such as a tendency for potentials to oscillate unstably in time and space, and an inability to handle materials with substantial conductivity.

The root of these problems lies in the disparate scales of time and distance (i.e., capacitance) which typify the charging process. The capacitance per unit area of a satellite is given by

$$\frac{C_{\infty}}{A} \approx \frac{\epsilon_0}{R} \approx 10 \text{ pf/m}^2 \quad (5.1)$$

where A is the satellite area and R its effective radius. Thus, with a typical charging current of 10^{-5} A/m² a satellite will charge at a rate

$$\dot{V} = J/C_{\infty} \sim 10^6 \text{ volts/sec.} \quad (5.2)$$

However, the process of true interest is differential charging, characterized by the thickness of dielectric coatings, $d \sim 10^{-4}$ m, leading to

$$\frac{C_D}{A} \approx \frac{\epsilon_0}{d} \sim 0.1 \text{ } \mu\text{f/m}^2 \quad (5.3)$$

Thus a similar current level produces

$$\dot{V}_D = J/C_D \sim 100 \text{ volts/sec.} \quad (5.4)$$

From Eq. (5.4) we see the desirability of performing simulations on a 0.1 - 10.0 second timescale, while Eq. (5.2) says that on such a scale small changes in net current will lead to wide, non-physical oscillations.

5.2 AN IMPLICIT CHARGING TREATMENT

The considerations of the previous section forced us to abandon the original "explicit" charging treatment used in the first version of NASCAP in favor of a more stable "implicit" algorithm. In simplified form, the basic equations are:

$$\text{Explicit: } C[V(t_2) - V(t_1)] = J(t_1)(t_2 - t_1) \quad (5.5a)$$

$$\text{Implicit: } C[V(t_2) - V(t_1)] = J(t_2)(t_2 - t_1) \quad (5.5b)$$

The obstacle to solving Eq. (5.5b) is that, while $J(t_1)$ is known, $J(t_2)$ is a complicated function of the unknown, $V(t_2)$. If, however, we make the approximation that

$$J(t_2) = J(t_1) + J'(V(t_2) - V(t_1)) \quad (5.6)$$

Eq. (5.5b) gives

$$V(t_2) - V(t_1) = \frac{J(t_1)(t_2 - t_1)}{C - J'(t_2 - t_1)} \quad (5.7)$$

If we take a case of $C = 10^{-11}$ f, $J(t_1) = 10^{-6}$ A, $t_2 - t_1 = 1$ sec, $J' = -10^{-8}$ A/volt ($J' < 0$ is required for physical stability) we find

$$\text{Explicit: } V(t_2) - V(t_1) = 10^5 \text{ volts} \quad (5.8a)$$

$$\text{Implicit: } V(t_2) - V(t_1) = 99.9 \text{ volts} \quad (5.8b)$$

That (5.8a) is unstable while (5.8b) is stable is indicated by plugging into (5.6), giving $J(t_2) = 10^{-3}$ A (explicit), or $J(t_2) = 10^{-9}$ A (implicit).

Implementation of the implicit algorithm in NASCAP is made more complex than solution of scalar equation (5.5b) by the matrix-vector nature of the charging problem. Far more difficulties, however, are raised by careful assessment of Eq. (5.6). For some processes, such as linear surface and bulk conductivity, (5.6) is exact and the matrix J' is known. For others, such as current collection from a plasma, it is adequate at best, and determination of J' is not a trivial matter. For still others, such as cutoff of low energy emitted electrons or emitter currents by potential barriers, (5.6) is totally inadequate. When these processes dominate, we must take the approach of estimating the final potential based on known conditions and determining a mean current consistent with the final potential.

5.3 OVERALL STRUCTURE OF THE LIMCEL ANALYSIS

The objective of the LIMCEL analysis is to determine appropriate coefficients and boundary conditions for, and to solve, the equation

$$C[V(t_2) - V(t_1)] = [J(t_2) + \sigma V(t_2)] (t_2 - t_1) \quad (5.9a)$$

which can also be written (using (5.6))

$$\left[\frac{\tilde{C}}{t_2 - t_1} - \tilde{\sigma} - \tilde{J}' \right] [\tilde{V}(t_2) - \tilde{V}(t_1)] = \tilde{J}(t_1) + \tilde{\sigma} \tilde{V}(t_1) \quad (5.9b)$$

Here \tilde{J} denotes the net current excluding current due to conductivity processes. On entry to LIMCEL the capacitance and conductivity matrices \tilde{C} and $\tilde{\sigma}$ are known, as is the initial potential $\tilde{V}(t_1)$. The explicit external current $\tilde{J}(t_1)$ is also known, although some recentering is required. Additional information used by LIMCEL includes potentials at points external to the satellite, the portion of $\tilde{J}(t_1)$ due to low energy emitted electrons, and information concerning active control emitters on the spacecraft. After an optional discharge analysis, LIMCEL returns the left hand side of Eq. (5.9a) to TRILIN for use in updating the total charge vector and POTENT then performs the full calculation of new potentials on and about the spacecraft. Within LIMCEL, Eq. (5.9b) is solved (usually several times) using the "Incomplete Cholesky Conjugate Gradient" (ICCG) method.^[3]

The LIMCEL analysis then proceeds in the following six phases (see block diagram, Figure 5.1):

1. Preliminary Phase. Prior to beginning the timestepping process a lumped-circuit-element model (Figure 5.2) of the spacecraft is constructed. The nodes of this model are the conducting satellite segments (maximum of 7) and the grid points and subdivision points located on insulating surfaces (maximum of 1024). (A further restriction is that the number of non-zero matrix elements in Eq. (5.9b) may not exceed 9537.)
2. Explicit Phase. The right hand side of (5.9b) is evaluated using known information. Also, data concerning low energy electron emission, external electric fields, and emitters is processed for later use. If no LONGTIMESTEP analysis was requested, control is returned to TRILIN.

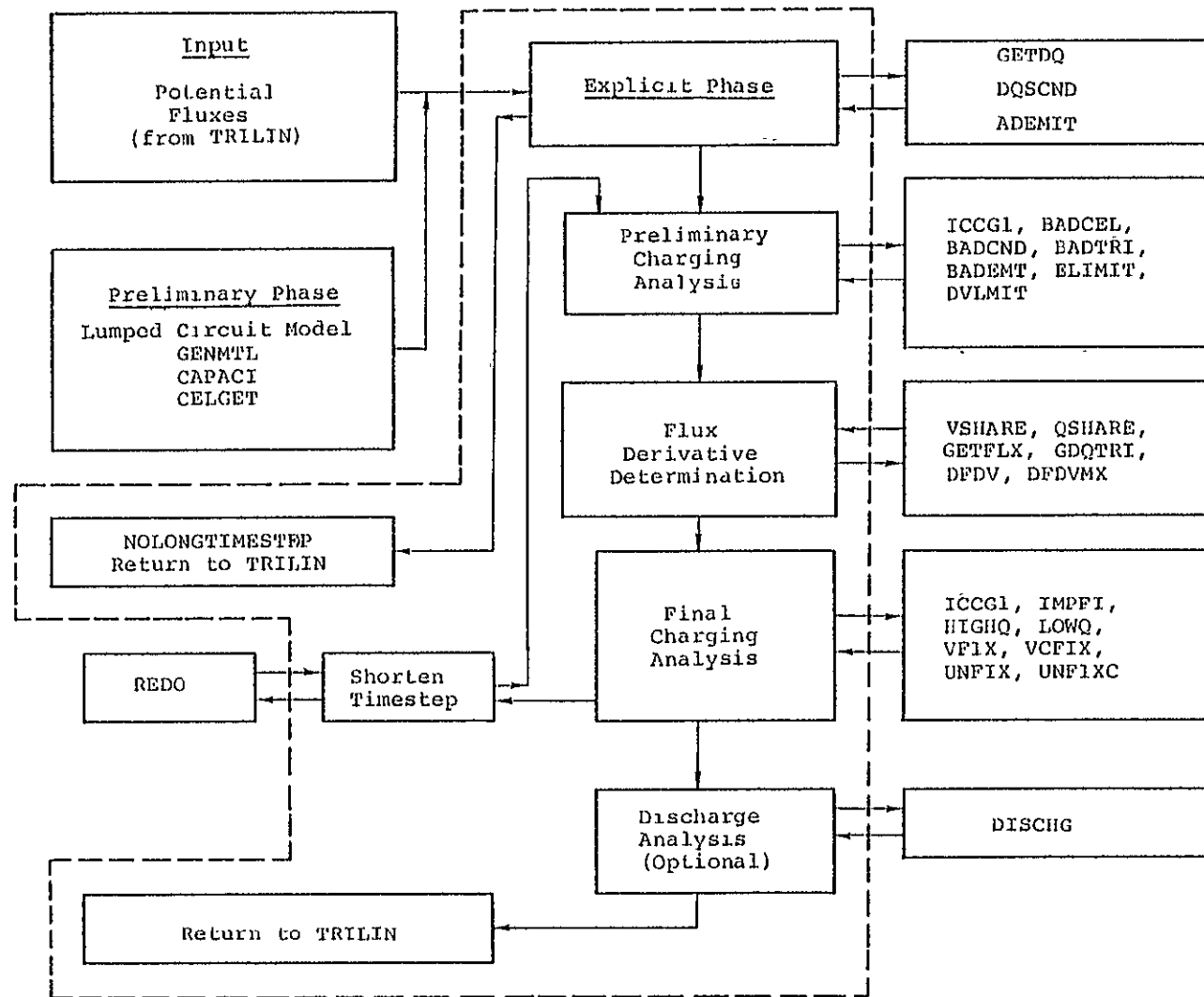


Figure 5.1. Block diagram of LONGTimestep option. Subroutine LIMCEL is enclosed by the dashed line.

3. Preliminary Charging Analysis. Those nodes for which approximation (5.6) is likely to be in error are identified and preliminary estimates of their final potentials are made. A set of "trial" potentials for all the nodes is formed for use in the next phase.
4. Flux Derivative Determination. The fluxes to the surface cells are calculated using "trial" potentials for the purpose of determining the matrix J'_{\sim} . The flux derivative matrix is assumed diagonal.
5. Final Charging Analysis. Equation (5.9b) is solved repeatedly for the final potentials, and the left hand side of (5.9a) is evaluated for the mean currents. Those constraints found to be unnecessary are removed. Nodes which remain constrained are set at potentials consistent with their mean currents. The left hand side of (5.9a) is evaluated for return to TRILIN.
6. Discharge Analysis (Optional). The discharge analysis is described elsewhere.

Throughout the LIMCEL segment use is made of the potential limiting input parameter, DVLIM. The "trial" potentials and flux derivatives are found consistent with the notion that DVLIM is the maximum potential change desired. If, during the final charging analysis, any conductor displays a greater potential change, the LIMCEL analysis is repeated with a shortened timestep.

5.4 PRELIMINARY PHASE: LUMPED CIRCUIT MODEL

The spacecraft lumped-circuit model constructed by NASCAP is shown schematically in Figure 5.2. The nodes of the circuit represent either conducting segments of the spacecraft, or points located on dielectric surfaces. The circuit elements are:

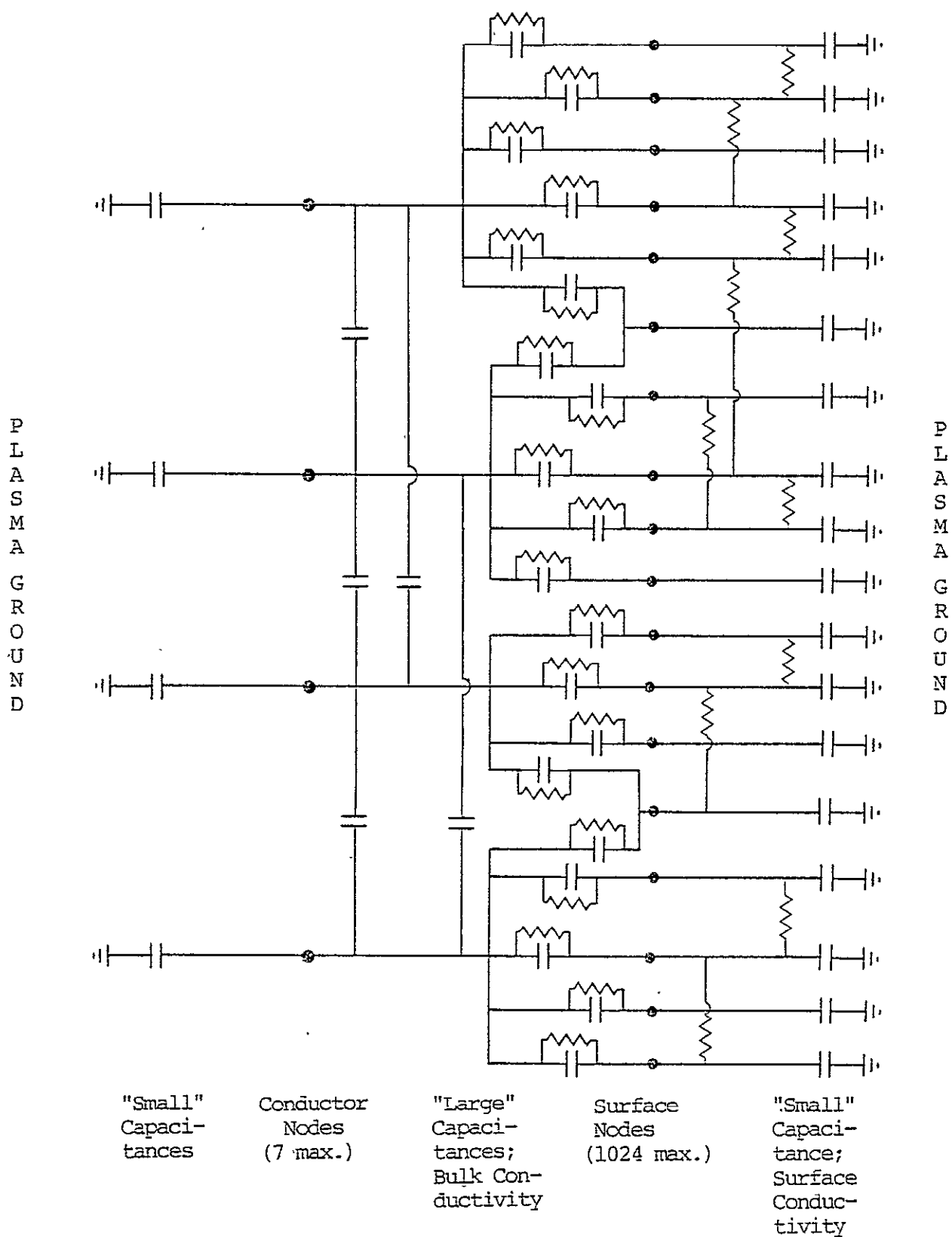


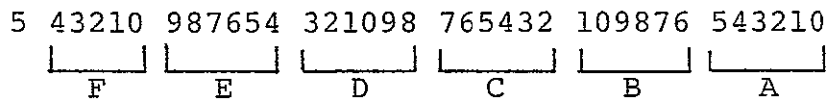
Figure 5.2. Lumped-circuit model of spacecraft constructed by NASCAP and used for LONGTIMESTEP option.

- a. "Small" capacitances, coupling circuit nodes to plasma ground.
- b. "Large" capacitances, coupling surface nodes to conductors, or conductors to each other.
- c. Resistors representing bulk and surface conductivity processes.

The matrix $[C - \sigma]$ corresponding to this network is sparse, symmetric, and positive definite — ideal for treatment by the ICCG inversion algorithm.

Formation of the circuit matrix begins with subroutine GENMTL, called automatically following OBJDEF from NASCAP through DRISCM. GENMTL first forms the PTLIST array (see Figure 5.3) listing all grid points and subdivide points on dielectric surfaces. (Boom nodes are added later by BOOM2.) The PTLIST establishes the index numbers of the circuit nodes in the circuit potential vector; conductor nodes are indexed sequentially following the surface nodes. Next the "matrix skeleton" is formed. The skeleton is an integer array indicating the non-zero matrix elements: the negative-entry (-i) corresponds to the ith diagonal element, and is followed by an arbitrary number of positive entries (j) (in order) indicating off-diagonal matrix elements between nodes i and j. GENMTL forms only those rows of the matrix corresponding to PTLIST nodes; rows corresponding to conductor nodes are added later by LSTMAT, taking into account conductors which are biased or held at fixed potential. Finally, GENMTL forms the surface conductivity matrix, σ_s .

Further development of the circuit model occurs in response to the CAPACI keyword. Subroutine CAPACI calls POTENT to calculate the potential about the spacecraft with a unit charge on spacecraft ground. This information is then used by CELGET to calculate the overall body capacitance, C_∞ ,



<u>Field</u>	<u>Bits</u>	
A	5-0	Conductor index; zero for multiconductor node.
B	11-6	Not used.
C	17-12	Z-coordinate } or subdivide node index.
D	23-18	
E	29-24	X-coordinate; 77 ₈ for subdivide nodes.
F	34-30	Grid index (boom nodes only).

Figure 5.3. Surface node list (PTLIST) entry format.

and to apportion it among the circuit nodes:

$$\begin{aligned}
 C_{\infty} &= \frac{Q}{V} = \frac{1}{V} = \frac{\epsilon_0}{V} \int \vec{E} \cdot \hat{n} \, ds \\
 &= \frac{\epsilon_0}{V} \sum A_i \vec{E}_i \cdot \hat{n}_i = \sum C_{\infty}^i
 \end{aligned}
 \tag{5.10}$$

where the sum runs over surface cells. The surface cell quantities C_{∞}^i are recentered among the surface nodes and conductors to obtain the circuit matrix quantities. Before exiting CELGET, the far right of Eq. (5.10) is renormalized to the far left. The renormalization factor is printed, and should be unity to within about 1 percent. (A renormalization factor substantially different from unity should not be accepted if the user plans to use the LONGTIMESTEP option.) Subroutine CELGET also forms the array of "large" capacitances for the surface nodes, and the bulk conductivity matrix elements.

Included in the PTLIST array are surface nodes having capacitive/resistive coupling to more than one conductor. These multiconductor points (maximum of 128) are indicated by a zero conductor index in their PTLIST entries. These entries are duplicated in the array MULTCN, which serves as a map to the arrays CMULT and SIGMLT in which the matrix elements are stored.

5.5 EXPLICIT PHASE

The explicit phase of LIMCEL (subroutines ADEMIT, GETDQ, and DQSCND) is concerned with transforming the relevant information available in NASCAP to arrays paralleling the circuit node list. ADEMIT is concerned with modification of charging by active control particle emitters. In cases where particles return to the satellite surface the fluxes are appropriately modified. The height and location of potential barriers seen by emitted particles, together with other information, is stored in the /EMITR2/ common block.

GETDQ is the major routine of this phase. It forms the following arrays:

- VPTS - the potential on each surface node.
- DQO - the net explicit charge accumulation on each circuit node, including emitter current and bulk conductivity.
- DQEMIT - the low-energy electron current emitted from each circuit node.
- EPTS - the effective electric field at each node:

$$EPTS(j) = \sum_i s(i) \vec{E}_i \cdot \hat{n}_i / \sum_i s(i) \quad (5.11)$$

where the sum is over surface cells, and $s(i)$ is the low energy electron current from cell i attributable to node j .

Finally, DQSCND modifies the explicit charges DQO to reflect the explicit contribution of surface conductivity.

5.6 PRELIMINARY CHARGING ANALYSIS

The preliminary charging analysis serves two functions: (1) to identify those circuit nodes for which Eq. (5.6) is an invalid approximation ("bad" nodes), and (2) to determine a set of "trial" potentials for use in the next phase. The first operation is to find the "bad" nodes. A node is marked "bad" if

1. It is a conductor to which a particle emitter is grounded, or
2. Its explicit current is caused to be positive by low energy electron emission, and its potential or effective electric field is positive (electron attracting).

Those nodes which have not been marked bad but are nonetheless electron attracting have their low energy emitted electron current reduced. Trial potentials are determined for the "bad" nodes such that secondary electrons or high energy emitted

currents will marginally escape, subject to the constraint that the potential change can be no greater than DVLIM. The ICCG potential solver is then called, and the preliminary trial potentials inspected for additional "bad" nodes. (For example, an uncharged, sunlit satellite initially has no "bad" nodes. However, it may return from ICCG charged many kilovolts positive, so that all photoemitting nodes will then be marked "bad".) If additional nodes are found "bad", ICCG generates a new set of preliminary trial potentials. Finally, the trial potentials are formed by subjecting the ICCG result to the constraint that no node may have a potential change larger than DVLIM.

5.7 DETERMINATION OF TRIAL POTENTIALS FOR FIXED NODES

When a circuit node is marked "bad" its potential is to be fixed such that the offending particle can marginally escape. Specializing to electrons (for ions, sign change and interchange of min and max are appropriate), that means

$$V_i = V_{\min} + \varepsilon/e \quad (5.12)$$

where ε is an energy characterizing the particle emission, and V_{\min} is the minimum potential occurring on an escaping particle trajectory at the next timestep. During the preliminary charging analysis the energy ε is set to zero for low-energy electrons and near the maximum emitter energy for emitters. This provisional value is to be refined during the final charging analysis.

Determination of the potential V_{\min} presents a more difficult problem. Since V_{\min} occurs somewhere in space, it is clearly beyond the scope of the circuit model. We approach this problem by dividing it into two questions:

1. What is the current value of this potential, $V_{\min}^{(0)}$?

2. How is this value likely to change in proceeding to the next timestep?

In answering these questions the emitter case is clearly the easier, since particle tracking information is available to give the value of $V_{\min}^{(0)}$, and the location of $V_{\min}^{(0)}$ sheds light on the second question. For the low energy emission case we guess

$$V_{\min}^{(0)} = \min(0, V_i^{(0)} - E_i^{(0)} \Delta x) \quad (5.13)$$

where $V_i^{(0)}$ is the current node potential, $E_i^{(0)}$ the current effective field [Eq. (5.11)], and Δx the mesh spacing. We then address the second question by supposing

$$V_{\min} - V_{\min}^{(0)} = \alpha (V_i - V_i^{(0)}) \quad (5.14)$$

so that Eq. (5.12) becomes

$$V_i = V_{\min}^{(0)} + \alpha (V_i - V_i^{(0)}) + \epsilon/e \quad (5.15a)$$

or

$$V_i = \left[V_{\min}^{(0)} - \alpha V_i^{(0)} + \epsilon/e \right] / (1 - \alpha) . \quad (5.15b)$$

For the low energy case we choose $\alpha = 0$ for $V_{\min} = 0$, and $\alpha = 1/3$ for $V_{\min} < 0$. (The value $1/3$ is usually an underestimate, but $\alpha \gtrsim 1/2$ tends to produce instabilities.) For the emitter case we choose

$$\alpha = 0.7 \text{ e } \min(1, R_C/R_B)$$

where R_C is the spacecraft's capacitive radius, R_B the radius at which $V_{\min}^{(0)}$ was found, and 0.7 has been inserted to insure stability. Finally, the potential is subject to the constraint

$$|V_i - V_i^{(0)}| < \text{DVLIM} .$$

The approximations involved in the foregoing treatment tend to produce a "multidimensional lag" in the timestepping process. For example, the appearance of a saddle point at timestep 8 will not be reflected in the surface potential until timestep 9, at which point it may be substantially underestimated. One gains, however, the advantage of being able to proceed stably toward a steady state with minimal use of the expensive POTENT routine and a minimal amount of particle tracking. One or two short timesteps are usually sufficient to resolve the multidimensional lag.

5.8 FLUX DERIVATIVE DETERMINATION

The purpose of including J' in Eq. (5.9b) is to assure that those properties of nature which cause physical stability in real satellites also provide mathematical stability in NASCAP. As was the case in the previous section, uncertainties are resolved in favor of providing additional mathematical stability.

The coding, then, proceeds as follows: _____

1. The trial circuit node potentials are used to find trial surface cell potentials (subroutine VSHARE).
2. Incident, backscattered, and secondary fluxes are calculated using the trial potentials (subroutine GETFLX).
3. The trial fluxes are compared with the original fluxes passed from TRILIN (subroutine GDQTRI).
4. The difference between the trial and original fluxes are recentered to the circuit nodes (subroutine QSHARE).
5. The current differences are divided by potential differences to obtain provisional values for the diagonal matrix J' (subroutine DFDV).

6. Final values of J' are determined to assure stability (subroutine DFDVMX):

For surface nodes:

$$J' = \min (J', -|J(t_1)|/(2*DVLIM))$$

For conductor nodes:

$$J' = \min (J', 0).$$

5.9 FINAL CHARGING ANALYSIS

The purpose of the final charging analysis is to determine the charge accumulation on each circuit node consistent with Eq. (5.9b) and the information known concerning the "bad" nodes. A flow chart of this portion of LIMCEL is shown in Figure 5.4.

First ICCG1 is called to solve Eq. (5.9b), and IMPFI evaluates the left hand side of (5.9a). At this point conductor potentials are checked to see if a timestep reduction is in order. Next HIGHQ examines charge accumulation on "bad" surface nodes to see if any are unphysically too far positive. If such nodes are found, they are unfixed and the analysis begun anew. If not, the "bad" surface nodes are examined to see if any are accumulating more negative charge than would be the case for total cutoff of low energy electron emission (subroutine LOWQ). If such nodes are found, $J(t_1)$ is replaced by the value it would have in event of total cutoff of low energy emission, the node is unfixed, and we once again begin the final charging analysis.

Thus when subroutine VFIX is executed all "bad" surface nodes satisfy

$$J(t_1) > \bar{J} > J(t_1) - L \quad (5.16)$$

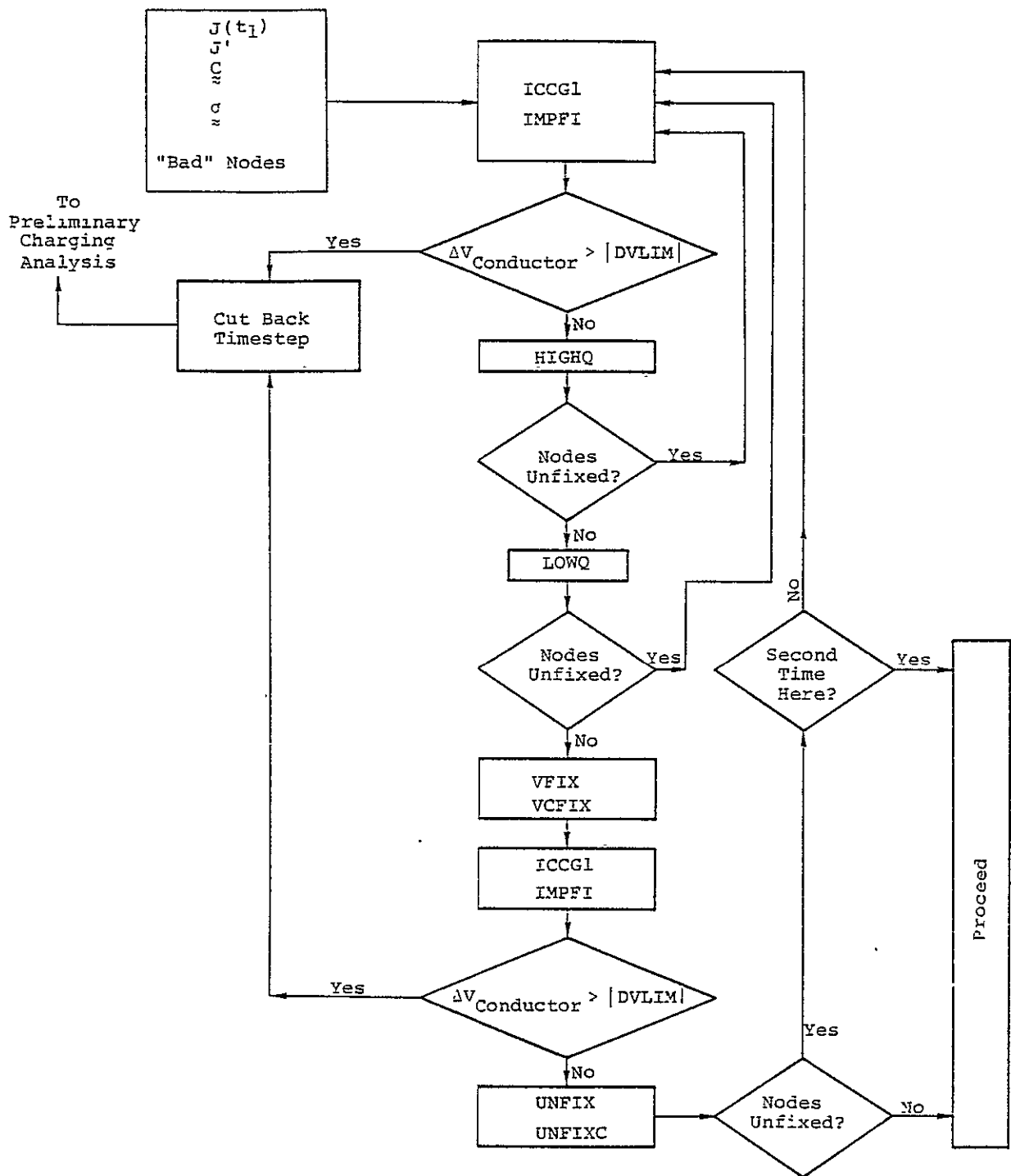


Figure 5.4. Flow chart of Final Charging Analysis portion of subroutine LIMCEL.

where L is the low energy electron emission current and \bar{J} the mean current calculated by IMPFI. VFIX determines the energy ϵ of Eq. (5.12) such that

$$\bar{J} = J(t_1) - L(1 - e^{-\epsilon/2}) \quad (5.17)$$

and redefines the constrained potentials of the "bad" nodes accordingly. The "2" appearing in (5.17) corresponds to the 2 eV characteristic energy of photo- and secondary-electrons. Subroutine VCFIX performs a similar function for conductor nodes, except that a more complex formulation than (5.17) is used for conductors to which emitters are grounded.

Since the constraint potentials have now been readjusted, ICCG1 and IMPFI must be called once again, and various unfixing checks made (UNFIX, UNFIXC). If more nodes are unfixed we once more again restart the final charging analysis, but this branch is taken only once. Otherwise, we are done.

Output of this section are the predicted potentials of all the circuit nodes and the corresponding charge accumulation. The predicted potentials are used in the optional discharge analysis. If discharges are found, the charges are modified accordingly. The charge accumulations are then returned to TRILIN for use by subroutine QUPDAT.

5.10 THE DECREASE IN EFFECTIVE PHOTOCURRENTS DUE TO SADDLE POINTS IN ELECTROSTATIC POTENTIALS NEAR DIFFERENTIALLY CHARGED SPACECRAFT

This section is a verbatim reproduction of a paper given at the 1978 IEEE Annual Conference on Nuclear and Space Radiation Effects, Albuquerque, New Mexico, July 18-21, 1978. The authors are M. J. Mandell, I. Katz, G. W. Schnuelle and P. G. Steen, Systems, Science and Software, and J. C. Roche, NASA-Lewis Research Center.

THE DECREASE IN EFFECTIVE PHOTOCURRENTS DUE TO
SADDLE POINTS IN ELECTROSTATIC POTENTIALS
NEAR DIFFERENTIALLY CHARGED SPACECRAFT*

I. INTRODUCTION

As interest in spacecraft charging has grown over the past decade, many spacecraft charging calculations have appeared in the literature. Such calculations may be characterized, roughly in order of increasing complexity, as

1. Equilibrium current balance calculations.^[1-3]
2. One-dimensional computer programs.^[4]
3. Lumped-circuit-element computer programs.^[5]
4. Multidimensional computer programs.^[6-8]

The first type of calculation simply predicts the floating potentials of surfaces having particular material properties in various environments. Such calculations demonstrate that spacecraft can indeed charge to high negative potentials, and determine the relative importance of various material and environmental properties. One-dimensional codes^[4] introduce the additional complication of a photoelectron sheath which can substantially modify the dynamics of charging and the final potential distribution.

Lumped-circuit-element codes^[5] model a complex satellite electrically as a network of capacitors and resistors. By assigning to each node a current-voltage characteristic $I_i(V_i)$, a dynamic charging calculation can be performed. However, since the code has no geometrical knowledge of the satellite, effects such as shadowing, incomplete particle trajectories, particle reflection, and photosheath effects are either totally neglected or inserted "by hand".

*This work was supported by the National Aeronautics and Space Administration, Lewis Research Center, Cleveland, Ohio under Contract NAS3-21050.

The purpose of this paper is to illustrate the presence of important multidimensional effects in spacecraft charging. Two-dimensional codes have been under development by Parker^[6] and by Laframboise.^[7] The calculation described below was performed using the three-dimensional NASA Charging Analyzer Program (NASCAP).^[8] NASCAP dynamically simulates the charging of an object made of conducting segments which may be entirely or partially covered with thin dielectric films. The object may be subject to either ground test (electron gun) or space (magnetospheric) environments. The simulation alternately (1) treats the accumulation and emission of charge by surface materials and its redistribution by conduction processes, and (2) calculates the electrostatic potentials on the object and in the surrounding space. Implicit algorithms allow simulations of long periods of time, and particle tracking capabilities enable calculation of such quantities as response of charged particle detectors. NASCAP also has extensive graphics capabilities.

II. STATEMENT OF PROBLEM

A. TEST OBJECT

The "satellite" to be charged is a 3-meter diameter sphere whose surface consists of a 10^{-4} m teflon coating over a conducting substrate. In NASCAP, a "sphere" is modeled as an object having 26 faces. This calculation was performed on a "sphere" having 158 surface cells and 144 surface nodes (Figure 1).

Some of the material properties ascribed to teflon are given in Table I. It is worth noting that the conductivity value, which is larger than indicated by low field measurements, may be appropriate to the equilibrium electric field of $\sim 10^7$ volts/meter.

B. ENVIRONMENT

The environment was an isotropic, Maxwellian plasma appropriate to a severe magnetospheric substorm, having a temperature of 20 keV and a density $n_e = n_i = 1 \text{ cm}^{-3}$. This plasma has a Debye length of one kilometer, so that the space charge contribution of the ambient particles is totally negligible. NASCAP was run in a mode in which each surface cell collected incident fluxes of electrons and protons appropriate to a spherical probe at the local surface potential. Sunlight was incident on one side of the sphere.

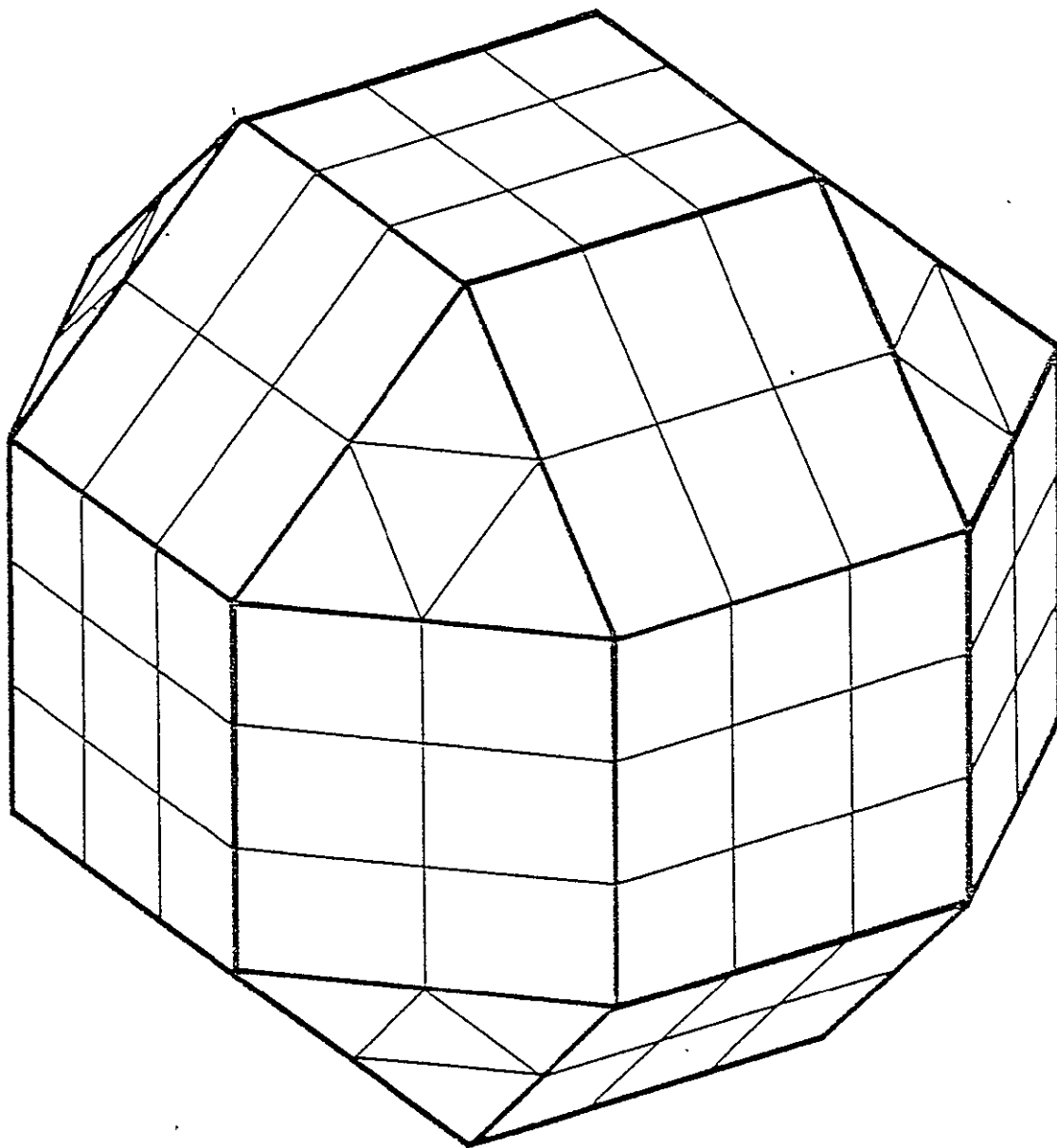


Figure 1. NASCAP representation of sphere used in this calculation, showing surface resolution.

TABLE I
TEFLON PROPERTIES USED IN THIS CALCULATION

Dielectric constant	2.0
Thickness	10^{-4} meters
Conductivity (bulk)	10^{-14} (ohm-m) $^{-1}$
Conductivity (surface)	(neglected)
Effective atomic number	10
Effective atomic weight	16.7
Density	2.2 gm-cm^{-3}
Secondary yield-electron impact	
δ_{max}	3.0
E_{max}	0.3 keV
Secondary yield-proton impact	
Yield for 1 keV proton	1.4
Energy for maximum yield	70 keV
Photoemission (normally incident sunlight)	$2 \times 10^{-5} \text{ A/m}^2$

III. APPROXIMATE PHOTOSHEATH MODEL FOR STRONG DIFFERENTIAL CHARGING

The sheath of low-energy electrons which can form near a positively charged surface is known to have complex structure, dynamics, and transport properties. NASCAP has the capability of determining photosheath currents through tracking of emitted particles. However, not only is such a procedure time-consuming, but it jeopardizes the numerical stability of the calculation. This is because photocurrents are sensitive to surface potential changes comparable to the two-volt characteristic energy of emitted electrons, and thus small compared with the kilovolt differential potentials of interest. The purpose of this section is to justify a principle which can be used to determine the potential of photoemitting surfaces. To this end, we first show that any substantial electric field can dominate space charge effects in determining photosheath structure. It then follows that the surface potential will attain a value such that the fraction of photoelectrons escaping over an electrostatic barrier is just that needed to maintain current balance.

Let us then consider space charge-limited emission in the presence of an external field. If the field is negative (i.e., into the surface) no sheath will form, so we will treat only positive fields. For the simple case of monoenergetic (energy E) electrons emitted normally from a plane surface, a virtual cathode will form at a distance d from the surface. The sheath thickness d is found using the space charge equation^[9]

$$\left(\frac{dV}{dx}\right)^2 = \left(\frac{dV}{dx}\right)^2_{x=d} - \frac{8J}{\epsilon_0} \left(\frac{mV}{2|e|}\right)^{1/2}$$

with the boundary condition

$$V(d) = 0$$

$$V(0) = E/|e|$$

$$\left(\frac{dV}{dx}\right)_{x=d} = \text{external field.}$$

Figure 2 shows the sheath thickness as a function of external field for the parameters $J = 3 \text{ nA/cm}^2$ and $E = 2 \text{ eV}$. It is apparent that any substantial positive external field will completely dominate space charge effects and suppress emission of low energy electrons. Taking into account the distributed spectrum of low-energy emitted electrons, we are led to the following principle:

Under conditions of strong differential charging a photoemitting surface will reach a potential such as to maintain a positive external electric field of a few volts per meter.

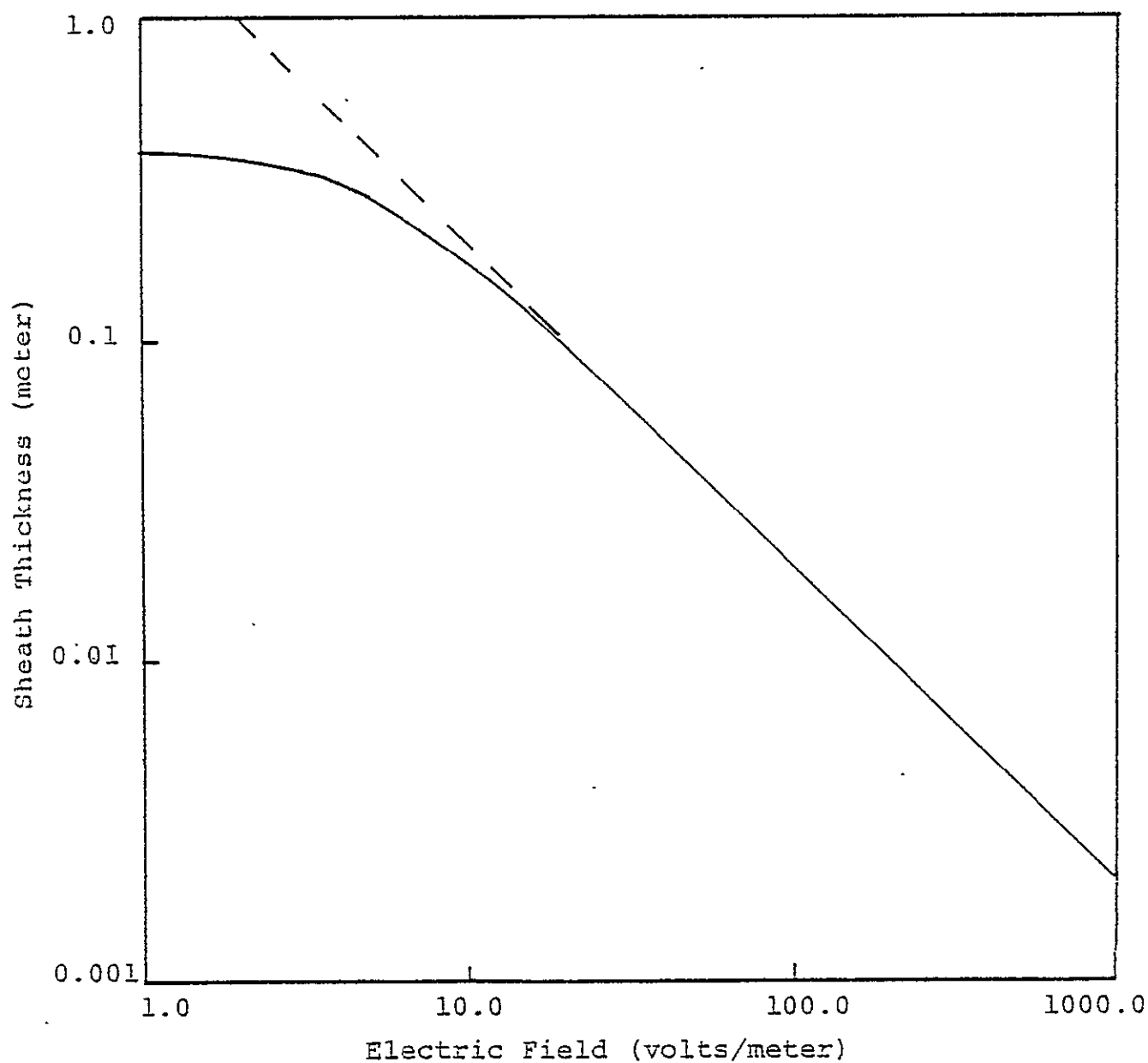


Figure 2. Electron sheath thickness outside a planar surface emitting 2 eV electrons as a function of electric field in the low current limit (dashed line) and for 3 nA/cm² emitted current (solid curve).

IV. RESULTS

NASCAP was run to calculate the electrostatic potentials on the surface of, and in the space surrounding, a sunlit teflon-coated sphere. Currents to the sunlit surfaces were determined based on the principle put forth in the previous section. From an initial uncharged state, the sphere reached a final steady state having 2.5 kV of differential charging. Figure 3 shows the potentials on a shaded and a sunlit surface cell as a function of time.

Figures 4-8 show the time development of the electrostatic field. (The satellite-sun line lies in the plane of these figures. Dark and sunlit cells are differentiated by shading.) For the first ~ 0.1 seconds the sphere charged uniformly (Figure 4). Over the next few seconds, the negative charge accumulated by the shaded surfaces began to dominate the electrostatic field, causing a saddle point to appear in front of a sunlit surface (Figures 5-6). At about 10 seconds the potential at the saddle point became negative. In accordance with the principle put forth in the previous section, the sunlit surface maintained a potential a few volts positive relative to the saddle point (Figure 7). Final steady state (Figure 8) is reached with the sunlit surface at -1.0 kV and the shaded surface at -3.6 kV.

The components of incident and emitted current are shown in Table II. It is apparent that low energy emitted electron currents are always dominant on the sunlit surface. In the final steady state, the net negative current incident upon the shaded side is balanced by conduction through the teflon, which has an internal field of 1.0×10^7 volts/meter.

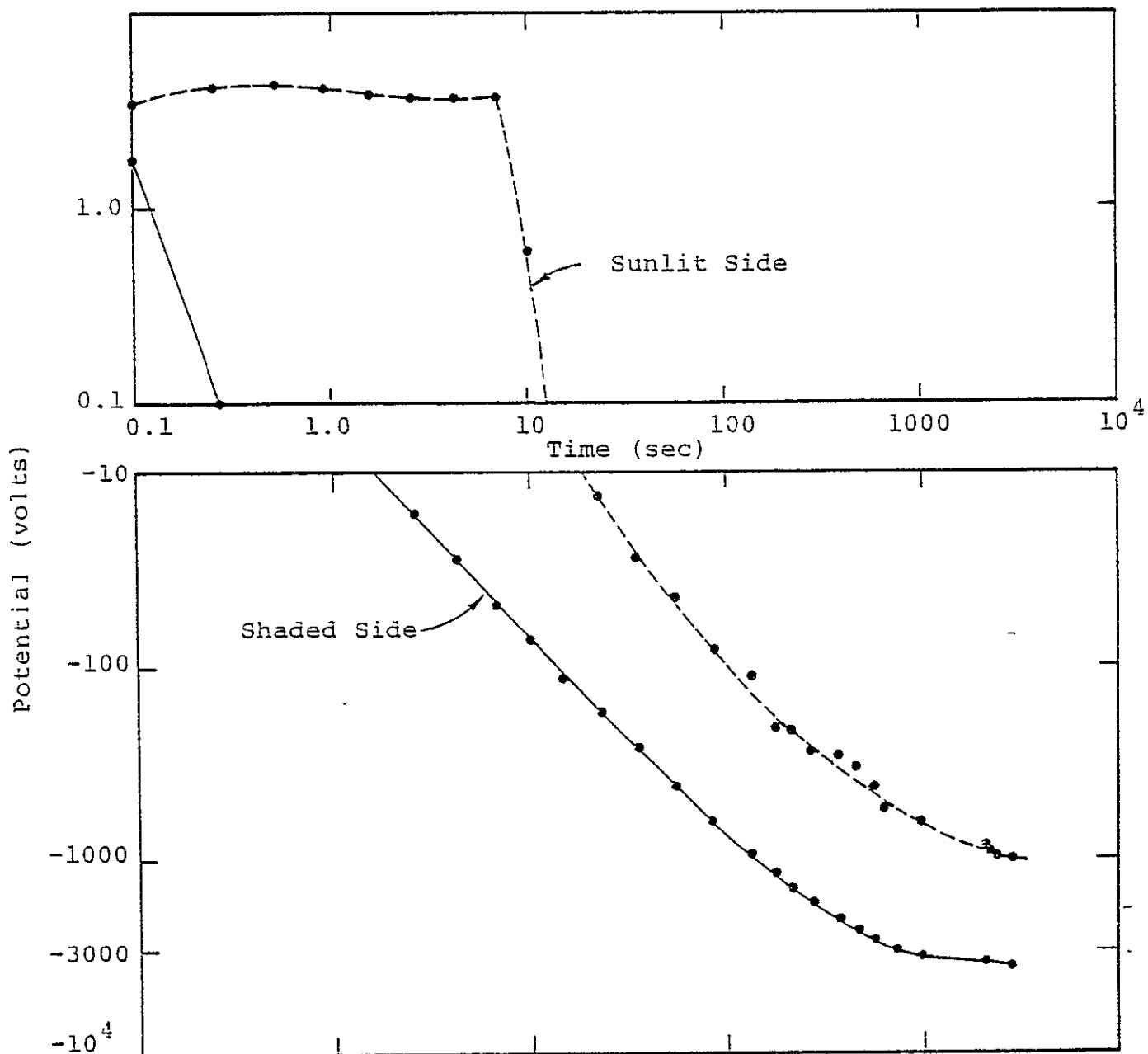


Figure 3. Potentials on shadowed and solar illuminated surfaces of a teflon sphere in a plasma ($N_e = 10^6/\text{m}^3$, $\theta = 20 \text{ keV}$).

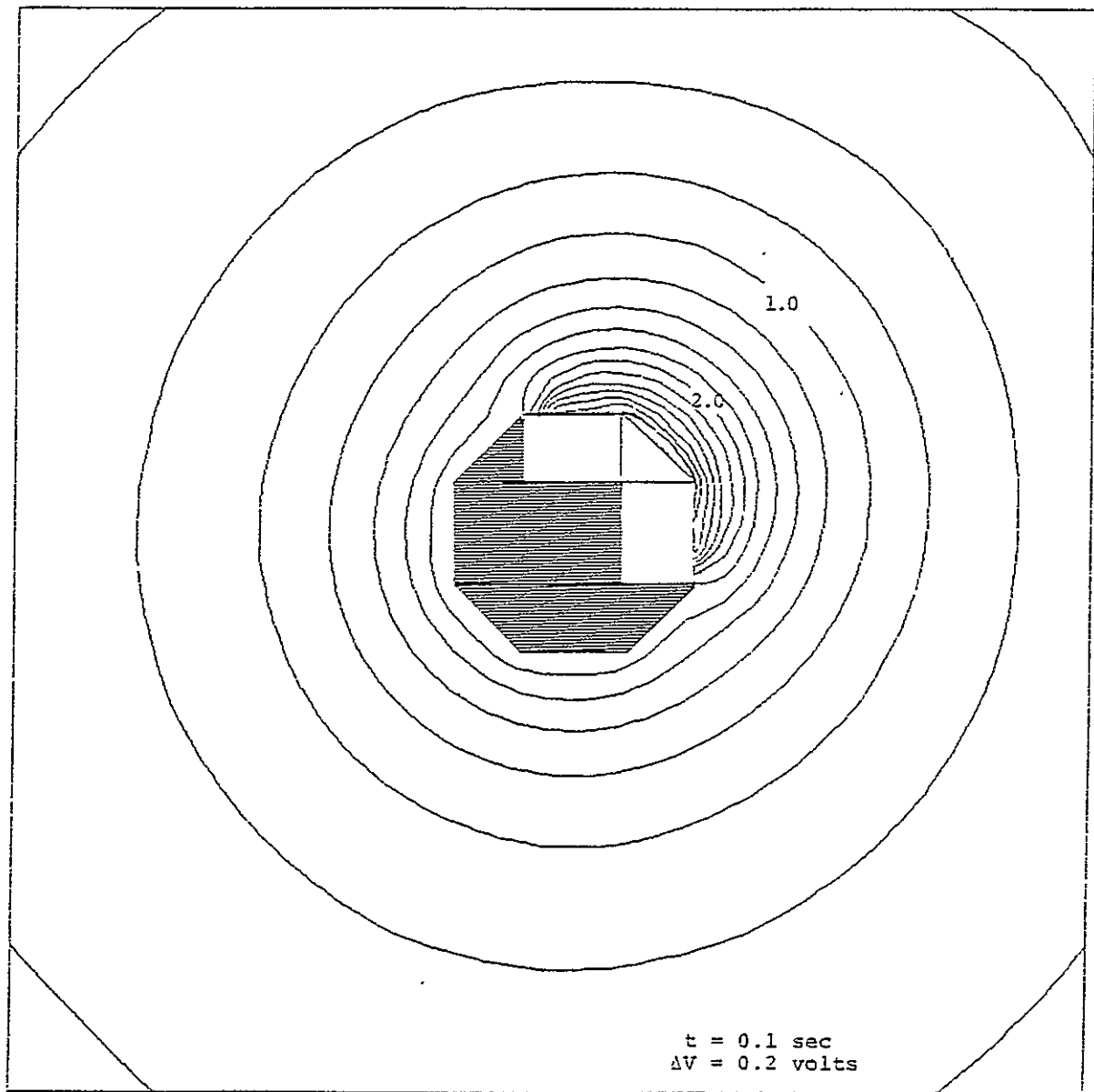


Figure 4. Potential contours about a sunlit sphere early in time.

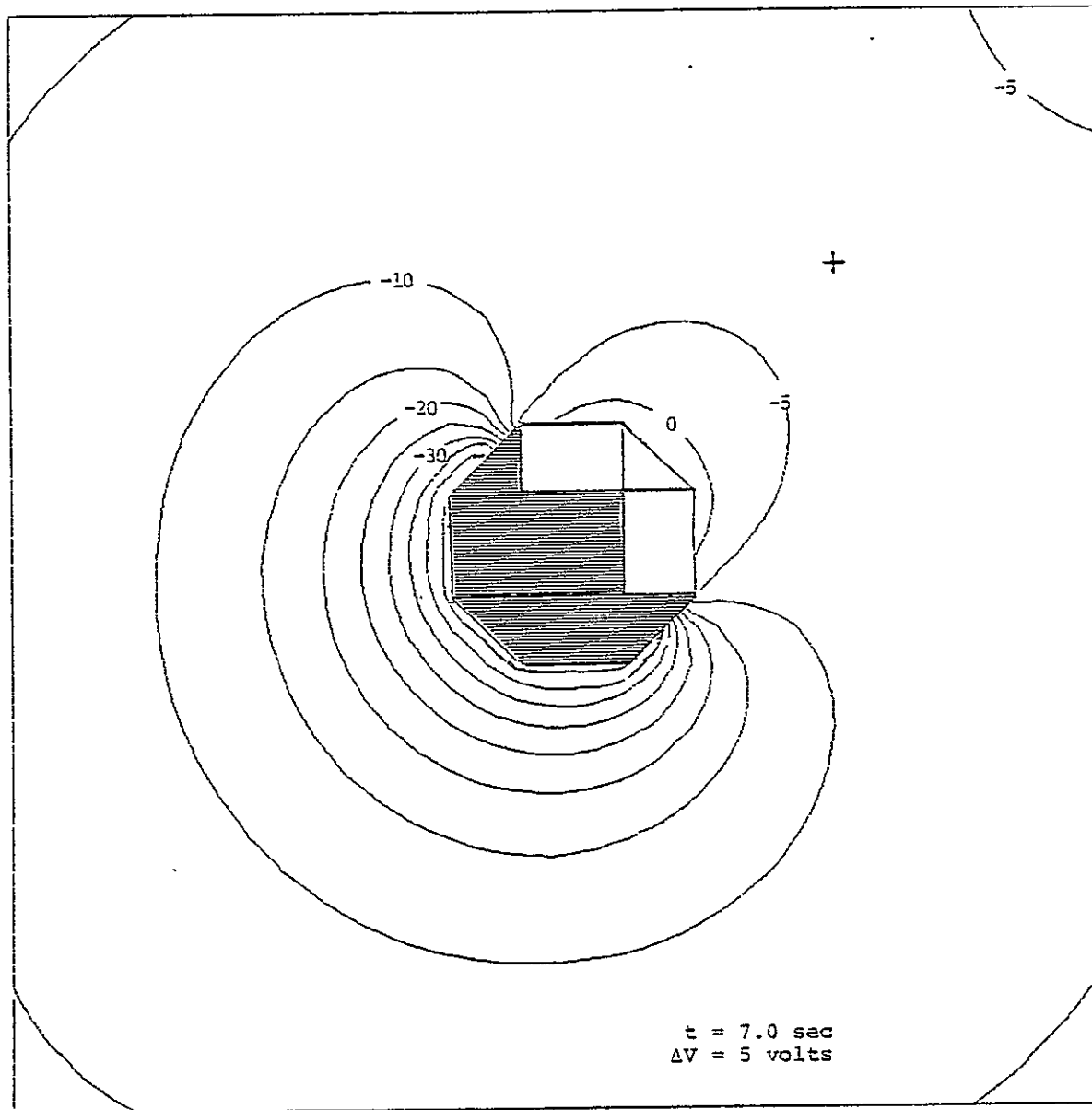


Figure 5. Potential contours around sunlit sphere showing early appearance of saddle point (x) at -5.6 volts.

ORIGINAL PAGE IS
OF POOR QUALITY

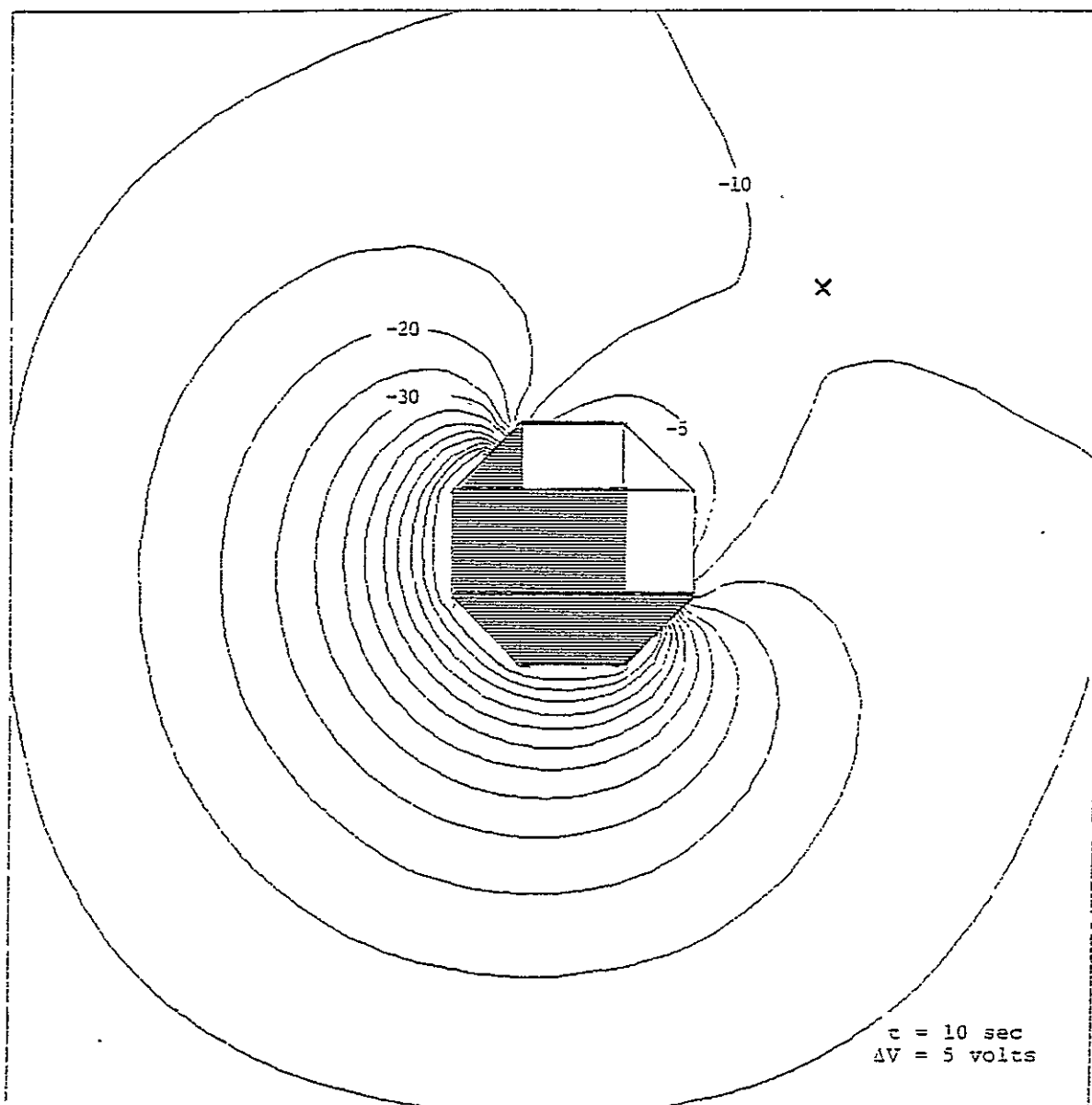


Figure 6. Potential contours around sunlit sphere showing fully formed saddle point at approximately -8 volts.

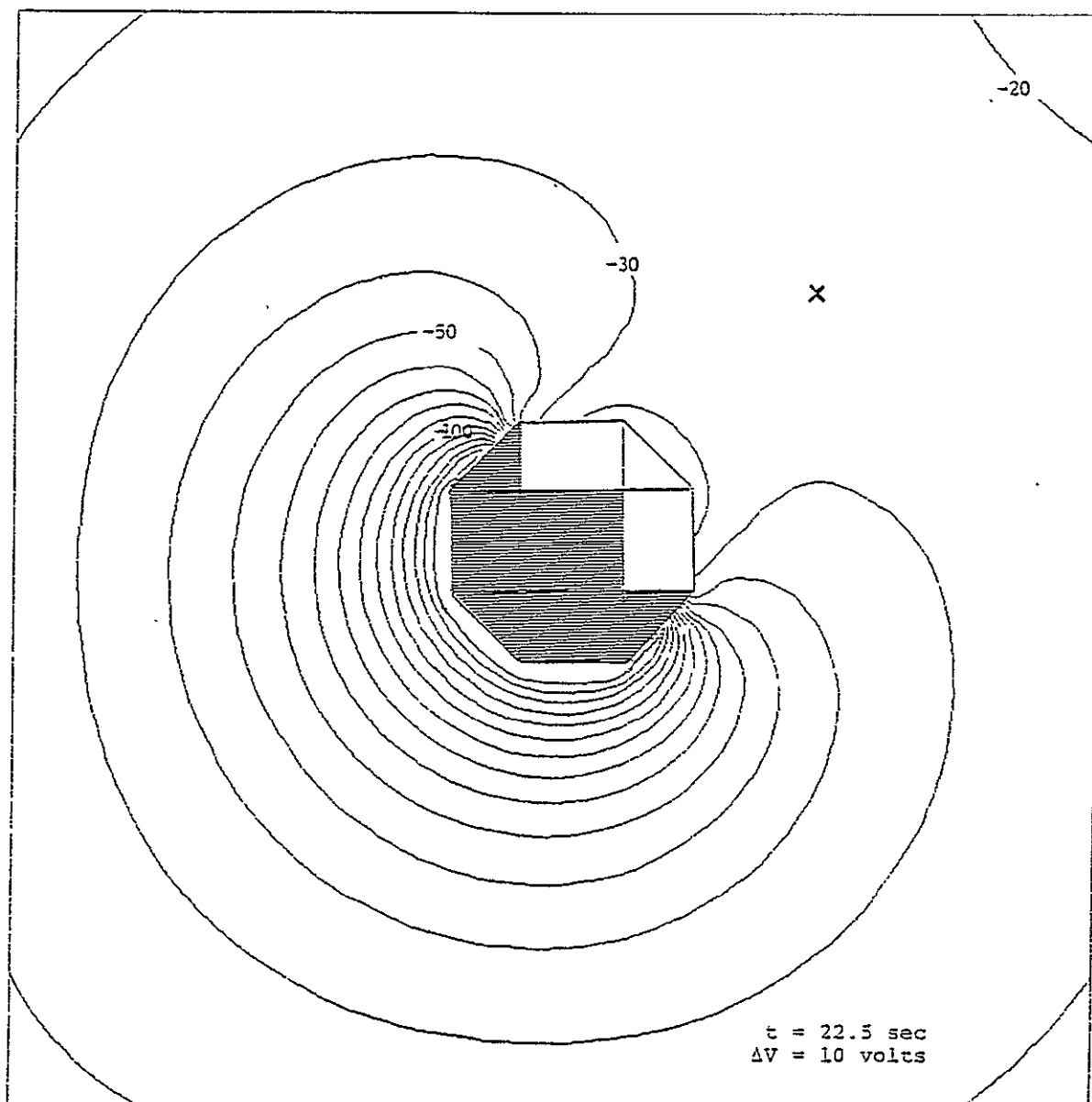


Figure 7. Potential contours about sunlit sphere showing saddle point at approximately -25 volts.

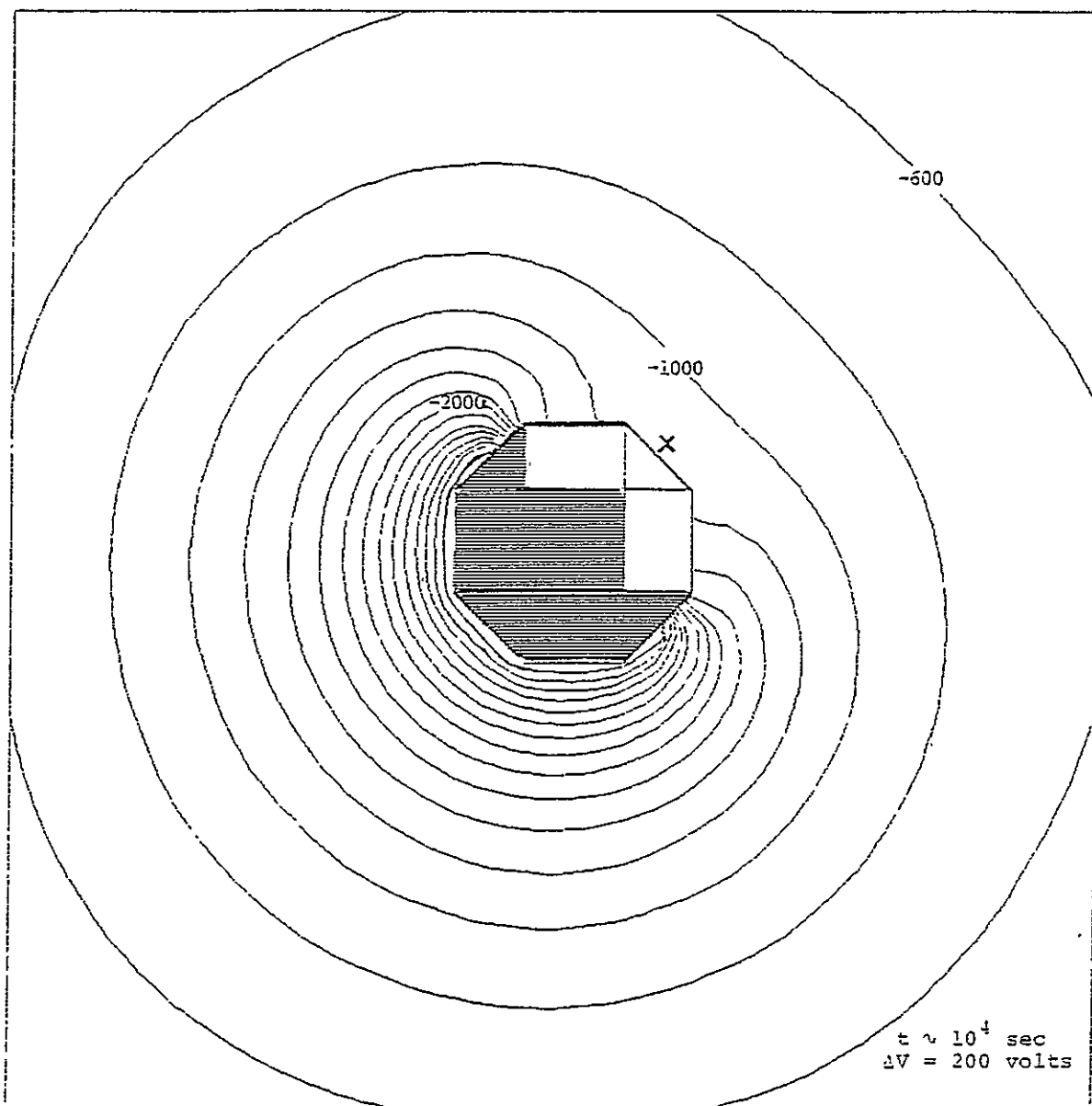


Figure 8. Steady state potential contours about sunlit sphere.

TABLE II
COMPONENTS OF INCIDENT AND EMITTED CURRENT (A/m²)

Source	Shaded Side		Sunlit Side	
	Initial	Final	Initial	Final
Incident Electrons	-3.78×10^{-6}	-3.16×10^{-6}	-3.78×10^{-6}	-3.58×10^{-6}
Resulting Backscatter	1.02×10^{-6}	8.49×10^{-7}	1.02×10^{-6}	9.62×10^{-7}
Resulting Secondaries (L)	1.23×10^{-6}	1.03×10^{-6}	1.23×10^{-6}	1.17×10^{-6}
Incident Protons	8.83×10^{-8}	1.04×10^{-7}	8.83×10^{-8}	9.31×10^{-8}
Resulting Secondaries (L)	9.15×10^{-7}	1.09×10^{-6}	9.15×10^{-7}	9.66×10^{-7}
Photocurrent (L)	0	0	2.00×10^{-5}	2.00×10^{-5}
Total	-5.34×10^{-7}	-9.45×10^{-8}	1.95×10^{-5}	1.96×10^{-5}

(L) - Indicates low energy emitted electrons subject to space charge or field limiting.

V. DISCUSSION

It is instructive to consider a lumped-circuit element solution to this problem (Figure 9). The shaded and sunlit surfaces are coupled to spacecraft ground by resistance R and capacitance C_D , and to plasma ground by capacitance C_P . Since $C_D \sim \epsilon_0 R^2/d$ and $C_P \sim \epsilon_0 R$, where d is the dielectric thickness and R the satellite dimension, $C_D \sim 10^4 C_P$. The current to the sunlit surface is dominated by the emitted photoelectrons, which are absent from the shaded side. As indicated in the figure, for $R = \infty$ the surfaces at equilibrium maintain their individual floating potentials, while finite resistivity ameliorates somewhat the degree of differential charging, but leads to no qualitative differences. It is only when multi-dimensional effects, manifested through the electric fields external to the satellite, are taken into account that a sunlit surface can develop a negative potential.

To further illustrate the saddle point effect, the problem was rerun under the assumption that the low-energy electrons are emitted with a characteristic energy of 50 volts. (Actual photoelectrons have energies of about 2 eV. However, the 50 volt choice leads to results more suitable to NASCAP spatial resolution.) The final potentials were -700 volts on the sunlit side and -3400 volts on the shaded side. Potential contours for this case are shown in Figure 10. The saddle point can be seen more clearly than in Figure 8 because of the higher positive electric field outside the sunlit surfaces. Trajectories for electrons of one to one hundred eV energies are shown in Figure 11. It is apparent that all the low-energy electrons return to the surface, while the highest energy particles escape over the saddle point.

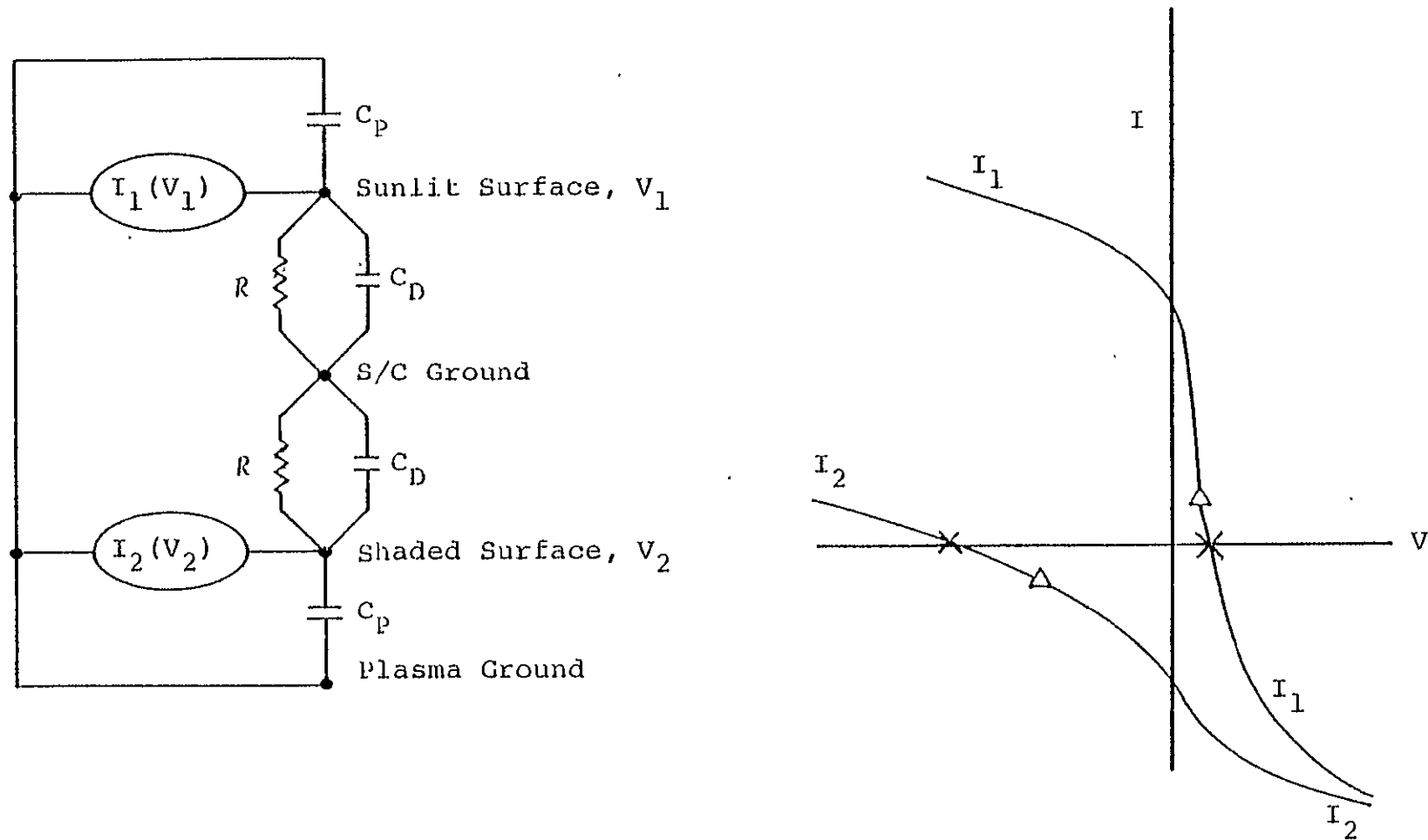


Figure 9. Lumped-circuit-element model and solution (schematic) for charging of sunlit sphere. On the I-V plot, the crosses indicate current balance for $R = \infty$, and the triangles for finite R .

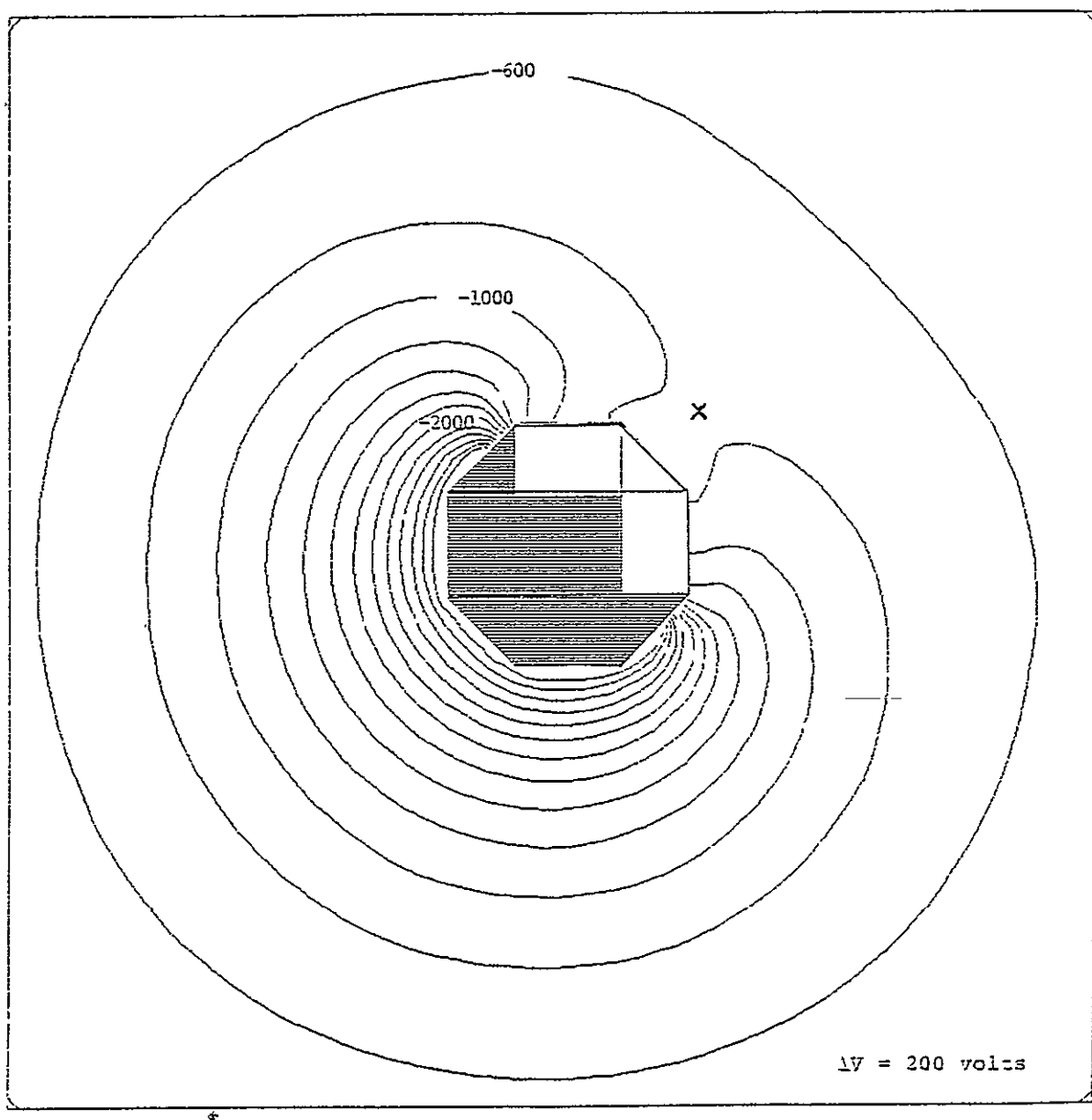


Figure 10. Steady state potential contours about a sunlit sphere whose low-energy emitted electrons are assumed to have a characteristic energy of 50 eV.

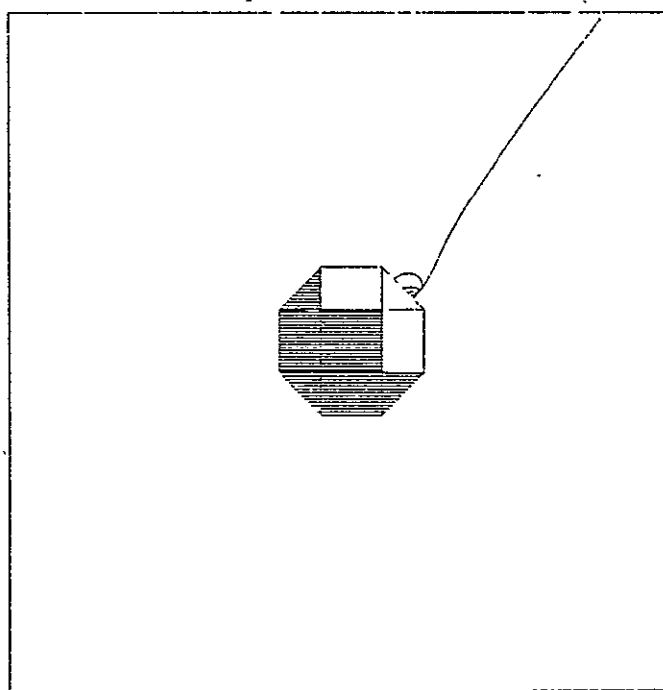
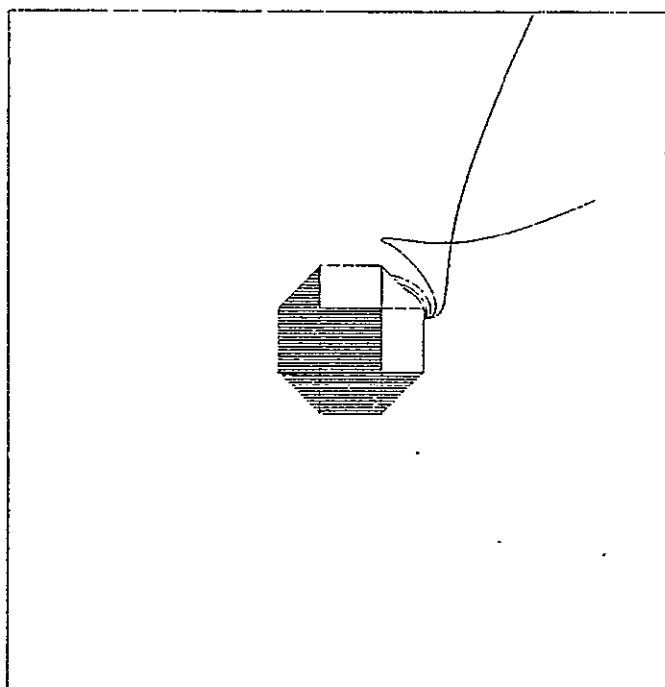


Figure 11. Trajectories of electrons emitted from two different surface cells in potential of Figure 10. Electron initial energies are logarithmically spaced from 1 to 100 eV.

VI. CONCLUSIONS

This relatively simple example illustrates the importance of multidimensional effects in spacecraft charging. In particular, the mechanism demonstrated here may have played a role in events where satellites ATS-5 and ATS-6 were observed to charge negatively in sunlight, whereas simple current balance would have predicted that photoemission would keep the sunlit side, if not the entire satellite, at a positive potential. Thus simple current balance calculations can lead to erroneous conclusions about equilibrium as well as dynamic charging. However, these errors need not be due to complex plasma-sheath-dynamic phenomena, but may be caused by relatively simple electrostatic effects.

A further conclusion is that a dielectric patch, when differentially charged to high negative potential, can, through its effect on particle trajectories, have an influence out of proportion to its area. Such effects have been suspected in cases of spurious particle detector response. Another possible effect might be to prevent escape of actively emitted electrons. This would annul the intended discharge of a satellite by low energy emitters.

In summary, multidimensional electrostatic effects play an important role in spacecraft charging. Surfaces at high negative potential can suppress emission of low energy electrons elsewhere. Such effects can explain observation of negative potentials on sunlit surfaces, and may seriously affect particle detector response and active potential control mechanisms.

REFERENCES

1. DeForest, S. E. (1972), "Spacecraft Charging at Synchronous Orbit," J. Geophys. Res. 77, 651.
2. Knott, K. (1972), "The Equilibrium Potential of a Magnetospheric Satellite in an Eclipse Situation," Planet. Space Sci. 20, 1137.
3. Prokopenko, S. M. L. and J. C. Laframboise (1976), "Prediction of Large Negative Shaded-side Spacecraft Potentials," Proc. Spacecraft Charging Technology Conference, AFGL-TR-77-0051, NASA-TMX-73537.
4. Rothwell, P. L., A. G. Rubin and G. K. Yates, "A Simulation Model of Time-dependent Plasma-Spacecraft Interaction," Proc. Spacecraft Charging Technology Conference.
5. Massaro, M. J., T. Green and D. Ling, "A Charging Model for Three-Axis Stabilized Spacecraft," Proc. Spacecraft Charging Technology Conference.
6. Laframboise, J. G. and S. M. L. Prokopenko, "Numerical Simulation of Spacecraft Charging Phenomena," Proc. Spacecraft Charging Technology Conference.
7. Parker, L. W., "Calculation of Sheath and Wake Structure About a Pillbox-shaped Spacecraft in a Flowing Plasma," Proc. Spacecraft Charging Technology Conference.
8. Katz, I., D. E. Parks, M. J. Mandell, J. M. Harvey and S. S. Wang (1977), "NASCAP, A Three-dimensional Charging Analyzer Program for Complex Spacecraft," IEEE Transactions on Nuclear Science 6, 2276.
9. Page, L. and N. Adams (1958), Principles of Electricity, Princeton: Van Nostrand, p. 253.

6. BOOMS

Booms are skinny cylinders — less than one grid unit in radius. They must be an integral number of grid units in length. Unlike other portions of NASCAP objects, booms are not confined to the innermost mesh. They are also unique in that the boom radius is a real number between zero and one. This allows very accurate modeling of boom volume and surface area.

The most severe restriction of the boom object is that booms must lie along grid lines. They can only point in the directions of the coordinate axes, and a boom crossing a mesh boundary must line up with a grid line in the outer (coarser) mesh.

In three-dimensional plots, booms are shown as skinny rectangular parallelepipeds. But within the NASCAP treatment, boom circumferences are truly round. All boom calculations are made appropriate for a curved, not a flat, surface.

6.1 BOOM DEFINITION

Booms are defined by giving starting and ending points, a radius, and a surface material. The definition routine expects to read 5 cards per boom, in the following order:

CARD 1. CCODE

FORMAT(A6)

CCODE must contain the literal 'BOOM'

CARD 2. CCODE,IXB,IYB,IZB,IGB,IXE,IYE,IZE,IGE

FORMAT(A6,4X,8I5)

CCODE must contain the literal 'AXIS'

IXB, IYB, and IZE give the starting coordinates of the axis, and IGB gives the starting grid. Similarly, the ending information is given in IXE, IYE, IZE, and IGE. Any offset applies only to coordinates in grid 1. Coordinates in outer grids are assumed to have OFFSET = (0,0,0).

CARD 3. CCODE, RADIUS

FORMAT(A6,4X,F10.0)

CCODE must contain the literal 'RADIUS'

RADIUS gives the boom radius in inner mesh units.

CARD 4. CCODE, MATERIAL

FORMAT(A6,4X,A6)

CCODE must contain the literal 'SURFAC'

MATERIAL must be a previously defined surface code.

CARD 5. CCODE

FORMAT(A6)

CCODE must contain the literal 'ENDOBJ'

6.2 RESTRICTIONS ON BOOMS

There are several restrictions which apply to booms:

1. Booms must be defined parallel to a coordinate axis.
2. Booms must not intersect one another, and there must be at least one node separating parallel booms.
3. Booms must intercept other objects only at (1,0,0), (0,1,0), (0,0,1), (-1,0,0), (0,-1,0), or (0,0,-1) surfaces.
4. Booms must not pass through objects.

5. Booms must pass from an inner grid towards outer , grids.
6. Booms may intercept grid interfaces at right angles to the interface; however, at least one node must separate each boom from grid interfaces which are not intercepted.
7. Booms may not approach within one unit or less the bottom of a thin plate.

6.3 BOOM CELL FLUX SUMMARY

Flux breakdown printouts can be obtained for boom surface cells. Boom surface cells come at the end of the surface cell list, continuing the cell numbering scheme.

To request a flux breakdown printout for a boom surface cell, first find its position on the boom cell list. Add this position number to the highest number for a non-boom cell — the last cell printed in the standard surface cell list. For example, to get a printout on the tenth (10) boom cell when there are five hundred and two (502) non-boom surface cells, insert in the RDOPT input file a card reading

```
SURFACE CELL          512
```

7. SUBDIVISION

NASCAP can now subdivide user-specified surface cells for finer potential resolution. Specified surface cells can be subdivided into 9, 16, or 25 nodes, depending on whether the user requests 1, 2, or 3 subdivisions.*

The major difficulties in this process are those of data management. Implementation required forty-odd new subroutines and changes to fifteen old ones.

The new code has been tested on some simple objects. It gives good results (see "RESULTS").

The sections which follow deal with various aspects of the implementation.

7.1 RESULTS

A test case was run on a surface with two conductors. The surface was four grid units (meters) square and one grid unit thick. One half was held at 100 V and the other at 200 V.

The following graphs (Figures 7.1 - 7.3) show the potential falloff as the conductor boundary was crossed on a line 1 cm above the surface.

The entire minus Y surface was subdivided to the maximum extent (NSUB = 3) so that the 4 x 4 grid became an effective 17 x 17 grid.

*The three subdivision limit is a storage limitation. The method is general and could be used for any number.

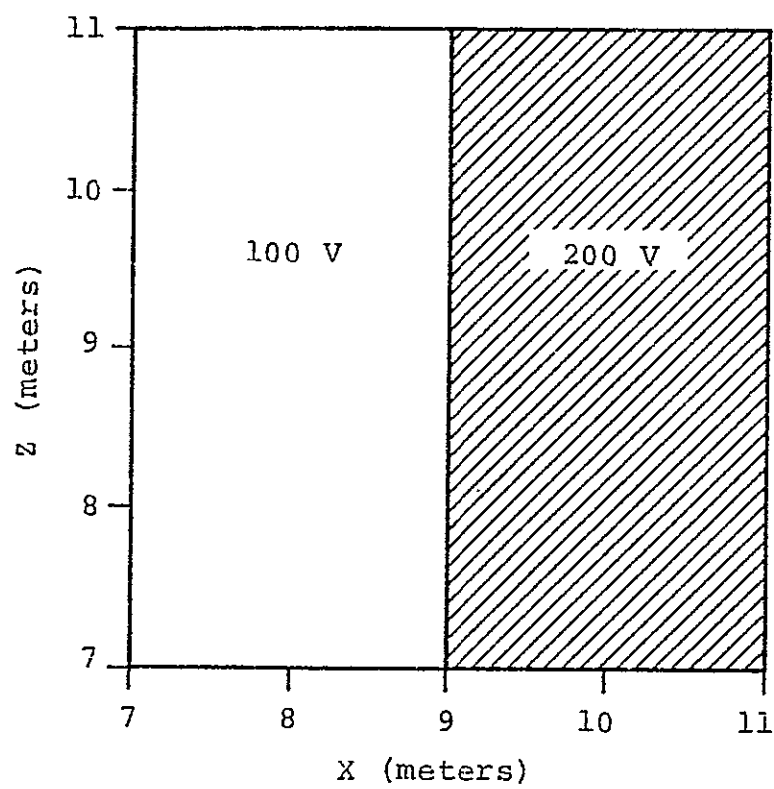


Figure 7.1. Plate with two fixed conductors; $Y = 8.00$.

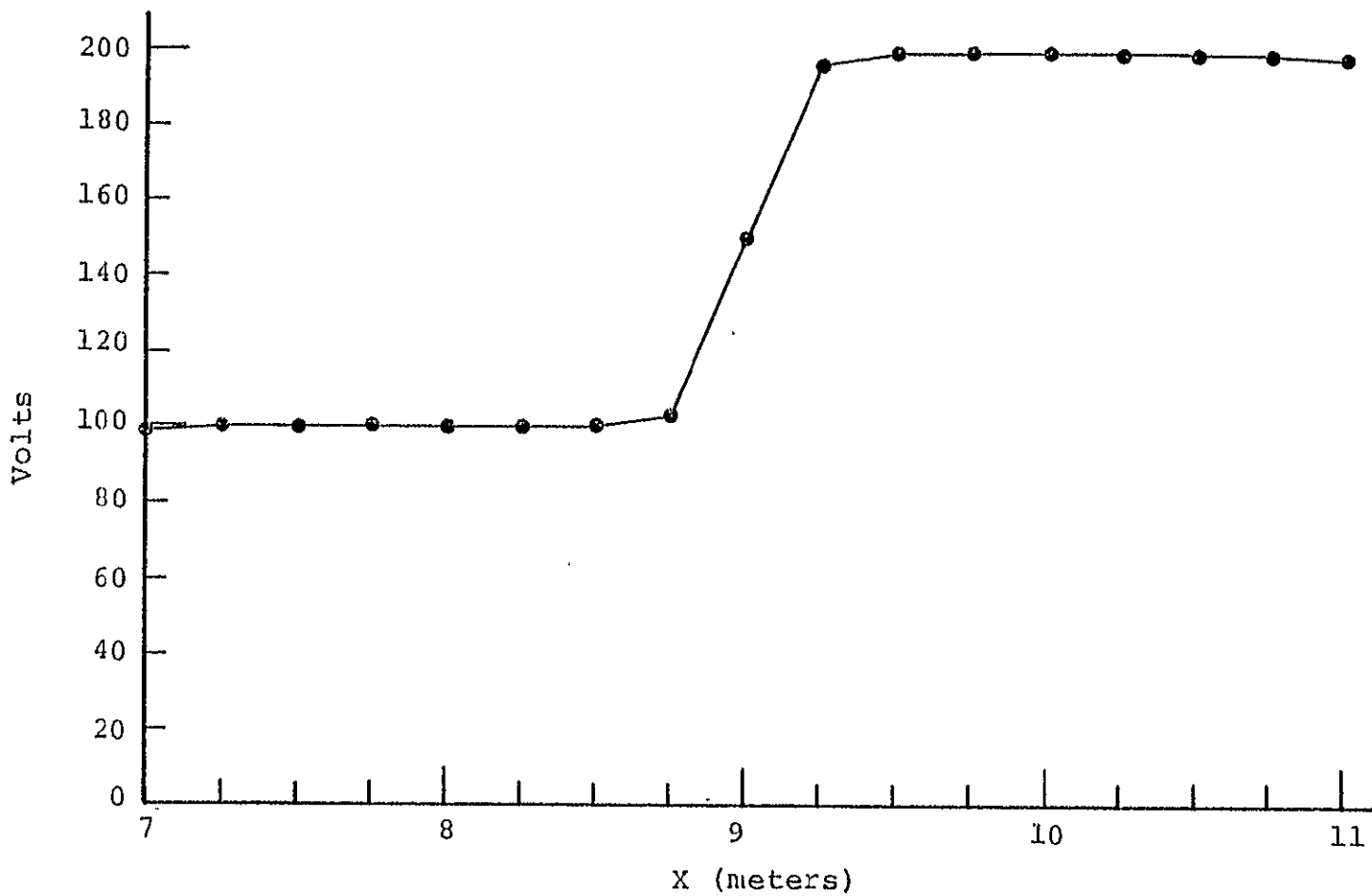


Figure 7.2. Potentials at subdivided points, 1 cm above surface; $z = 8.5$, $y = 7.99$.

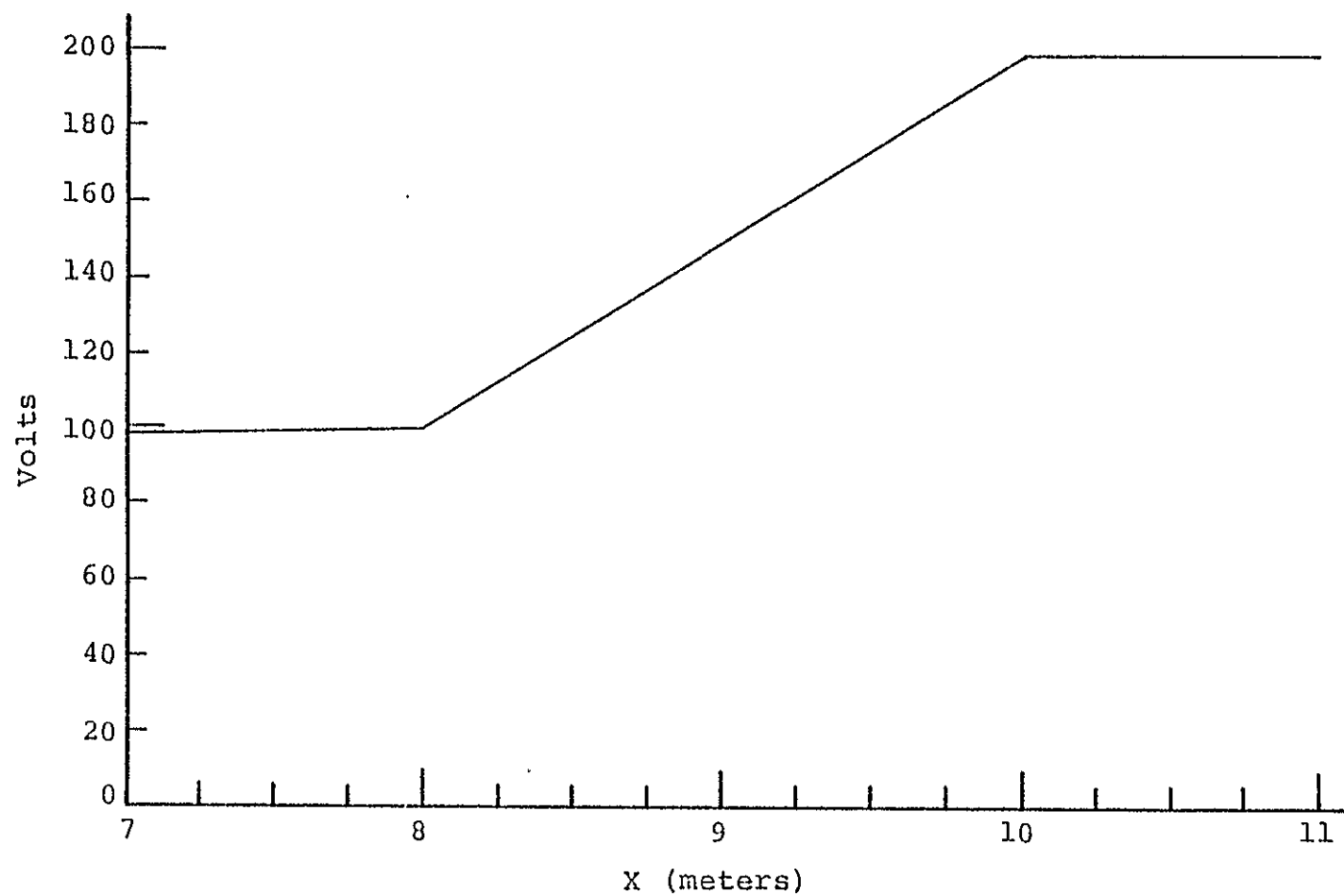


Figure 7.3. No subdivided points, bilinear interpolation potentials; $z = 8.5$, $y = 7.99$.

7.2 CELLS AND ELTS

NASCAP deals with two basic geometric types — surface cells and volume elements. Surface cells are basically two-dimensional structures about one grid unit to a side. They define the spacecraft volume by enclosing it. The spacecraft is a three-dimensional object with surface cells making up its skin.

Volume elements fill space. Most of them are cubes with edges of one grid unit. Some cubic volume elements coincide with volume occupied by the spacecraft. These volume elements inside the spacecraft are said to be "filled". Filled volume elements do not figure into NASCAP calculations.

Sometimes the spacecraft boundary cuts across a volume element. Such an element is divided into two pieces. One piece is filled — it does not exist. The remaining piece, the "empty" piece, becomes a non-cubic volume element — a tetrahedron perhaps, or a wedge, or a truncated cube.

Every surface cell is either the border between two volume elements, or the border between two parts of a single volume element — one filled and one empty.

In the following pages, surface cells will be referred to simply as "cells". Volume elements will be called "volume elts" or "elts". Cells have two dimensions. Elts have three.

7.3 FACES AND EDGES

Subdivision is initiated when a user specifies a surface cell or set of cells which is (are) of special interest. The user wants a more accurate potential value for points on the cell than is obtained with bilinear interpolation from the corners. Subdivision creates a number of new nodes in between the regular grid nodes. These new nodes will have a role in all of NASCAP's potential calculations.

By far the most complicated part of the potential calculation is the coproduct $A \times U = AUN$. Coproduct terms are calculated for each surface cell and each volume elt. Cells and elts that have subdivided nodes must be treated in a special way.

The center cell in Figure 7.4 has been subdivided. It has two extra nodes on each edge and a group of four additional nodes toward the center of the face. This cell is a face-subdivided cell, or FACE-SD cell. Each of the four cells marked "E" is subdivided along one edge, the edge they share with the face-sd cell. Cells with one subdivided edge are called EDGE-SD cells. There are special coproduct routines for face-sd cells and edge-sd cells.

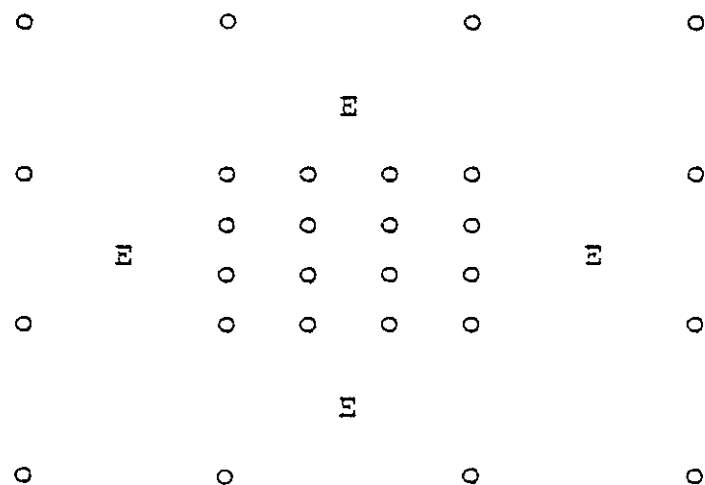


Figure 7.4. Extra nodes on subdivided cell.

As noted in the section CELLS AND ELTS, a surface cell is often the border between two volume elts — one filled and one empty. Any subdivided cell must form such a border. The filled elt is ignored. The empty elt in front of the cell must be included in coproduct calculations.

An empty elt that lies against a face-sd cell is a FACE-SD elt. An elt lying against an edge-sd cell is an EDGE-SD elt. There are special coproduct routines for face-sd elts and edge-sd elts.

Subdivided cells and elts have by definition extra nodes. Extra nodes that lie on a cell edge are called EDGE nodes. Extra nodes not along an edge, i.e., nodes not shared by two cells, are called FACE nodes.

If N is the number of subdivisions, a face-sd cell has N edge nodes along each edge. The cell has N^2 face nodes and four grid nodes. The total is $N^2 + 4N + 4$ or $(N + 2)^2$ nodes on this surface.

In summary, the extra nodes used by NASCAP for subdivision are classified as face nodes or edge nodes. Surface cells and volume elements are changed by the introduction of these new nodes. The four new types of cells and elts are called:

- Face-sd cells.
- Edge-sd cells.
- Face-sd elts .
- Edge-sd elts .

7.4 SDINPU - OBJECT DEFINITION

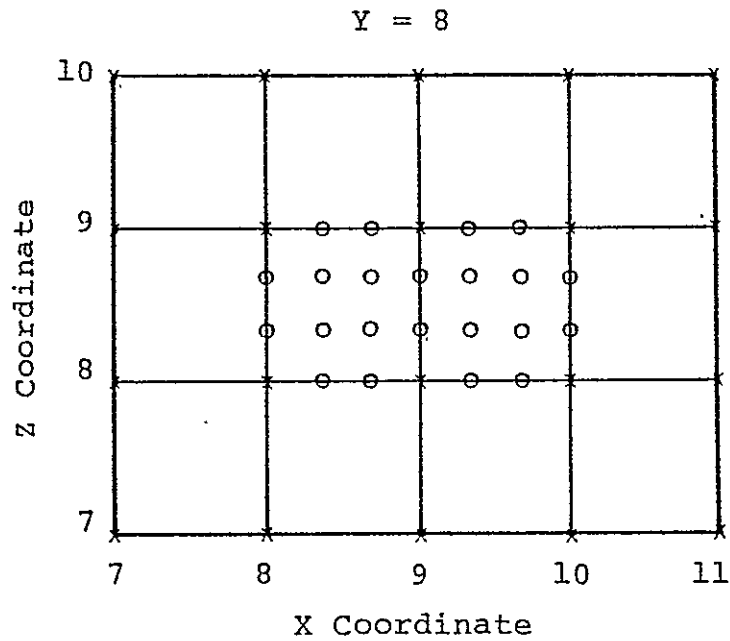
The user specifies which cells are to be face-sd. This choice is limited by several restrictions (see "RESTRICTIONS" section). The object definition word "FINER" initiates this process by causing a call to subroutine SDINPU. The first three integers on the "FINER" card are the origin of a rectangular group of surface cells which are to be face-sd. The next three integers are the ΔX , ΔY , and ΔZ of the rectangle, one of which must be zero. The final integer is NSUB, the number of subdivisions in each direction. NSUB is either 1, 2, or 3, and is the same for all subdivided surfaces. If different NSUB's are specified, the one on the last FINER card is the one that counts.

The input is in the usual I5 format starting in column 11.

Example:

```
FINER      8      8      8      2      0      1      2
```

subdivides the surface cell with corners (8,8,8), (9,8,8), (8,8,9), (9,8,9) and the one next to it (9,8,8), (10,8,8), (9,8,9), (10,8,9).



x Denotes Grid Point

o Denotes Subdivision Point

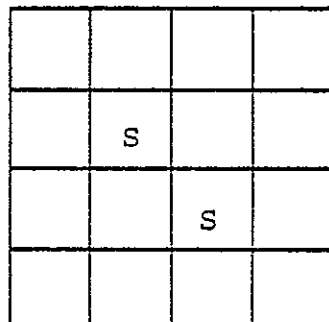
There can be any number of FINER cards so long as the total number of face+sd cells does not exceed MXFACE (presently = 50).

7.5 RESTRICTIONS

The basic restrictions on the use of subdivision are listed below. A set of examples which clarify these restrictions follows.

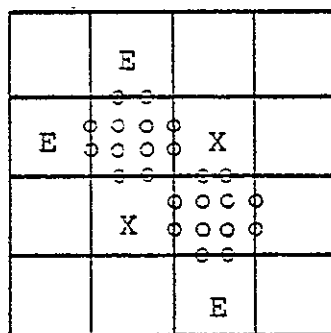
1. Only square surface cells and empty cubic volume elts may be subdivided.
2. An edge-sd cell or elt may have only one edge subdivided.
3. A face-sd cell or elt may have only one face and the four edges of that face subdivided.
4. Only cells and elts in the innermost mesh may be subdivided, and a subdivided volume elt may not touch the edge of the innermost mesh.

SURFACE CELL INCONSISTENCIES



NOT ALLOWED

The above configuration of face-sd cells leaves two cells with multiple sd edges. The next drawing clarifies the situation.



NOT ALLOWED

Same Situation (NSUB = 2)

The cells marked "E" are acceptable edge-sd cells. The cells marked "X" are edge-sd cells with two subdivided edges. A simple solution to this problem is shown in the next drawing.

	E	E	
E	S	S	E
E	S	S	E
	E	E	

ACCEPTABLE

The cells marked "S" have been specified by the user as face-sd cells. The program will classify the cells marked "E" as edge-sd cells. In many situations, if nearby cells cannot be selected as single face-sd cells, the solution is to subdivide a larger area including the cells of interest.

		S	
		S	

NOT ALLOWED

The cell between the two face-sd cells is double edge-sd.

	E	S	E
	E	S	E
	E	S	E

ACCEPTABLE

	S		
	S	S	
	S		

NOT ALLOWED

Two double edge-sd cells.

	E	E	
E	S	S	E
E	S	S	E
E	S	S	E
	E	E	

ACCEPTABLE

	E		
E	S	E	
	E	E	
	E	S	E
		E	

ACCEPTABLE

S	S	S
S	S	S

NOT ALLOWED

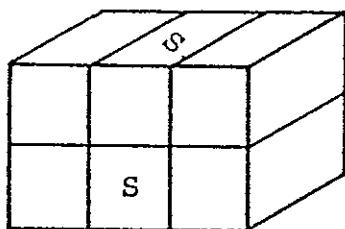
Edge-sd cell triangular not square

S	S	S
S	S	

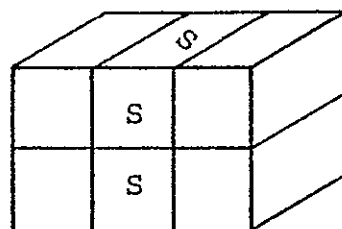
NOT ALLOWED

S	S	S

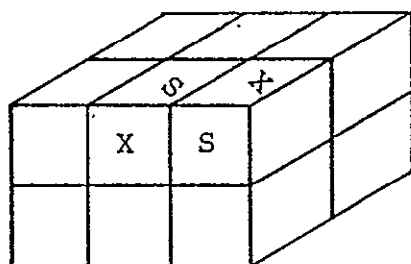
ACCEPTABLE



NOT ALLOWED

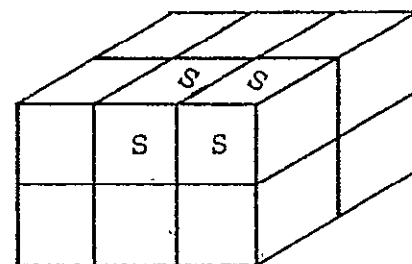


ACCEPTABLE

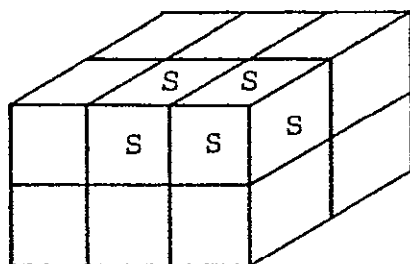


NOT ALLOWED

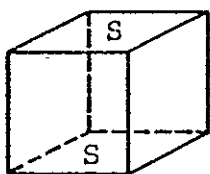
Cells marked "X" are
double edge-sd



NOT ALLOWED



ACCEPTABLE



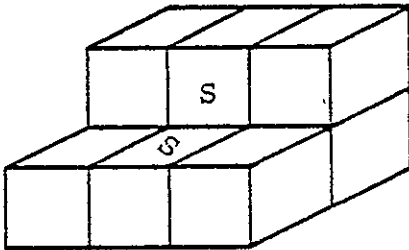
NOT ALLOWED

Four faces of unit
cube are double
edge-sd

Be careful at corners. The reader should verify that if the object being considered is a unit cube in space, there must be 0, 1, or 6 subdivided surface cells. There is no legal way to subdivide 2, 3, 4, or 5 of the surfaces.

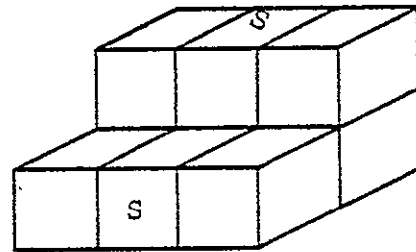
VOLUME ELT INCONSISTENCIES

It is possible for the surface cells to be subdivided in a consistent way, while at the same time one or more volume elts are inconsistent. Some examples:



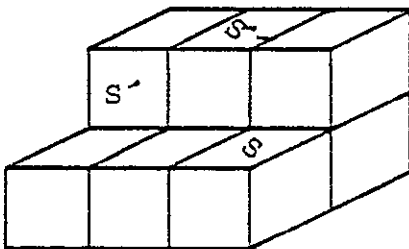
NOT ALLOWED

A double face-sd volume elt

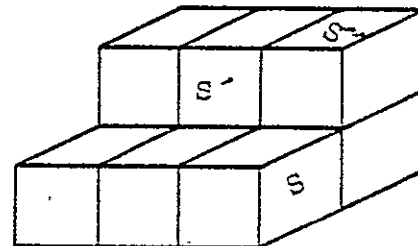


NOT ALLOWED

The same elt is double edge-sd

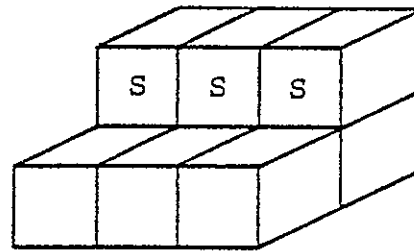


S, S' NOT ALLOWED
S, S'' NOT ALLOWED
S', S'' NOT ALLOWED



S, S' NOT ALLOWED
S, S'' NOT ALLOWED
S', S'' NOT ALLOWED

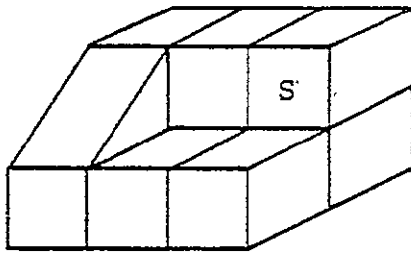
There is no easy solution to inconsistency problems
on concave surfaces.



ACCEPTABLE

SURFACE CELLS THAT ARE NOT SQUARE

It is easy to remember that surface cells that are not square cannot be subdivided. But remember also that volume elts which have any non-square face cannot be subdivided.



NOT ALLOWED

Edge-sd elt has diagonal
on one face

7.6 · SDLIST

User input selects which surface cells are to be face-sd. It remains to identify face-sd elts, edge-sd cells, and edge-sd elts.

Face-sd elts are easily found. There are two volume elts sandwiching each face-sd surface cell. One of them must be a filled volume elt. The other must be empty. The empty elt is designated face-sd.

To identify edge-sd cells and elts, a list of subdivided edges must be created. There are four sd edges for each sd face, but some edges are shared by two sd faces. Redundancies are eliminated.

Once the sd edges are listed each surface cell is tested to see if it has an edge on this list. If it does, and if it is not a face-sd cell, it is designated an edge-sd cell.

Any edge in space is the intersection of four volume elts. For each subdivided edge, a test is run on the four volume elts it touches.

If the elt is empty and not already subdivided, it becomes an edge-sd elt. If it has already been noted as subdivided, a check is run for consistency. An edge-sd elt must have only one subdivided edge, and a face-sd elt must have one subdivided face and four subdivided edges.

In addition to identifying subdivided cells and elts, SDLIST creates four lists which are used by many other subdivision routines. They are:

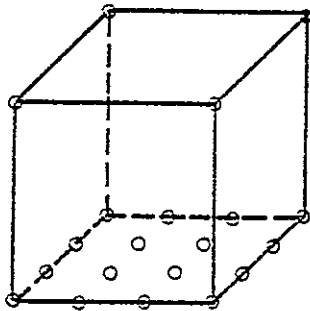
- An index of sd faces (LOFACE).
- An index of sd edges (LOEDGE).
- A list of sd cells (JSUBBR).
- A list of sd elts (LTABBR).

7.7 RESIDUALS AND SUBDIVISION

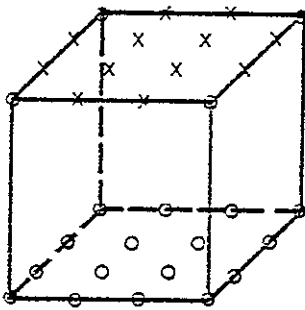
The most basic operation in the coproduct section is residual calculation.

We know how to calculate residuals for the vertices of a rectangular parallelepiped with a node at each vertex. We do not know how to calculate residuals for a rectangular parallelepiped with extra nodes lying along an edge or on a face.

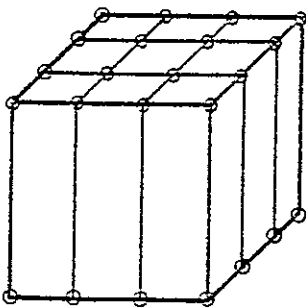
Therefore, we break sd cells and elts into smaller pieces that are easy to handle. The manner of breakup is shown in the following diagrams.



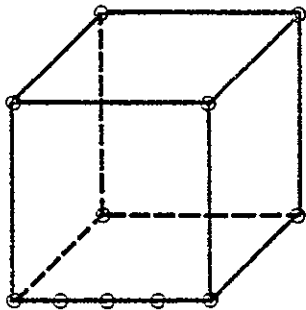
A face-sd elt showing all node points (NSUB = 2).



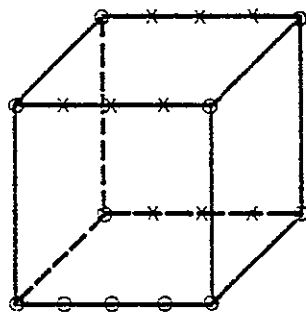
Values are interpolated for imaginary nodes.



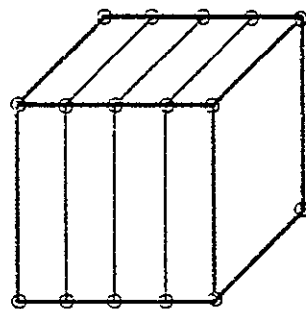
So the elt can be broken into 9 rectangular parallelepipeds for residual calculation.



An edge-sd elt with all nodes shown (NSUB = 3).



Imaginary edge nodes are interpolated.



For breakup into four rectangular parallelepipeds.

DICER is the subroutine that handles face-sd cells and elts. SLICE takes care of edge-sd cells and elts.

7.8 STORAGE

The student of NASCAP will realize that at the time when COPROD calculates AUN for volume elements of the inner grid, there is some effort expended to make room for three large (17 x 17 x 33) arrays. U, AUN, and the element table are all necessary for this calculation.

The AUN calculation for a subdivided element requires these three arrays plus SDAUN plus SDYOU plus the edge and face index arrays. These additional arrays total only about five thousand words, but there is no place to put them.

The solution is to create an abbreviated element table including only subdivided elts. Then after the usual calculation has been made for non-subdivided elts, the element table is dispensed with. The space it occupied is written over with the abbreviated element table and the other subdivision information. The large U and AUN arrays remain where they were.

The IOBJ file, formerly not used, now holds information for subdivision. The arrays, in the order stored, showing maximum dimensions, are:

```
SDARR (18*MXFACE)
SDYOU (18*MXFACE)
SDDIV (18*MXFACE)
SDAUN (18*MXFACE)
SDPEE (18*MXFACE)
SDROUS (18*MXFACE)
LOFACE (MXFACE)
LOEDGE (3*MXFACE)
LTABBR (2,6*MXFACE)
JSUBBR (4*MXFACE)
```

In the current code MXFACE = 50. This is the maximum number of subdivided faces allowed. The implicit limit on

number of subdivided edges is $=3*MXFACE$, maximum number of subdivided elts $=6*MXFACE$, and maximum number of subdivided cells $=4*MXFACE$.

The first six sd arrays correspond to existing CG arrays. LOFACE and LOEDGE are the index arrays for faces and edges. LTABBR and JSUBBR are abbreviated element table and surface cell list.

JSUBBR is just selected entries from the JSURF list. The surface cell location is encoded. However, the spacial location of a volume element listed in the element table is known by its position in the element table. So for our condensed version we need two words for each elt.

Word 1 = SQUISH — encoding of elt origin.

Word 2 = element table entry for subdivided elt.

7.9 INTERNAL REPRESENTATION

Faces and Edges

Sd faces and sd edges are represented by single word entries in the sd face index list and sd edge index list.

Any face on the grid is determined uniquely by a normal direction and an origin. The normal direction is given as 1, 2, or 3, corresponding to plus or minus X, plus or minus Y, or plus or minus Z direction, respectively. The origin is the lowest X, Y, and Z coordinate on the face.

Any edge on the grid is similarly determined by its direction and origin. Notice that while this scheme uniquely identifies a face among faces or an edge among edges, confusion will result if faces and edges are mixed. The face with direction (normal direction) 3 at origin (8,8,8) is a square parallel to the X-Y plane with corners at (8,8,8),

(9,8,8), (8,9,8), and (9,9,8). The edge with direction 3 at (8,8,8) is a line segment from (8,8,8) to (8,8,9).

For subdivided faces and edges, the index word is formed by subroutine SQUISH. SQUISH forms an integer by adding $10^6 \cdot \text{direction} + 10^4 \cdot \text{X coordinate} + 10^2 \cdot \text{Y coordinate} + 10^0 \cdot \text{Z coordinate}$. The reverse transformation is accomplished by EXPAND.

Cells

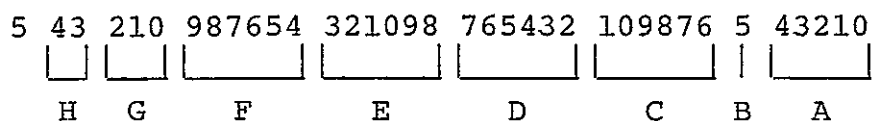
The surface cell list is encoded as in Figure 7.5. The lowest order 5 bits hold the material number for a surface.

Material numbers 11 - 20 inclusive are used for face-sd cells. Numbers 21 - 30 are for edge-sd cells.

The material number mod 10 is used to reference material properties stored in the MATPR array.

Elt

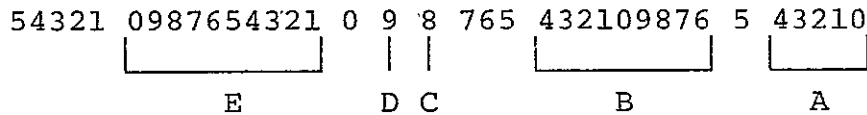
The element table for volume elements is described in Figure 7.6. A face-sd elt is set to element type 10. An edge-sd element is element type 11.



<u>Field</u>	<u>Bits</u>	
A	4-0	Material index
B	5	Set for right-triangular 100 surfaces and for 111 surfaces whose enclosing volume cell is mostly empty
C	11-6	Direction of surface normal (in crystallographic notation)
D	17-12	Z-coordinate
E	23-18	Y-coordinate
F	29-24	X-coordinate
G	32-30	Conductor index
H	34-33	Orientation code for right-triangular 100 surfaces

Figure 7.5. Surface cell list (JSURF) entry format.

CODE FOR ELEMENT TABLE [LTBL(NX,NY,NZ)].



<u>Field</u>	<u>Bits</u>	
A	4-0	Elt-type code
B	14-6	Orientation code
C	18	Set if elt is completely filled (interior)
D	19	Set for an empty special elt
E	30-21	Index used to reference PHOJ array to determine low energy electron currents

ORIENTATION CODE

3 x 3 bits. Each group of 3 contains 1, 2 or 3 in the lower 2 bits, with the high bit set for negative.

Code $(-)^{m_1} i_1, (-)^{m_2} i_2, (-)^{m_3} i_3$

takes (r_1, r_2, r_3) to $(-)^{m_1} r_{i_1}, (-)^{m_2} r_{i_2}, (-)^{m_3} r_{i_3}$

e.g., the following codes take a point to (x,y,z):

<u>Octal Code</u>	<u>Dec. Code</u>	<u>Point</u>
123	1,2,3	(x,y,z)
365	3,-2,-1	(-z,-y,x)
532	-1,3,2	(-x,z,y)
176	1,-3,-2	(x,z,-y)
567	-1,-2,-3	(-x,-y,-z)
617	-2,1,-3	(y,-x,-z)

Figure 7.6. Element table codes and orientation codes.

7.10 SIGNIFICANT SUBDIVISION CONSTANTS

Most of these constants are computed in SDLIST. The exception is NSUB which is user-specified.

NSUB

The number of subdivision points that lie between adjacent grid points on a subdivided surface.

NUMFA, NUMED

NUMFA is the total number of subdivided faces. NUMED is the total number of subdivided edges ($\text{NUMED} \leq 4 \cdot \text{NUMFA}$).

NSDELT, NSDURF

NSDELT is the number of sd volume elts, NSDURF the number of sd surface cells.

LENTRU

This is the number of extra nodes, i.e., the number of subdivided points. It is the sum $\text{NSUB} \cdot \text{NUMED} + \text{NSUB}^2 \cdot \text{NUMFA}$.

7.11 SIGNIFICANT SUBDIVISION ARRAYS

The first four arrays are constructed by SDLIST. They keep track of what goes where. The last six arrays are where what goes. They are the data arrays used by TRILIN, and they are the object of the complex indexing schemes that subdivision routines deal with. Unless noted, the arrays are one-dimensional.

LOFACE, LOEDGE

These are the index arrays used for storage of sd point information. Each sd face or sd edge has a one-word entry in the table. The entry is an encoding (from SQUISH) of the low index grid node of the face or edge, and the direction of the face or edge. The direction of an edge is the direction it points — the direction of a face its normal direction.

From the location of an entry corresponding to the sd face or edge, the storage location of its points (in SDYOU, SDAUN) is known.

JSUBBR

This is an abbreviated version of the surface cell list JSURF, including only those cells that are subdivided.

LTABBR (2, NSDELT)

An abbreviated version of the element table LTABL, including only subdivided elts. An extra word is needed to indicate the location of elts. In LTABL (17,17,33) location is equivalent to position in the array.

SDYOU, SDAUN, SDPEE, SDARR, SDDIV, SDROUS

These are the arrays used by TRILIN to compute potentials at subdivided points. They correspond to the grid point arrays U, AUN, P, R, DIV, and ROUS, respectively. The "SD" arrays are one-dimensional, as subdivided points are not arranged in an orderly three-dimensional fashion.

PSURF (NSUB, NSUB, NUMFA), PED (NSUB, NUMED)

These arrays are a more convenient way to reference the SDYOU array. SDYOU begins with face subdivision points (PSURF) and ends with edge subdivision points. Consequently PSURF (1,1,1) is equivalenced to SDYOU (1). PED (1,1) is equivalent to $\text{SDYOU} (\text{NSUB}^2 \cdot \text{NUMFA} + 1)$, the location of the first edge sd point.

RSURFS (NSUB, NSUB, NUMFA), REDS (NSUB, NUMED)

Like PSURF and PED, but these arrays are equivalenced to locations in the SDAUN array. RSURFS (1,1,1) equiv SDAUN (1) ... REDS (1,1) equiv $\text{SDAUN} (\text{NSUB}^2 \cdot \text{NUMFA} + 1)$.

7.12 SUBDIVISION SUBROUTINE SUMMARIES

BAKINT

Calling Sequence: SUBROUTINE BAKINT (TERP, NPT, BEG, XEND)

Called By: EMPDI, EMPSLI

Purpose: Linear back-interpolation. Values stored in TERP for one, two, or three equally spaced points are back-interpolated to endpoints BEG and XEND.

BILBAK

Calling Sequence: SUBROUTINE BILBAK (RESARR, NSUB)

Purpose: Bilinear back-interpolation. The values of the top face ($Z = 2$) of a subdivided cube, stored in RESARR, are back-interpolated to the four corners. NSUB is the number of subdivisions = 1, 2, or 3.

BILINT

Calling Sequence: SUBROUTINE BILINT (VT, DIPOT, NSUB)

Purpose: Bilinear interpolation. Vertex values from VT are interpolated for values on the top face of a subdivided cube. DIPOT stores the results.

CLOKRO

Calling Sequence: SUBROUTINE CLOKRO (VFROM, VTO)

Purpose: Clockwise rotation of cube. Vertex values in VFROM are rotated 90° around an axis parallel to the Z axis, resulting in cube VTO. The rotation is clockwise looking from plus Z.

CORNAD

Calling Sequence: SUBROUTINE CORNAD (IJK, NORM, PIECE,
BIGARR, NX, NY, NZ)

Called By: GETDIV, EDGADD, CORNAD

Purpose: Add to surface corners. Finds locations in BIGARR corresponding to corner nodes of square surface cell with origin IJK and normal NORM. Adds PIECE to each of these locations.

COTELL

Calling Sequence: SUBROUTINE COTELL (AUN, UP)

Purpose: Prints out all non-zero values in two big arrays (17 x 17 x 17).

DIAGCA

Calling Sequence: SUBROUTINE DIAGCA (DX, DY, DZ)

Purpose: Diagonal calculation. Calculates diagonal term of coproduct for vertices of a given rectangular parallelepiped. It is $1/9 (DY \cdot DZ / DX + DX \cdot DZ / DY + DX \cdot DY / DZ)$.

DICER

Calling Sequence: SUBROUTINE DICER (VT, AUT, IABC, IJK,
NSUB, DZ, NUMFA, LOFACE, PSURF, RSURFS,
NUMED, LOEDGE, PED, REDS)

Called By: SUBDIV, SURFSD

Purpose: Residual calculation for face-sd cells and elts. DICER retrieves U values, makes successive calls to RESID or TRIRES, and stores the resulting AUN values.

Arguments include the vertex U values (VT) and the origin (IJK) and orientation (IABC) of the subdivided face. U values for subdivided points are found in PSURF and PED arrays.

FILDI performs a bilinear interpolation for the top face. The subdivided object can now be treated as a set of $(NSUB + 1)^2$ rectangular parallelepipeds.

TRIRES or RESID is called for each of the rectangular parallelepipeds.

The residual (AUN values) on top are back-interpolated to the vertices by EMPDI. Residuals of sd nodes are added to RSURFS and REDS arrays. Vertex residuals are returned in AUT.

(See also section "RESIDUALS AND SUBDIVISION".)

EDGABC

Calling Sequence: SUBROUTINE EDGABC (NSID, IFAABC, NSIABC)

Purpose: Generate orientation vector for an edge. NSIABC is returned as the orientation vector of side number NSID of the face with orientation vector IFAABC.

EDGADD

Calling Sequence: SUBROUTINE EDGADD (IJK, NORM, PIECE,
BIGARR, NX, NY, NZ, SMLARR, NUMFA, LOFACE,
NUMED, LOEDGE)

Called By: QUPDAT, GETDIV

Purpose: Add to nodes of edge-sd surface. Locations corresponding to sd points are found in SMLARR. Corner points are in BIGARR. Add in the following proportions:

Edge-sd nodes: $2 \cdot \text{PIECE}$.

Corner nodes on sd edge: $1 \cdot \text{PIECE}$.

Corner nodes opposite sd edge: $(\text{NSUB} + 1) \cdot \text{PIECE}$

This distribution corresponds to uniformly distributed charge or back-interpolation from $(\text{NSUB} + 1)$ equal rectangular parallelepipeds.

EDGETE

Calling Sequence: SUBROUTINE EDGETE (IXELT, IXEDGE, LTABLE,
NX, NY, NZ, NSDEL, LTABBR)

Called By: EDLTAB

Purpose: Edge test for possible sd elt. Checks elt with origin IXELT to see if edge-sd. Other possibilities are that it may be filled or already sd. If already sd, a consistency check is made. If not already sd and empty, the element table is altered.

EDGIND

Calling Sequence: SUBROUTINE EDGIND (NSID, IABC, IJK, ISQ)

Purpose: Edge index code. For edge number NSID of the given face (IABC, IJK), the edge index code (ISQ) is returned.

EDLTAB

Calling Sequence: SUBROUTINE EDLTAB (IXFAC, LTABLE, NX, NY, NZ, NSDELT, LTABBR)

Purpose: Edge-sd elt test. Given a sd face, test the eight elts (call EDGETE) that share one edge with this face. See if they are edge-sd.

EMPDI

Calling Sequence: SUBROUTINE EMPDI (RESARR, AUT, FACRES, EDGRES, NSUB)

Called By: DICER

Purpose: Break RESARR array into component parts. Calls BILBAK for back-interpolation of top ($Z = 2$) face of subdivided cube. Puts vertex values into AUT, sd face into FACRES, and sd edge into EDGRES.

Complements FILDI.

EMPSLI

Calling Sequence: SUBROUTINE EMPSLI (RESARR, AUT, EDGRES, NSUB)

Called By: SLICE

Purpose: Breaks single edge RESARR into vertex values (AUT) and one edge values (EDGRES).

Complements FILSLI.

EXPAND

Calling Sequence: SUBROUTINE EXPAND (IX, IDIR, IJK)

Purpose: Expand single word code into direction (IDIR = 1, 2 or 3) and origin (IJK). Inverse operation of SQUISH.

FACADD

Calling Sequence: SUBROUTINE FACADD (IJK, NORM, PIECE, BIGARR, NX, NY, NZ, SMLARR, NUMFA, LOFACE, NUMED, LOEDGE)

Called By: QUPDAT, GETDIV

Purpose: Add to nodes of face-sd surface. Locations of sd face and edge points in SMLARR, grid points in BIGARR. For even distribution, sd face nodes get 4 * PIECE, edge nodes get 2 * PIECE, corner nodes get 1 * PIECE.

Similar to EDGADD.

FACETE

Calling Sequence: SUBROUTINE FACETE (LTELT, IJK, IABC, LTABLE, NX, NY, NZ, NSDELT, LTABBR)

Called By: FALTAB

Purpose: Test for face-sd elts. Alter element table if elt is empty and not already sd. Otherwise test for consistency.

Similar to EDGETE.

FACIND

Calling Sequence: SUBROUTINE FACIND (IABC, IJK, ISQ)

Purpose: Index code for face. Construct one-word index code (ISQ) for face with orientation IABC on elt with origin IJK.

FALTAB

Calling Sequence: SUBROUTINE FALTAB (IXORG, NORM, LTABLE,
NX, NY, NZ, NSDELT, LTABBR)

Purpose: Face-sd elt test. Given an sd face, test (call FACETE) the elt in front and behind. One should be filled, the other face-sd.

FDOT

Calling Sequence: FUNCTION FDOT (VONE, VTWO, LENGTH)

Purpose: Floating dot product. Take dot product of two real vectors of given length.

FILDI

Calling Sequence: SUBROUTINE FILDI (VT, FRECK, XNOTCH, DIPOT,
NSUB)

Called By: DICER

Purpose: Fill DIPOT (5,5,2) array from its component parts — vertices (VT), face (FRECK), and edges (XNOTCH). Top face is interpolated. Preparation for calls to residual routine.

Complements EMPDI.

FILLAR

Calling Sequence: SUBROUTINE FILLAR (ICORN, P, FILLIN, PSURF,
PED, LOFACE, LOEDGE)

Purpose: Fill an array (FILLIN) with potential values for an area that includes sd nodes.

FILSLI

Calling Sequence: SUBROUTINE FILSLI (VT, XNOTCH, SLIPOT,
NSUB)

Called By: SLICE

Purpose: Build SLIPOT (5,2,2) from vertices (VT), one subdivided edge (XNOTCH), and three edge interpolation.

Similar to FILD I.

Complements EMPSLI.

FINDED

Calling Sequence: SUBROUTINE FINDED (IJK, NORM, NUMFA,
LOFACE, NUMED, LOEDGE, IFOND, JSID)

Purpose: Find an edge. Get storage location of the edge for a surface that is edge-sd. Will not work for face-sd cell.

GENVER

Calling Sequence: SUBROUTINE GENVER (IJK, NORM, IHAVER)

Purpose: Generate vertices. Returns in IHAVER (3,4) the coordinates of the four corners of a surface with origin IJK and normal NORM.

IDOT

Calling Sequence: FUNCTION IDOT (JV, KV, NLEN)

Purpose: Integer dot product. Value is dot product of two integer arrays with length NLEN.

INDEX

Calling Sequence: FUNCTION INDEX (IDENT, IARRAY, LENGTH)

Purpose: Look up index number. IARRAY is an array of index codes of given length. If IDENT corresponds to one of the entries INDEX returns the entry number. If it is not on the list, value of INDEX is 0.

LININT

Calling Sequence: SUBROUTINE LININT (BEG, XEND, NPT, TERP)

Purpose: Linear interpolation BEG and XEND are the values at the endpoints. TERP returns with values for NPT equally spaced intermediate points ($NPT \leq 3$).

LONEDG

Calling Sequence: SUBROUTINE LONEDG (IJK, IOR, IXED)

Purpose: Edge index code for one sd edge. Given elt origin (IJK) and sd edge orientation (IOR) returns edge index code IXED.

MAFILL

Calling Sequence: FUNCTION MAFILL (LTAB)

Purpose: Filled elt test. MAFILL \neq 0 if element table entry LTAB refers to a completely filled element.

MATMUL

Calling Sequence: SUBROUTINE MATMUL (ARRAY, VECTOR, RESULT, NDIM)

Purpose: Matrix multiplication. The square array is multiplied by the vector to yield the result. All are real-valued.

OFFSET

Calling Sequence: SUBROUTINE OFFSET (IABC, IOFF)

Purpose: Compute offset (IOFF) from elt origin corresponding to orientation vector IABC.

PTAA, PTAB, PTAC

Calling Sequence: SUBROUTINE PTAC (LABEL, ID, JD, KD, ARRAY, IR, JR, KR)

Purpose: Print array. PTAA for one-dimensional arrays, PTAB for two-dimensional and PTAC for three-dimensional. The array is dimensioned (ID, JD, KD). Values are printed for $X = 1, IR \dots Y = 1, JR \dots Z = 1, KR$. The label is printed first.

PTAQ

Calling Sequence: SUBROUTINE PTAQ (LABEL, Q)

Purpose: Print a cube. The array Q (2,2,2) is taken to represent the vertices of a cube. The values are printed in a format suggesting a perspective drawing of a cube.

RESID

Calling Sequence: SUBROUTINE RESID (SKIN, SKOUT, AL, S)

Called By: DICER, SLICE

Purpose: Calculate residuals for subsection of a volume elt. SKIN holds U values for the vertices of a rectangular parallelepiped with $dx = dy = S, dz = AL$. SKOUT returns corresponding AUN values.

TRIRES performs the same function for surface cells.

SDINPU

Calling Sequence: SUBROUTINE SDINPU (no arguments)

Called By: INPUT

Purpose: Input subdivision information. Takes user specification for subdivided area, and alters surface cell list (JSURF) for face-sd cells. Sets NSUB.

SDLIST

Calling Sequence: SUBROUTINE SDLIST (LTABLE, NX, NY, NZ, IOBJIN)

Purpose: Alter lists and make new lists for subdivision. Surface cell list and element table altered for sd cells and elts. Forms lists of sd faces, sd edges, sd cells, and sd elts. Some of the work done through calls to FALTAB and EDLTAB.

SLICE

Calling Sequence: SUBROUTINE SLICE (UT, AUT, IABC, IJK, NSUB, DZ, NUMFA, LOFACE, PSURF, RSURFS, NUMED, LOEDGE, PED, REDS)

Called By: SUBDIV, SURFSD

Purpose: Residual calculation for edge-sd cells and elts. Structure is parallel to DICER (see DICER). Difference is that only one edge has sd nodes and three edges must be interpolated (see section "RESIDUALS AND SUBDIVISION").

SPILSD

Calling Sequence: SUBROUTINE SPILSD (ICORN, IDELTS, P,
FILLIN, PSURF, PED, LOFACE, LOEDGE)

Purpose: Output. Prints potential values for given rectangular area including some subdivided cell(s).

SQUISH

Calling Sequence: SUBROUTINE SQUISH (IDIR, IJK, ISQ)

Purpose: Produce index code ISQ. The four numbers IDIR and IJK(3) are encoded into one word.

Inverse operation to EXPAND.

SUBDIV

Calling Sequence: SUBROUTINE SUBDIV (UP, AUN, NX, NY, NZ,
DOTPRO, SDYOU, SDAUN, NUMFA, LOFACE,
NUMED, LOEDGE, NSDELT, LTABBR)

Called By: ISPACE

Purpose: Subdivided elt residual calculation, top level routine. Cycle over sd elts. For each retrieve vertex U values and transform to standard orientation. Call DICER or SLICE. Add resulting vertex AUN values (residuals) to grid node AUN array.

Similar to SURFSD.

SUBSCR

Calling Sequence: SUBROUTINE SUBSCR (ICORN, LH, MV, MYORG,
LITLH, LITMV)

Called By: FILLAR

Purpose: Subscript computation for data organizing routine FILLAR. Given offsets of a single square cell in area of interest, returns grid coordinates of square origin and FILLAR coordinates for sd points.

SURFSD

Calling Sequence: SUBROUTINE SURFSD (UP, AUN, NX, NY, NZ,
UPCOND, AUCON, SDYOU, SDAUN, NUMFA, LOFACE,
NUMED, LOEDGE, NSDURF, JSUBBR)

Called By: ISPACE

Purpose: Sd surface cell residual calculation, top level routine. Cycles over sd surface cells. For each, retrieves U values for four corners and underlying conductor. Translates edge-sd cell into standard orientation. Calls DICER or SLICE. Adds grid node AUN values (residuals) to AUN array.

Similar to SUBDIV.

TRANSD

Calling Sequence: SUBROUTINE TRANSD (VFROM, VTO, NS)

Called By: SURFSD

Purpose: Transform edge-sd cells. Sd edge is on bottom (minus Z) face. It is side number 1, 2, 3, or 4. TRANSD transforms the vertices to bring sd edge to side 1. Also performs inverse transformation.

TRIRES

Calling Sequence: SUBROUTINE TRIRES (SKIN,SKOUT, DX, DY, DZ)

Called By: DICER, SLICE

Purpose: Residual calculation for rectangular parallelepiped section of surface cell. DZ is the effective thickness of surface cell. DX and DY depend on NSUB and whether surface cell is face-sd or edge-sd. Performs appropriate matrix multiplications with a damping term and scalar multiplication by the dielectric constant for this cell.

Similar to RESID which handles volume elts.

UNSURF

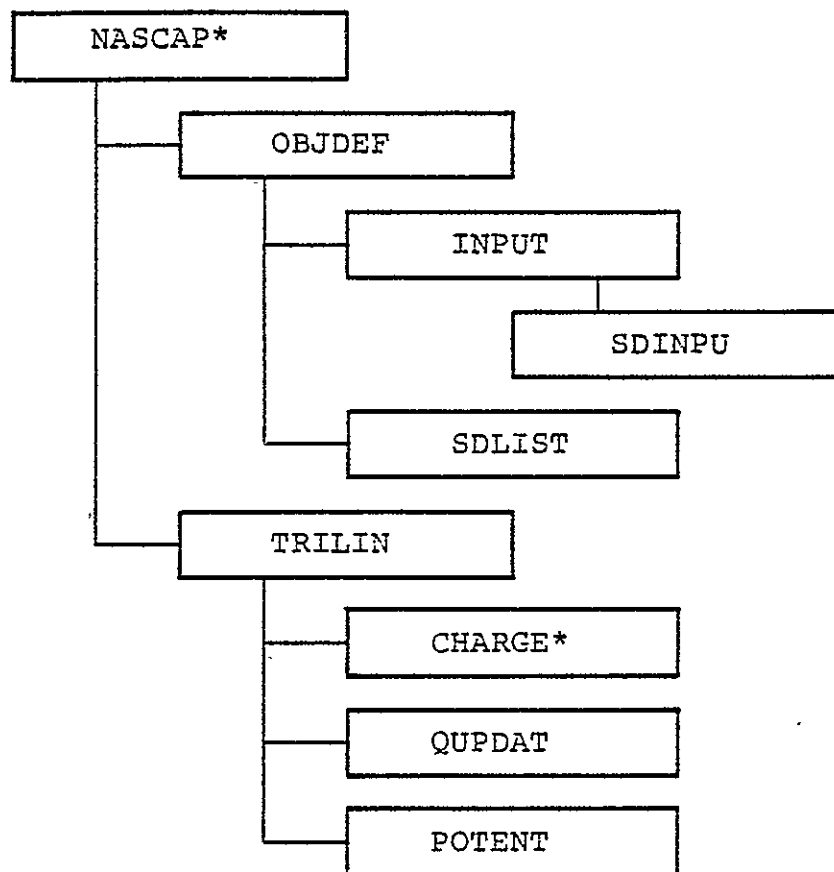
Calling Sequence: SUBROUTINE UNSURF (JSUWOR, MCONDU, IJK,
NORM, MATL, DUMA, DUMB)

Purpose: Decodes entry in surface cell list (JSURF) for information about a single cell.

7.13 CODE STRUCTURE

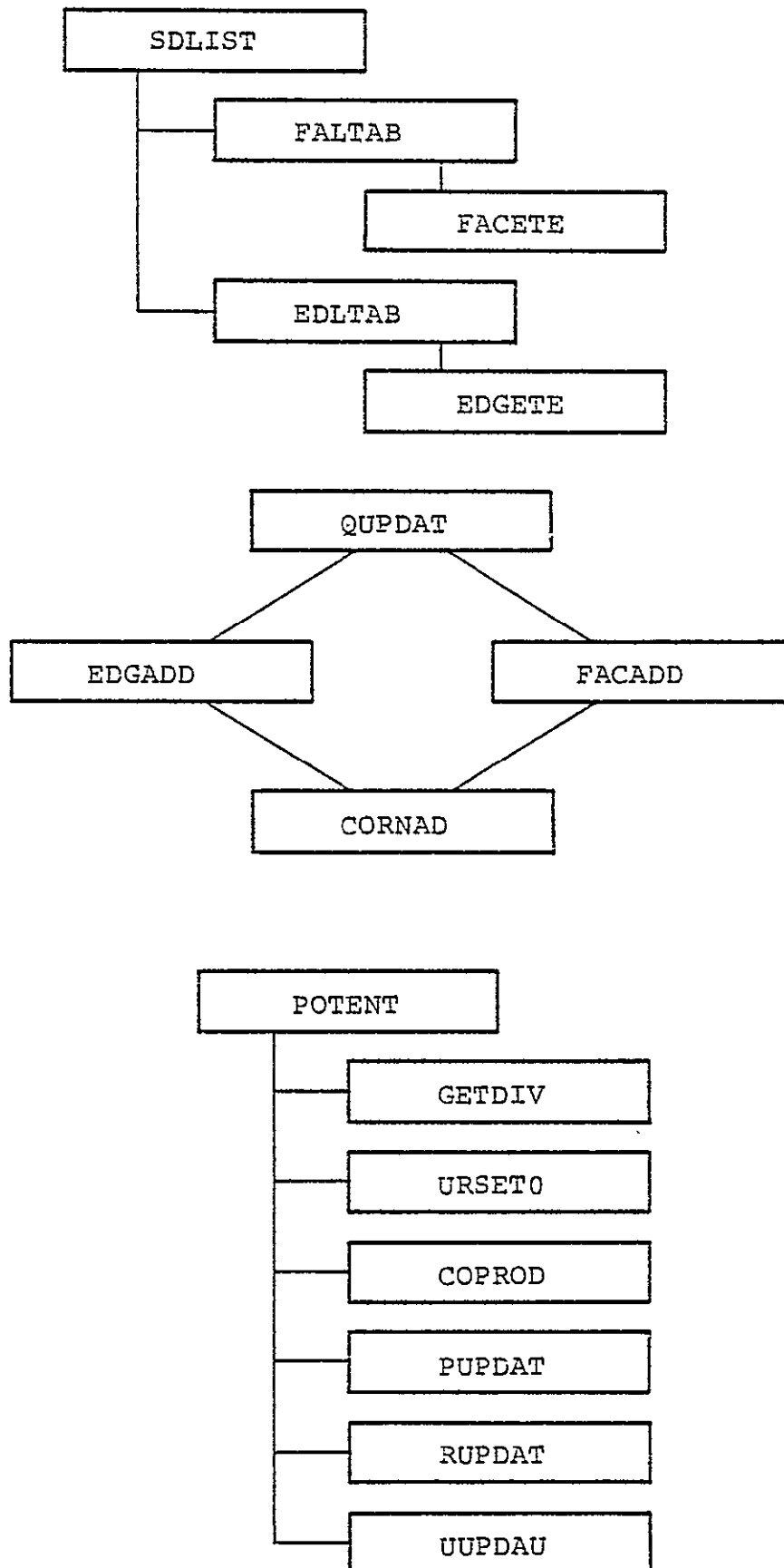
The following diagrams illustrate the new subdivision routines and old routines that have been altered for subdivision. For the sake of clarity, some routines are included even though they have not been changed. These are marked with an asterisk (*).

LEVEL 1

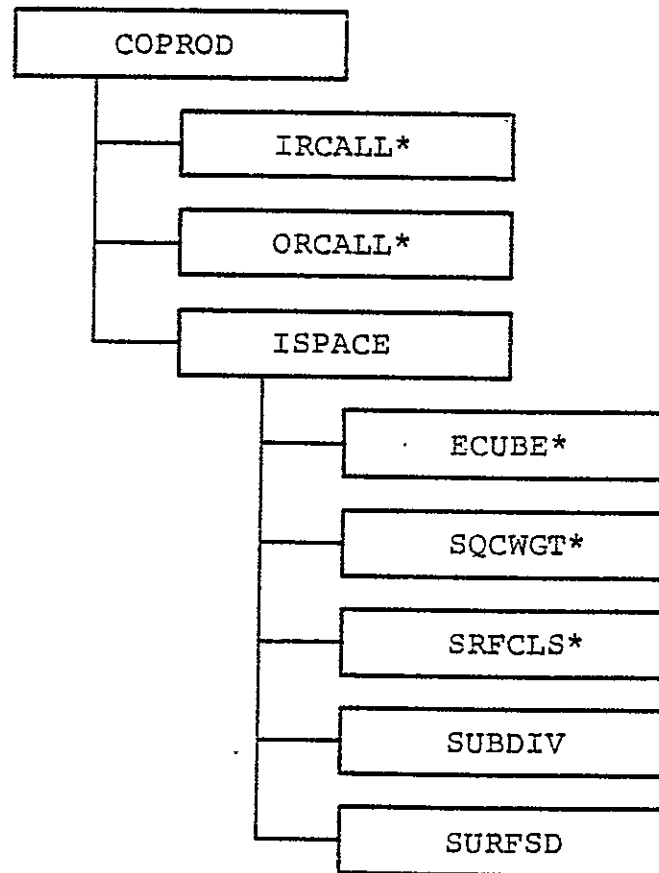
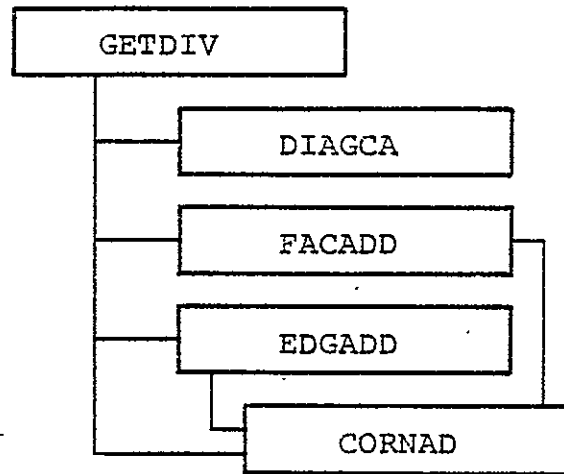


* Not changed by subdivision.

LEVEL 2

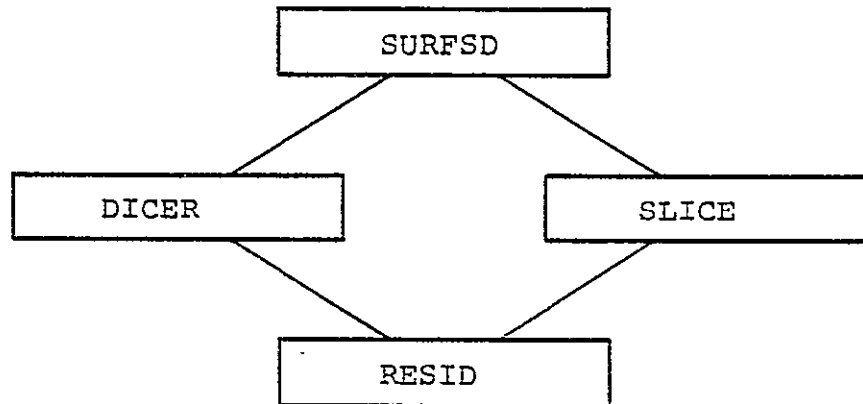
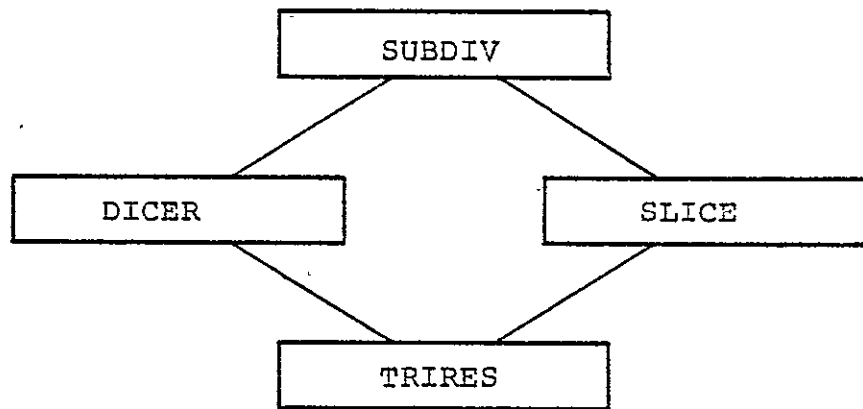


LEVEL 3

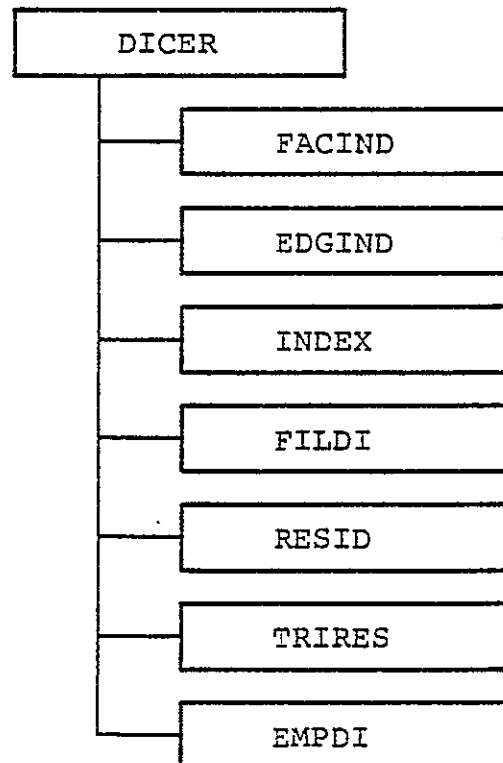
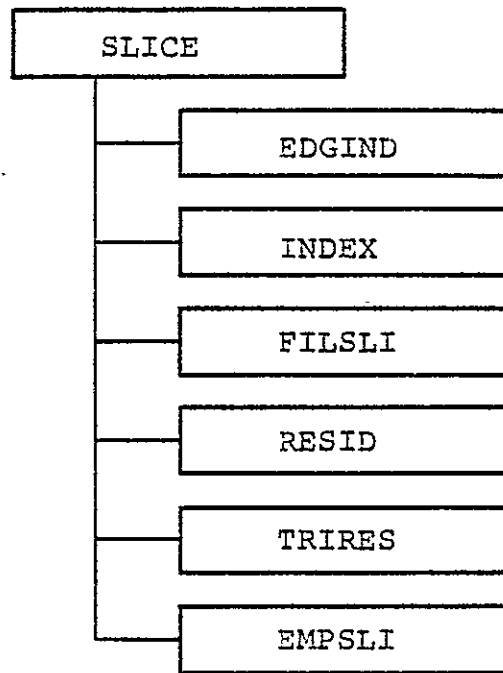


*Not changed by subdivision.

LEVEL 4



LEVEL 5



8. PARTICLE DETECTORS

NASCAP contains a set of routines which permit the user to obtain a fine resolution calculation of the energy flux density function as observed at user-specified locations on the satellite. The routines have been constructed so that the calculations render information in a form which resembles that which might be obtained experimentally from a particle detector located on the satellite. In order to use the routines the NASCAP user must specify that a particle detector is located upon one or more surface cells of the satellite model. In terms of a spherical coordinate system which is located upon the surface cell the user may then elect to have the energy flux density (as observed by the detector) plotted as a function of any one of the three variables: detector polar angle, detector azimuthal angle, and kinetic energy of the incident particles. One variable is selected as the independent variable to be swept through a user-specified range of values while the other two remain fixed at user-selected values.

In addition, the user may provide a description of the particle detector's resolution. The calculated value of the energy flux density is then obtained as an integral average over the detector's angular and energy apertures.

The energy flux density for each detector which the user has "activated" is calculated and plotted as a function of the selected independent variable at user-selected points within the NASCAP runstream. Plots for both electron and proton energy flux density are combined on a single overlay plot. A separate plot is made for each detector.

Also available to the user is an option to plot the particle trajectories generated during reverse-trajectory evaluation of the energy flux density function. If this

option is selected then each time a detector flux plot is generated, a set of particle plots is also generated. In order to constrain the number of plotted trajectories to a reasonable number, only one particle trajectory is plotted for each value of the selected independent variable at which the detector energy flux density integral is evaluated even though more particle trajectories may have been generated. (Referring to Eq. (8.10) in the section entitled "Detector Energy Flux Density Measurement", the trajectory which gets plotted is the one for which $i = j = k = 1$.) Separate plots of particle trajectories projected onto the Y-Z, X-Z and X-Y planes are produced for each of the two particle species - electrons and protons. Thus six particle plots are produced for each detector at each multiple of the NASCAP time cycle step selected. (Note the potential for an excessive number of plots if care is not exercised!) Each particle plot also includes a silhouette of the satellite.

8.1 SPECIFICATION OF DETECTOR ORIENTATION

In order to specify the direction in which a particle detector is to measure energy flux density it is necessary for the NASCAP user to be familiar with three different right-handed coordinate systems.

1. The Satellite Coordinate System

This is the coordinate system in which the satellite building blocks are defined.

2. The Surface Cell Coordinate System

This system is obtained by performing the following operations on the satellite coordinate system:

- a. The X-Y plane is rotated counterclockwise through an angle ϕ about the Z-axis until the +X-axis coincides with the X-Y plane projection of the surface cell normal vector.
- b. The Z-X plane is rotated counterclockwise through an angle ψ about the Y-axis until the +Z-axis coincides with the cell normal vector.
- c. The origin of the system (obtained by successive rotations in a. and b. is translated to the center of the surface cell face.

The procedure of a - b is illustrated in the following diagram. The double-primed coordinate axes are for the cell system while the unprimed coordinate axes are for the satellite system. Table 8.1 lists ψ and ϕ for each of the 26 possible cell normals which NASCAP can produce.

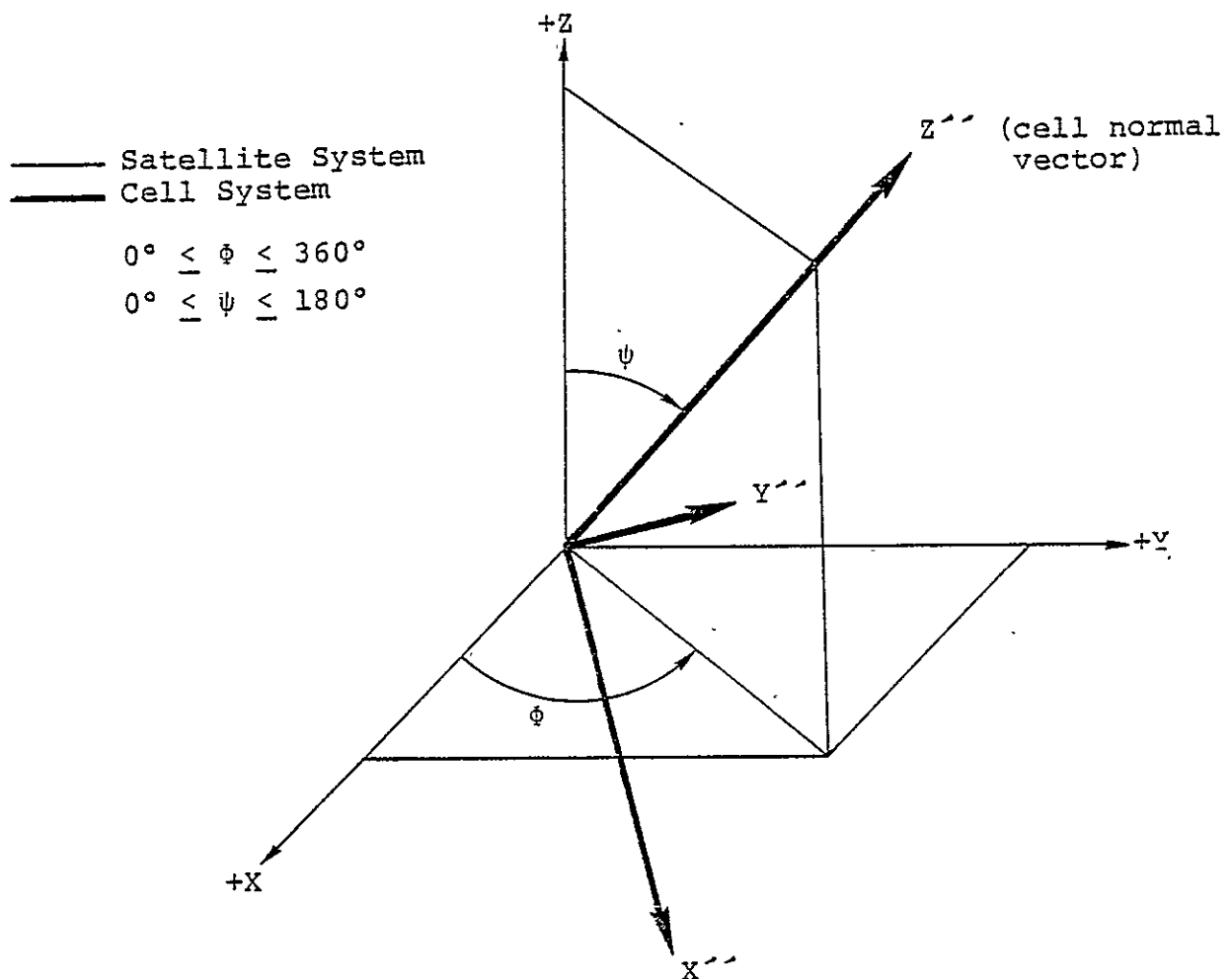


Table 8.1. Cell Coordinate System Rotation With Respect to Satellite System

<u>Cell Normal Type</u>	<u>ψ</u>	<u>ϕ</u>
-1 -1 -1	125.26°	225.00°
-1 -1 0	90.00	225.00
-1 -1 1	54.74	225.00
-1 0 -1	135.00	180.00
-1 0 0	90.00	180.00
-1 0 1	45.00	180.00
-1 1 -1	125.26	135.00
-1 1 0	90.00	135.00
-1 1 1	54.74	135.00
0 -1 -1	135.00	270.00
0 -1 0	90.00	270.00
0 -1 1	45.00	270.00
0 0 -1	180.00	0.00
0 0 0	-	-
0 0 1	0.00	0.00
0 1 -1	135.00	90.00
0 1 0	90.00	90.00
0 1 1	45.00	90.00
1 -1 -1	125.26	315.00
1 -1 0	90.00	315.00
1 -1 1	54.74	315.00
1 0 -1	135.00	0.00
1 0 0	90.00	0.00
1 0 1	45.00	0.00
1 1 -1	125.26	45.00
1 1 0	90.00	45.00
1 1 1	54.74	45.00

The surface cell coordinate system is the coordinate system in which the NASCAP user can specify the direction in which the detector is to be pointed. This is done most conveniently by transforming the rectangular surface cell coordinate system into a spherical one. The detector orientation is then specified by ϕ , the azimuthal angle and θ , the polar angle. The following table contains a few key combinations that may help to clarify the use of ϕ and θ .

<u>ϕ</u>	<u>θ</u>	<u>Direction Detector Points</u>
0°	0°	+Z axis of cell system (cell normal)
0°	90°	+X axis of cell system
90°	90°	+Y axis of cell system
180°	90°	-X axis of cell system
270°	90°	-Y axis of cell system

When measuring the energy flux density function it is probably the energy dependence of the function which will be of interest so that θ and ϕ will be maintained at fixed values. It is possible, however, to display the energy flux density as a function of either θ or ϕ for a user-specified angular range. This might be a desirable thing to do in cases for which the detector does not have a clear view in all directions (i.e., the detector might be shadowed in some directions by other parts of the satellite).

8.2 THE DETECTOR COORDINATE SYSTEM

This system is obtained by performing the following operations on the surface cell coordinate system. Let \vec{v} be the vector which points in the direction in which the detector energy flux density is to be measured. (\vec{v} has coordinates ϕ, θ in the spherical coordinate system of the surface cell.)

- a. The X-Y plane is rotated counterclockwise through the angle ϕ about the Z axis until the +X axis coincides with the projection of \vec{v} onto the X-Y plane of the surface cell coordinate system.
- b. The Z-X plane is rotated counterclockwise through the angle θ about the Y axis until the +Z axis coincides with \vec{v} .

The NASCAP user will normally not be directly concerned with the details of how the detector coordinate system relates to the other two coordinate systems. All that one need be aware of is that the +Z axis of the detector coordinate system is the central axis of the hemispherical cap which is used to model the angular aperture of the detector. (See Section 8.4, "Detector Energy Flux Density Measurement".)

8.3 CALCULATION OF ENERGY FLUX AT A CELL SURFACE

In order to obtain an expression for the energy flux density measured by a detector located at a given surface cell of the satellite model it is helpful to first consider the general problem of calculating the total energy flux which is incident at the surface of the cell due to the ambient plasma environment. Let \hat{k} be the unit normal vector for the surface cell. Using the cell's rectangular coordinate system (obtained by appropriate rotation of the satellite coordinate system) with the +Z axis in the direction of \hat{k} , the energy flux at the cell surface center is calculated as follows:

$$\vec{E}_O = -\hat{k} \int_{-\infty}^{\infty} \int_{-\infty}^{\infty} \int_{-\infty}^{\infty} \left(\frac{m|\vec{V}_O|^2}{2e} \right) \frac{1}{e} \left\{ (e\vec{V}_O \cdot \hat{k}) f_O(\vec{V}_O) \right\} d^3V_O$$

where \vec{E}_O = energy flux vector (eV/(M²-sec)) at cell surface

$$\vec{V}_O = v_x \hat{i} + v_y \hat{j} + v_z \hat{k} \quad (\text{velocity at surface})$$

$$d^3V_O = dv_x dv_y dv_z$$

$f_O(\vec{V}_O)$ = phase space density function evaluated at the surface for particles with velocity \vec{V}_O .

m = mass of incident particles.

e = charge of incident particles (electrons or protons).

To evaluate the integral it is expedient to change from rectangular to spherical coordinates. The necessary substitutions are:

$$v_o = |\vec{V}_o|$$

$$d^3V_o = v_o^2 \sin\theta \, d\theta \, d\phi \, dv_o$$

$$(e\vec{V}_o \cdot \hat{k}) = ev_o \cos\theta$$

With these the energy flux integral transforms into

$$\begin{aligned} \vec{E}_o &= -\hat{k} \int_0^\infty \int_0^{2\pi} \int_0^{\pi/2} \left(\frac{mv_o^2}{2e} \right) \left\{ ev_o \cos\theta f_o(\theta, \phi, v_o) \right\} v_o^2 \sin\theta \, d\theta \, d\phi \, dv_o \\ &= -\hat{k} \int_0^\infty \int_0^{2\pi} \int_0^1 \left(\frac{m}{2e} \right) v_o^5 f_o(\mu, \phi, v_o) \frac{d\mu^2}{2} \, d\phi \, dv_o \end{aligned}$$

where $\mu = \cos\theta$.

Next we change variables from v_o (the magnitude of the velocity at the surface) to E_o (the kinetic energy at the surface of the cell).

Let

$$\frac{1}{2} m v_o^2 = e E_o \quad (\text{factor } e \text{ because } E_o \text{ is in eV})$$

$$dv_o = \frac{e dE_o}{mv_o}$$

Then the energy flux integral becomes

$$\begin{aligned} \vec{E}_o &= -\hat{k} \int_0^\infty \int_0^{2\pi} \int_0^1 2 \left(\frac{e}{m} \right)^2 E_o^2 f_o(\mu, \phi, E_o) \frac{d\mu^2}{2} \, d\phi \, dE_o \\ &= -\hat{k} \int_0^\infty \int_0^{2\pi} 2 \left(\frac{e}{m} \right)^2 E_o^2 f_o(E_o, \vec{\Omega}_o) \mu \, d\Omega \, dE_o \end{aligned} \quad (8.1)$$

where we have introduced the solid angle Ω as an integration variable for notational convenience.

Finally we introduce the energy flux density function $G(E, \Omega)$. From the definition we know that

$$\vec{E}_O = -\hat{k} \int_0^\infty \int_0^{2\pi} G_O(E_O, \vec{\Omega}_O) \mu \, d\Omega \, dE_O \quad (8.2)$$

Comparison of the integrands in Eqs. (8.1) and (8.2) yields the identity

$$2\left(\frac{e}{m}\right)^2 f_O(E_O, \vec{\Omega}_O) = \frac{G_O(E_O, \vec{\Omega}_O)}{E_O^2} \quad (8.3)$$

This equation provides the key to correct evaluation of G at the cell surface by reverse trajectory particle tracking. Since f is a constant along a particle trajectory we have for particles emitted at the cell surface with initial energy E_O and velocity vector in the direction of $\vec{\Omega}_O$:

$$f_O(E_O, \vec{\Omega}_O) = f_\infty(E_\infty, \vec{\Omega}_\infty) \quad (8.4)$$

$$\frac{G_O(E_O, \vec{\Omega}_O)}{E_O^2} = \frac{G_\infty(E_\infty, \vec{\Omega}_\infty)}{E_\infty^2} \quad (8.5)$$

where

f_O = phase space density function evaluated at cell surface.

f_∞ = phase space density function evaluated at infinity.

G_O = energy flux density function evaluated at cell surface.

G_{∞} = energy flux density function evaluated at infinity.

E_0 = initial kinetic energy of particle to be tracked.

E_{∞} = kinetic energy of particle after reverse trajectory tracking to infinity.

$\vec{\Omega}_0$ = initial velocity direction vector of particle at cell surface.

$\vec{\Omega}_{\infty}$ = velocity direction vector for particle after reverse trajectory tracking to infinity.

Therefore, if the energy flux density function G is known at infinity then using reverse trajectory particle tracking the energy flux at the surface of the cell may be computed from

$$\tau_{E_0} = -\hat{k} \int_0^{\infty} \int_0^{2\pi} E_0^2 \left\{ \frac{G_{\infty}(E_{\infty}, \vec{\Omega}_{\infty})}{E_{\infty}^2} \right\} \mu \, d\Omega \, dE_0 \quad (8.6)$$

This equation is used (with slight modification) in the following section to arrive at an expression for the energy flux density which is measured by a particle detector located on the surface cell.

8.4 DETECTOR ENERGY FLUX DENSITY MEASUREMENT

Consider an ideal particle detector located at the center of a surface cell and oriented such that the +Z axis of the detector's rectangular coordinate system points in the direction in which the energy flux density is to be measured. Assume that the detector's rectangular coordinate system is transformed into a spherical coordinate system and that \vec{n} is the unit normal pointing in the direction in which the particle detector is pointing. If the detector responds to particles having energy E_0 then the measured value for the energy flux density will be

$$\begin{aligned} \frac{\partial^2 \vec{E}_0}{\partial E_0 \partial \vec{\Omega}} &= -\vec{n} E_0^2 \cdot \left\{ 2 \left(\frac{e}{m} \right)^2 f_0(E_0, \vec{n}) \right\} \mu \\ &= -\vec{n} E_0^2 \left\{ \frac{G_\infty(E_\infty, \vec{\Omega}_\infty)}{E_\infty^2} \right\} \mu \end{aligned} \quad (8.7)$$

where

\vec{E}_0 = energy flux vector at cell surface.

f_0 = phase space density function evaluated at cell surface.

E_0 = kinetic energy (in eV) of particles at cell surface.

ϕ = azimuthal angle in detector coordinate system.

θ = polar angle in detector coordinate system.

E_∞ = kinetic energy (in eV) of particles after reverse trajectory tracking to infinity.

$\vec{\Omega}_\infty$ = velocity direction vector for particles after reverse trajectory tracking to infinity.

m = mass of particles.

$G_{\infty}(E, \vec{\Omega})$ = energy flux density function (i.e., tabulated Deforest data, for example. Units are eV/(sec-cm²-sr-eV).)

In practice, a real detector responds to a finite range of particle energies and velocity vectors so that the energy flux density observed by the detector is really $\partial^2 \vec{E}_O / \partial E_O \partial \Omega$ averaged over the energy and angular apertures of the detector. Thus, in general, the value which the detector yields is of the form

$$\frac{\partial^2 \vec{E}_O}{\partial E_O \partial \Omega} = \frac{-\vec{n} \int_0^{\infty} \int_0^{2\pi} W(E_O, \vec{\Omega}) E_O^2 \left\{ \frac{G_{\infty}(E_{\infty}, \vec{\Omega}_{\infty})}{E_{\infty}^2} \right\} \cos \theta \, d\Omega \, dE_O}{\int_0^{\infty} \int_0^{2\pi} W(E_O, \vec{\Omega}) \, d\Omega \, dE_O} \quad (8.8)$$

where $W(E_O, \vec{\Omega})$ is a weight function which describes the characteristics of the detector's energy and angular apertures.

In the current version of NASCAP it has been assumed that the energy aperture of a detector is a rectangular weight function which has a value of 1 from E to $E + \Delta E$ and 0 elsewhere. The angular aperture is assumed to be a hemispherical cap of "width" $\Delta \theta$ in the polar angle. (The vector \vec{n} passes through the center of this cap.) The weight has a value of 1 anywhere on the cap and 0 elsewhere. Therefore, NASCAP detectors compute the energy flux density from

$$\begin{aligned}
\frac{\overline{\partial^2 \tilde{\epsilon}_O}}{\partial E_O \partial \Omega} &= \frac{-\vec{n} \int_E^{E+\Delta E} \int_0^{2\pi} \int_{\cos^2 \Delta \theta}^1 E_O^2 \left\{ \frac{G_\infty(E_\infty, \vec{\Omega}_\infty)}{E_\infty^2} \right\} \frac{d\mu^2}{2} d\phi dE_O}{\int_E^{E+\Delta E} \int_0^{2\pi} \int_0^{\Delta \theta} \sin \theta d\theta d\phi dE_O} \\
&= \frac{-\vec{n} \int_E^{E+\Delta E} \int_0^{2\pi} \int_{\cos^2 \Delta \theta}^1 E_O^2 \left\{ \frac{G_\infty(E_\infty, \vec{\Omega}_\infty)}{E_\infty^2} \right\} \frac{d\mu^2}{2} d\phi dE_O}{(1 - \cos \Delta \theta) 2\pi \Delta E} \quad (8.9)
\end{aligned}$$

where $\mu = \cos \theta$.

This integral is evaluated by a three-dimensional approximation formula which uses the mid-point rule with n_ϕ points to compute the integral over ϕ , the mid-point rule with n_ψ points to compute the integral over μ^2 , and the even-order Gauss-Legendre formula with n_ϵ points to compute the integral over E_O . The composite formula used is:

$$\begin{aligned}
\frac{\overline{\partial^2 \tilde{\epsilon}_O}}{\partial E_O \partial \Omega} &\approx -\vec{n} \left\{ \left(\frac{2\pi}{n_\phi} \right) \sum_{i=1}^{n_\phi} \frac{(1 - \cos^2 \Delta \theta)}{2n_\psi} \sum_{j=1}^{n_\psi} \left(\frac{\Delta E}{2} \right) \sum_{k=1}^{n_\epsilon/2} \left\{ W_k \epsilon_k^2 F(\phi_i, \mu_j^2, \epsilon_k) \right. \right. \\
&\quad \left. \left. + W_{-k} \epsilon_{-k}^2 F(\phi_i, \mu_j^2, \epsilon_{-k}) \right\} \right\} \frac{1}{(1 - \cos \Delta \theta) 2\pi \Delta E} \\
&= -\vec{n}_\gamma \sum_{i=1}^{n_\phi} \sum_{j=1}^{n_\psi} \sum_{k=1}^{n_\epsilon/2} \left\{ W_k \epsilon_k^2 F(\phi_i, \mu_j^2, \epsilon_k) + W_{-k} \epsilon_{-k}^2 F(\phi_i, \mu_j^2, \epsilon_{-k}) \right\} \quad (8.10)
\end{aligned}$$

where

$$\epsilon_k = \frac{\Delta E}{2} (\chi_k + 1) + E$$

$$\phi_i = \frac{2\pi}{n_\phi} (i - 1/2)$$

$$\mu_j^2 = \Delta\mu^2 (j - 1/2) + (1 - n_\psi \Delta\mu^2) \quad \{\psi \text{ denotes } \mu^2\}$$

and

$$\Delta\mu^2 = (1 - \cos^2 \Delta\theta) / n_\psi$$

$$\gamma = \frac{(1 + \cos \Delta\theta)}{4 n_\psi n_\phi} \quad (\text{multiply by } 10^{-4} \text{ to put units in cm}^{-2})$$

$$F(\phi_i, \mu_j^2, \epsilon_k) = \frac{G_\infty(E_\infty, \vec{\Omega}_\infty)}{E_\infty^2} \bigg|_{ijk} \quad (\text{returned by FSPACE})$$

E_∞ and $\vec{\Omega}_\infty$ are the final energy and velocity vector respectively of a particle after reverse trajectory tracking from the center of the surface cell (beginning with initial velocity specified by ϕ_i , μ_j^2 , and ϵ_k) to infinity.

The χ_k and W_k are the Gauss-Legendre integration coefficients for n_ϵ an even integer. (Note that $\chi_k = -\chi_{-k}$ and $W_k = W_{-k}$.) A slightly modified formula is used to permit $n_\epsilon = 1$. (Also note that $-1 \leq \chi_k \leq 1$ for all k .)

It should be noted that although the detector energy flux integral includes only contributions from the ambient plasma environment it is possible that some particle trajectories will yield $E_\infty < 0$. This could occur if the particle originates from another part of the satellite, for example.

For detector particle trajectory plotting purposes all particles must be tracked regardless of origin. Therefore, a test is made within the innermost integral summation loop to determine if $E_{\infty} \geq 0$. If it is not then no attempt is made to evaluate G and G is assumed to be 0.

8.5 NASCAP PARTICLE DETECTOR ACTIVATION

Each of up to twenty particle detectors is activated by the appearance of a detector keyword definition sequence in the NASCAP runstream. A detector keyword definition sequence consists of a "DETECT" keyword card which is optionally followed by one or more of the keyword cards to be described below. A detector keyword definition sequence is terminated either by an "END" keyword card or else by another detector keyword definition sequence. If more than one detector is to be activated "simultaneously" the associated keyword definition sequences must be consecutive. The last detector keyword definition sequence to appear on the NASCAP keyword file must always be terminated by an "END" card. In addition, if no other NASCAP runstream options are to follow the detect keyword sequences a second "END" card should follow the detect "END" card. The reason for this is that the first "END" terminates the detector run while the last "END" terminates the NASCAP runstream.

If it is desired to call the detector routine more than once from the NASCAP runstream using the same set of detector options then the detector keyword definition sequence(s) should reside upon its (their) own separate file.

If the FORTRAN file number used is 23, for example, then each time a DETECT 23 card appears in the NASCAP runstream detector routine execution will be initiated using the detector keyword options in file 23. If the detector keyword options reside in a file other than the NASCAP runstream then the DETECT card on the runstream should only be followed by an "END" card if no other functions are to be performed by NASCAP following detection. As an example, assume the detector keyword file is 23 and that following detection, we desire to do HIDCEL followed by TRILIN and finally another detect. The NASCAP runstream would look like:

```

.
.
.
.
DETECT 23
HIDCEL
TRILIN
DETECT 23
END

```

If, on the other hand, the detector keywords are to be inserted in the NASCAP runstream itself then the runstream might look something like:

```

.
.
DETECT
ICELL 210 } first detector run
AUTOS    }
END      }
HIDCEL
TRILIN
DETECT
ICELL 210 } second detector run
AUTOS    }
END      }
END

```

8.6 NASCAP DETECTOR SCRATCH FILES

The NASCAP detector routines require the use of two scratch files. The NASCAP file IAUN is used as a temporary file for storing detector flux measurement information. In general, the user need not concern himself with this. The other file used is the NASCAP file IPART. It is the user's responsibility to make sure this file has been assigned for scratch usage. Since the file is used for particle trajectory plotting it is recommended that additional space beyond the computing system default for normal files be allocated. The default value of IPART is -28. (The negative value is required to indicate that an old NASCAP routine, PARPLT, is not to be activated. The absolute value of IPART is used by the detector routines, however.) On the UNIVAC 1100/81 machine it is recommended that the runstream include the card

```
@ASG,T 28,F///1000
```

prior to the @XQT card.

8.7 DETECTOR KEYWORD INPUT FILE

At the beginning of each detector keyword sequence (appearance of the "DETECT" card) all parameters which describe the properties of the detector being activated assume a set of default values. The NASCAP user then has the option of changing any of these values to suit his requirements. This is accomplished by including one or more of the cards to be described below. The contents of each card consists of a mnemonic keyword, left justified in card columns 1-6, and possibly the value of a data variable associated with the keyword. The type of data required (if any) is determined by applying the standard FORTRAN convention for variable types to the keyword. Variables must appear in columns 21-30 of the keyword card. The format used is I10 for INTEGER type and F10.0 for REAL type. In a few cases an option may be specified by a card having the form keyword = option where option is another mnemonic name. This type of card requires that there be no embedded blanks between the keyword, equal sign, and option.

8.8 DESCRIPTION OF DETECTOR PARAMETER OPTIONS BY KEYWORD

8.8.1 General Detector Definition Parameters

ICELL Index number of the surface cell at which a detector is to be activated. The detector will be placed at the center of this surface cell. The acceptable range is $1 < \text{ICELL} \leq 1250$. The default value is $\text{ICELL} = 1$. (It should be remarked that the same value of ICELL may be specified in more than one detector keyword sequence so that it is possible to simulate several types of detectors, each located on the same surface all within the same run.)

COMMEN This card is for programmer convenience in identifying the purpose of keyword cards in the detector keyword input file. If this card appears, columns 7-72 may contain any comment the user desires. It is echoed back on the keyword listing at execution time but is otherwise ignored.

8.8.2 Detector Aperture Definition Parameters

NP Number of points used for integration over the detector aperture azimuthal angle (n_ϕ in Eq. (8.10)). Acceptable range is $\text{NP} \geq 1$. Default is $\text{NP} = 1$.

NMU2 Number of points used for integration over the transformed detector aperture polar angle parameter μ^2 (n_ψ in Eq. (8.10)). Acceptable range is $\text{NMU2} \geq 1$. Default is $\text{NMU2} = 1$.

NE Number of points used for integration over the detector energy aperture (n_ϵ in Eq. (8.10)). Acceptable range is $\text{NE} = 1$ or $2 < \text{NE} < 12$ where NE must be an even integer. Default is $\text{NE} = 1$.

NSTP Maximum number of steps per particle allowed during reverse trajectory tracking. Acceptable range is $1 < \text{NSTP} \leq 500$. Default is $\text{NSTP} = 100$. In practice, values around 300 or more are likely to be necessary.

DTH Polar angular width of the hemispherical cap used to model the detector angular aperture ($\Delta\theta$ in Eq. (8.10)). Acceptable range is $0.0^\circ \leq \text{DTH} \leq 90.0^\circ$. The default is $\text{DTH} = 0.0^\circ$.

DE Width of detector energy aperture in eV (ΔE in Eq. (8.10)). Acceptable range is $DE \geq 0.0$. Default is $DE = 0.0$.

8.8.3 Independent Variables and Fixed Parameters

INDVAR Keyword = option type variable used to select independent variable for detector energy flux density plots. The acceptable options and their results are:

<u>Option</u>	<u>Independent Variable</u>	<u>Independent Variable Axis Scale Type</u>
ENERGY	E	Log
PHI	ϕ	Linear
THETA	θ	Linear

Default is INDVAR=ENERGY.

N Number of increments used for the independent variable (number of points on the detector flux plot horizontal-axis.) Acceptable range is $3 \leq N \leq 500$. Default is $N = 100$.

Any one of the following three keywords (parameters) may be selected as the independent variable for detector flux plots (see INDVAR above). If a parameter is selected as the independent variable then the value specified by the associated keyword below is the starting value of the parameter. (The ending value is selected using the keyword FINALV.) Otherwise the parameter is held fixed at the value specified by the associated keyword card for all points which the independent variable assumes.

ENERGY Kinetic energy (in eV) of particles incident at the detector (E in Eq. (8.10)). Acceptable range is $ENERGY > 0.0$. Default value is $ENERGY = 10.0$.

PHI Azimuthal angle ϕ of the detector (in degrees) as measured in the spherical coordinate system of the cell at which the detector is located. Acceptable range is $0.0^\circ \leq PHI \leq +360.0^\circ$. Default is $PHI = 0.0$.

THETA Polar angle θ of the detector (in degrees) as measured in the spherical coordinate system of the cell at which the detector is located. Acceptable range is $-90.0^\circ \leq THETA \leq +90.0^\circ$. Default is $THETA = 0.0$.

(Note: Letting PHI, THETA, and DTH assume their default values will produce a detector which looks along the normal to the surface cell ICELL upon which it is located.)

FINALV Final value (in appropriate units) of the independent variable selected by INDVAR. If INDVAR=THETA then acceptable range is $-90.0^\circ \leq \text{FINALV} \leq +90.0^\circ$. If INDVAR=PHI acceptable range is $\text{FINALV} \leq 720^\circ$. If INDVAR=ENERGY acceptable value is $\text{ENERGY} < \text{FINALV} < 50,000$ eV. Default value is 4.999×10^4 eV (assumes default INDVAR=ENERGY was used). If INDVAR \neq ENERGY then the user must explicitly input a value for FINALV.

8.8.4' Plot Scaling Options

PSCALE Proton to electron energy flux density scale factor. This factor determines the separation of the proton and electron flux density curves on the overlay plot generated by the detector routines. The proton flux values are multiplied by the factor $10.0 \times \text{PSCALE}$ before plotting. The acceptable range is $\text{PSCALE} > 0.0$. Default is $\text{PSCALE} = 5$.

LWPEN Line width of pen used to draw the proton flux curve. The default is $\text{LWPEN} = 3$ raster increments. (The electron flux curve is always drawn with a line 1 raster increment wide.) The acceptable range is $1 \leq \text{LWPEN} \leq 10$.

FLXMIN Minimum value for the logarithmic energy flux density scale on detector plots. (The scale is in units of $\text{eV}/(\text{cm}^2\text{-sec-sr-eV})$.) The acceptable range is $\text{FLXMIN} > 0.0$. Default is $\text{FLXMIN} = 10^4$. (This parameter is ignored if the AUTOS option is in effect.)

FLXMAX Maximum value for the logarithmic energy flux density scale on detector plots. The acceptable range is $\text{FLXMAX} > \text{FLXMIN}$. Default is $\text{FLXMAX} = 10^{12}$. (This parameter is ignored if the AUTOS option is in effect.)

AUTOS If this card is included the detector routines will automatically select the scale limits FLXMIN and FLXMAX at execution time so that a reasonable portion of the data is displayed. If this card appears then any values specified for FLXMIN and FLXMAX are ignored. The default is manual scaling by the user as specified by FLXMIN and FLXMAX. The AUTOS option is highly recommended, however.

8.8.5 Reverse Trajectory Particle Tracking

PLPART If this card is included in a detector keyword definition sequence then particle trajectory plots will be produced for the detector.

VCODE Tolerance limit for the maximum distance in code units which particles are permitted to move at the first timestep after emission from the detector cell. Acceptable range is $0.0 < \text{VCODE} \leq 10.0$. The default is $\text{VCODE} = 0.3$ inner grid units.

8.8.6 Specification of Environment for Detectors

The detector routines require that the environment flux definition file be present. The only acceptable flux types are TYPE 3, Maxwell or DeForest. If NASCAP is using some other flux type than this then a special flux file must be prepared and activated by doing a RDOPT and setting IFLUX to the detector flux file unit number just prior to doing DETECT. Following DETECT it may be necessary to do RDOPT to reset IFLUX to the correct file number to be used for further computations performed by TRILIN.

9. PARTICLE EMITTERS

9.1 LOW DENSITY PARTICLE EMITTERS: GENERAL DESCRIPTION

NASCAP has the capability to simulate satellite charging effects which result from one or more low density particle emitters placed at user-specified cell locations. Given that a particle emitter is to reside upon a particular surface cell of the satellite model the NASCAP user may, via keyword input, specify a number of parameters which describe the emitter's characteristics. Included among these are: type of particles emitted (electrons or protons), total emission current, and direction of emission (specified in terms of the polar and azimuthal angles in a spherical coordinate system which is located upon the emitter's surface cell). In addition, the user may choose one of several current density functions to represent the energy and angular characteristics of the emitter gun. If desired, the user may elect to have the trajectories which result from emitter gun forward particle tracking plotted at specified multiples of the NASCAP time cycle. (The satellite surface cell currents are, of course, corrected to include emitter current contributions at each NASCAP time-step whether or not plots are produced.) Separate plots of particle trajectories projected onto the X-Y, Y-Z, and Z-X planes are produced for each of up to five particle emitters which the user may have activated. Optionally, particle trajectories for all emitters may be combined on a single set consisting of three two-dimensional projection views. The user may also elect to have the three projection views plotted more than once, each time using a different maximum grid boundary. This permits the fine details of particles returning to the satellite to be viewed while also displaying the details of particles circling in large radii due to the presence of a magnetic field, for example. Each particle trajectory plot also includes a silhouette projection of the satellite.

With a few minor exceptions, the sets of parameters which describe the characteristics of the emitters may be specified independently of one another. Thus one could, for example, define an electron emitter with a beam current of $1 \mu\text{a}$ on surface cell 1 and a proton emitter with a beam current of $10 \mu\text{a}$ on surface cell 470. The conductors underlying these two cells must be different, however. (See "Restrictions" section.)

9.2 SPECIFICATION OF EMITTER BEAM ORIENTATION

Particle emitter beam orientation is defined in virtually the same way as detector orientation. (See the section entitled "Specification of Detector Orientation".) One difference to be noted is that in the case of a detector, energy flux may be displayed as a function of θ or ϕ by "sweeping" one variable or the other through a specified range while the other remains fixed. It is assumed that an emitter does not change its orientation during satellite charging calculations, however, so that θ and ϕ always remain fixed at user-selected values for each emitter. It should also be noted that the detector coordinate system (which shall now be referred to as the emitter coordinate system) is the coordinate system in which the integral of the emitter's current density function is performed.

9.3 PARTICLE EMITTER BEAM CURRENT REPRESENTATION

The emission current density functions of NASCAP particle emitters contain a single energy spectral peak and are non-zero only over a finite spatial range. In particular the emitter current is envisioned as flowing out from the geometric center of the surface cell upon which the emitter is located and through a small hemispherical cap of width $\Delta\theta$ in the polar angle. (The Z-axis of the emitter coordinate system passes through the center of this cap.) NASCAP generates a finite representation of the emission current by emitting a discrete set of particles. The angles and energies with which particles are emitted are chosen in an optimized manner so that the total emission current is divided equally among each particle of the set. Each particle is "pushed"^{*} in the electrostatic^{**} and magnetic fields external to the satellite until it is identified as either having hit some part of the satellite thus representing a returning fraction of the total current or else as having escaped, thus representing a current fraction to the environment.

* Particle pushing is done by solving the Lorentz force equation using the leap-frog scheme of Boris. See Reference 4. Boris' procedure has been expanded to permit re-centering of the equations in time. Thus the timestep may be dynamically increased or decreased as appropriate to keep particles moving at velocities commensurate with the NASCAP grid in which they are located.

** Tracking of particles which pass out of the highest NASCAP grid continues using a monopole electric field, the magnitude of which is obtained from the total charge on the satellite.

9.4 DISCRETE PARTICLE EMISSION ANGLES AND ENERGIES

The present version of NASCAP offers the user two choices for emission angle selection. One choice is the uniform distribution, a special case of which results in each particle representing the same solid angle fraction of the current. The other choice is a cosine θ distribution in which a disproportionate number of particles are emitted at angles "close" to the axis of the hemispherical cap (Z-axis of the emitter coordinate system). Two choices for the energy spectrum of the beam are also provided. Either choice results in an approximate representation of a mono-energetic peak in the energy spectrum — the difference between the two choices being the mathematical form of the approximation function. The emission angles and energy distribution functions available are listed below. (Any angular dependence may be combined with any energy dependence.)

9.4.1 Uniform Angular Current Density Dependence

For each of n_e discrete energies, n_ϕ n_θ particles are emitted. The initial emission velocity direction vector of each particle (measured in the emitter coordinate system) is

$$\vec{V}_{ij} = (\sin\theta_j \cos\phi_i)\hat{i} + (\sin\theta_j \sin\phi_i)\hat{j} + (\cos\theta_j)\hat{k} \quad (9.1)$$

where

$$\phi_i = \frac{2\pi}{n_\phi} (i - 1/2) \quad i = 1, 2, \dots, n_\phi$$

$$\theta_j = \frac{\Delta\theta}{n_\theta} (j - 1/2) \quad j = 1, 2, \dots, n_\theta$$

For the special choice of $n_\phi = n_\theta$ each particle represents the same solid angle fraction of the emitted current.

9.4.2 Cosine θ Angular Current Density Dependence

For each of n_ϵ discrete energies, n_ϕ n_θ particles are emitted. The initial velocity direction vector of each particle (measured in the emitter coordinate system) is

$$\vec{v}_{ij} = (\sin\theta_j \cos\phi_i)\hat{i} + (\sin\theta_j \sin\phi_i)\hat{j} + (\cos\theta_j)\hat{k}$$

where

$$\begin{aligned}\phi_i &= \frac{2\pi}{n_\phi} (i - 1/2) \quad i = 1, 2, \dots, n_\phi \\ \theta_j &= \sin^{-1} \left(\frac{(j-1/2) \sin\Delta\theta}{n_\theta} \right) \quad j = 1, 2, \dots, n_\theta\end{aligned}\tag{9.2}$$

9.4.3 Gaussian Energy Current Density Dependence

A Gaussian function may be used as an approximation to a mono-energetic spectrum. The current density function for the Gaussian approximation is

$$J(\epsilon) = \frac{I_B}{\sqrt{2\pi} \sigma} \exp \left(-\frac{1}{2} \left(\frac{\epsilon - \epsilon_0}{\sigma} \right)^2 \right)$$

where I_B is the total beam emission current.

It is easy to show that

$$\int_{-\infty}^{\infty} J(\epsilon) d\epsilon = I_B .$$

Since a real current distribution is not defined for negative energies the Gaussian function is only an approximate representation. However, one can show that

$$\lim_{\sigma \rightarrow 0} J(\epsilon) = I_B \delta(\epsilon - \epsilon_0) ,$$

and

$$\int_0^{\infty} J(\epsilon) d\epsilon \rightarrow I_B \quad \text{for } \epsilon_0 > 0 \text{ and } \frac{\sigma}{\epsilon_0} \ll 1 .$$

Thus the mono-energetic energy peak can be represented to any degree of accuracy desired simply by choosing σ/ϵ_0 small enough. It is worth noting that ~68 percent of the current falls in the range $\epsilon = \epsilon_0 \pm \sigma$ and ~92 percent of the current falls in the range $\epsilon = \epsilon_0 \pm 2\sigma$.

NASCAP chooses the discrete energy representation of the Gaussian energy distribution as follows:

$$\epsilon_i = F^{-1} \left(1 + \frac{(1/2 - i)}{n_\epsilon} \right) \quad i = 1, 2, \dots, n_\epsilon$$

where

$$F(X) = \int_X^{\infty} \frac{1}{\sqrt{2\pi} \sigma} \exp \left\{ -\frac{1}{2} \left(\frac{\epsilon - \epsilon_0}{\sigma} \right)^2 \right\} d\epsilon \quad (9.3)$$

This choice results in the following equality being satisfied:

$$\int_{\epsilon_i}^{\epsilon_{i+1}} J(\epsilon) d\epsilon = \frac{I_B}{n_\epsilon} \quad (9.4)$$

where we define $\epsilon_0 = 0$ and $\epsilon_{n_\epsilon+1} = \infty$.

Thus each discrete energy ϵ_i represents the same fraction ($1/n_\epsilon$) of the total emitted current. Furthermore, half of this fraction is a result of energy in the range $\epsilon_{i-1} < \epsilon \leq \epsilon_i$ and half is a result of energy in the range $\epsilon_i \leq \epsilon < \epsilon_{i+1}$.

9.4.4 Rational Energy Current Density Dependence

A rational function may be used as an approximation to a mono-energetic spectrum. The current density function used by NASCAP for the rational approximation is

$$J(\epsilon) = \frac{\mu I_B}{\left(\pi/2 + \tan^{-1} \mu\right)} \left\{ \frac{\alpha^2 \epsilon_0 \epsilon}{\left(\epsilon^2 - \epsilon_0^2\right)^2 + \left(\epsilon_0 \epsilon \alpha\right)^2} \right\} \quad (9.5)$$

where I_B = total emitter beam current

$$\mu = \sqrt{2 - \alpha^2} / \alpha \quad \text{and} \quad \alpha = \sigma / \epsilon_0$$

This density function has the property that

$$\lim_{\sigma \rightarrow 0} J(\epsilon) = I_B \delta(\epsilon - \epsilon_0)$$

and

$$\int_0^\infty J(\epsilon) d\epsilon = I_B \quad \text{for all } \sigma / \epsilon_0 < \sqrt{2}.$$

NASCAP chooses the discrete energy representation of the rational energy distribution according to Eq. (9.3) with the integrand for $F(X)$ replaced by the rational density function divided by I_B . This choice of energies also results in the satisfaction of the equality given by Eq. (9.4).

9.5 NASCAP PARTICLE EMITTER ACTIVATION

In order to activate low density particle emitters a special keyword file must be prepared. Each of up to five low density particle emitters is defined by the appearance of an emitter keyword definition sequence on this file. Each emitter keyword definition sequence consists of an "EMITER" keyword card which is optionally followed by one or more of the keyword cards described below. An emitter keyword definition sequence is terminated either by an "END" keyword card or else by another emitter keyword definition sequence. If more than one emitter is to be activated the associated keyword definition sequences must be consecutive. The last keyword sequence to appear on the emitter definition file must always be terminated by an "END" card.

Once the special emitter keyword file has been prepared all that is necessary to enable the emitter(s) during the charging portion of subsequent TRILIN calls is to place a card on the NASCAP keyword input file (done using RDOPT from the runstream) which has the keyword "EMITTE" in columns 1-6 and the FORTRAN unit number of the emitter keyword file in columns 29-30. If the emitter(s) have been activated by a previous RDOPT/TRILIN sequence then they may be deactivated by the keyword "NOEMIT" (appearing in the NASCAP keyword file) for subsequent TRILIN charging calculations.

9.6 NASCAP EMITTER SCRATCH FILES

The NASCAP emitter routines require the use of two scratch files. The NASCAP file IAUN is used as a temporary file for storing emitter fluxes to surface cells and other associated data. In general, the user need not concern himself with this. The other file used is the NASCAP file IPART. It is the user's responsibility to make sure this file has been assigned for scratch usage. Since the file is used for particle trajectory plotting it is recommended that additional space beyond the computing system default for normal files be allocated. The default value of IPART is -28. (The negative value is required to indicate that an old NASCAP routine, PARPLT, is not to be activated. The absolute value of IPART is used by the emitter routines, however.) On the Univac 1100/81 machine it is recommended that the runstream include the card

```
@ASG,T 28,F///1000
```

prior to the @XQT card.

9.7 EMITTER KEYWORD FILE PREPARATION

At the beginning of each emitter keyword sequence (appearance of the "EMITER" card in the emitter keyword file) all parameters which describe the properties of the emitter being activated assume a set of default values. The NASCAP user then has the option of changing any of these values to suit his requirements. This is accomplished by including one or more of the cards to be described below. The contents of each card consists of a mnemonic keyword, left-justified in card columns 1-6 and possibly the value of a data variable associated with the keyword. The type of data required (if any) is determined by applying the standard FORTRAN convention for variable types to the keyword. Values of variables must appear in columns 21-30 of the keyword card. The format used is I10 for INTEGER and F10.0 for REAL data.

9.8 DESCRIPTION OF EMITTER PARAMETER OPTIONS BY KEYWORD

9.8.1 Emitter Dependent Parameters

ICELL	Index number of the surface cell at which an emitter is to be activated. The acceptable range is $1 \leq \text{ICELL} \leq 1250$. The default value is $\text{ICELL} = 1$.
NPHIS	Number of discrete azimuthal angles at which particles are emitted (N_ϕ in Eqs. (9.1) and (9.2)). Acceptable range is $\text{NPHIS} \geq 1$. Default is $\text{NPHIS} = 1$.
NTHETS	Number of discrete polar angles at which particles are emitted (N_θ in Eqs. (9.1) and (9.2)). Acceptable range is $\text{NTHETS} \geq 1$. Default is $\text{NTHETS} = 1$.
NENGs	Number of discrete energies at which particles are emitted (N_ϵ in Eq. (9.3)). Acceptable range is $1 \leq \text{NENGs} \leq 50$. Default is $\text{NENGs} = 1$.
NSTEPS	Maximum allowable number of discrete time steps each of the $\text{NPHIS} \times \text{NTHETS} \times \text{NENGs}$ emitted particles may be tracked before concluding a particle has escaped to the environment. Acceptable range is $1 < \text{NSTEPS} \leq 2500$. Default is $\text{NSTEPS} = 500$. (Only the first 800 points of a particle's trajectory can appear in particle plots.)
DTHETA	Polar angular width (in degrees) of the hemispherical cap used to model the emitter gun aperture ($\Delta\theta$ in Eqs. (9.1) and (9.2)). Acceptable range is $0.0^\circ \leq \text{DTHETA} \leq 90.0^\circ$. Default is $\text{DTHETA} = 1.0^\circ$.
JTYPE	Index number of desired emitter gun current density function. The acceptable range is $1 \leq \text{JTYPE} \leq 4$. Default is $\text{JTYPE} = 1$. The types are as follows: <u>JTYPE</u> 1 Uniform angular, Gaussian energy distribution 2 Cosine θ angular, Gaussian energy distribution 3 Uniform angular, Rational energy distribution 4 Cosine θ angular, Rational energy distribution Remark: For a detailed description of the current distribution see the section entitled "Discrete Particle Emission Angles and Energies". The central peak energy ϵ_0 of any distribution is set by the keyword ENERGY and the width of the distribution in energy is specified by the keyword SIGMA. The Gaussian energy distribution has the attractive

property that ~68 percent of the current emitted is due to particles in the range of ENERGY \pm SIGMA. The NENGs discrete energies are selected so that an equal amount of the emitted current is represented by each energy.

ENERGY	Energy at which the central peak of the emitter current density function occurs. Acceptable range is ENERGY > 0.0. Default is ENERGY = 1000.0 eV.
SIGMA	Dispersion of the emitter current density function in eV (σ in Eqs. (9.3) and (9.5)). Acceptable range is SIGMA \geq 0.0. Default is SIGMA = 0.1 eV.
ISPEC	Emitter particle species type. The acceptable values are ISPEC = 1 for an electron emitter and ISPEC = 2 for a proton emitter. Default is proton emitter (ISPEC = 2).
PHI	Azimuthal angle ϕ of the emitter (in degrees) as measured in the spherical coordinate system of the <u>cell</u> at which the emitter is located. Acceptable range is $0.0^\circ \leq \text{PHI} \leq +360.0^\circ$. Default is PHI = 0.0° .*
THETA	Polar angle θ of the emitter (in degrees) as measured in the spherical coordinate system of the <u>cell</u> at which the emitter is located. Acceptable range is $-90.0^\circ \leq \text{THETA} \leq +90.0^\circ$. Default is THETA = 0.0° .*
BEAMI	Total emitter beam current in amps. Acceptable range is BEAMI > 0.0. Default is BEAMI = 10^{-6} amps.
VEDOWN	Tolerance limit for the maximum distance in code units which a particle is permitted to move at each timestep of particle tracking. If the limit is exceeded the timestep will be halved successively until the tolerance limit is met. Acceptable range is VEDOWN > 0.0. Default value is VEDOWN = 0.3. (The limit is automatically scaled by the factor 2^{iG-1} where iG is the index of the grid in which the particle is located.)

* Note: Letting PHI and THETA assume their default values and setting DTHETA = 0.0 will produce an emitter which points along the normal to the surface cell ICELL upon which it is located.

VEUP (VEDOWN/VEUP) is the tolerance limit for the minimum distance in code units which a particle must move at each timestep of particle tracking. If the limit is exceeded the timestep will be successively tripled until the limit is met. Default value is VEUP = 5.0. (If the default for VEUP and VEDOWN is used then the minimum distance a particle in grid 1 may move per timestep is $0.3/0.5 = 0.06$ inner grid units. As with VEDOWN, VEUP is also scaled by 2^{iG-1} .)

Normally the boundary of a particle trajectory plot is adjusted to correspond to the boundary of the highest grid into which any of the NPHIS*NTHETS*NENGs emitted particles fell during tracking. Unfortunately particles circling in small magnetic fields tend to make very large loops, i.e., into grid 12 or higher. Thus the automatic plot boundary selection frequently obscures details of individual particles returning to the object in grid 1. (The object silhouette is only plotted if the boundary of the plot corresponds to grid 6 or lower and fine details are usually only apparent if the boundary of the plot is set to grid 4 or lower.) In addition there may be some cases in which it is desirable to have the same set of particle trajectories plotted more than once, each time using a different maximum grid boundary for the plot. The following three keywords provide the user with the capability to deal with these problems and special requirements. (Note that these three keywords only have an effect if JCYCEM ≥ 1 — see Section 9.8.2.) Also note that these three keywords correspond to REAL data variables.

ALPHA Grid number to which the boundary of the particle trajectory plots corresponds to. (Note that all grids which are higher than 2 but fall inside the plot edge are automatically outlined for reference on the trajectory plots.) Acceptable range is integral ALPHA > 0.0 , i.e., ALPHA = 0.0, 1.0, 2.0, If ALPHA = 0.0 then the boundary of the plot will be automatically adjusted to correspond to the highest grid into which any of the NPHIS*NTHETS*NENGs particles fell during tracking. Default value is ALPHA = 0.0.

BETA Number of different plots of same set of trajectories desired (only has an effect if $\text{ALPHA} \geq 1.0$). Each trajectory plot is made using a different grid boundary (see GAMMA). The acceptable range is integral BETA such that $1.0 \leq \text{BETA} \leq 4.0$. The default is $\text{BETA} = 1.0$.

GAMMA Increment factor for grid boundaries of successive trajectory plots. If $\text{BETA} > 1.0$ then the same trajectories will be drawn on BETA different plots. The grid boundaries are incremented for each successive plot as follows:

$$\text{IG} = \text{ALPHA} + (\text{I}-1) * \text{GAMMA} \quad \text{for } \text{I} = 1, \dots, \text{BETA}$$

Acceptable range is integral $\text{GAMMA} \geq 0.0$. Default is $\text{GAMMA} = 0.0$.

Note that the highest grid value selected for plotting boundaries by ALPHA, BETA, and GAMMA should not exceed LIMGRD if useful plots are to be obtained.

9.8.2 Emitter Independent Parameters *

SCALEV	Scale factor for the tolerance limit VEDOWN for particle tracking in grids higher than 2. (Note that VEDOWN/VEUP is also affected by this.) Default is SCALEV = 1.0. Acceptable range is SCALEV > 0.0.										
LIMGRD	Highest grid in which particle tracking is permitted. If particle passes outside this grid it will be assumed to have escaped to infinity. Default value is LIMGRD = 6. Acceptable range is LIMGRD ≥ 1. (Note that particles which exit from the highest NASCAP computational grid** are tracked using a monopole potential.)										
PRFLUX	If this keyword appears in the emitter file then a listing of all non-zero flux contributions to surface cells due to each particle emitter will be printed at the completion of each particle tracking cycle. (It is recommended that this card be included.)										
IPRNT	<p>If this card is included then an optional one-line summary is printed for each particle at the completion of tracking. The information appearing in this line is as follows:</p> <table><tr><td>IPHI</td><td>index number of discrete azimuthal angle at which the particle was emitted.</td></tr><tr><td>ITH</td><td>index number of discrete polar at which the particle was emitted.</td></tr><tr><td>IEK</td><td>index number of discrete energy at which the particle was emitted.</td></tr><tr><td>VINIT</td><td>initial code velocity with which particle was emitted (in inner grid units/timestep).</td></tr><tr><td>VIN</td><td>initial velocity with which particle was emitted (in meters/second).</td></tr></table>	IPHI	index number of discrete azimuthal angle at which the particle was emitted.	ITH	index number of discrete polar at which the particle was emitted.	IEK	index number of discrete energy at which the particle was emitted.	VINIT	initial code velocity with which particle was emitted (in inner grid units/timestep).	VIN	initial velocity with which particle was emitted (in meters/second).
IPHI	index number of discrete azimuthal angle at which the particle was emitted.										
ITH	index number of discrete polar at which the particle was emitted.										
IEK	index number of discrete energy at which the particle was emitted.										
VINIT	initial code velocity with which particle was emitted (in inner grid units/timestep).										
VIN	initial velocity with which particle was emitted (in meters/second).										

* If any of these keyword cards appear in any one of the one or more emitter keyword definition sequences on the NASCAP keyword input file then the parameter value will apply to all activated emitters.

** The current version of NASCAP restricts particle tracking using explicitly calculated potentials from TRILIN to the first two grids even if potentials were computed in more than this number of grids.

JCLAST Index number of volume cell which particle was in at step just before hitting the satellite. If the trajectory was incomplete this will be 0. (Note the volume index is not necessarily the same as the surface cell index!)

PXYZ Potential (in volts) at the particle position at the last timestep completed prior to hitting the satellite or abandoning tracking.

IR Index number of grid in which the particle was in at the last timestep completed prior to hitting the satellite or abandoning tracking.

ISTP Number of discrete steps which this particle was tracked for before it hit the satellite or tracking was abandoned.

Note in cases where the message *EMISSION SUPRESSED* appears prior to the trajectory end summary the values for JCLAST, PXYZ, IR, and ISTP are not correct. Also if the warning that 50 emission suppressions have taken place is printed then values of these variables for trajectories which follow may not be correct. Setting the value of the INTEGER field on this card to 1 or 2 will produce a myriad of additional diagnostic output and is not recommended unless only one or two particles are being tracked. In general more than sufficient information can be obtained by leaving the data field blank (0).

CYMULT This parameter sets the "cyclotron" time limit. If a particle passes out of the highest grid* then this parameter essentially specifies the number of revolutions in the magnetic field which particles are permitted to make before concluding that they have escaped. That is to say tracking beyond the time at which a particle exits from the highest grid* is done for at most $(CYMULT * (2\pi m / (eB)))$ additional seconds before concluding that the particle has escaped. In special cases where there is no magnetic field present this parameter has a different use. Let T be the time which a particle requires to pass out of the highest grid*. If it passes out of this grid and

* loc. cit.

there is no magnetic field then it will be tracked for a maximum of $T \times \text{CYMULT}$ additional seconds before concluding it has escaped. Acceptable range is $0.0 \leq \text{CYMULT} \leq 10.0$. The default is $\text{CYMULT} = 1.0$. (In cases of no \vec{B} -field it will probably be necessary to set $\text{CYMULT} \geq 5.0$ if premature tracking termination is to be avoided.)

- JCYCEM Emitter particle trajectory plot flag. JCYCEM = 0 implies no plots. JCYCEM ≥ 1 implies that particle trajectory plots will be produced for all emitters every JCYCEM time cycles performed by TRILIN, beginning with cycle 1. Default is JCYCEM = 0.
- IPLTYP Particle trajectory plot type selection. IPLTYP = 0 implies separate sets of trajectory projection views for each emitter. IPLTYP = 1 implies all emitter trajectory plots combined in a single set of three two-dimensional projection views. IPLTYP only has an effect if JCYCEM ≥ 1 . Default is IPLTYP = 1.
- COMMEN This card is for programmer convenience in identifying the purpose of keyword cards on the keyword input file. If this card appears, columns 7-72 may contain any comment the user desires. It is echoed back on the keyword listing at execution time but is otherwise ignored.

9.9 KEYWORD CARD PROCESSING ERRORS

Following each emitter keyword definition sequence NASCAP performs an extensive set of checks to assure that an acceptable set of parameters has been defined. If the set is found unacceptable then diagnostic information is printed for each offending parameter and program execution is aborted. If no errors are detected then a summary of all parameters for each activated emitter is printed on the NASCAP output listing.

9.10 SPECIAL RESTRICTIONS

1. If more than one emitter is simultaneously activated no two emitters may have the same underlying conductor. No error check for this condition is explicitly made so that results may be unpredictable if this constraint is violated.

9.11 ADDITIONAL OPERATION NOTES

1. Most of the printed output produced by the emitter routines is self-explanatory. The particle emitter energies printed are the actual energies with which each of NPHIS*NTHETS particles are emitted at. The particle emitter energy weights printed on the output currently have no function within the program and should be ignored by the user.
2. In general, the quantities printed following the heading ***** SUMMARY OF PARTICLE TRACKING FOR EMITTER XX - AT - CYCLE - XXX ***** have been derived from a consideration of all NPHIS*NTHETS*NENGS particles which were emitted.
3. A number of diagnostic **WARNING** statements may be printed during particle tracking. These warnings are only intended to be informative about how the tracking algorithm is progressing and should only be cause for concern if something "bad" happens afterward such as an ***ERROR*** message and/or execution abort call to RETRNO before execution of the emitter routines is completed during the charging cycle of TRILIN.

10. AMBIENT CHARGE DENSITY

A local net charge density can develop in a neutral ambient plasma near an object because of the unequal attraction for the electrons and ions in the plasma. Our treatment assumes that the net charge density developed in the ambient plasma is linear in the local potential. Thus Poisson's equation,

$$\epsilon_0 \nabla^2 \phi = -\rho \quad (10.1)$$

becomes

$$\epsilon_0 \nabla^2 \phi \cong \left(\frac{1}{\lambda^2} \right) \phi, \quad (10.2)$$

where λ is an effective Debye length. Laframboise and Parker have shown^[5] that for a Maxwellian plasma, the correct linear term is generated using

$$\left(\frac{1}{\lambda^2} \right) = \left(\frac{1}{\lambda_D^2} \right) \left(1 + \frac{T_e}{T_i} \right) \quad (10.3)$$

where $\lambda_D = (4\pi n_\infty e^2 / kT_e)^{-1/2}$ is the true Debye length, n_∞ is the plasma density far from the object, and T_e and T_i are the electron and ion temperatures, respectively. We have used these approximations to develop an ambient space charge correction for NASCAP.

We must find a variational functional which is appropriate for the governing equation of the system, Eq. (10.2). The surface terms enter the equations as previously derived, and we must reconsider only the volume term. The correct free volume functional is

$$f_V = \frac{1}{2} \epsilon_o (\nabla\phi) \cdot (\nabla\phi) + \frac{1}{2} \left(\frac{1}{\lambda^2} \right) \phi^2 \quad (10.4)$$

The requirement $\delta f_V = 0$ yields Eq. (10.2). In a finite element formulation we have

$$f_V = \int_V \left\{ \frac{1}{2} \epsilon_o \phi^i \phi^j \nabla N^i \cdot \nabla N^j + \frac{1}{2} \left(\frac{1}{\lambda^2} \right) N^i N^j \right\} dV \quad (10.5)$$

Extremizing with respect to ϕ^i yields

$$[\epsilon_{ij} + \lambda_{ij}] \phi^j = 0 \quad (10.6)$$

where

$$\epsilon_{ij} = \epsilon_o \int_V \nabla N^i \cdot \nabla N^j dV \quad (10.7)$$

$$\lambda_{ij} = \left(\frac{1}{\lambda^2} \right) \int_V N^i N^j dV = \left(\frac{1}{\lambda^2} \right) L_{ij} \quad (10.8)$$

Matrix elements L_{ij} have been calculated for each of the 5 distinct standard cell types; these new elements are given at the end of Chapter 10. The matrix elements ϵ_{ij} are of course identical to the corresponding terms derived in the absence of space charge. The iterative solution of the potential equations proceeds exactly as before, but with the elements $[\epsilon_{ij} + \lambda_{ij}]$ entering wherever only ϵ_{ij} occurred previously.

We have also recast the boundary conditions for the problem to be compatible with the presence of the ambient sheath. When IOUSER = 2 is selected, the routine SETALL now sets the outer boundary to

$$\phi(r) = \left[\frac{Qe}{4\pi\epsilon_0 r} \right] \left[\frac{\exp(R_0/\lambda)}{R_0/\lambda + 1} \right] \exp(-r/\lambda) , \quad (10.9)$$

where R_0 is an average radius for the object, and Q is the charge on the object. Equation (10.9) represents the correct analytical solution of Eq. (10.2) for a spherical object.

The above ideas have been implemented by the following changes or additions to the indicated NASCAP routines:

SUBROUTINE FLXDEF: Additions to calculate the effective Debye length, λ .

SUBROUTINE SETALL: Additions to calculate R_0 , the average object radius, and to set the boundary potential according to Eq. (10.9).

SUBROUTINE SCLIN: New routine to calculate the matrix sum $[\epsilon_{ij} + \lambda_{ij}]$, given λ .

The routine SCLIN is called once per timestep by POTENT, and the resulting matrix sum is stored in COMMON/WGTS/ to be accessed by routines ECUBE and SQCWGT during the potential iterations.

Minor changes in routines SQCWGT, ECUBE, POTENT, and all the input routines were required as well. A new keyword, "ISC", has been introduced; the above procedures are invoked by inputting a value of 1 for ISC.

10.1 RESULTS

Sample results are shown in Figures 10.1 - 10.4. Figures 10.1 - 10.3 show potential contours around an aluminum cube of edge 2 m as the Debye length decreases from 33 m to 1 m. The cube is fixed at -100 V while the boundary is grounded in these calculations, and the potential contours run from -5 to -100 volts in all figures. The development of the ambient sheath is clearly reflected in the changing potential contours. Figure 10.4 shows the change of capacitance of a 1 m aluminum cube in unbounded space as the Debye length changes. The ability of the object to store charge is dramatically increased by the presence of the ambient sheath, as expected.

Notice that the amount of computation required for each potential iteration is essentially unchanged when the linear ambient correction is included, since the matrix sum $[\epsilon_{ij} + \lambda_{ij}]$ is calculated before the time-consuming iteration procedure is entered. Since the matrices λ_{ij} are more positive definite than the corresponding ϵ_{ij} , the convergence is rapid, and fewer iterations are required. The overall computing requirement is therefore usually reduced when the ambient terms are included, so that we have been able to extend the range of applicability of NASCAP without a concomitant increase in running time.

POTENTIAL CONTOURS ALONG THE X-Y PLANE OF Z = 9

ZMIN = -.10000+03 ZMAX = -.52569+00 ΔZ = .50000+01

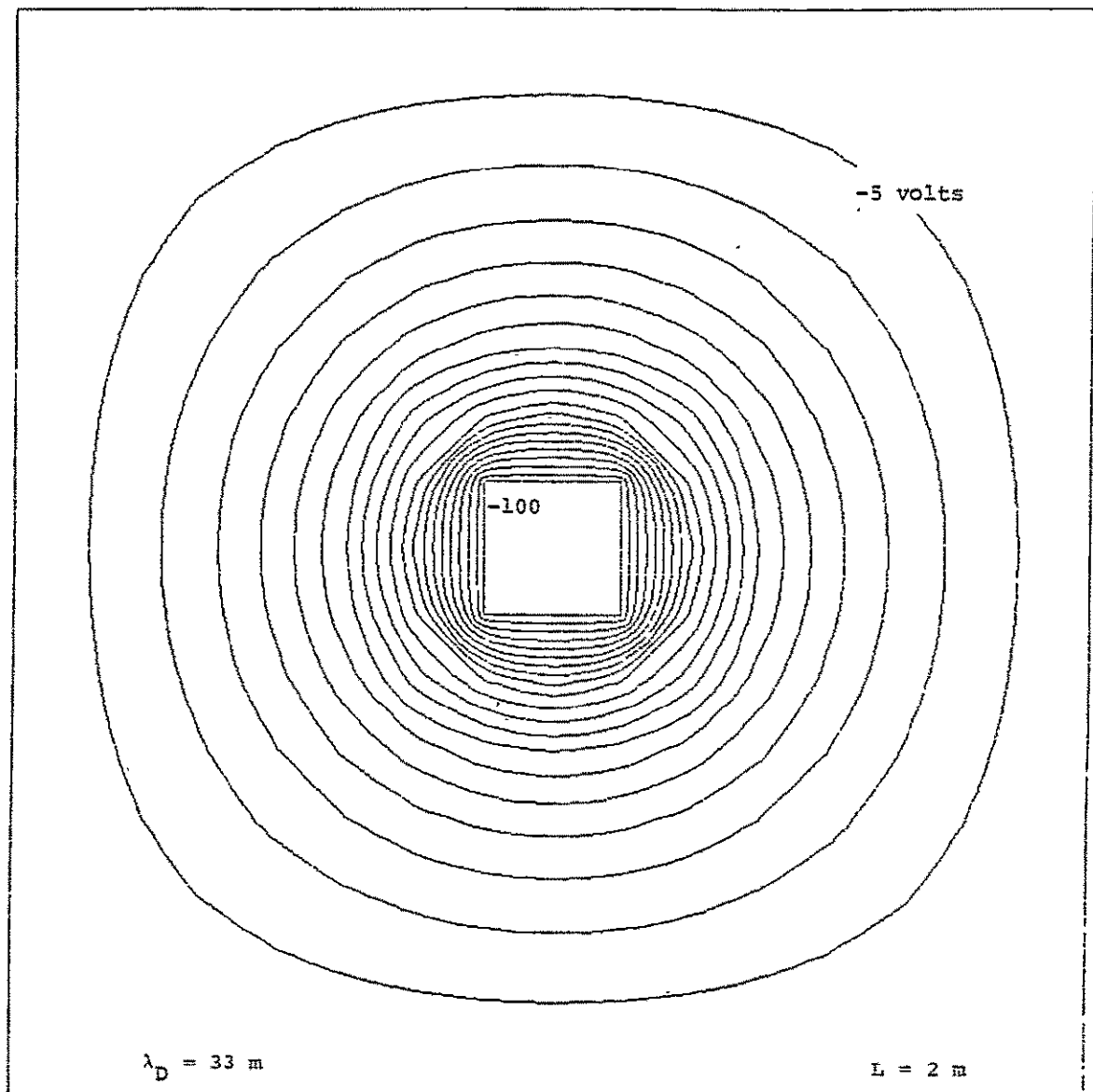


Figure 10.1. Potential contours around a 2 m aluminum cube, including the effect of ambient charge density.

POTENTIAL CONTOURS ALONG THE X-Y PLANE OF Z = 9

ZMIN = -.10000+03 ZMAX = -.12065+00 ΔZ = .50000+01

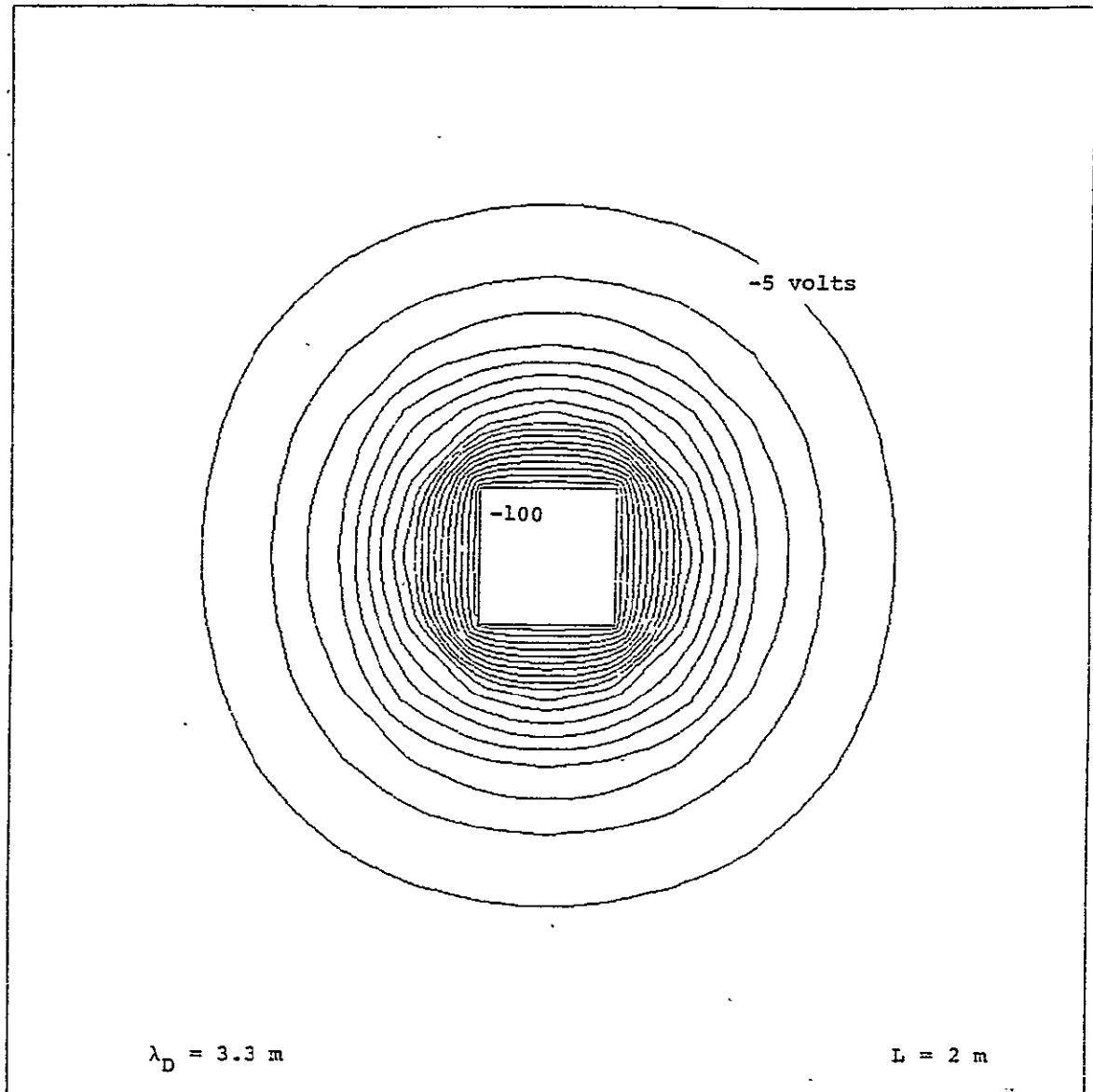


Figure 10.2. Potential contours around a 2 m aluminum cube, including the effect of ambient charge density.

POTENTIAL CONTOURS ALONG THE X-Y PLANE OF Z = 9

EMIN = -.10000+03 ZMAX = -.87434-04 ΔZ = .50000+01

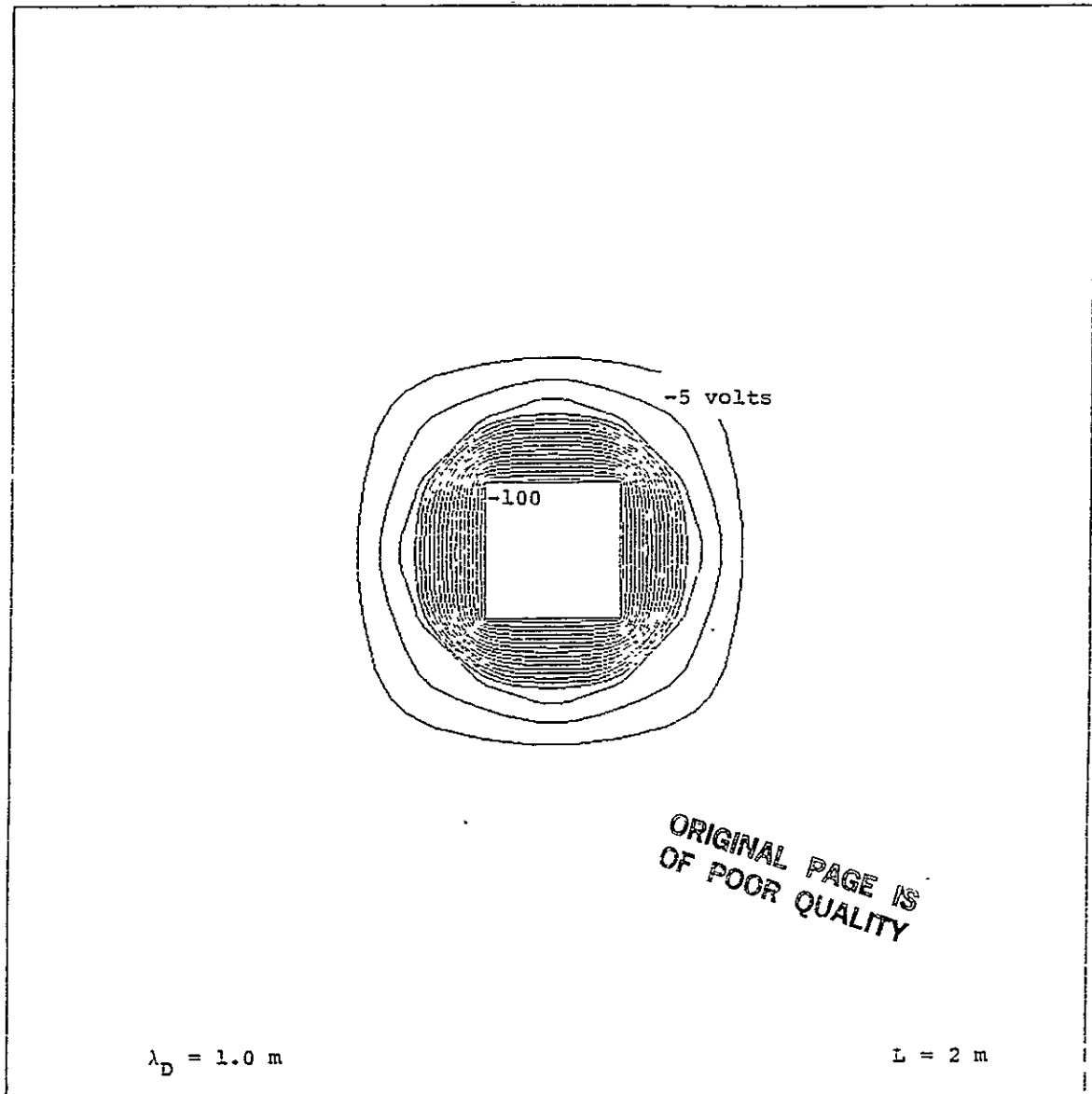


Figure 10.3. Potential contours around a 2 m aluminum cube, including the effect of ambient charge density.

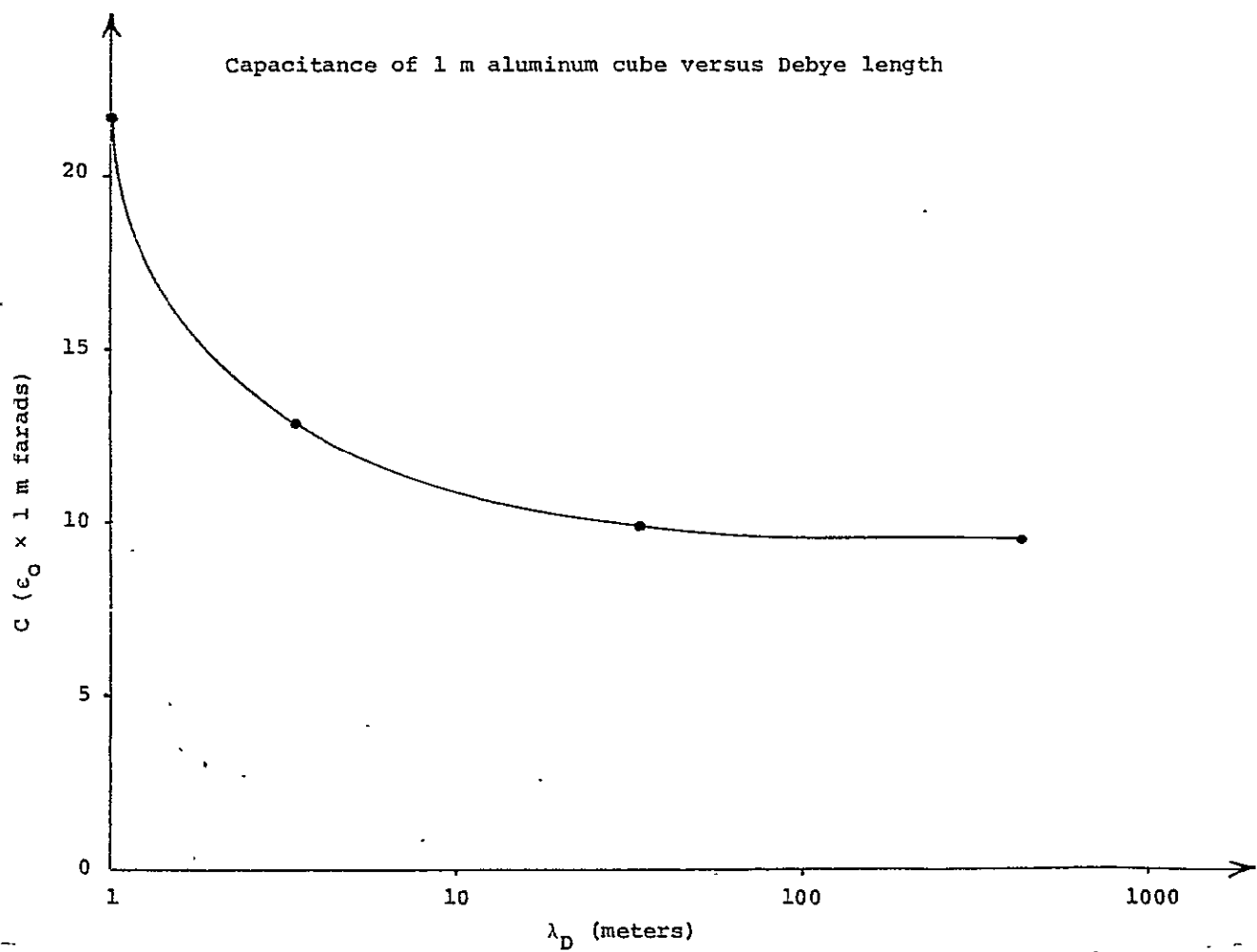


Figure 10.4. Capacitance of a 1 m aluminum cube versus Debye length.

MATRIX ELEMENTS FOR SQUARE OF POTENTIAL.

(Format)

Description

Standard Orientation

$$\text{Potential Function} = \sum_i N^i \phi_i$$

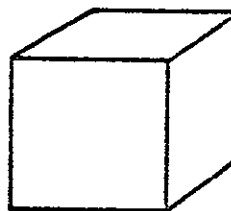
$$\text{Matrix, } L_{ij}: \int d\Omega \phi^2 = \sum_{ij} L_{ij} \phi_i \phi_j$$

<u>Point Index</u>	<u>Cube Corner</u>
1	0 0 0
2	1 0 0
3	0 1 0
4	1 1 0
5	0 0 1
6	1 0 1
7	0 1 1
8	1 1 1

Standard Cell 0

Empty trilinear cube

Orientation: Arbitrary



Potential Function:

i	N^i
1	$(1-x)(1-y)(1-z)$
2	$(1-z)(1-y)x$
3	$(1-x)y(1-z)$
4	$(1-z)yx$
5	$z(1-y)(1-x)$
6	$x(1-y)z$
7	$zy(1-x)$
8	xyz

$L_{ij}^{(0)}$

1/27								
1/54	1/27							
1/54	1/108	1/27						
1/108	1/54	1/54	1/27					
1/54	1/108	1/108	1/216	1/27				
1/108	1/54	1/216	1/108	1/54	1/27			
1/108	1/216	1/54	1/108	1/54	1/108	1/27		
1/216	1/108	1/108	1/54	1/108	1/54	1/54	1/27	

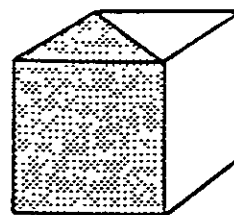
Standard Cell 1

Half-Empty Wedge

$$1 < x + y < 2$$

$$0 < z < 1$$

Orientation: Right angle along
line 7-8



Potential Function:

i	N^i
1	0
2	$(1-y)(1-z)$
3	$(1-x)(1-z)$
4	$(x+y-1)(1-z)$
5	0
6	$(1-y)z$
7	$(1-z)z$
8	$(x+y-1)z$

$L_{ij}^{(1)}$

0								
0	1/36							
0	1/72	1/36						
0	1/72	1/72	1/9					
0	0	0	0	0				
0	1/72	1/144	1/144	0	1/36			
0	1/144	1/144	1/144	0	1/72	1/36		
0	1/144	1/144	1/18	0	1/72	1/72	1/9	

Standard Cell 2

Cube with diagonal line on one face

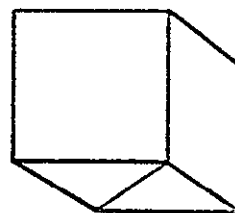
Orientation: Line from 2 to 3

Potential Function:

i	N^i
1	$(1-x-y)(1-z)(1-x-y)$
2	$[x\theta(1-x-y) + (1-y)\theta(x+y-1)](1-z)$
3	$[y\theta(1-x-y) + (1-x)\theta(x+y-1)](1-z)$
4	$(x+y-1)(1-z)\theta(x+y-1)$
5	$(1-x)(1-y)z$
6	$x(1-y)z$
7	$(1-x)yz$
8	xyz

As a simplification, these cells have been treated as if they were type 0 cells. Previous experience with matrix elements of $|\nabla\phi|^2$ indicated that the calculated potentials were insensitive to such an approximation.

$L_{ij}^{(2)} = L_{ij}^{(0)}$ as defined previously.

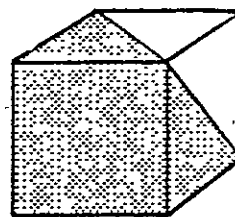


Standard Cell 3

Tetrahedron

$$2 < x + y + z < 3$$

Orientation: Empty corner at
point 8



Potential Function:

i	N^i
1	0
2	0
3	0
4	$1-z$
5	0
6	$1-y$
7	$1-x$
8	$x+y+z-2$

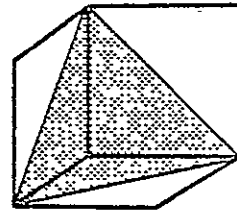
$L_{ij}^{(3)}$

0								
0	0							
0	0	0						
0	0	0	$1/60$					
0	0	0	0	0				
0	0	0	$1/120$	0	$1/60$			
0	0	0	$1/120$	0	$1/120$	$1/60$		
0	0	0	$1/120$	0	$1/120$	$1/120$	$1/60$	

Standard Cell 4

Truncated Cube

Orientation: 000 corner (point 1)
missing



As a simplification, these cells are treated as if they were type 0 cells. A value for the potential at point 1 is generated by extrapolation from the potentials at points 2 through 8, the matrix elements for type 0 cells is applied (multiplied by a factor of 5/6 to account for the reduced volume), and the results are interpolated back to the seven real points. The results of this procedure are equivalent to introducing a matrix for type 4 cells given by

$$\underline{L}^{(4)} = (5/6) \underline{T}^\dagger \underline{L}^{(0)} \underline{T}$$

where \underline{T} is a matrix which performs the extrapolation, and $\underline{L}^{(0)}$ is the matrix defined previously for type 0 cells.

The extrapolation scheme used is

$$P_1 = P_m + (P_m - P_a)$$

where

$$P_m = \frac{1}{3} (P_2 + P_3 + P_5) = \text{potential at midpoint of triangular face}$$

$$P_a = \frac{1}{4} (P_4 + P_6 + P_7 + P_8) = \text{average potential behind the triangular face}$$

This particular scheme was chosen since it yields elements a matrix $L_{ij}^{(4)}$ which is positive definite, and whose elements are all non-negative. The exact $L_{ij}^{(4)}$ must satisfy these requirements.

Thus the matrix T is given by

$$T_{11} = 0 \quad T_{ii} = 1, \quad 2 \leq i \leq 8$$

$$T_{12} = T_{13} = T_{15} = 2/3$$

$$T_{14} = T_{16} = T_{17} + T_{18} = -1/4$$

All other $T_{ij} = 0$.

The resulting $L_{ij}^{(4)}$ is:

$$L_{ij}^{(4)}$$

.00000							
.00000	.06516						
.00000	.04201	.06516					
.00000	.01157	.01157	.02894				
.00000	.04201	.04201	.00000	.06516			
.00000	.01157	.00000	.00579	.01157	.02894		
.00000	.00000	.01157	.00579	.01157	.00579	.02894	
.00000	.00129	.00129	.01447	.00129	.01447	.01447	.03086

11. SURFACE CONDUCTIVITY

The first part of this chapter (Section 11.1) is a paper by Rotenberg, Mandell, and Parks reproduced verbatim. This gives an analytical discussion of bulk and surface conductivity.

The second section (11.2) shows how the analytical model is incorporated into the NASCAP code.

11.1 EFFECTS OF BULK AND SURFACE CONDUCTIVITY OF THE POTENTIAL
DEVELOPED BY DIELECTRICS EXPOSED TO ELECTRON BEAMS*

Manuel Rotenberg^{**}, Myron J. Mandell and Donald E. Parks

Systems, Science and Software
P. O. Box 1620
La Jolla, California 92038

* This work supported by the National Aeronautics and Space
Administration, Lewis Research Center, under Contract NAS3-
21050.

** Permanent Address: University of California, La Jolla,
California 92093

ABSTRACT

The charging and discharging of a dielectric material which has bulk and surface conductivities is discussed. Two model problems are solved. In the first problem, a semi-infinite dielectric plane, attached to an infinite grounded conducting substrate and exposed to a monoenergetic electron beam, is analyzed. Bulk and surface conductivities, and secondary emission characteristics are taken into account as parameters. In the second problem the dielectric is charged but the electron beam is shut off so only the bulk and surface conductivities enter the calculation. The principal result of the latter calculation is to show that steep tangential gradients develop in the presence of surface conductivity during decay, and that for asymptotic times the temporal behavior, for a fixed position, is proportional to $t^{-1/2}$, rather than exponential as expected in the presence of bulk conductivity.

1. INTRODUCTION

This study of charging and discharging of dielectric materials is motivated by the importance that has been attached in recent years to the effects produced by charging of satellite surfaces exposed to the magnetospheric environment. Under substorm conditions surfaces are exposed to electrons with temperatures of the order of 10 keV and thermal plasma currents of the order of 1 nanoampere per square centimeter. Thus, on a time scale of a few minutes, large potential differences (~ 10 keV) may develop between the surface of the thin dielectric ($\sim 10^{-2}$ cm) and an underlying conductor, producing electric fields of the order of 10^6 volts/cm. At such field levels, the occurrence of electrical discharges, with concomitant RF noise and material degradation effects, is expected. Such expectations are confirmed by both laboratory and space data. One suggested means¹⁻⁵ for mitigating these effects is to develop dielectric materials with sufficient (bulk or surface) conductivity to suppress the development of excessive electric fields.

Laboratory experiments investigating charging and discharging phenomena typically involve exposure in high vacuum of thin dielectric films mounted on conducting substrates to several kilovolt electron beams carrying currents in the nanoamp/cm² range. The dielectric materials and configurations tested include kapton, teflon, nonconductive paints, solar cell arrays, second surface mirrors and optical solar reflectors. The electric fields which develop in the bulk of the dielectric and near the interface between dielectric films and metal substrates are a determining factor in the occurrence of discharges. The fields in turn are determined by the electrical characteristics of the material, in particular bulk and surface conductivities and secondary emission yields. However, it is very difficult to measure by conventional means the very low conductivities typical of spacecraft materials.

In the present study, we consider the role of conductivity and secondary emission in establishing the temporal and spatial dependence of potential difference $V(x,t)$ between the dielectric surface and the underlying conductor in conditions which simulate the space environment. In particular the analysis describes the spatial and temporal variation of potential near the edge which separates the dielectric coated and exposed metallic surfaces, and the manner in which it depends on material properties.

When the charging current is turned off, the analysis of the discharging behavior provides a basis for measurement of bulk and surface conductivities. In addition, it will be shown that the resistance of the dielectric-conductor edge interface, if it is significant, can be measured indirectly.

2. DIELECTRIC CHARGING

Consider a thin dielectric on a grounded conducting plane (Figure 1). The dielectric thickness is small compared with any lateral dimension. Thus the electric field perpendicular to the plane is V/d . Parallel to the surface of the dielectric the field is $\partial V/\partial x$. (We suppose no y -variation.) Let j_{net} be the net current density (incident minus secondary emission) impinging upon the dielectric in a perpendicular direction.

The incident current is assumed to be uniform over the surface of the dielectric. The continuity equation reads

$$\frac{\partial \sigma}{\partial t} = j_{\text{net}} - \frac{1}{\rho} \frac{V}{d} + \frac{1}{\omega} \frac{\partial^2 V}{\partial x^2} \quad (1)$$

where

σ is the charge density

ρ is the bulk resistivity

ω is the surface resistivity

d is the thickness of the dielectric

If the dielectric is semi-infinite in extent with its edge at $x = 0$, and is initially uncharged, the boundary conditions for (1) are

$$V(x,0) = 0; V(0,t) = 0; \partial V(\infty,t)/\partial x = 0. \quad (2)$$

In typical cases, both the intensity of incident current and its energy (thus secondary yield) are functions of the surface potential. Secondary yield is a non-linear function of incident energy,⁶ therefore to cast Eq. (1) into a tractable form, we assume $j_{\text{net}}(x)$ varies linearly near its zero value (see Figure 2) as a function of local potential

$$j_{\text{net}}(x) = \gamma[V_0 - V(x)] \quad (3)$$

where V_0 is the equilibrium potential for a perfect dielectric ($\omega = \rho = \infty$) of infinite extent, and use Gauss' Law in the form

$$\sigma = \kappa \epsilon_0 V/d \quad (4)$$

where κ is the dielectric constant. Using Eqs. (3) and (4), (1) becomes

$$\frac{\partial V}{\partial t} = -kV + D \frac{\partial^2 V}{\partial x^2} + \frac{d\gamma}{\kappa \epsilon_0} V_0 \quad (5)$$

where k is defined as the inverse time constant

$$k \equiv \frac{d}{\kappa \epsilon_0} \left(\gamma + \frac{1}{\rho d} \right) \quad (6)$$

and

$$D \equiv \frac{d}{\kappa \epsilon_0 \omega} \quad (7)$$

is defined as the diffusion constant. It is convenient to write (5) in the dimensionless form

$$\frac{\partial W}{\partial \tau} = -W + \frac{\partial^2 W}{\partial \xi^2} + 1 \quad (8a)$$

$$W(\xi, 0) = 0; W(0, \tau) = 0; \partial W(\infty, \tau) / \partial \xi = 0 \quad (8b)$$

where

$$\begin{aligned} \tau &= kt \\ \xi &= (k/D)^{1/2} x \\ W &= V/(\Gamma V_0) \\ \Gamma &= D\gamma\omega/k = \gamma\rho d/(\gamma\rho d + 1) \end{aligned} \quad (9)$$

Equation (8) is solved in a straightforward manner by Laplace transforms:

$$\begin{aligned}
 W(\xi, \tau) = & 1 - e^{-\xi} - e^{-\tau} \operatorname{erf}\left(\frac{\xi}{2\tau^{1/2}}\right) \\
 & + \frac{1}{2} \left[e^{-\xi} \operatorname{erfc}\left(\tau^{1/2} - \frac{\xi}{2\tau^{1/2}}\right) - e^{+\xi} \operatorname{erfc}\left(\tau^{1/2} + \frac{\xi}{2\tau^{1/2}}\right) \right]
 \end{aligned}
 \tag{10}$$

This function is plotted in Figure 3.

The asymptotic solutions to Eq. (8) are

$$W(\xi, \infty) \rightarrow 1 - e^{-\xi} \tag{11}$$

and

$$W(\infty, t) \rightarrow 1 - e^{-\tau} \tag{12}$$

so it might be thought that a useful approximate solution to (8) is

$$W(\xi, \tau) \approx (1 - e^{-\xi}) (1 - e^{-\tau}) \tag{13}$$

Comparison with the exact solution shows that Eq. (13) is a poor approximation. In particular, (13) fails to exhibit the rapid rise to a constant value as a function of ξ for $\tau \lesssim 1$.

3. DIELECTRIC DISCHARGING

Assume the incident current is shut off after the dielectric reaches its equilibrium potential distribution. This time is defined as $\tau = 0$ for the discharging problem. The governing equation is (5) with γ set to zero. For convenience, the normalized variables used in the charging problem will be retained:

$$\frac{\partial W}{\partial \tau} = -s_o W + \frac{\partial^2 W}{\partial \xi^2} \quad (14a)$$

The boundary conditions are now

$$W(\xi, 0) = 1 - e^{-\alpha \xi}; \quad W(0, \tau) = 0; \quad \partial W(\infty, \tau) / \partial \xi = 0 \quad (14b)$$

where $s_o \equiv k_o/k$, $k_o = 1/(\rho k \epsilon_o)$. The distance scale α has been introduced into the initial condition to compensate for beam deflection as the dielectric is being charged. It will be seen that for $\tau \gg \xi^2$, the results are independent of α .

The solution to Eq. (14) is

$$\begin{aligned} W(\xi, \tau) = e^{-s_o \tau} \left\{ \operatorname{erf} \left(\frac{\xi}{2\tau^{1/2}} \right) \right. \\ \left. - \frac{1}{2} e^{\alpha^2 \tau} \left[e^{-\alpha \xi} \operatorname{erfc} \left(\alpha \tau^{1/2} - \frac{\xi}{2\tau^{1/2}} \right) \right. \right. \\ \left. \left. - e^{+\alpha \xi} \operatorname{erfc} \left(\alpha \tau^{1/2} + \frac{\xi}{2\tau^{1/2}} \right) \right] \right\} \quad (15) \end{aligned}$$

which is plotted in Figure 4. If $\xi \ll \tau^{1/2}$ it is seen that the W is a linear function of ξ ; the appropriate limit of (15) yields

$$W(\xi, \tau) = e^{-s_o \tau} \xi / (\pi \tau)^{1/2} \quad (16a)$$

or, in terms of unscaled variables,

$$V(x,t) = V_0 \exp [-t/(\rho\kappa\epsilon_0)] (C\omega)^{1/2} \frac{x}{(\pi t)^{1/2}} \quad (16b)$$

where $C = \kappa\epsilon_0/d$ is the capacity per unit area of the dielectric.

Equations (15) and (16), together with Figure 4, constitute our main result. The exponential factor is expected for the discharge through a dielectric of non-zero bulk conductivity when the surfaces are uniformly charged initially. When there is surface conductivity, however, the charge becomes non-uniform toward the edge of the dielectric and results, for a fixed x , in the inverse square root behavior in time. This non-uniform charge distribution is of practical importance since it produces large potential gradients tangential to the dielectric surface, the existence of which could lead to sporadic surface discharges.

4. SURFACE CURRENT

If the conducting substrate of the dielectric is grounded through a current measuring device, the surface current at $x = 0$ is measured. (It will be shown subsequently that the bulk current is small compared to the surface current for a reasonable choice of parameters.) The surface current is given by

$$\begin{aligned} j_{\text{surf}}(0,t) &= -\frac{1}{\omega} \frac{\partial V}{\partial x} \\ &= -V_0 \exp\left[-t/(\rho\kappa\epsilon_0)\right] \left(\frac{C}{\omega}\right)^{1/2} \frac{1}{(\pi t)^{1/2}} \end{aligned} \quad (17)$$

The time constant $\rho\kappa\epsilon_0$ is typically $\sim 10^5$ seconds so the exponential factor can be replaced by unity.

5. BULK CURRENT

The bulk current density is given by

$$j_{\text{bulk}}(\xi, \tau) = \frac{1}{\rho d} V(\xi, \tau) \quad (18)$$

If V is taken to be its maximum value, TV_0 , then

$$\begin{aligned} I_{\text{bulk}}/I_{\text{surf}} &< \frac{\text{area}}{\text{perimeter}} \frac{1}{\rho} \left(\frac{\pi\omega}{\kappa\epsilon_0 d} \right)^{1/2} t^{1/2} \\ &\approx \frac{\text{area}}{\text{perimeter}} \times 10^{-2} t_{\text{sec}}^{1/2} \text{ (meters)} \end{aligned} \quad (19)$$

where it has been assumed that

$$\rho = 10^{16} \text{ } \Omega\text{-meters}$$

$$d = 10^{-4} \text{ meters}$$

$$\omega = 10^{13} \text{ } \Omega/\square$$

If the dielectric sample is taken to be a square $\overline{10 \text{ cm}}$ on a side, the ratio of bulk-to-surface current is about $10^{-3} t_{\text{sec}}^{1/2}$. Thus observations could be made for about 10^4 seconds before the bulk current became an appreciable fraction of the surface current. The area-to-perimeter ratio could be improved by using a smaller sample, but if this were carried too far, the one-dimensional analysis breaks down.

6. DISCUSSION

The time and space dependence of two problems have been analyzed; the charging of a semi-infinite dielectric film by a uniform beam, and the subsequent discharge of the film after the beam has been turned off.

The basic assumptions in the charging problem are that the secondary emission is a linear function of the beam energy, and that the electrical properties of the dielectric can be clearly divided into bulk and surface sensitivities. There is a further assumption that the beam current is independent of time and spatial coordinates.

The discharge problem retains only the assumptions regarding the resistivities and for this reason may be more reliable. Two independent measurements can be made to test the assumptions: potential measurements near the dielectric edge to test Eq. (16b), and the current measurements from the conducting plate to ground to test Eq. (17).

Potential measurements near the edge of the dielectric may not extrapolate to zero at $x = 0$ as demanded by Eq. (16b); this would be an indication that the edge of the dielectric presents a non-negligible resistance to the surface current. Thus suppose that the voltage at $x = 0$ is found by extrapolation from interior measurements to be $V'_0(t)$, and that the total current leaking to the conducting plate across the edge of the dielectric is $I(t)$. Then the resistance of the edge is $R_e = V'_0(t)/I(t)$. If the edge of the dielectric is ℓ meters long then the relevant intrinsic quantity is the edge conductivity per unit length

$$g = (1/\ell) (I/V'_0) \text{ mho/meter} \quad (20)$$

The independence of g over time is a necessary behavior (but not sufficient) for the edge, bulk and surface resistances to be independent of potential.

REFERENCES

1. P. A. Robinson, Jr., "The Behavior of Partially Metalized Kapton for Spacecraft Charging Control," AIAA/DGLR 13th International Electric Propulsion Conference, San Diego, CA, April 25-27, Paper No. 78-675, 1978.
2. A. E. Eagles, R. E. Schmidt, L. J. Amore and V. J. Belanger, "Transparent Antistatic Satellite Materials," General Electric, Space Division, AFML-TR-77-174, Part I, October 1977.
3. J. E. Gilligan, R. E. Wolf and C. Ray, "Electrically Conductive Paints for Satellites," in Proceedings of the Spacecraft Charging Technology Conference, edited by C. P. Pike and R. L. Lovell, AFGL-TR-77-0051/NASA TMX-73537, pp. 593-612, 1977.
4. N. J. Stevens, C. K. Purvis and J. V. Staskus, "Insulator Edge Voltage Gradient Effects in Spacecraft Charging Phenomena," IEEE Transactions on Nuclear Science, NS-25, p. 1304, December 1978.
5. Spacecraft Charging by Magnetospheric Plasmas, Progress in Aeronautics and Astronautics, Vol. 47, edited by A. Rosen, AIAA, 1976.
6. A. J. Dekker, "Secondary Electron Emission," Solid State Physics, 6, p. 251, 1958.

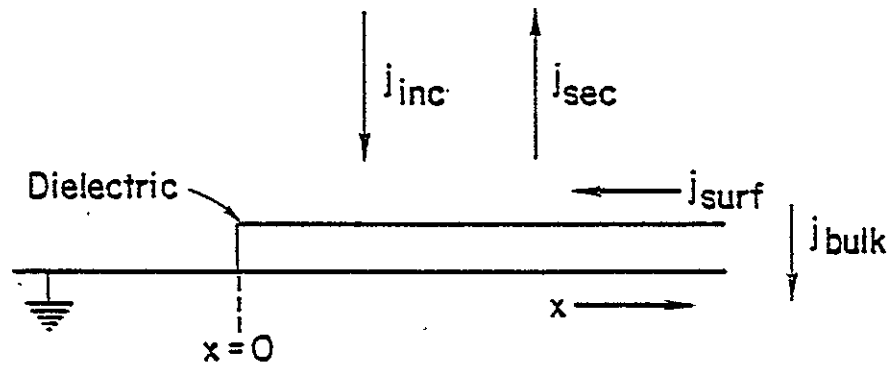


Figure 1. Definitions of the coordinate system and the various currents. The net incident current is $j_{net} = j_{inc} - j_{sec}$. The dielectric has a thickness d and a dielectric constant κ .

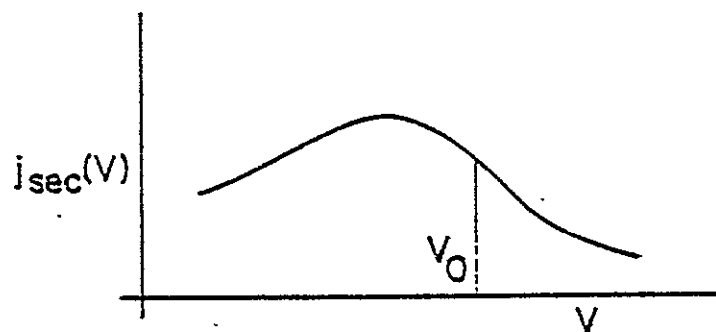


Figure 2. A typical secondary current characteristic. V_0 is the point at which $j_{net} = 0$. The slope of the curve at this point is defined as γ .

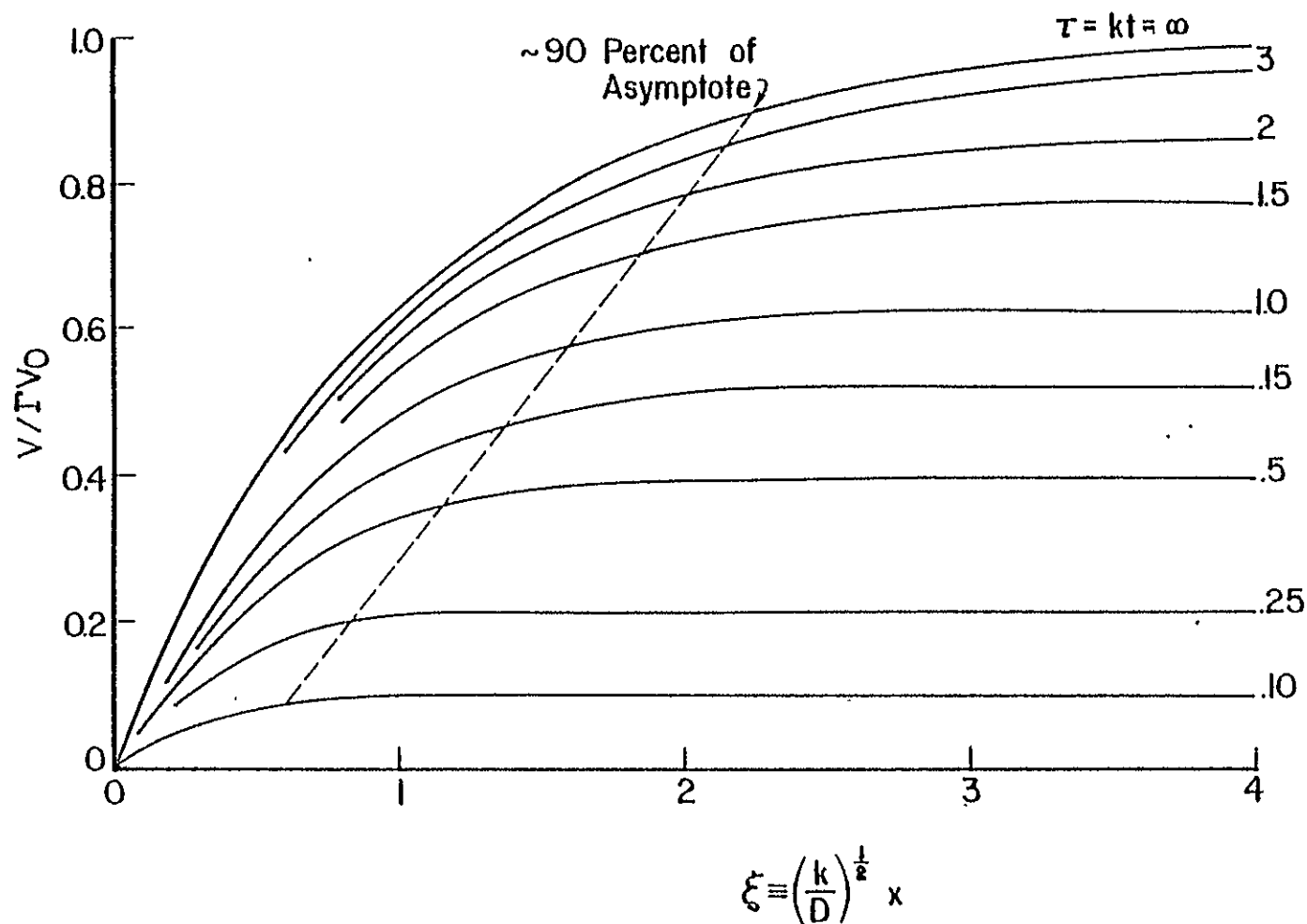


Figure 3. Plot of Eq. (10), the solution to the dielectric charging problem. The line showing the value of the normalized potential at 90 percent of its value at $\xi = \infty$ was found numerically. The abscissa is the scaled distance from the edge of the dielectric; the ordinate is the voltage across the dielectric as a fraction of the ultimate voltage.

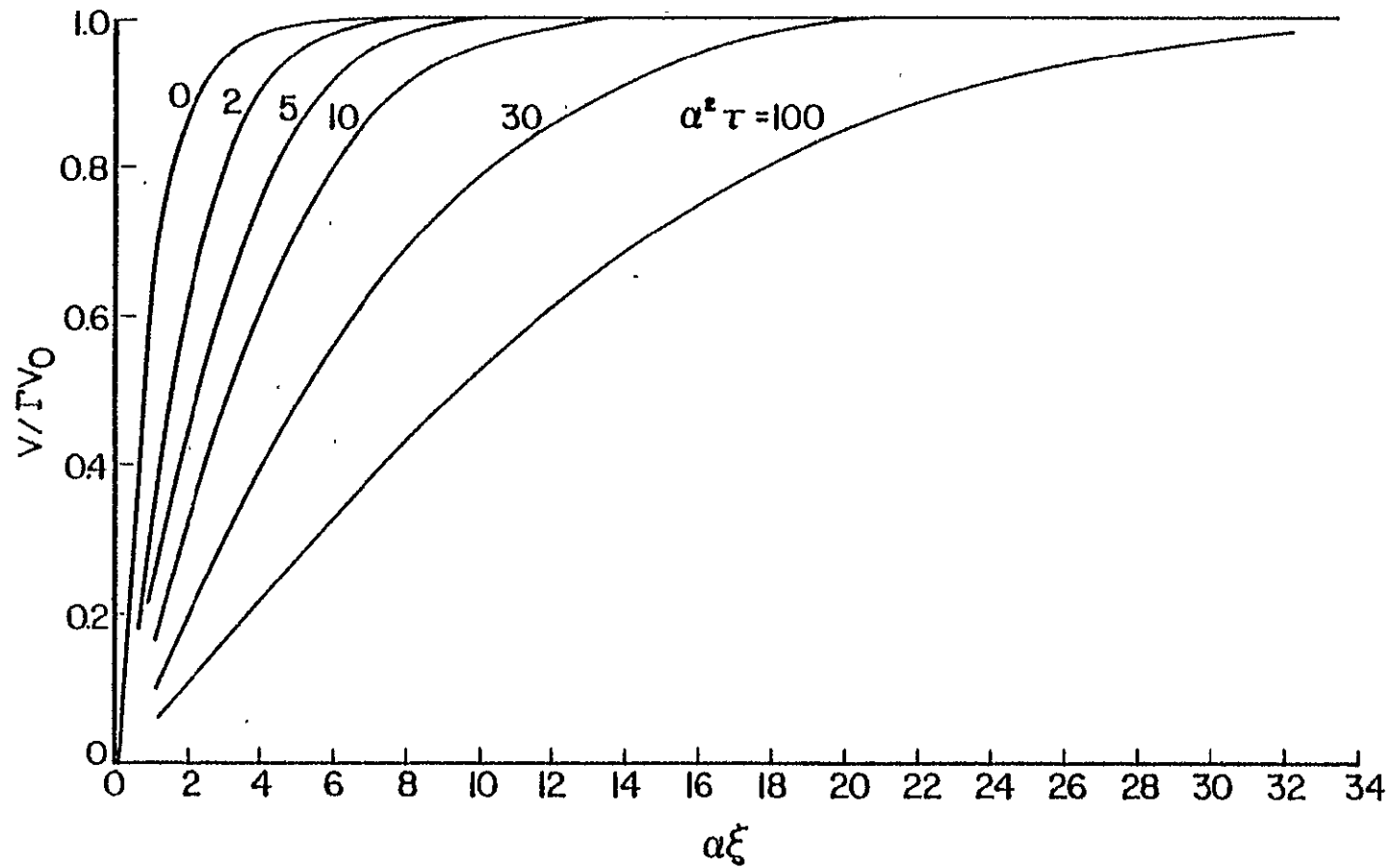


Figure 4. The solution to Eq. (14); the normalized potential as a function of normalized distance from the edge of the dielectric. The parameter is normalized time. The abscissa is the scaled distance from the edge of the dielectric; the ordinate is the voltage across the dielectric as a fraction of the initial voltage.

11.2 SURFACE CONDUCTIVITY

NASCAP treats surface conductivity as a redistribution of charge among the nodes of a surface cell due to bilinearly interpolated surface fields in that cell. The resultant matrix elements are shown on the following page. For an insulating material, surface conductivity is activated by specifying a positive surface resistivity value (Ω/\square) as material property 14. This also produces conductivity at a dielectric-metal edge. A negative value indicates surface conductivity is to be ignored. The ignoring feature is important, since there is a limit of 9537 matrix elements in the circuit model.

SELECTED SURFACE RESISTIVITIES (Ω/\square)	
Teflon (TFE)	10^{13}
Teflon (FEP)	$>10^{16}$
Kapton	10^{16}
Mylar	10^{16}
RTVxxx	10^{12}
Epoxy	10^{11}
Glass (quartz)	10^{19}

Surface Conductivity m.e.'s

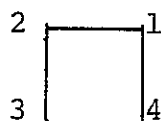
Units are $\sigma_s/\epsilon_o\Delta$, where

σ_s = surface conductivity (mhos)

$\epsilon_o = 8.85 \times 10^{-12}$ farads/meter

Δ = mesh size (XMESH)

Square

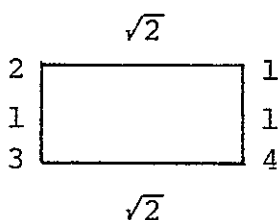


$$\sigma_{11} = -2/3$$

$$\sigma_{12} = \sigma_{14} = 1/6$$

$$\sigma_{13} = 1/3$$

Rectangle



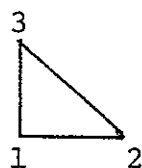
$$\sigma_{11} = -7 \sqrt{2}/12$$

$$\sigma_{12} = \sqrt{2}/12$$

$$\sigma_{13} = \sqrt{2}/4$$

$$\sigma_{14} = \sqrt{2}/4$$

Right Triangle



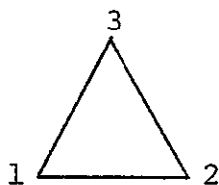
$$\sigma_{11} = -1$$

$$\sigma_{12} = \sigma_{13} = 1/2$$

$$\sigma_{22} = \sigma_{33} = -1/2$$

$$\sigma_{23} = 0$$

Eq. Triangle



$$\sigma_{11} = \sigma_{22} = \sigma_{33} = -4/3\sqrt{3}$$

$$\sigma_{12} = \sigma_{13} = \sigma_{23} = 2/3\sqrt{3}$$

12. DISCHARGE, PATCH, SPACE CHARGE DENSITY PLOTS

12.1 THREE FURTHER MODIFICATIONS

These three code modifications proved to be simpler tasks than many of the previously described extensions. Yet they significantly expand NASCAP capabilities.

The DISCHARGE facility identifies sites of spacecraft discharge. It involves a new keyword (read by RDOPT) and two new material properties (read by OBJDEF).

PATCHR and PATCHW are two new object types to be used in defining complicated objects. They are very much like the RECTANGLE and WEDGE objects. The difference is the way they interact with the hidden line HIDCEL routine.

Space charge density plots can be obtained using the keyword SHEATH (read by RDOPT).

12.2 NASCAP DISCHARGE ANALYSIS

A discharge facility has now been implemented in NASCAP. To invoke it, specify the RDOPT option DISCHARGE, with the relaxation factor DCHGF in columns 21-30. The breakdown potentials are specified as material properties 15 and 16 (both positive):

Property 15: Maximum absolute potential attainable by material.

Property 16: Maximum potential of a dielectric surface relative to its underlying conductor, or a non-grounded conducting surface relative to spacecraft ground.

Analysis is performed immediately preceding return to TRILIN from LIMCEL. In the case of a plasma discharge (property 15 exceeded) charge is removed from the lowest numbered non-fixed conductor, as well as charge transfer from dielectric surface to underlying conductor. If property 16 is exceeded,

the obvious charge transfer takes place. The amount of charge transfer is governed by the "relaxation factor" DCHGF, with $DCHGF = 1.$ indicating total short, and $DCHGF = 0.$ indicating minimum charge transfer.

Example 1. A grounded aluminum cube, partially covered with teflon, is exposed to a charging environment. The teflon surface is set to discharge to its conducting substrate with a 50 percent relaxation factor when differentially charged to 1 kV. The final portion of LIMCEL printout for timestep 4 (126 seconds to 286 seconds) is shown in Figure 12.1. During this time the teflon surface charged from \sim -890 volts to \sim -1800 volts, exceeding the discharge threshold. Discharges were registered on all the teflon surface cells, and charge was transported from the surface to the conductor. At the beginning of timestep 5 the teflon surface was seen to have a potential of \sim -500 volts.

Example 2. The partially covered aluminum cube of example 1 was allowed to float. The aluminum surfaces were set to discharge to test tank ground at a potential of 5 kV, with a 70 percent relaxation factor. During timestep 13 the aluminum charged from -4700 volts to -5900 volts. (The teflon surfaces remained 500 volts negative relative to the aluminum.) As shown in Figure 12.2, a discharge was registered at the lowest numbered aluminum surface cell. At the beginning of timestep 14 the aluminum cube was at \sim -1500 volts.

PREDICTED NODE POTENTIALS

NODE	V-PRED	DO	V-DLD	PTLIST
1	-1664.36	-469210.10	-812.88	001010131001
2	-1732.91	-928202.57	-849.60	001011131001
3	-1664.38	-469208.42	-812.89	001012111001
4	-1732.92	-928201.45	-849.60	001012121001
5	-1767.27	-922546.40	-863.15	001012131001
6	-1732.91	-928202.55	-849.60	001110131001
7	-1806.68	-1835623.16	-889.09	001111130001
8	-1732.92	-928200.65	-849.61	001112111001
9	-1806.69	-1835621.80	-889.09	001112120001
10	-1804.84	-1833437.08	-888.50	001112130001
11	-1664.38	-469208.42	-812.89	001210111001
12	-1732.92	-928201.47	-849.60	001210121001
13	-1767.27	-922546.43	-863.15	001210131001
14	-1732.92	-928200.65	-849.61	001211111001
15	-1806.69	-1835621.80	-889.09	001211120001
16	-1804.84	-1833437.05	-888.50	001211130001
17	-1767.28	-922544.52	-863.16	001212111001
18	-1804.84	-1833435.39	-888.50	001212120001
19	-1803.35	-1374050.16	-887.96	001212130001

SUM(DO) = -2.21256995+07

SUM(CS*DV) = -1.43792356+04

DOO = 2.21113212+07

V-C = 0.00000000

ORIGINAL PAGE IS
OF POOR QUALITY

DISCHARGE ANALYSIS ---				50.0% RELAXATION	
CELL	4	AT	-1.73+03 VOLTS	DISCHARGE	TO UNDERLYING CONDUCTOR
CELL	8	AT	-1.73+03 VOLTS	DISCHARGE	TO UNDERLYING CONDUCTOR
CELL	10	AT	-1.78+03 VOLTS	DISCHARGE	TO UNDERLYING CONDUCTOR
CELL	11	AT	-1.78+03 VOLTS	DISCHARGE	TO UNDERLYING CONDUCTOR
CELL	15	AT	-1.73+03 VOLTS	DISCHARGE	TO UNDERLYING CONDUCTOR
CELL	16	AT	-1.78+03 VOLTS	DISCHARGE	TO UNDERLYING CONDUCTOR
CELL	18	AT	-1.78+03 VOLTS	DISCHARGE	TO UNDERLYING CONDUCTOR
CELL	20	AT	-1.78+03 VOLTS	DISCHARGE	TO UNDERLYING CONDUCTOR
CELL	21	AT	-1.78+03 VOLTS	DISCHARGE	TO UNDERLYING CONDUCTOR
CELL	22	AT	-1.80+03 VOLTS	DISCHARGE	TO UNDERLYING CONDUCTOR
CELL	23	AT	-1.80+03 VOLTS	DISCHARGE	TO UNDERLYING CONDUCTOR
CELL	24	AT	-1.80+03 VOLTS	DISCHARGE	TO UNDERLYING CONDUCTOR

Figure 12.1. Discharge printout -- grounded aluminum cube.

PREDICTED NODE POTENTIALS

NODE	V-PRED	DO	V-OLD	PTLIST
1	-6465.78	-197.85	-5250.02	001010131001
2	-6449.86	-397.47	-5232.71	001011131001
3	-6465.88	-197.85	-5250.10	001012111001
4	-6449.89	-397.48	-5232.73	001012121001
5	-6423.79	-400.08	-5206.93	001012131001
6	-6449.86	-397.47	-5232.71	001110131001
7	-6433.80	-798.36	-5215.96	001111130001
8	-6449.91	-397.49	-5232.74	001112111001
9	-6433.81	-798.40	-5215.97	001112120001
10	-6414.39	-802.40	-5196.76	001112130001
11	-6465.88	-197.86	-5250.10	001210111001
12	-6449.89	-397.49	-5232.73	001210121001
13	-6423.79	-400.08	-5206.93	001210131001
14	-6449.91	-397.49	-5232.74	001211111001
15	-6433.81	-798.40	-5215.97	001211120001
16	-6414.39	-802.40	-5196.76	001211130001
17	-6423.85	-400.12	-5206.97	001212111001
18	-6414.40	-802.45	-5196.77	001212120001
19	-6401.58	-603.99	-5184.30	001212130001

SUM(DQ) = -9.58511560+03

SUM(CS#OV) = -1.96546086+04

DQC = -1.60014203+04

V-C = -5.91873303+03

DISCHARGE ANALYSIS --- 70.0% RELAXATION
CELL 1 AT -5.92+03 VOLTS DISCHARGE TO PLASMA OR TANK GROUND

Figure 12.2. Discharge printout - floating aluminum cube.

12.3 PATCH SURFACES

The object definition routines INPUT, RECTAN, and WEDGE have been rewritten to accept two new object types: "PATCHR" and "PATCHW". These two objects are identical to the previous objects "RECTAN" and "WEDGE", respectively, except that no A2-type (shadowing) surfaces are defined for PATCHR and PATCHW. The new objects can be used to change the surface cell composition of selected areas on large, previously defined surfaces when the outline of the entire object is not to be altered.

Before the new keywords were implemented, the list of A2 surfaces was becoming unreasonably large for objects with complicated surface composition patterns, such as SCATHA. The changes described above allow the A2 surface list to remain sensibly related to the geometrical complexity of an object, rather than to the complexity of the surface composition.

12.4 SPACE CHARGE DENSITY

The NASCAP space charge density plotting subroutine RHOSHE may be invoked by the keyword SHEATH. It obtains to first order the space charge due to low energy photo- and secondary-electrons emitted from surface cells (not, as yet booms). The contour levels are in units of code units of charge per cubic mesh unit. The effect of space charge on the spacecraft potential (in volts) is comparable to the maximum contour level.

To convert a contour level, z , to MKS units (coul/m^3), multiply by ϵ_0/Δ^2 , where Δ is the mesh size in meters:

$$\rho(\text{coul}/\text{m}^3) = \frac{\epsilon_0 z}{\Delta^2} \sim 10^{-9} z$$

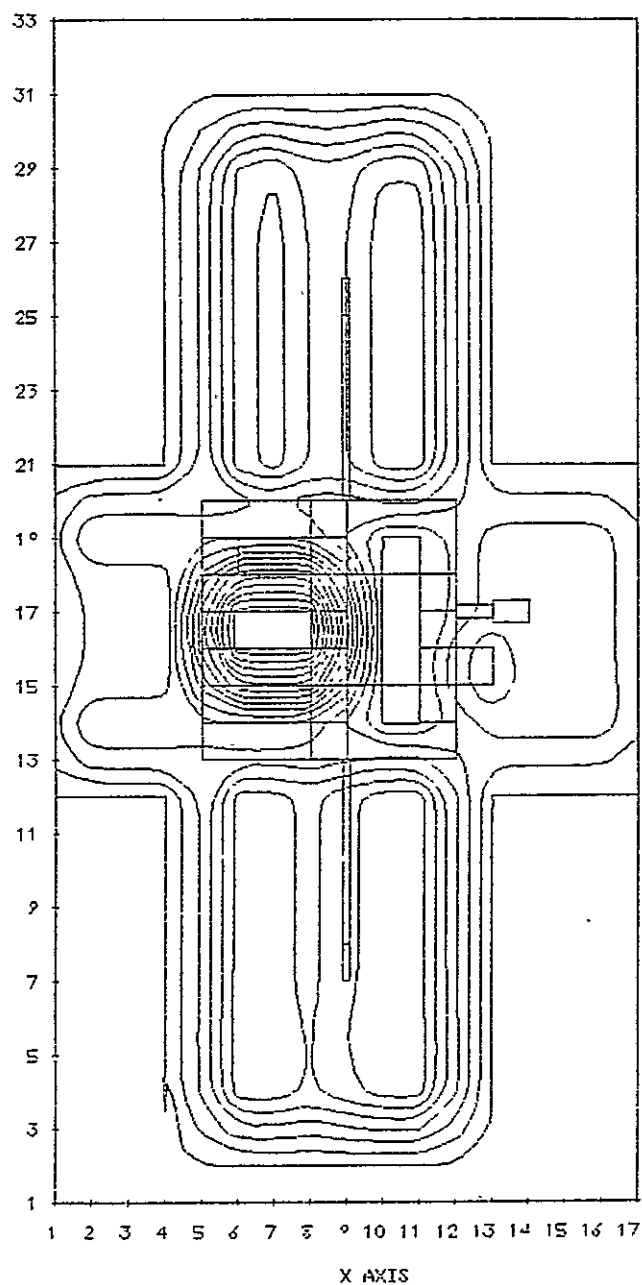
To obtain electrons per cm^3 , divide by a further $q_e \times 10^{+6}$

$$\rho(\text{el}/\text{cm}^3) = \frac{10^{-6}}{q_e} \frac{\epsilon_0}{\Delta^2} z \sim 10^4 z$$

Figures 12.3 and 12.4 show space charge contours for the small SCATHA model in an extreme environment. The first picture is for an uncharged satellite, and shows that the largest space charge is in the cavity, where it has a value of $z = -.29 = -5 \times 10^{-11} \text{ coul/m}^3 = 300 \text{ el/cm}^3$. The second is for the spacecraft at -675 volts, and shows no space charge except in the cavity, where it attains a peak value half that of the first figure.

SHEATH CONTOURS ALONG THE X-Z PLANE OF Y = 9

ZMIN = -.29312+00 ZMAX = .00000 ΔZ = .20000-01



ORIGINAL PAGE IS
OF POOR QUALITY

Figure 12.3. Space charge density contours about small SCATHA model, uncharged in severe substorm.

SHEATH CONTOURS ALONG THE X-Z PLANE OF Y = 9

ZMIN = -.15236+00 ZMAX = .00000 ΔZ = .10000-01

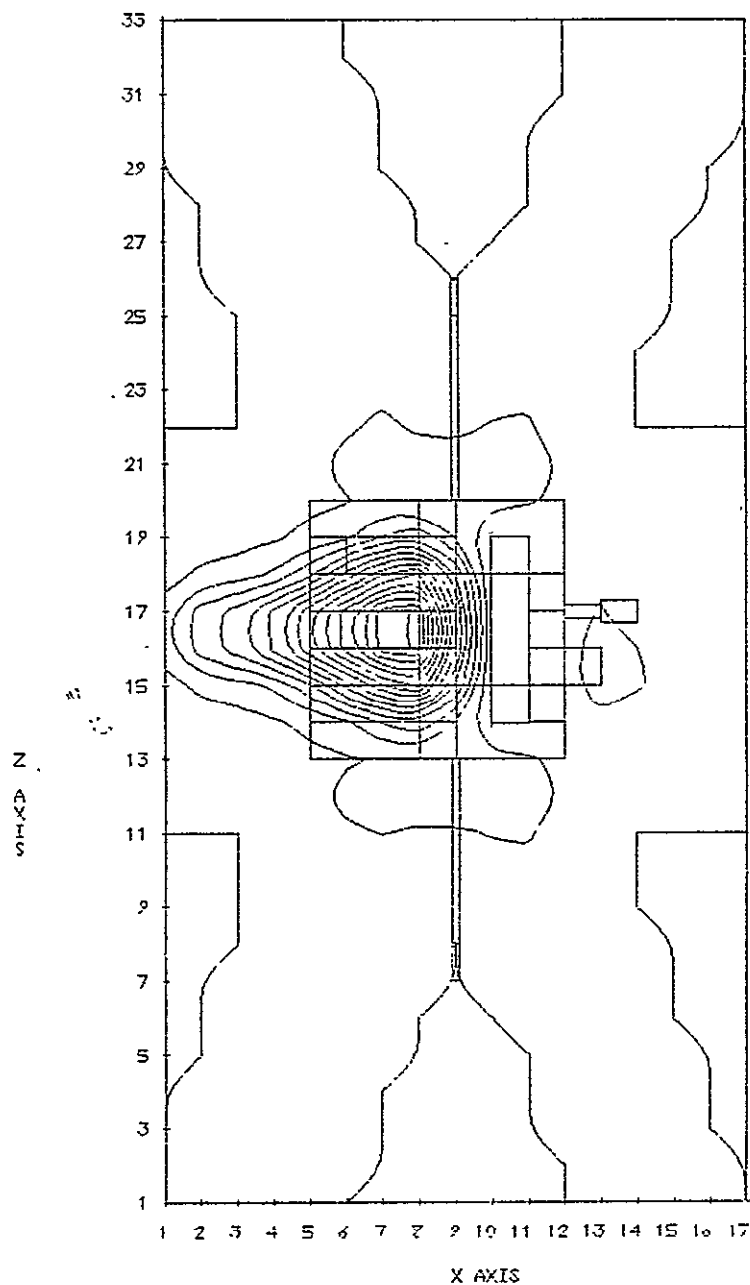


Figure 12.4. Space charge density contours about small SCATHA model charged to -675 volts.

13. SHADOWING CALCULATIONS

Systems, Science and Software performed a calculation of percentage solar illumination for SCATHA experiments. The resulting tables show experiment illumination for the various solar orientations that SCATHA will assume. Detailed results are given in Systems, Science and Software Report SSS-R-78-3658, May 1978, "SCATHA Experiment Shadowing Study".

The source code and relocatables and data files were delivered to NASA-LeRC. This section documents those items.

13.1 CODES AND DATA FILES

A Univac 1100/80 16-track program file tape has been delivered to NASA-LeRC. This tape contains nine program files, any of which could be reloaded to mass storage using the @COPY,G command. Of the nine files on the tape the ones which are significant to NASA-LeRC are probably the first five. It is suggested that NASA-LeRC retain copies of all nine files, however, for possible future reference. The contents of the first five files are as follows:

1. SHADOW This file contains all of the source and relocatable elements for the shadowing program as well as an absolute element generated on the Univac 1100/80 at S³. The absolute element contains S³ plot package routines, however, and it is recommended that NASA-LeRC remap the program. (See next section.)
2. STARTRUN This is a symbolic element file which contains all of the canned runstreams used to generate the 33 SCATHA shadow tables.
3. OBJSCA This symbolic element file contains polygon definition keyword cards for each of the objects on SCATHA which were significant for the shadow tables requested.
4. ALOBJ This symbolic element file contains combinations of elements from OBJSCA used to make up the complete shadowed object polygon sets.

5. A2OBJ This symbolic element file contains combinations of elements from OBJSCA used to make up the complete shadowing object polygon sets.

The S³ 1100/80 run which copied the nine files to tape is reproduced in Figure 13.1 and should assist NASA-LeRC in making their own copy of the tape.

```
1       @MSG PLEASE MOUNT NEW UNLABELED SAVE TAPE A3 PER ROST
2       @ASSG,TJ TAPE,U9
3       @REWIND TAPE.
4       @MARK TAPE.
5       @MARK TAPE.
6       @REWIND TAPE.
7       @COPY,GM SHADOW,TAPE
8       @COPY,GM STARTRUN,TAPE
9       @COPY,GM OBJSCA,TAPE
10       @COPY,GM A1OBJ,TAPE
11       @COPY,GM A2OBJ,TAPE
12       @COPY,GM SAMTEC,TAPE
13       @COPY,GM AVERAGE,TAPE
14       @COPY,GM NEUMAIN,TAPE
15       @COPY,GM SCASHADOW,TAPE
16       @MARK TAPE.
17       @MARK TAPE.
18       @REWIND TAPE.
19       @REWIND TAPE.
20       @FREE TAPE.
```

Figure 13.1. Generation of shadow program tape sent to NASA-LeRC. S³ tape number was N1976 (unlabeled).

13.2 REMAPPING AT NASA-LeRC

The shadow programs utilize the S³ routines

S3DATE,
S3ETIM,
S3TICK,
S3WARN.

If equivalent routines are not available at NASA/LeRC then the following dummy subroutines could probably be implemented with the only loss in flexibility being the capability of writing restart dumps periodically or writing a restart dump and gracefully terminating before exceeding the CPU time limit.

```
SUBROUTINE S3DATE (DATE,TIME)
DATE = 0
TIME = 0
RETURN
END
```

```
SUBROUTINE S3ETIM (ZTIME)
ZTIME = 0
RETURN
END
```

```
SUBROUTINE S3TICK (TIME)
TIME = 0.0
RETURN
END
```

```
SUBROUTINE S3WARN (*,LIMTIM,LIMPAG)
RETURN
END
```


Once these dummy routines have been written and compiled they should be mapped with the relocatables in the SHADOW file using the following procedure:

Assume that the relocatable for the NASA/LeRC version of the four routines discussed above are already in TPF\$. Then

```
@COPY,R SHADOW.
```

```
@MAP
```

```
@COPY,A NAME$,SHADOW.ABS
```

```
@PACK SHADOW.
```

If undefined references to the routines SETUPV, SETUAV, DXDYV, GRID1V, TYPEV, and possibly DTLIN appear they should be ignored.

13.3 DESCRIPTION OF PROGRAM RUNSTREAM INPUT

Immediately following the @XQT SHADOW.ABS control card the program expects to find the following in the runstream:

Card 1: 6 character file identifier selected by the user.
Appears in card col. 1-6.

Card 2,3: Two 78 character run description lines — any text chosen by the user. The text should be centered on these cards for neat appearance on the output listing.

The remaining data cards in the runstream consist of one or more sets of the following card sequences:

- A. Task command keyword card. (Card col. 1-7 left-justified.)
- B. SHDATA NAMELIST data cards to select options for the keyword command specified by A.

The available keyword commands and their functions are:

NEWFILE: A brand-new shadow table (or segment of) is to be generated. At completion of this command the table will be written onto FORTRAN logical file number LUNNEW.

RESTART: Resume calculation using an old shadow table residing on FORTRAN logical file number LUNOLD which was not completely filled during a previous run due to excessive execution time.

EXTEND: Extend an old shadowing table. The old table resides on FORTRAN logical unit LUNOLD and the new table containing the old entries plus the new segment calculated is written onto file LUNNEW.

MERGE: Shadow tables on files LUNOLD and LUNNEW are merged into a new file which is written onto LUNMRG. No actual shadow calculations result from this command.

PRINTO: Produce a line printer listing of the shadow table residing on file LUNOLD.

PRINTN: Produce a line printer listing of the shadow table residing in LUNNEW.

PRINTM: Produce a line printer listing of the shadow table on LUNMRG.

INSERT: Insert entries into a shadow table "by hand". (Following the SHDATA namelist another namelist FIXUP is also expected. This namelist contains the one-dimensional array SHTAB of shadow entries and NFILE — the number of entries in the table. The dimension of SHTAB is SHTAB(NPHI,NTHETA). If NPHI = 360, NTHETA = 26, for example, and we wish to set SHTAB(231,14) = 0.31 then the FIXUP namelist would be

\$FIXUP SHTAB(5271)=0.31,\$END,

for example. This command assumes the table to be added to already exists on LUNOLD. The new table will be written to LUNNEW. LUNMRG is used as a scratch file.

END: All tasks for the run are complete. Terminate execution.

The variables which may appear in the SHDATA namelist, their functions, and default values are as follows:

IUNIT1: Logical unit number upon which the shadowed object A1 polygon definition keyword cards reside. Default is IUNIT1 = 10.

IUNIT2: Logical unit number upon which the shadowing object A2 polygon definition keyword cards reside. Default is IUNIT2 = 11.

LUNOLD: Logical unit number of old shadow table file.

LUNMRG: Logical unit number of merged shadow table.

LUNNEW: Logical unit number of new shadow table file.

ICMPR: Flag set as follows:
 0: shadow table in full 2-D format.
 1: shadow table in compressed format with zero entries removed.

Currently ICMPR = 1 has not been fully implemented. Therefore the user should not attempt to input a value for ICMPR. The default is, of course, ICMPR = 0.

APHI: Lower limit for azimuthal angle ϕ in table (in degrees). Default is APHI = 1.0.

BPHI: Upper limit for azimuthal angle ϕ in table (in degrees). Default is BPHI = 360.0.

NPHI: Number of azimuthal angles (rows) in table.
 Note: This parameter should, in general, remain the same for keyword command/SHDATA namelist sequences which appear in the runstream after the first and in subsequent runs which involve the same table. Default is NPHI = 360. (This is the maximum allowable value.)

ATHETA: Lower limit for polar angle θ in table (in degrees). Default is ATHETA = 80.0.

BTHETA: Upper limit for polar angle θ in table (in degrees). Default is BTHETA = 100.0.

NTHETA: Number of polar angles (columns) in table.
 Note: Remarks about NPHI apply here also. Default is NTHETA = 21. Maximum allowable value is NTHETA = 26.

JP: Starting index for azimuthal angles.

NP: Ending index for azimuthal angles.

JT: Starting index for polar angles.

NT: Ending index for polar angles.

If a new table segment is being generated then the range of the table filled is

SHTAB(I,J) for I = JP, ..., NP

and

J = JT, ..., NT

The angle corresponding to I, J is

$$\phi_i = \text{DPHI} * (I-1) + \text{APHI}$$

$$\theta_j = \text{DTHETA} * (J-1) + \text{ATHETA}$$

where

$$\text{DPHI} = (\text{BPHI} - \text{APHI}) / (\text{NPHI} - 1)$$

$$\text{DTHETA} = (\text{BTHETA} - \text{ATHETA}) / (\text{NTHETA} - 1).$$

INONES: If INONES \neq 0 set all entries in table in range specified by JP, NP, JT, NT to 1.0. (No actual shadow calculation performed. Facilitates insertion by hand of large areas of the table which are known before-hand to be total shadow.) Default is INONES = 0.

LIST: If LIST \neq 0 then a complete listing of the table on file LUNNEW is produced following completion of shadowing calculations.

13.4 OBJECT DEFINITION FILES

If a shadowing calculation is to be performed then the A1 and A2 polygon definition files must be available to the program. The data cards on these files must be in the following format:

First Card: *A1DEF or *A2DEF

{ polygon keyword definition cards for each
object in the shadowed (shadowing) polygon
set.

Last Card: *END A1 or *END A2

For the SCATHA satellite a special file (OBJSCA) has been prepared which contains polygon definitions for each of the SCATHA objects deemed significant to the shadowing study. The name of each element in this file, in general, corresponds to the associated SCATHA object which is defined by the element. The individual objects for a particular shadowing table are selected from the file OBJSCA and combined (using the @ED processor of the Univac 1100) into shadowing object (A2) and shadowed object (A1) polygon sets. A number of these sets can be found in the files A1OBJ and A2OBJ. In many cases, however, the elements needed from OBJSCA were simply combined using @ED within the runstream used to generate the shadow table.

13.5 RUNSTREAMS

A special symbolic element file called STARTRUN has been provided with the program. This file contains all of the canned runstreams used to generate the 33 SCATHA shadow tables.

Many of the tables were generated segment-by-segment using several consecutive @START commands using elements from the STARTRUN file. In most of these cases there is an additional @COPY operation required between @STARTs to make the output file from a previous run available to the next.

As a simple example we shall consider the generation of the shadow table for the ML12-6 TQCM aperture. This shadow table was generated in four segments. All segments were generated within the same runstream, however, so only a single batch run was required. The runstream for this table is contained in STARTRUN.ML6AP, a listing of which is reproduced in Figure 13.2. The appropriate shadowing object sets for ML12-6 are as follows:

SHADOWING OBJECT SET AND APPROXIMATE SUN ANGLE RANGES:

<u>Shadowing Objects</u>	<u>Approximate Sun Angles</u>
1. SC2-1(B).boom and sheath electric field sensor	$23^{\circ} \leq \phi \leq 48^{\circ}$ $89^{\circ} \leq \theta \leq 97^{\circ}$
2. SC11-1(B) boom and magnetic field sensor	$188^{\circ} \leq \phi \leq 201^{\circ}$ $90^{\circ} \leq \theta \leq 95^{\circ}$
3. Main satellite body: The ML12-6 radiator surface and aperture are not visible to the sun for the range	$0^{\circ} \leq \phi \leq 22^{\circ}$ $202^{\circ} \leq \phi \leq 360^{\circ}$
4. ML12-6 door: Test Calculations showed that shadowing was im- portant only at sun angles for which $\theta > 100^{\circ}$. Thus the door was not included in the shadowing object set for the ML12-6 surfaces.	

```

@ED C.ML6AP
READ-ONLY MODE
ED 314.00-04/20-18:39-(0>)
EDIT
0:LNP!
  1:@RUN PGS,11070-00,STEEN-P,S600
  2:@ES@U.BIG-NAME,N
  3:SCATHA SHADOW
  4:TABLE FOR ML12
  5:CONTAMINATION
  6:EXPERIMENT(XML6AP)
  7:@UCE A1,A1OBJ
  8:@UCE A2,A2OBJ
  9:@UCE O,OBJSCA
10:@UCE S,SCASHADOW
11:@UCE N,NEUMAIN
12:@ACG,T 10.
13:@ACG,T 11.
14:@ACG,PUR XOLD.
15:@ACG,PUR XNEW.
16:@UCE 20,XOLD
17:@UCE 22,XNEW
18:@ED O.BLANK,10.
19:I @A1DEF
20:ADD O.ML12-6IN
21:I @ENDR1
22:LNP!
23:@ED O.BLANK,11.
24:I @A2DEF
25:ADD O.SC2-1BOOM
26:ADD O.SC2-1SPHERE
27:I @ENDR2
28:LNP!
29:@ACG,T 12.
30:@ED O.BLANK,12.
31:I @A2DEF
32:ADD O.SC11-1
33:I @ENDR2
34:LNP!
35:@ACG,PUR XML6AP.
36:@XOT N.
37:XML6AP
38:                ML12-6 APERTURE SHADOWED BY SC2-1(B) AND SC11-1(B)
39:

```

ORIGINAL PAGE IS
OF POOR QUALITY

Figure 13.2. Runstream used to generate shadowing table for ML12-6 aperture.


```

40: NEWFILE
41: $CHDATA
42: JTIME=100, LMTIM=30,
43: JP=23, NP=49,
44: JT=0, NT=20,
45: $END
46: EXTEND
47: $CHDATA LUNOLD=22, LUNNEW=20, IUNIT2=12,
48: JP=184, NP=201,
49: JT=1, NT=21,
50: $END
51: EXTEND
52: $CHDATA LUNOLD=20, LUNNEW=22,
53: INONES=1,
54: JP=202, NP=360, JT=1, NT=21,
55: $END
56: EXTEND
57: $CHDATA LUNOLD=22, LUNNEW=20,
58: INONES=1,
59: JP=1, NP=22, JT=1, NT=21,
60: $END
61: END
62: @PMD, GED
63: @COPY 20, XML6AP
64: @FREE XML6AP
65: @NOT AVERAGE.
66: $AVG PNORM=0.0, -0.3746, 0.9272, $END
67: @ES+U.BIG-NAME, N
68: SHADOW
69: TABLE
70: END
71: BOX 33
72: @FIN

```

SCAN:72

EOF:72

0:EXI

NO CORRECTIONS APPLIED.

The polygon definition for the ML12-6 aperture is found in OBJSCA.ML12-6IN. The required A1 polygon definition file is prepared in lines 18-22 of the runstream using the editor. The polygon definition for the SC2-1(B) boom and sphere are found in OBJSCA.SC2-1BOOM and OBJSCA.SC2-1SPHERE, respectively. Since these two objects shadow over a different range than the SC11-1 they are placed on their own file at lines 23-28. The definition for SC11-1 is found in OBJSCA.SC11-1 and is placed on another file by lines 29-34. Line 35 assigns a permanent file onto which the final shadow table is to be copied. At line 37 program execution begins. (The absolute program element was assumed to be in file NEWMAN - at NASA/LeRC this will be in the file SHADOW instead.) After reading the identifiers in lines 37-39 the first segment of the table involving shadowing by SC2-1(B) is generated by lines 40-45.

The second segment involving shadowing by SC11-1 is generated by lines 46-50. Note that the output file from lines 40-45 becomes the input file for lines 46-50. Finally the main satellite body shadowing effect is inserted in two segments by lines 51-55 and 56-60. (Note the exchange of input and output shadow table files again.) The END command word at line 61 terminates execution and the completed shadow table is copied onto the save file at line 63. Line 65-66 uses the completed table as input to compute and print out the integral averages requested by Dave Hall for this experiment. If a printed copy of the final shadow table is desired it could be obtained by setting LIST = 1 at line 57 or by making a subsequent PRINTO run with the file XML6AP assigned to unit 20 - the LUNOLD file.

14. MATCHG - A MATERIAL CHARGING CODE

14.1 INTRODUCTION

MATCHG is a zero dimensional code that charges a surface using the same material formulations found in the NASCAP code. The surface potential, V , is just

$$V = Q/C ,$$

where Q is the charge per unit area and C is the capacitance per unit area

$$Q = \int j dt$$

$$C = \frac{\epsilon \cdot \epsilon_0}{d}$$

The code models either a monotonic electron beam or a spherical probe approximation to a Maxwellian flux of ions and electrons. The initial version contains no conductivity effects.

Output includes tables and plots of electron backscatter and secondary emission versus energy and the surface potential versus time.

Section 14.2 describes how to use the code and Section 14.3 contains two sample runs.

14.2 USE OF THE CODE

Material data is read off unit 8. The format is that used in the NASCAP object definition file, i.e., a material name followed by three lines of properties. The code allows properties to be changed interactively so that the material properties file need not be modified. MATCHG is designed for an 80-line terminal. On EXEC 8, this can be set by @@TTY W,80. The code will prompt the user. Below are listed appropriate responses to questions. In general YES is the only affirmative response recognized and a carriage return (cr) will suffice for a negative response, but NO, or anything but YES, will also be interpreted as a negative.

To terminate execution reply to the MATERIAL prompt with STOP.

Prompts and acceptable responses are listed below.

<u>PROMPT</u>	<u>RESPONSES</u>
EMISSION FORMULATION	{ cr, leaves it unchanged ANGLE, regular formulation NORMAL, normal emission formula only
MATERIAL	{ cr, leaves it unchanged, if first call stops the program STOP, stops the code ALUMINUM } Provided in TEFLON } MATCHG.DATA KAPTON } SIO2 } MGO }
PRINT	{ YES, lists material properties (<u>must</u> be called if properties are to be changed) NO No list cr

<u>PROMPT</u>	<u>RESPONSES</u>
CHANGE ANY MATERIAL PROPERTIES	{ cr NO YES
[property]	{ cr - leave value unchanged [value] - new value
FLUX TYPE	{ cr - remain unchanged (not first time) 1 - monoenergetic electron beam 2 - Maxwellian with electrons and protons
NEW PARAMETERS ?	{ cr NO YES
[flux parameter]	{ cr - leave value unchanged [value] - new value
GENERATE A TABLE?	{ cr NO YES - makes table of electron secondary, electron back-scatter, and proton generated electron secondary yields versus incident energy for normally incident particles ..
PLOT ()?	{ cr NO YES - makes plot
CHARGE?	{ cr NO YES - charges sample
FULL PRINT?	{ cr - prints first and last cycle NO current balances YES - prints every cycle potentials and every fifth cycle current balances

<u>PROMPT</u>	<u>RESPONSES</u>
CHARGING POSITIVE - STOP?	{ cr - continue NO YES - return to main program (code does not terminate execution)
PRINT A CHARGING TABLE?	{ cr NO YES - prints voltage and current versus time
PLOT?	{ cr NO YES - plots <u>absolute</u> value of potential versus time

14.3 SAMPLE RUNS

The first sample run is for ALUMINUM and shows most of the possible types of output. The second run is for KAPTON and shows how little output can be produced and still produce meaningful parameter variations.

```

$TTY M.132
-33COMPLETE
>H35,A MRP
READY
>USE 8.MRP
READY
\3COPY.A MCHG.ABS
FURPUR 27R3-1      E35 SL73R1 07/13/78 09:21:05
1 ARS
>XQT

```

WELCOME TO MATCH6 - A MATERIAL CHARGING PROGRAM

```

EMISSION FORMULATION IS ANGLE
SECONDARY EMISSION FORMULATION>NORMAL
EMISSION FORMULATION IS NORMAL
MATERIAL>ALUMINUM
PRINT >YES

```

ORIGINAL PAGE IS
OF POOR QUALITY

PREPROCESSING OF MATERIAL PROPERTIES

MATERIAL 1: ALUMIN

PROPERTY	INPUT VALUE	CODE VALUE
1 DIELECTRIC CONSTANT	1.00+00 (NONE)	1.00+00 (NONE)
2 THICKNESS	1.00-03 METERS	1.00-03 MESH
3 CONDUCTIVITY	-1.00+00 MHQ/M	-1.00+00 MHQ/M
4 ATOMIC NUMBER	1.30+01 (NONE)	1.30+01 (NONE)
5 DELTA MAX >COEFF	9.70-01 (NONE)	7.21+00 (NONE)
6 E-MAX >DEPTH<-1	3.00-01 KEY	1.73-02 ANG-01
7 RANGE	2.60+02 ANG.	3.38+02 ANG.
8 EXPONENT > RANGE	1.30+00 (NONE)	4.15+02 ANG.
9 RANGE > EXPONENT	2.40+02 ANG.	1.30+00 (NONE)
10 EXPONENT	1.73+00 (NONE)	1.73+00 (NONE)
11 YIELD FOR 1KEV PROTONS	1.36+00 (NONE)	1.36+00 (NONE)
12 MAX DE/DX FOR PROTONS	4.00+01 KEY	4.00+01 KEY
13 PHOTOCURRENT	4.00-05 A/M<<2	4.00-05 A/M<<2
14 SURFACE RESISTIVITY	0.00 OHMS	0.00 V-S/Q

CHANGE ANY MATERIAL PROPERTIES>YES

```

DIELECTRIC CONSTANT >2.0
THICKNESS >1.E-2
CONDUCTIVITY >2
ATOMIC NUMBER >
DELTA MAX >COEFF >
E-MAX >DEPTH<-1 >
RANGE >
EXPONENT > RANGE >
RANGE > EXPONENT >
EXPONENT >
YIELD FOR 1KEV PROTONS >
MAX DE/DX FOR PROTONS >
PHOTOCURRENT >
SURFACE RESISTIVITY >

```

MATERIAL 1: ALUMIN

PROPERTY	INPUT VALUE	CODE VALUE
1 DIELECTRIC CONSTANT	2.00+00 (NONE)	2.00+00 (NONE)
2 THICKNESS	1.00-02 METERS	1.00-02 MESH
3 CONDUCTIVITY	2.00+00 MHQ/M	2.00+00 MHQ/M
4 ATOMIC NUMBER	1.30+01 (NONE)	1.30+01 (NONE)
5 DELTA MAX >COEFF	9.70-01 (NONE)	7.21+00 (NONE)
6 E-MAX >DEPTH<-1	3.00-01 KEY	1.73-02 ANG-01
7 RANGE	2.60+02 ANG.	3.38+02 ANG.
8 EXPONENT > RANGE	1.30+00 (NONE)	4.15+02 ANG.
9 RANGE > EXPONENT	2.40+02 ANG.	1.30+00 (NONE)
10 EXPONENT	1.73+00 (NONE)	1.73+00 (NONE)
11 YIELD FOR 1KEV PROTONS	1.36+00 (NONE)	1.36+00 (NONE)
12 MAX DE/DX FOR PROTONS	4.00+01 KEY	4.00+01 KEY
13 PHOTOCURRENT	4.00-05 A/M<<2	4.00-05 A/M<<2
14 SURFACE RESISTIVITY	0.00 OHMS	0.00 V-S/Q

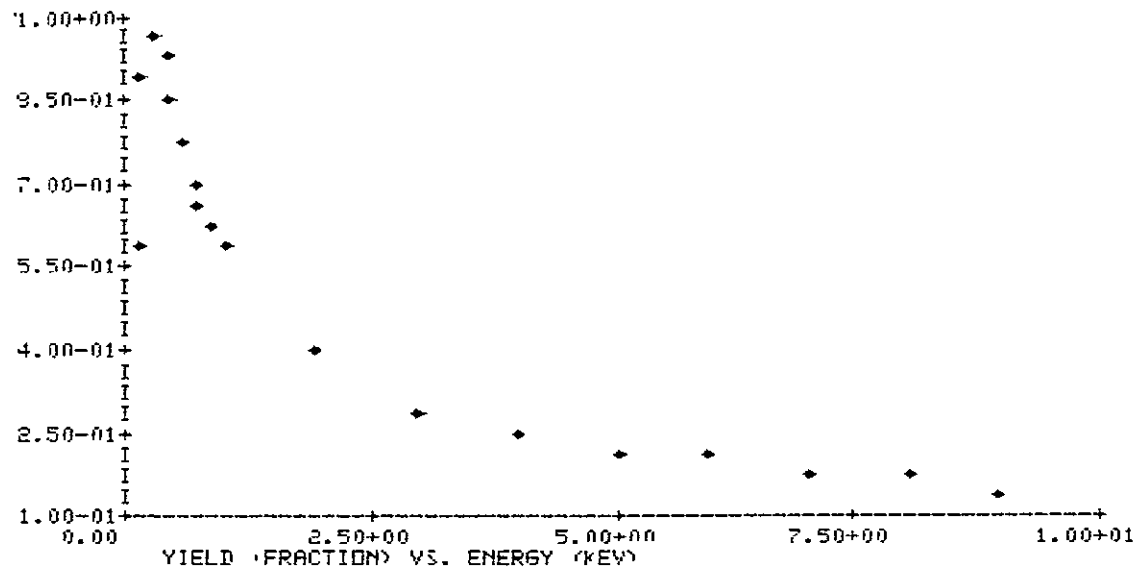
```

ENTER FLUX TYPE 1=BEAM 2=MAXWELLIAN >1
BEAM VOLTAGE = 2.0+01 KEV BEAM CURRENT = 1.0-05 AMPS / M<<2
NEW PARAMETERS ? >YES
BEAM VOLTAGE (KEY)>12
BEAM CURRENT (AMP/M<<2) >
BEAM VOLTAGE = 1.2+01 KEV BEAM CURRENT = 1.0-05 AMPS / M<<2
GENERATE A TABLE >YES

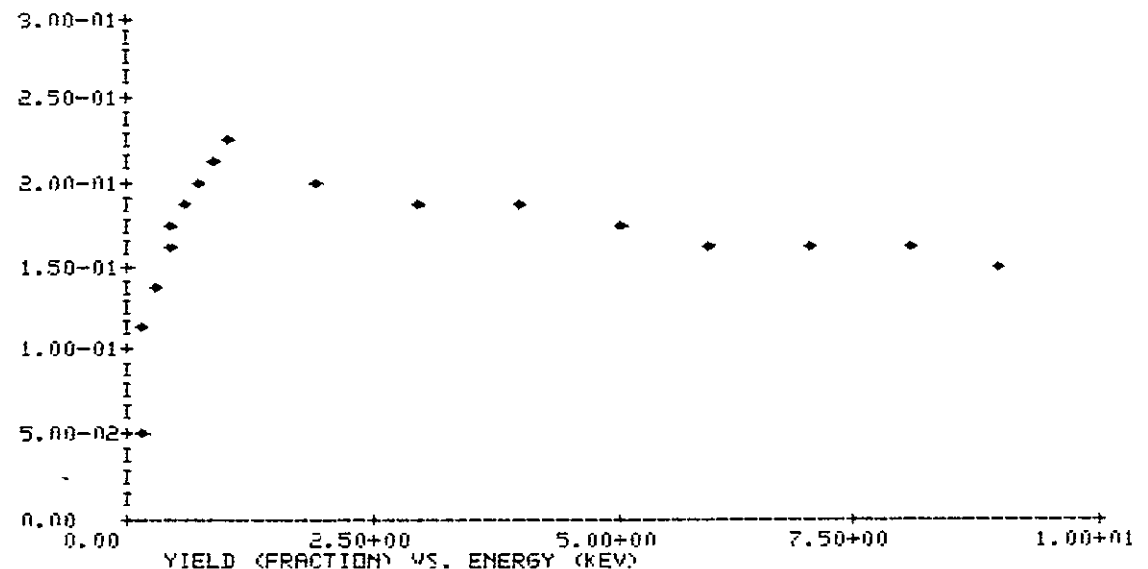
```


ENERGY (KEV)	EL. SEC.	EL. BkSCAT.	PP. SEC.
.100	.500	.054	.429
.200	.898	.108	.605
.300	.970	.138	.739
.400	.931	.159	.852
.500	.955	.175	.950
.600	.779	.187	1.039
.700	.714	.197	1.118
.800	.659	.206	1.193
1.000	.577	.219	1.327
2.000	.384	.204	1.832
3.000	.302	.192	2.191
4.000	.254	.182	2.473
5.000	.221	.174	2.703
6.000	.198	.167	2.897
7.000	.180	.162	3.062
8.000	.166	.157	3.206
9.000	.154	.154	3.331
10.000	.144	.151	3.441
20.000	.092	.139	4.055
30.000	.071	.137	4.257
40.000	.058	.137	4.301
50.000	.050	.137	4.274

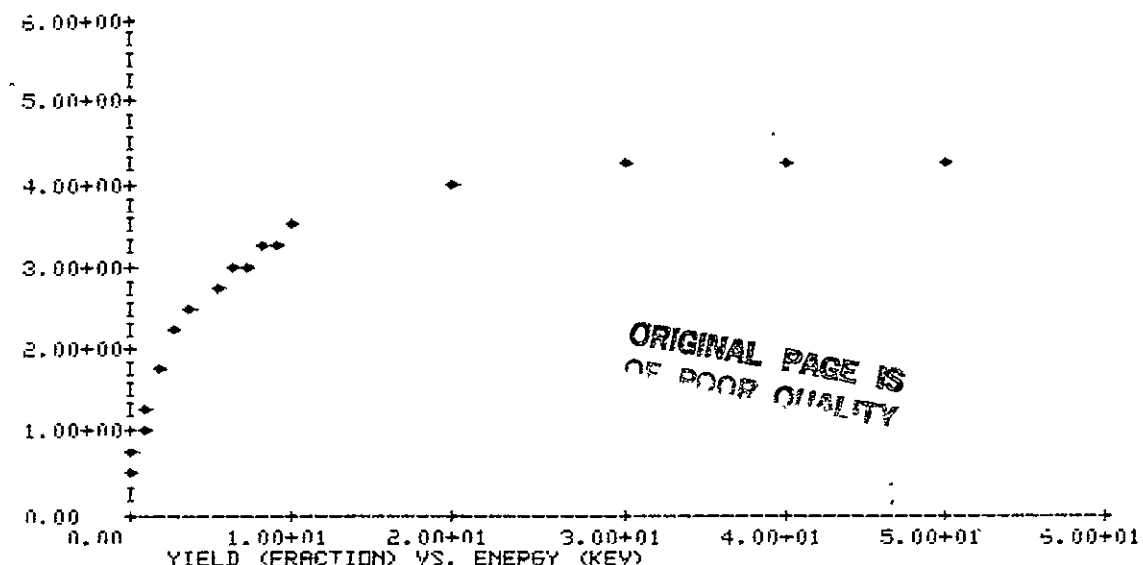
PLOT SECONDARY ELECTRONS? >YES



PLOT BACKSCATTERED ELECTRONS ?>YES



PLOT PROTON SECONDARIES ? >YES



ORIGINAL PAGE IS
OF POOR QUALITY

CHARGE ? >YES

FULL PRINT ?>YES

CYCLE	1	TIME	0.00	SECONDS	POTENTIAL	0.00	VOLTS
INCIDENT	ELECTRON CURRENT				-1.00-05		
	SECONDARY ELECTRONS				1.28-06		
	BACKSCATTERED ELECTRONS				1.46-06		
INCIDENT	PROTON CURRENT				0.00		
	SECONDARY ELECTRONS				0.00		

NET CURRENT -7.26-06 AMPS/M**2

CYCLE	2	TIME	2.93-01	SECONDS	POTENTIAL	-1.18+03	VOLTS
CYCLE	3	TIME	5.86-01	SECONDS	POTENTIAL	-2.34+03	VOLTS
CYCLE	4	TIME	8.78-01	SECONDS	POTENTIAL	-3.47+03	VOLTS
CYCLE	5	TIME	1.17+00	SECONDS	POTENTIAL	-4.58+03	VOLTS
CYCLE	6	TIME	1.46+00	SECONDS	POTENTIAL	-5.64+03	VOLTS

INCIDENT	ELECTRON CURRENT				-1.00-05		
	SECONDARY ELECTRONS				1.91-06		
	BACKSCATTERED ELECTRONS				1.65-06		
INCIDENT	PROTON CURRENT				0.00		
	SECONDARY ELECTRONS				0.00		

NET CURRENT -6.44-06 AMPS/M**2

CYCLE	7	TIME	1.76+00	SECONDS	POTENTIAL	-6.66+03	VOLTS
CYCLE	8	TIME	2.05+00	SECONDS	POTENTIAL	-7.52+03	VOLTS
CYCLE	9	TIME	2.34+00	SECONDS	POTENTIAL	-8.51+03	VOLTS
CYCLE	10	TIME	2.63+00	SECONDS	POTENTIAL	-9.31+03	VOLTS
CYCLE	11	TIME	2.93+00	SECONDS	POTENTIAL	-9.99+03	VOLTS

INCIDENT	ELECTRON CURRENT				-1.00-05		
	SECONDARY ELECTRONS				3.82-06		
	BACKSCATTERED ELECTRONS				2.04-06		
INCIDENT	PROTON CURRENT				0.00		
	SECONDARY ELECTRONS				0.00		

NET CURRENT -4.14-06 AMPS/M**2

CYCLE	12	TIME	3.22+00	SECONDS	POTENTIAL	-1.05+04	VOLTS
CYCLE	13	TIME	3.51+00	SECONDS	POTENTIAL	-1.09+04	VOLTS
CYCLE	14	TIME	3.81+00	SECONDS	POTENTIAL	-1.11+04	VOLTS
CYCLE	15	TIME	4.10+00	SECONDS	POTENTIAL	-1.13+04	VOLTS
CYCLE	16	TIME	4.39+00	SECONDS	POTENTIAL	-1.14+04	VOLTS

INCIDENT	ELECTRON CURRENT				-1.00-05		
	SECONDARY ELECTRONS				7.57-06		
	BACKSCATTERED ELECTRONS				1.91-06		
INCIDENT	PROTON CURRENT				0.00		
	SECONDARY ELECTRONS				0.00		

NET CURRENT -5.19-07 AMPS/M**2

CYCLE	17	TIME	4.68+00	SECONDS	POTENTIAL	-1.14+04	VOLTS
CYCLE	18	TIME	4.98+00	SECONDS	POTENTIAL	-1.14+04	VOLTS
CYCLE	19	TIME	5.27+00	SECONDS	POTENTIAL	-1.14+04	VOLTS
CYCLE	20	TIME	5.56+00	SECONDS	POTENTIAL	-1.14+04	VOLTS
CYCLE	21	TIME	5.86+00	SECONDS	POTENTIAL	-1.15+04	VOLTS

INCIDENT	ELECTRON CURRENT				-1.00-05		
	SECONDARY ELECTRONS				8.17-06		
	BACKSCATTERED ELECTRONS				1.81-06		
INCIDENT	PROTON CURRENT				0.00		
	SECONDARY ELECTRONS				0.00		

```

-----
CYCLE 22  TIME 6.15+00 SECONDS  NET CURRENT -1.52-08 AMPS/M**2  POTENTIAL -1.15+04 VOLTS
CYCLE 23  TIME 6.44+00 SECONDS  POTENTIAL -1.15+04 VOLTS
CYCLE 24  TIME 6.73+00 SECONDS  POTENTIAL -1.15+04 VOLTS
CYCLE 25  TIME 7.03+00 SECONDS  POTENTIAL -1.15+04 VOLTS
CYCLE 26  TIME 7.32+00 SECONDS  POTENTIAL -1.15+04 VOLTS
INCIDENT ELECTRON CURRENT -1.00-05
      SECONDARY ELECTRONS 8.19-06
      BACKSCATTERED ELECTRONS 1.81-06
INCIDENT PROTON CURRENT 0.00
      SECONDARY ELECTRONS 0.00

```

```

-----
CYCLE 27  TIME 7.61+00 SECONDS  NET CURRENT -4.06-10 AMPS/M**2  POTENTIAL -1.15+04 VOLTS
CYCLE 28  TIME 7.90+00 SECONDS  POTENTIAL -1.15+04 VOLTS
CYCLE 29  TIME 8.20+00 SECONDS  POTENTIAL -1.15+04 VOLTS
CYCLE 30  TIME 8.49+00 SECONDS  POTENTIAL -1.15+04 VOLTS
CYCLE 31  TIME 8.78+00 SECONDS  POTENTIAL -1.15+04 VOLTS
INCIDENT ELECTRON CURRENT -1.00-05
      SECONDARY ELECTRONS 8.19-06
      BACKSCATTERED ELECTRONS 1.81-06
INCIDENT PROTON CURRENT 0.00
      SECONDARY ELECTRONS 0.00

```

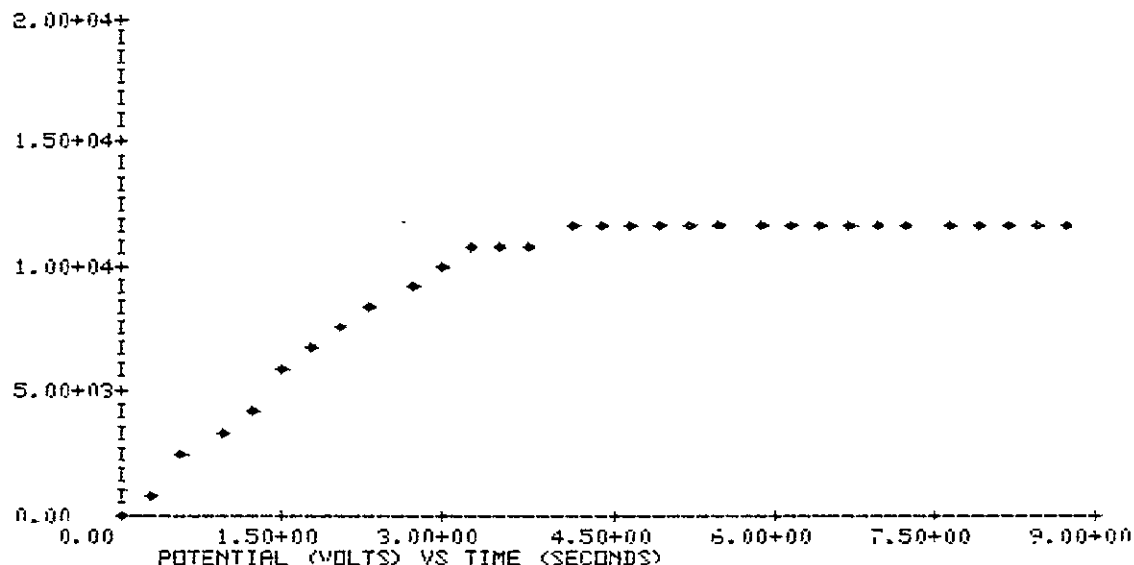
```

-----
NET CURRENT -1.11-11 AMPS/M**2
PRINT A CHARGING TABLE? >YES

```

T (SEC)	V (VOLTS)	I (AMPS/M**2)
0.00	0.00	-7.26-06
5.86-01	-2.34+03	-7.01-06
1.17+00	-4.58+03	-6.67-06
1.76+00	-6.66+03	-6.16-06
2.34+00	-8.51+03	-5.38-06
2.93+00	-9.99+03	-4.14-06
3.51+00	-1.09+04	-2.37-06
4.10+00	-1.13+04	-9.52-07
4.68+00	-1.14+04	-2.65-07
5.27+00	-1.14+04	-6.42-08
5.86+00	-1.15+04	-1.52-08
6.44+00	-1.15+04	-3.57-09
7.03+00	-1.15+04	-8.36-10
7.61+00	-1.15+04	-1.97-10
8.20+00	-1.15+04	-4.62-11
8.78+00	-1.15+04	-1.11-11

PLOT ? >YES



EMISSION FORMULATION IS NORMAL
 SECONDARY EMISSION FORMULATION
 MATERIAL >STOP

>EXIT)

>

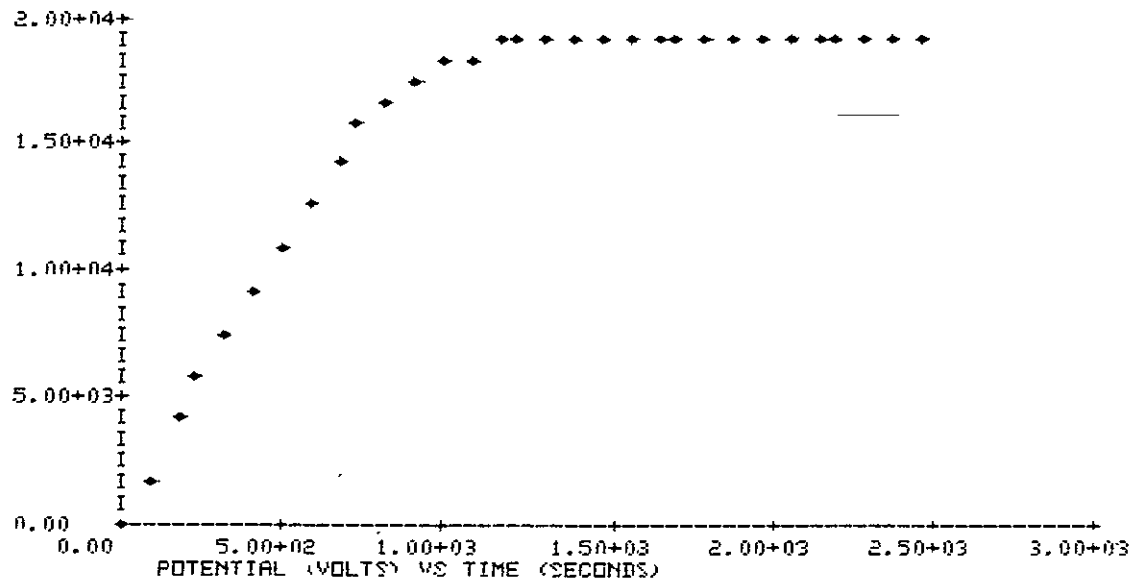
3XOT

WELCOME TO MATCH6 - A MATERIAL CHARGING PROGRAM

```

EMISSION FORMULATION IS ANGLE
SECONDARY EMISSION FORMULATION>
MATERIAL>KAPTON
PRINT >
ENTER FLUX TYPE 1=BEAM 2=MAXWELLIAN >1
BEAM VOLTAGE = 2.0+01 KEV BEAM CURRENT = 1.0-05 AMPS / M**2
NEW PARAMETERS ? >
GENERATE A TABLE ?>
CHARGE ? >YES
FULL PRINT ?>
CYCLE 1 TIME 0.00 SECONDS POTENTIAL 0.00 VOLTS
INCIDENT ELECTRON CURRENT -1.00-05
SECONDARY ELECTRONS 1.88-06
BACKSCATTERED ELECTRONS 5.70-07
INCIDENT PROTON CURRENT 0.00
SECONDARY ELECTRONS 0.00
NET CURRENT -7.55-06 AMPS/M**2
CYCLE 31 TIME 2.46+03 SECONDS POTENTIAL -1.90+04 VOLTS
INCIDENT ELECTRON CURRENT -1.00-05
SECONDARY ELECTRONS 9.63-06
BACKSCATTERED ELECTRONS 1.37-06
INCIDENT PROTON CURRENT 0.00
SECONDARY ELECTRONS 0.00
NET CURRENT -3.71-12 AMPS/M**2
PRINT A CHARGING TABLE? >
PLOT ?>YES

```



```

EMISSION FORMULATION IS ANGLE
SECONDARY EMISSION FORMULATION>
MATERIAL>
PRINT >YES

```

PREPROCESSING OF MATERIAL PROPERTIES

MATERIAL 1: KAPTON

PROPERTY	INPUT VALUE	CODE VALUE
1 DIELECTRIC CONSTANT	3.50+00 (NONE)	3.50+00 (NONE)
2 THICKNESS	1.00-04 METERS	1.00-04 MESH
3 CONDUCTIVITY	1.00-14 MHO/M	1.00-14 MHO/M
4 ATOMIC NUMBER	5.00+00 (NONE)	5.00+00 (NONE)
5 DELTA MAX >CDEFF	2.10+00 (NONE)	3.05+01 (NONE)
6 E-MAX >DEPTH-1	1.50-01 KEV	4.62-02 ANG-01
7 RANGE	-1.00+00 ANG.	7.73+02 ANG.
8 EXPONENT > RANGE	0.00 (NONE)	0.00 ANG.
9 RANGE > EXPONENT	1.42+00 ANG.	1.51+00 (NONE)
10 EXPONENT	9.20+00 (NONE)	1.00+00 (NONE)
11 YIELD FOR 1KEV PROTONS	1.40+00 (NONE)	1.40+00 (NONE)
12 MAX DE/DX FOR PROTONS	7.00+01 KEV	7.00+01 KEV
13 PHOTOCURRENT	2.00-05 A/M-2	2.00-05 A/M-2
14 SURFACE RESISTIVITY	1.40+01 OHMS	1.24-10 V-S/O

CHANGE ANY MATERIAL PROPERTIES>

ENTER FLUX TYPE 1=BEAM 2=MAXWELLIAN >2

TE = 1.0+00 KEV NE = 1.0+06 M-3 TI = 1.0+00 KEV NI = 1.0+06 M-3

NEW PARAMETERS ? >NO

GENERATE A TABLE ?>NO

CHARGE ? >YES

FULL PRINT ?>NO

CYCLE	1	TIME	0.00	SECONDS	POTENTIAL	0.00	VOLTS
INCIDENT ELECTRON CURRENT				-8.46-07			
SECONDARY ELECTRONS				1.24-06			
BACKSCATTERED ELECTRONS				2.32-07			
INCIDENT PROTON CURRENT				1.97-08			
SECONDARY ELECTRONS				7.11-08			

NET CURRENT 7.15-07 AMPS/M-2

FLUX IS POSITIVE - WANT TO STOP? >NO

CYCLE	31	TIME	2.60+00	SECONDS	POTENTIAL	1.48+00	VOLTS
INCIDENT ELECTRON CURRENT				-8.47-07			
SECONDARY ELECTRONS				5.93-07			
BACKSCATTERED ELECTRONS				2.33-07			
INCIDENT PROTON CURRENT				1.97-08			
SECONDARY ELECTRONS				3.40-08			

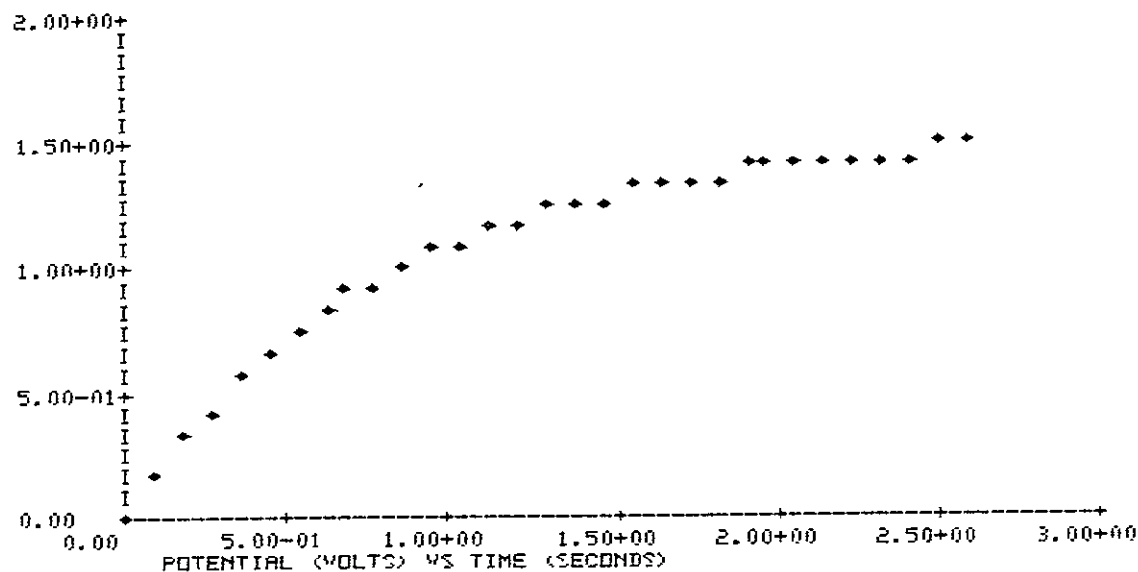
NET CURRENT 3.20-08 AMPS/M-2

PRINT A CHARGING TABLE? >YES

T (SEC)	V (VOLTS)	I (AMPS/M-2)
0.00	0.00	7.15-07
1.73-01	3.17-01	5.23-07
3.46-01	5.55-01	3.98-07
5.20-01	7.40-01	3.10-07
6.93-01	8.86-01	2.47-07
8.66-01	1.00+00	1.99-07
1.04+00	1.10+00	1.62-07
1.21+00	1.18+00	1.33-07
1.39+00	1.24+00	1.10-07
1.56+00	1.30+00	9.11-08
1.73+00	1.34+00	7.60-08
1.91+00	1.38+00	6.37-08
2.08+00	1.41+00	5.34-08
2.25+00	1.43+00	4.50-08
2.43+00	1.46+00	3.79-08
2.60+00	1.48+00	3.20-08

PLOT >>YES

ORIGINAL PAGE IS
OF POOR QUALITY



```

EMISSION FORMULATION IS ANGLE
SECONDARY EMISSION FORMULATION>
MATERIAL>
PRINT >
ENTER FLUX TYPE 1=BEAM 2=MAXWELLIAN >
TE = 1.0+00 KEV NE = 1.0+06 M-3 TI = 1.0+00 KEV NI = 1.0+06 M-3
NEW PARAMETERS ? >
GENERATE A TABLE ?>
CHARGE ? >YES
FULL PRINT ?>

```

CYCLE	1	TIME	0.00	SECONDS	POTENTIAL	0.00	VOLTS
INCIDENT	ELECTRON CURRENT				-8.46-07		
	SECONDARY ELECTRONS				1.24-06		
	BACKSCATTERED ELECTRONS				2.32-07		
INCIDENT	PROTON CURRENT				1.97-08		
	SECONDARY ELECTRONS				7.11-08		

```

NET CURRENT 7.15-07 AMPS<M++2
FLUX IS POSITIVE - WANT TO STOP? >YES

```

```

EMISSION FORMULATION IS ANGLE
SECONDARY EMISSION FORMULATION>NORMAL
EMISSION FORMULATION IS NORMAL
MATERIAL>
PRINT >
ENTER FLUX TYPE 1=BEAM 2=MAXWELLIAN >
TE = 1.0+00 KEV NE = 1.0+06 M-3 TI = 1.0+00 KEV NI = 1.0+06 M-3
NEW PARAMETERS ? >
GENERATE A TABLE ?>
CHARGE ? >YES
FULL PRINT ?>

```

CYCLE	1	TIME	0.00	SECONDS	POTENTIAL	0.00	VOLTS
INCIDENT	ELECTRON CURRENT				-8.46-07		
	SECONDARY ELECTRONS				6.44-07		
	BACKSCATTERED ELECTRONS				2.32-07		
INCIDENT	PROTON CURRENT				1.97-08		
	SECONDARY ELECTRONS				3.56-08		

```

NET CURRENT 9.58-08 AMPS/M**2
FLUX IS POSITIVE - WANT TO STOP? >YES
EMISSION FORMULATION IS NORMAL
SECONDARY EMISSION FORMULATION>
MATERIAL>
PRINT >
ENTER FLUX TYPE 1=BEAM 2=MAXWELLIAN >
TE = 1.0+00 KEV NE = 1.0+06 M-3 TI = 1.0+00 KEV NI = 1.0+06 M-3
NEW PARAMETERS ? >YES
TE (KEV) >5
NE (M**3) >
TI (KEV) >5
NI (M**3) >
TE = 5.0+00 KEV NE = 1.0+06 M-3 TI = 5.0+00 KEV NI = 1.0+06 M-3
GENERATE A TABLE ?>
CHARGE ? >YES
FULL PRINT ?>

```

```

CYCLE 1 TIME 0.00 SECONDS POTENTIAL 0.00 VOLTS
INCIDENT ELECTRON CURRENT -1.89-06
SECONDARY ELECTRONS 5.40-07
BACKSCATTERED ELECTRONS 4.24-07
INCIDENT PROTON CURRENT 4.41-08
SECONDARY ELECTRONS 1.58-07

```

```

NET CURRENT -6.25-07 AMPS/M**2
CYCLE 31 TIME 7.43+03 SECONDS POTENTIAL -3.68+03 VOLTS
INCIDENT ELECTRON CURRENT -9.07-07
SECONDARY ELECTRONS 3.07-07
BACKSCATTERED ELECTRONS 2.03-07
INCIDENT PROTON CURRENT 7.66-08
SECONDARY ELECTRONS 2.98-07

```

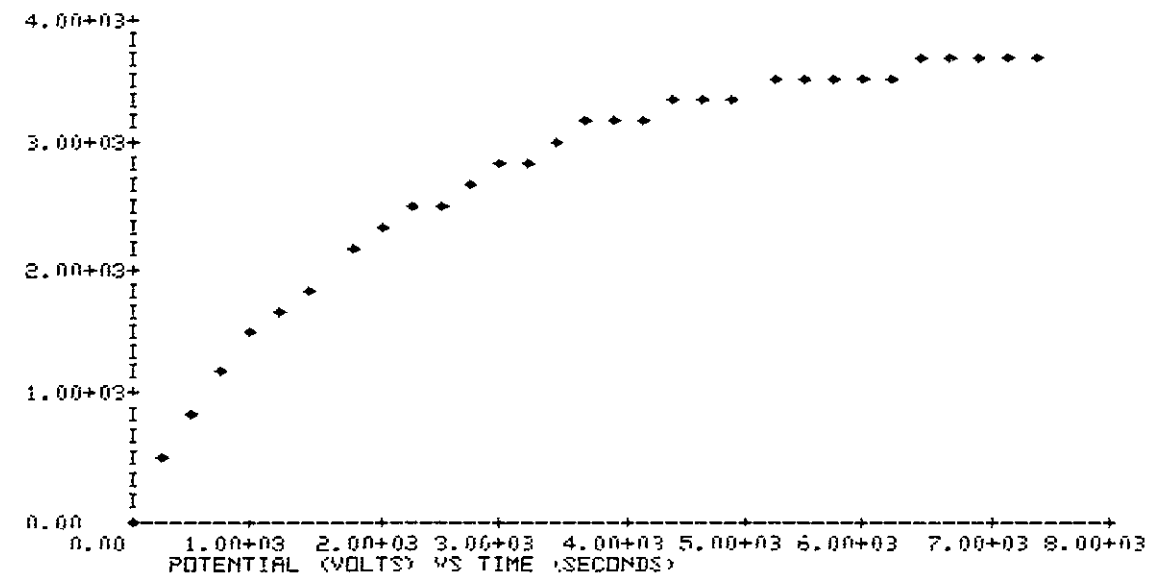
```

NET CURRENT -2.22-08 AMPS/M**2
PRINT A CHARGING TABLE? >YES

```

T (SEC)	V (VOLTS)	I (AMPS/M**2)
0.00	0.00	-6.25-07
4.95+02	-3.06+02	-4.68-07
9.90+02	-1.42+03	-3.59-07
1.49+03	-1.90+03	-2.90-07
1.98+03	-2.27+03	-2.21-07
2.48+03	-2.57+03	-1.76-07
2.97+03	-2.91+03	-1.41-07
3.47+03	-3.00+03	-1.14-07
3.96+03	-3.16+03	-9.21-08
4.46+03	-3.28+03	-7.48-08
4.95+03	-3.39+03	-6.08-08
5.45+03	-3.47+03	-4.96-08
5.94+03	-3.54+03	-4.05-08
6.44+03	-3.59+03	-3.31-08
6.93+03	-3.64+03	-2.71-08
7.43+03	-3.68+03	-2.22-08

PLOT ?>YES



```

EMISSION FORMULATION IS NORMAL
SECONDARY EMISSION FORMULATION>ANGLE
EMISSION FORMULATION IS ANGLE
MATERIAL/
PRINT >
ENTER FLUX TYPE 1=BEAM 2=MAXWELLIAN >
TE = 5.0+00 KEV NE = 1.0+06 M-3 TI = 5.0+00 KEV NI = 1.0+06 M-3
NEW PARAMETERS ? >
GENERATE A TABLE ?>
CHARGE ? >YES
FULL PRINT ?>

```

CYCLE	1	TIME	0.00	SECONDS	POTENTIAL	0.00	VOLTS
INCIDENT	ELECTRON CURRENT			-1.89-06			
	SECONDARY ELECTRONS			1.28-06			
	BACKSCATTERED ELECTRONS			4.24-07			
INCIDENT	PROTON CURRENT			4.41-08			
	SECONDARY ELECTRONS			3.16-07			

```

NET CURRENT 1.69-07 AMPS/M**2
FLUX IS POSITIVE - WANT TO STOP? >YES
EMISSION FORMULATION IS ANGLE
SECONDARY EMISSION FORMULATION>
MATERIAL>STOP

```

```

(EXIT)
>

```

FIN

```

PUNID: B48 ACCT: 11073-00 PROJECT: KATZ-I
TIME: TOTAL: 00:00:12.041 CBSECS: 000000323
CPU: 00:00:02.573 I/O: 00:00:01.409
CD/EP: 00:00:08.059 WAIT: 00:27:56.287

3UAS USED: 0.0419
IMAGES READ: 141 PAGES: 21
START: 09:14:14 JUL 13,1978 FIN: 09:42:29 JUL 13,1978
♦TERMINAL INACTIVE♦
;

```


15. CDC 6600 CONVERSION

Two versions of NASCAP were converted to run on the CDC 6600 machine. A version without booms, subdivision, emitters, or detectors was converted in April 1978. The up-to-date version was converted in October 1978.

The task was completed in three stages. First, a machine independent set of NASCAP subroutines was created. Second, new versions of all machine dependent subroutines were created for the 6600. Third, the complete set of subroutines was loaded and executed on the 6600.

15.1 MACHINE INDEPENDENT SUBROUTINES

FORTRAN IV Extended Version on the CDC 6600 differs from FORTRAN V on UNIVAC machines in several ways. The most significant differences for the purpose of this conversion were:

1. Non-executable Statements -- order of these is ignored by UNIVAC, significant on CDC. Octal DATA statements also differ.
2. PARAMETER Statements -- used heavily in NASCAP, not allowed on CDC.
3. Bit Manipulation -- FLD in FORTRAN V, replaced by SHIFT and MASK on CDC.
4. Data Transfer -- different commands for efficient file communication.
5. Graphics Routines -- totally different graphics packages.
6. Different machine word lengths.

Our aim was to produce subroutine versions which were not affected by differences 1-6, for as many subroutines as possible. Differences 1 and 2 were easily handled in all

subroutines. We rearranged the order of statements and replaced all parameter variables with their current values.

Differences 3, 4, and 5 were handled by the introduction of a new "layer" of subroutines. Bit manipulation (difference 3) occurs in several dozen subroutines. Rather than make duplicate versions of these by replacing FLD with SHIFT and MASK, we created two new subroutines KBITS and SETBTS. We replaced each FLD bit manipulation with an equivalent call to KBITS or SETBTS. Now, any of the several dozen subroutines will run on either machines. We have duplicate versions of KBITS and SETBTS which use the UNIVAC or the CDC bit manipulation commands. Similarly, file input and output (difference 4) are handled by routines MOVDAT and CELLIO. All graphics routines (difference 5) now refer to a set of seven basic subroutines which are machine dependent.

Difference 6 was more stubborn. In many places it seemed awkward to try to use the above technique. We had to settle for making some machine dependent subroutines by changing "10A6" formats to "6A10" formats.

15.2 MACHINE DEPENDENT SUBROUTINES

After granting independence to as many NASCAP subroutines as possible, we were left with about forty machine dependent subroutines. Most of them fall into the following categories:

1. "Extra layer" routines, as described in Section 15.1.
2. Routines with "6A10" changed to "10A6".
3. Local system routines.
4. A few routines with UNIVAC compiler commands.

It was a straightforward process to rewrite these for the CDC 6600.

15.3 LOAD AND EXECUTE

Loading of NASCAP on the 6600 required a new program segmentation to be devised. Execution naturally exposed a few oversights in the earlier phases of the process. However, both were accomplished without encountering particular problems. No unusual solutions were employed.

16. SCATHA CHARGING ANALYSIS

Chapter 16 is a verbatim reproduction of a paper given at the 1978 USAF/NASA Spacecraft Charging Technology Conference. This paper is a clear summary of the SCATHA model analysis which was performed using NASCAP.

CHARGING ANALYSIS OF THE SCATHA SATELLITE*

G. W. Schnuelle, D. E. Parks, I. Katz,
M. J. Mandell, P. G. Steen, J. J. Cassidy
Systems, Science and Software

A. Rubin
Air Force Geophysics Laboratory

ABSTRACT

We describe here a detailed model of the geometrical, material, and electrical properties of the SCATHA satellite for use with the NASA Charging Analyzer Program (NASCAP). Charging calculations in an intense magnetospheric substorm environment demonstrate that: (1) long booms can significantly perturb the potentials near the spacecraft, and (2) discharging by sunlight or by active control can cause serious time-dependent differential charging problems.

1. INTRODUCTION

We have developed a detailed model of the SCATHA satellite for use with the NASA Charging Analyzer Program (NASCAP).^[1,2] The model accounts for such geometrical complexities as booms, shadowing, and the presence of insulating materials over portions of the conducting ground of the space vehicle. The effects of photoemission and secondary emission caused by electron and ion impact, active control devices such as electron and ion beams, and surface and bulk conductivity are included in the model. To our knowledge, this model represents the most complete and realistic treatment of spacecraft charging attempted to date for any satellite.

Section 2 below describes the SCATHA model employed in NASCAP. A detailed shadowing study was performed for a geometrically more accurate SCATHA model; this work is described in Section 3. We have performed charging calculations for one

* This work supported by the National Aeronautics and Space Administration, Lewis Research Center, under Contract NAS3-21050.

environment using the present model, and the results of these calculations are described in Section 4. Preliminary conclusions of this study are summarized in Section 5.

2. SCATHA MODEL DEVELOPMENT

The NASCAP program allows the specification of the geometrical, material, and electrical properties of a spacecraft in considerable detail. We have attempted to incorporate the most current and complete information available for SCATHA into our model. However, the present model is meant primarily to illustrate the intended level and scope of our study, rather than to provide the final word on a model specification. The NASCAP code allows model features to be easily altered to make our model a more faithful representation of the SCATHA satellite if the need arises.

Perspective views of our gridded model are shown in Figures 1 and 2. The main body of the satellite is represented as a right octagonal cylinder, with the aft cavity visible in Figure 2. The OMNI antenna and the SC9 cluster of experiments are visible on the forward surface of the satellite. Our model reproduces the actual SCATHA geometrical features extremely well, as shown in Table 1. Note in particular that the treatment of booms in NASCAP allows the actual boom radii to be reproduced exactly in the model. The requirements in NASCAP that booms parallel coordinate axes and intercept mesh points in all grids effectively force any long booms to pass through the center of the innermost mesh. Therefore, our present model includes only the SC6, SC11, and the two SC2 booms, with the orientations fixed at right angles to one another.

Figure 3 illustrates the computational space in which NASCAP solves Poisson's equation for this model. Monopole boundary conditions are imposed on the edges of the outermost grid, which is a rectangular prism of dimensions $1.6 \times 1.6 \times 3.2$ m. The zone size decreases by a factor of 2 in each of the four

successive inner grids, so that the effective resolution is 11.5 cm near the satellite body. (Local mesh refinement techniques in NASCAP allow a resolution of 2.5 cm for selected zones on the satellite.)

Our model includes the specification of 15 distinct exposed surface materials, each of which is specified by the values of some 13 user-supplied parameters. The surface materials are described in Table 2. We have attempted to find experimentally measured values for all parameters; where this has not been possible, suitable estimates based on the properties of similar materials have been used. Table 3 lists the values employed in the calculations reported here. The analytical expressions in which these parameters are used to evaluate net surface currents are described in detail in Reference 5. The formulation of electron backscattering in NASCAP has been somewhat modified recently, and the newer treatment is described in Appendix A. The exposed materials are illustrated in Figure 4 in which the locations of several of the SCATHA experiments are also shown. Experiments at the ends of SCATHA booms are modeled as a single boom segment whose radius is adjusted to match the exposed surface area of the actual experiment.

The model includes six distinct underlying conductors: spacecraft ground, the reference band, and the four experiments SC2-1, SC2-2, SC6-1 and SC6-2. Each of these underlying conductors is capacitively coupled to spacecraft ground, and each can be separately biased with respect to ground. A seventh conductor could be introduced to underlay the solar cells at an appropriate bias. In this study the reference band was allowed to float and all other conductors were biased to the ground potential.

NASCAP has extensive capabilities to model particle emitters and detectors located on the spacecraft body, as described previously (Reference 2). These features of NASCAP can be used in the analysis of the operation of, for example, the SCATHA

experiments SC4, SC5, SC6, SC7, and SC9. Such studies should be particularly helpful in determining the influence of spacecraft fields on particles emitted during active control, and in determining the source of particles seen at detector sites.

3. SHADOWING STUDY

For the SCATHA shadowing study, we were required to generate percent shadowing tables for various experiments. We were able to generate accurate tables using relatively small amounts of computer time: less than 5 minutes Univac 1100/81 time was required for a table of 7560 entries.

Since the geometrical capabilities of the NASCAP shadowing routines are more general than the rest of the code, we were able to employ a SCATHA model for shadowing in which each experiment was treated geometrically in much finer detail than in the model described in Section 2. Figure 5 shows the level of detail in a perspective view of the ML12-7 experiments on the forward surface. Booms were placed at their actual locations on the satellite, and the experiments at the boom ends were given a great deal of geometrical complexity. Figure 6 shows the SC2-1, SC1-4, and SC6-1 booms as they were resolved in the shadowing study.

These detailed geometrical shapes were input to the usual NASCAP shadowing routines (HIDCEL) for table generation. The tables cover satellite rotation in 1° increments for the satellite plane deviations from the sun line of -5° to $+5^\circ$.

4. CHARGING CALCULATIONS

The model was subjected to an extremely intense substorm described by a superposition of two Maxwellian plasmas with the following parameters:

$$\begin{array}{ll}
\theta_{e1} = 40,000 \text{ eV} & \theta_{e2} = 100 \text{ eV} \\
\theta_{i1} = 20,000 \text{ eV} & \theta_{i2} = 100 \text{ eV} \\
n_{e1} = 10 \text{ cm}^{-3} & n_{e2} = 10 \text{ cm}^{-3} \\
n_{i1} = 10 \text{ cm}^{-3} & n_{i2} = 10 \text{ cm}^{-3}
\end{array}$$

The effects of ambient space charge were neglected in the solution of Poisson's equation here, since the mean satellite radius, r_s , is much smaller than the plasma Debye length, λ_D .

$$\begin{array}{l}
r_s \sim 100 \text{ cm} \\
\lambda_D \sim 700 \sqrt{\frac{\theta}{n_e}} \sim 2200 \text{ cm} \\
r_s/\lambda_D \sim 0.05
\end{array}$$

There was no sunlight present in the first calculation described below.

Potential contours during the initial overall charging phase ($\sim 10^{-3}$ seconds) are shown in Figures 7 and 8. The question of whether booms have a significant effect on the sheath potentials is clearly answered by examining Figure 9, which shows potential contours in a plane a half meter below the plane of the booms. Figure 10 shows similar contours in a calculation with the booms omitted; the distortion of contours by the booms is obvious. While the boom radii are small, ~ 2 cm, the effect on potentials is related to the boom capacitance, which varies only logarithmically with radius. This results in long range potential interactions from thin booms, where the characteristic decay distance is closer to the boom length than to the boom radius.

The rapid initial charging is followed by a much slower development of differential charging, as illustrated in Figure 11. For this example the maximum differential developed after 22 seconds was 700 volts and the maximum field strength

in a dielectric layer was 24,000 volts/cm. Figure 12 shows contours in the plane of the booms after 22 seconds; note the differential charging developed at the boom ends due to variations in the material properties between the experiments and the boom coatings.

The two Maxwellian description of the plasma leads to a low overall charging voltage of only -7.3 keV despite the presence of a plasma component with an electron temperature of 40 keV. For the particular case we have studied here, low energy protons are being collected at an enormous rate and these, augmented by the secondary electrons they produce, balance the incident electron current. NASCAP uses a proton collection model in which the collection increases linearly with voltage, which is valid in the present case where r_s/λ_D is small, as discussed by Laframboise.^[4] Table 4 shows the detailed current balance near equilibrium for the boom surface material in the presence of the double Maxwellian environment described above. Also shown in Table 4 is a similar breakdown for the same material subjected only to the high energy single Maxwellian component. The equilibrium potential is -32 keV in this case, indicating that the final potentials reached would have been much lower had we employed a single Maxwellian plasma model. For both plasma models, the final potentials reached will depend on the exact values employed for the proton and electron induced secondary yields. Great care should be exercised in the determination of the values and associated error estimates for parameters which affect the production of secondary electrons in these and similar calculations.

Finally, the atomic number dependence of backscatter coefficients tends to make high-Z materials charge less negatively than other elements. For SCATHA, this means that the magnitude of the boom potentials will be significantly lower than most other surfaces, since exposed platinum constitutes much of its surface area.

We have performed a similar calculation on this model in which the sunlight was turned on after 22 seconds of charging in eclipse. The photoemission results in strong differential charging (~ 3 keV) along the booms, as shown in Figure 13. In our model the boom surfaces are very weakly capacitively coupled to the grounded cable shields which extend the length of the booms, while the experiments at the ends of the SC2 and SC6 booms are coupled closely to spacecraft ground. This weak coupling has the effect of allowing the booms to react rapidly to environmental perturbations compared to the rest of the satellite, leading to temporary conditions of high differential charging. We have observed similar effects when discharging the satellite with an electron gun.

The potentials near the satellite in sunlight are dominated by the monopole field of the spacecraft body. A photoemitting boom surface element can discharge only to the value of the local monopole potential, since further discharge is limited by immediate reflection of photoelectrons. This has the amazing consequence that the booms, strongly perturbing in eclipse, now seem to disappear in the potential contours near the satellite body. Note that significant differential charging in sunlight along the SC2 booms will certainly persist at equilibrium due to large differences between the photoemission from surfaces on booms and on the SC2-1 and SC2-2 experiments. Our calculations neglect any effective surface conductivity parallel to the booms due to the presence of a photosheath. The surface conductivity features of NASCAP could easily be invoked to simulate this effect, which would reduce the magnitude of the differential charging observed here.

The calculations reported here were performed on the UNIVAC 1100/81 computer at Systems, Science and Software. Each cycle of charging and solution of the potential equations

required approximately 15 minutes CPU time during differential charging, and 5 minutes CPU time when no differential charging occurred. Approximately 10 cycles of each type were required for the calculations reported here. We have developed a second SCATHA model for testing purposes in which the zone size is twice that of the model presented here and the booms are shortened; computer times are reduced by roughly 80 percent for this model, and all of the results described above can be observed in calculations using the smaller model. The half-scale model will be useful whenever fine resolution on the satellite surfaces is not required.

5. CONCLUSIONS

We have completed the development of a detailed model of the SCATHA satellite. Preliminary results from calculations in one magnetospheric environment indicate that:

- The presence of a low energy component in a two Maxwellian description of the magnetospheric environment reduces the maximum charging of a satellite relative to that found for a single Maxwellian.
- The booms have substantial impact on potentials near the spacecraft in eclipse.
- The use of high atomic number coatings, such as platinum on the booms, may increase the severity of differential charging.
- Discharging by sunlight or by active control may lead to transient increases in differential charging along the booms due to the weak coupling of the booms to spacecraft ground.

Our calculations demonstrate that the prediction of spacecraft potentials for SCATHA is an exceedingly complex problem, in which the full capabilities of the NASCAP treatment of geometrical features, material properties, and dynamic interaction with the environment are utilized. We plan to continue this study of SCATHA using NASCAP with particular emphasis on boom perturbations and the effects of active control.

APPENDIX A. ELECTRON BACKSCATTER

Electron backscatter is modeled in NASCAP as a function of electron energy and mean atomic number of backscattering material. The formulation first used in NASCAP^[5] was valid only for low Z-materials. To remove this restriction we have used a formula of Burke^[6] to obtain the backscatter coefficient for isotropically incident electrons as

$$\eta_1 = 0.475 Z^{0.177} - 0.40 . \quad (A1)$$

The backscatter coefficient for normal incidence, η_0 , is then found by solving the equation

$$\eta_1 = 2[1 - \eta_0(1 - \ln \eta_0)] / (\ln \eta_0)^2 \quad (A2)$$

which comes from assuming the angular dependent backscatter coefficient^[7] to be

$$\eta(\theta) = \eta_0 \exp[-(\ln \eta_0) (1 - \cos\theta)] . \quad (A3)$$

The energy dependence^[4] is then taken to be

$$\eta_0(\epsilon) = \gamma(\epsilon) (\eta_0 + 0.1 \exp(-\epsilon/5)) \quad (A4)$$

$$\gamma(\epsilon) = \begin{cases} 0 & \epsilon < 50 \text{ eV} \\ \ln(20 \epsilon) / \ln 20 & 50 \text{ eV} < \epsilon < 1 \text{ keV} \\ 1 & \epsilon > 1 \text{ keV} \end{cases}$$

where ϵ is in keV.

The energy dependent η_0 from (A4) is then used in (A2) or (A3) to calculate the relevant backscatter coefficient.

REFERENCES

1. Katz, I., Parks, D. E., Mandell, M. J., Harvey, J. M. and Wang, S. S., "NASCAP, A Three-Dimensional Charging Analyzer Program for Complex Spacecraft," IEEE Transactions on Nuclear Science, 6, 1977, p. 2276.
2. Katz, I., Cassidy, J. J., Mandell, M. J., Schnuelle, G. W., Steen, P. G. and Roche, J. C., "The Capabilities of the NASA Charging Analyzer Program," paper presented at USAF/NASA Spacecraft Charging Technology Conference, 31 October - 2 November 1978.
3. Steen, P. G., "SCATHA Experiment Shadowing Study," Systems, Science and Software Topical Report SSS-R-78-3658, May 1978.
4. Laframboise, J. G., UTIAS Report No. 100, 1966.
5. Katz, I., Parks, D. E., Mandell, M. J., Harvey, J. M., Brownell, Jr., D. H., Wang, S. S. and Rotenberg, M., "A Three-Dimensional Dynamic Study of Electrostatic Charging in Materials," NASA-CR-135256, August 1977.
6. Burke, E. A., "Soft X-ray Induced Electron Emission," IEEE Transactions on Nuclear Science, NS-24, 1977, pp. 2505-2509.
7. Darlington, E. H. and Cosslett, V. E., "Backscattering of 0.5-10 keV Electrons from Solid Targets," J. Phys. D5, 1972, p. 1969.

Table 1. Comparison of Actual SCATHA Geometrical Features to Gridded NASCAP Model

Zone Size = 4.53 in. (11.5 cm)

	<u>SCATHA</u>	<u>MODEL</u>
Radius	33.6 inches	32.0 inches
Height	68.7	68.0
Solar Array Height	29	27.2
Bellyband Height	11.3	13.6
SC9-1 Experiment	$9.2 \times 6 \times 8$	$9.1 \times 4.5 \times 9.1$
SC6-1 Boom	1.7 (radius)	1.7
	118 (length)	113.2
Surface Area	2.16×10^4 sq. in.	2.11×10^4 sq. in.
Solar Array Area	1.23×10^4	1.15×10^4
Forward Surface Area	0.36×10^4	0.34×10^4

Table 2. Exposed Surface Materials

GOLD:	gold plate
SOLAR:	solar cells, coated fused silica
WHITEN:	non-conducting white paint (STM K792)
SCREEN:	SC5 screen material, a conducting fictitious material which absorbs but does not emit charged particles
YELLOWC:	conducting yellow paint
GOLDPD:	88 percent gold plate with 12 percent conductive black paint (STM K748) in a polka dot pattern
BLACKC:	conductive black paint (STM K748)
KAPTON:	kapton
SIO2:	SiO ₂ fabric
TEFLON:	teflon
INDOX:	indium oxide
YGOLDC:	conducting yellow paint (50 percent) gold (50 percent)
ML12:	ML12-3 and ML12-4 surface, a fictitious material whose properties are an average of the properties of the several materials on the ML12 surfaces
ALUM:	aluminum plate
BOOMAT:	platinum banded kapton

Table 3. Material Properties for Exposed Surfaces^a

Property ^b	GOLD	SOLAR	WHITEN	SCREEN	BLACKC YELOWC	GOLDPD	KAPTON
1	-	4.00+00	3.50+00	-	3.50+00	-	3.50+00
2	1.00-03	1.79-04	5.00-05	1.00-03	5.00-05	1.00-03	1.25-04
3	∞	1.00-14	5.90-14	∞	5.00-10	∞	1.00-14
4	7.90+01	1.00+01	5.00+00	1.00+00	5.00+00	7.01+01	5.00+00
5	8.80-01	4.10+00	2.10+00	0.00	2.10+00	1.03+00	2.10+00
6	8.00-01	4.10-01	1.50-01	1.00+00	1.50-01	7.20-01	1.50-01
7	8.30+01	-1.00+00	-1.00+00	1.00+01	-1.00+00	8.30+01	-1.00+00
8	1.63+00	0.00	0.00	1.50+00	0.00	1.63+00	0.00
9	3.46+01	2.30+00	1.05+00	0.00	1.05+00	3.46+01	1.42+00
10	7.00-01	2.08+01	9.80+00	1.00+00	9.80+00	7.00-01	9.80+00
11	4.00-01	1.36+00	1.40+00	0.00	1.40+00	4.00-01	1.40+00
12	5.00+01	4.00+01	7.00+01	1.00+00	7.00+01	5.00+01	7.00+01
13	2.90-05	2.00-05	2.00-05	0.00	2.00-05	2.90-05	2.00-05
	SIO2	TEFLON	INDOX	YGOLDC	ALUMIN	BOOMAT ^c	ML12
1	4.00+00	2.00+00	-	-	-	2.00+00	-
2	2.75-04	1.25-04	1.00-03	1.00-03	1.00-03	5.00-03	1.00-03
3	2.75-12	1.00-14	∞	∞	∞	1.00-10	∞
4	1.00+01	1.00+01	2.44+01	4.20+01	1.30+01	6.34+01	6.00+00
5	2.40+00	3.00+00	1.40+00	1.49+00	9.70-01	1.86+00	1.00+00
6	4.00-01	3.00-01	8.00-01	4.80-01	3.00-01	5.90-01	3.00-01
7	-1.00+00	-1.00+00	-1.00+00	-1.00+00	2.60+02	8.30+01	-1.00+00
8	0.00	0.00	0.00	0.00	1.30+00	1.63+00	0.00
9	1.02+00	2.00+00	7.18+00	1.02+01	2.40+02	3.46+01	2.00+00
10	2.00+01	1.67+01	5.55+01	4.20+01	1.73+00	7.00-01	1.20+01
11	1.40+00	1.40+00	1.36+00	1.00+00	1.36+00	4.00-01	1.40+00
12	7.00+01	7.00+01	4.00+01	6.00+01	4.00+01	5.00+01	7.00+01
13	2.00-05	2.00-05	3.20-05	2.40-05	4.00-05	2.72-05	2.10-05

Table 3. (Continued)

^aThe materials are described in Table 2.

^bThe thirteen properties are as follows (see Reference 4 and Appendix A for further details):

Property 1:	Relative dielectric constant for insulators (dimensionless).
Property 2:	Thickness of dielectric film or vacuum gap (meters).
Property 3:	Electrical conductivity (mho/m). The value ∞ indicates a vacuum gap over a conducting surface.
Property 4:	Atomic number (dimensionless).
Property 5:	Maximum secondary electron yield for electron impact at normal incidence (dimensionless).
Property 6:	Primary electron energy to produce maximum yield at normal incidence (keV).
Properties 7-10:	Range for incident electrons. <u>Either</u> : $\text{Range} = P_7 E^{P_8} + P_9 E^{P_{10}}$ <p>where the range is in angstroms and for the energy in keV,</p> <p><u>or</u></p> <p>$P_7 = -1$. to indicate use of an empirical range formula</p> <p>$P_9 = \text{density (g/cm}^3\text{)}$</p> <p>$P_{10} = \text{mean atomic weight (dimensionless)}$.</p>
Property 11:	Secondary electron yield for normally incident 1 keV protons.
Property 12:	Proton energy to produce maximum secondary electron yield (keV).
Property 13:	Photoelectron yield for normally incident sunlight (A/m ²).

^cThe dielectric constant and thickness for the boom surfaces were chosen to reflect the effective capacitance to the underlying cable shield.

Table 4. Components of Incident and Emitted Currents (10^{-5} A/m²) for Boom Surface Material Near Steady State.

	<u>Double Maxwellian</u>	<u>Single Maxwellian</u>
Potential	-7000 Volts	-32,000 Volts
Incident Electrons	-4.6	-2.3
Resulting Backscatter	2.7	1.4
Resulting Secondaries	.7	.4
Incident Protons	.6	.2
Resulting Secondaries	.6	.3

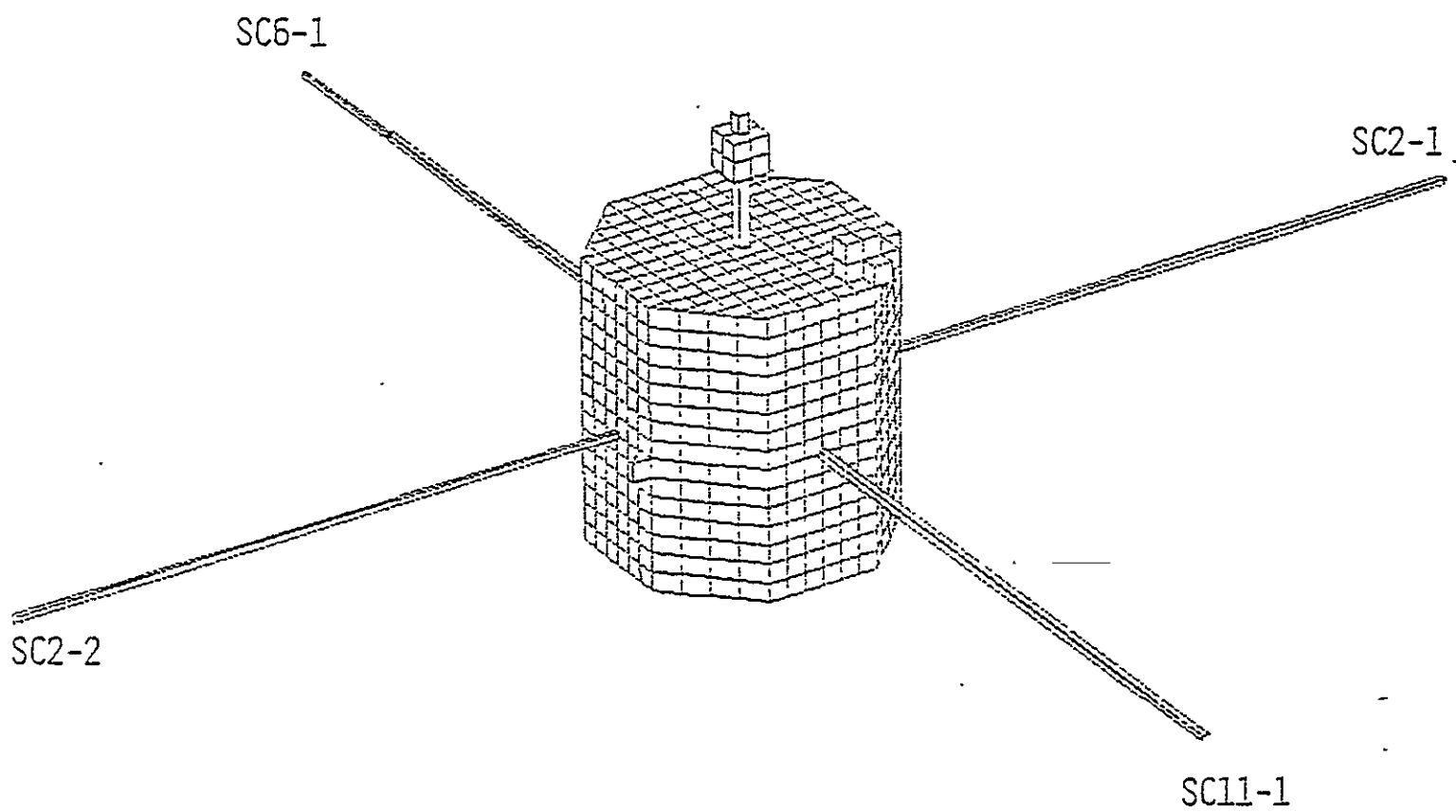


Figure 1. SCATHA model: side view. The 50 m antenna and the SC1-4 boom are not included in this model.

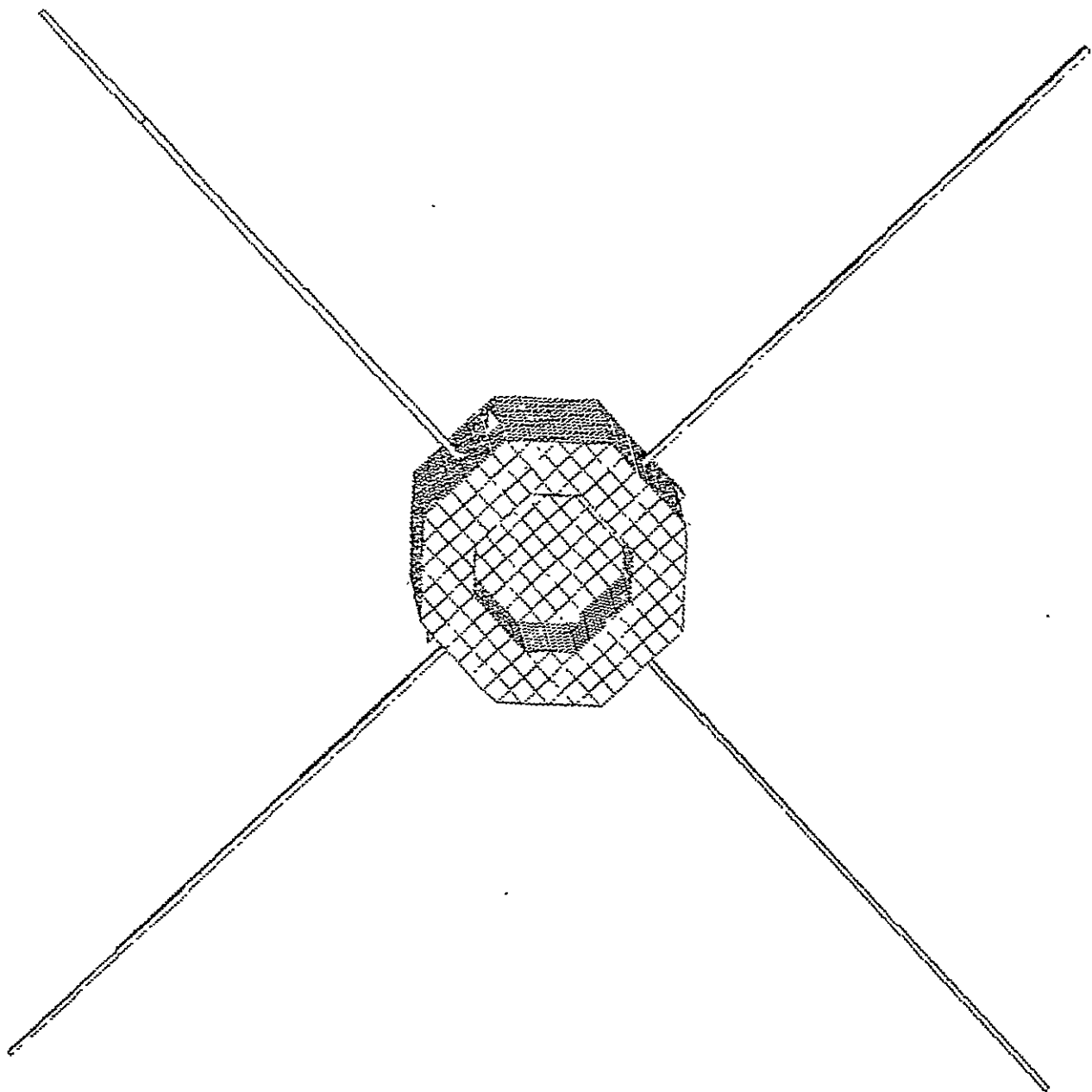


Figure 2. SCATHA model: bottom view with aft cavity visible.

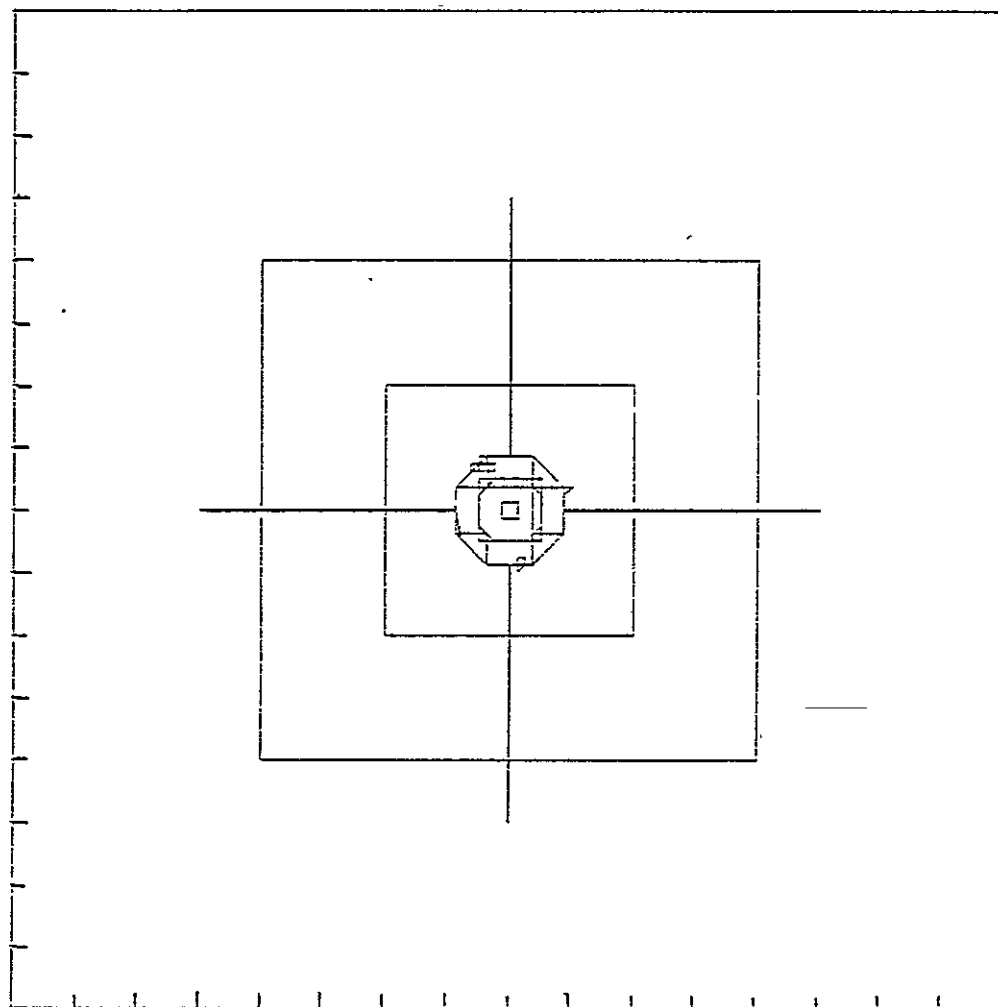


Figure 3. Computational space surrounding the SCATHA model, showing the nesting of the grids. The tic marks along the axes indicate the outer grid zone size; the zone size decreases by a factor of two in successive grids.

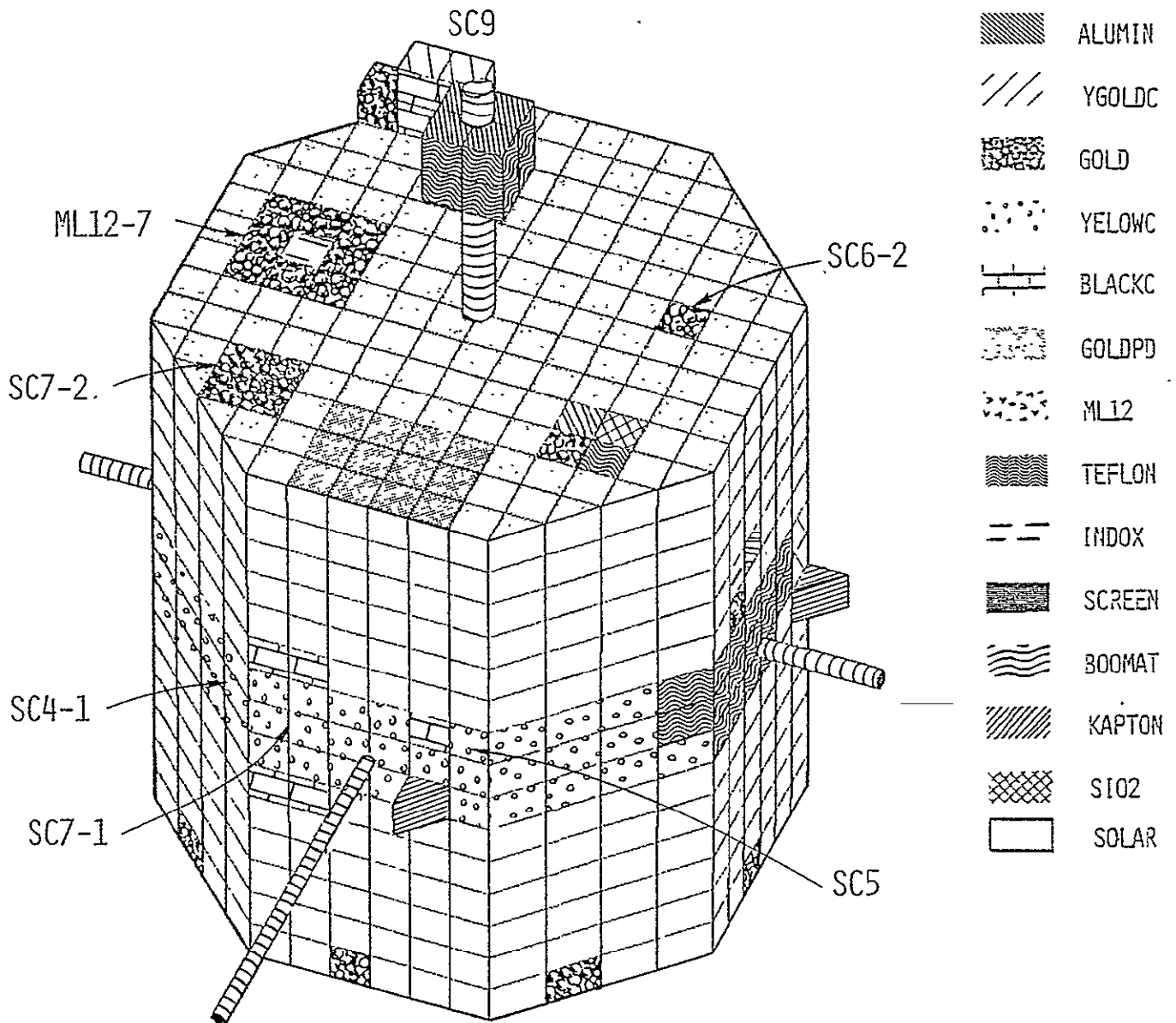


Figure 4a. SCATHA model with exposed surface materials illustrated.

ORIGINAL PAGE IS
OF POOR QUALITY

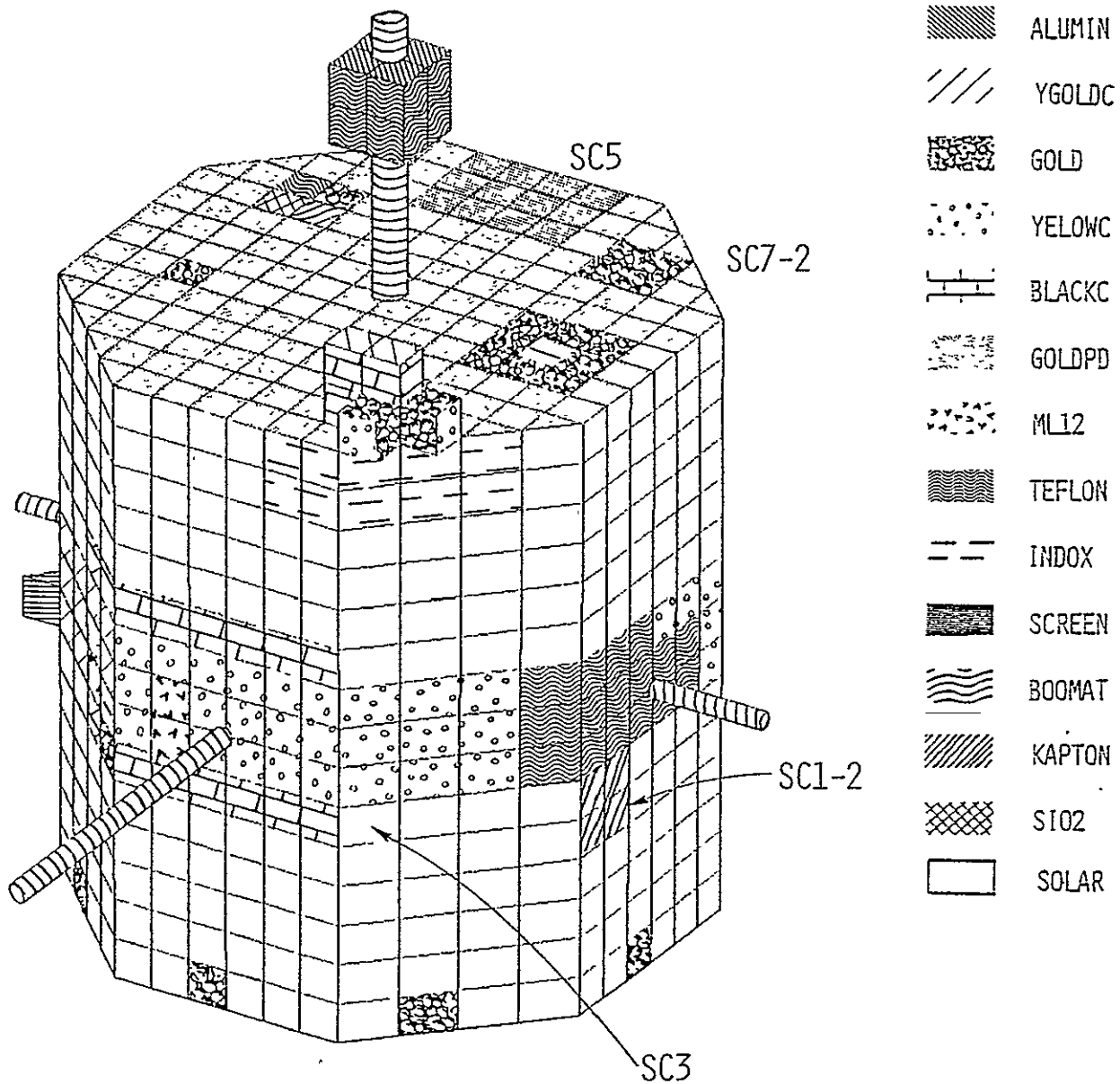


Figure 4b. SCATHA model with exposed surface materials illustrated.

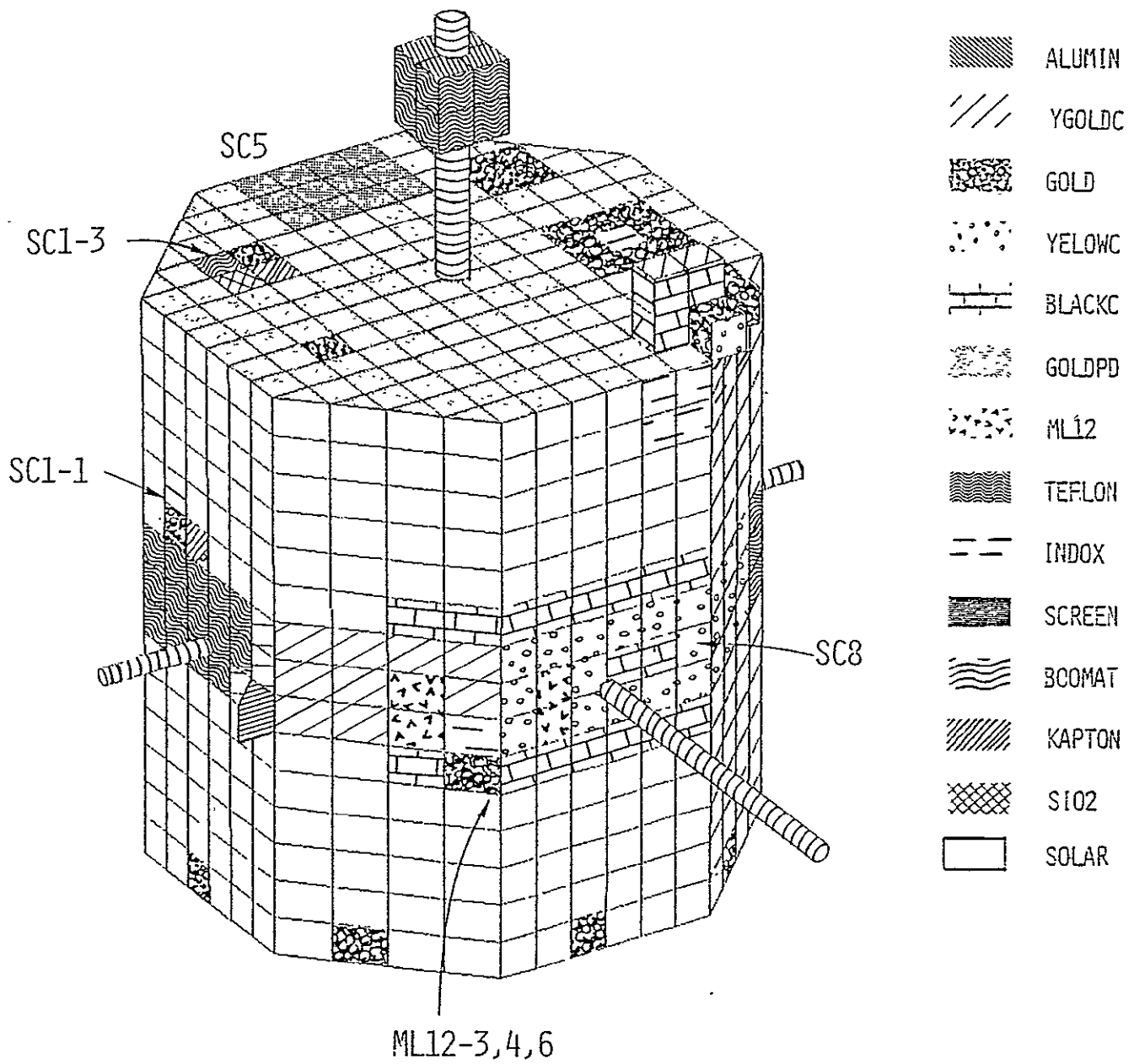


Figure 4c. SCATHA model with exposed surface materials illustrated.

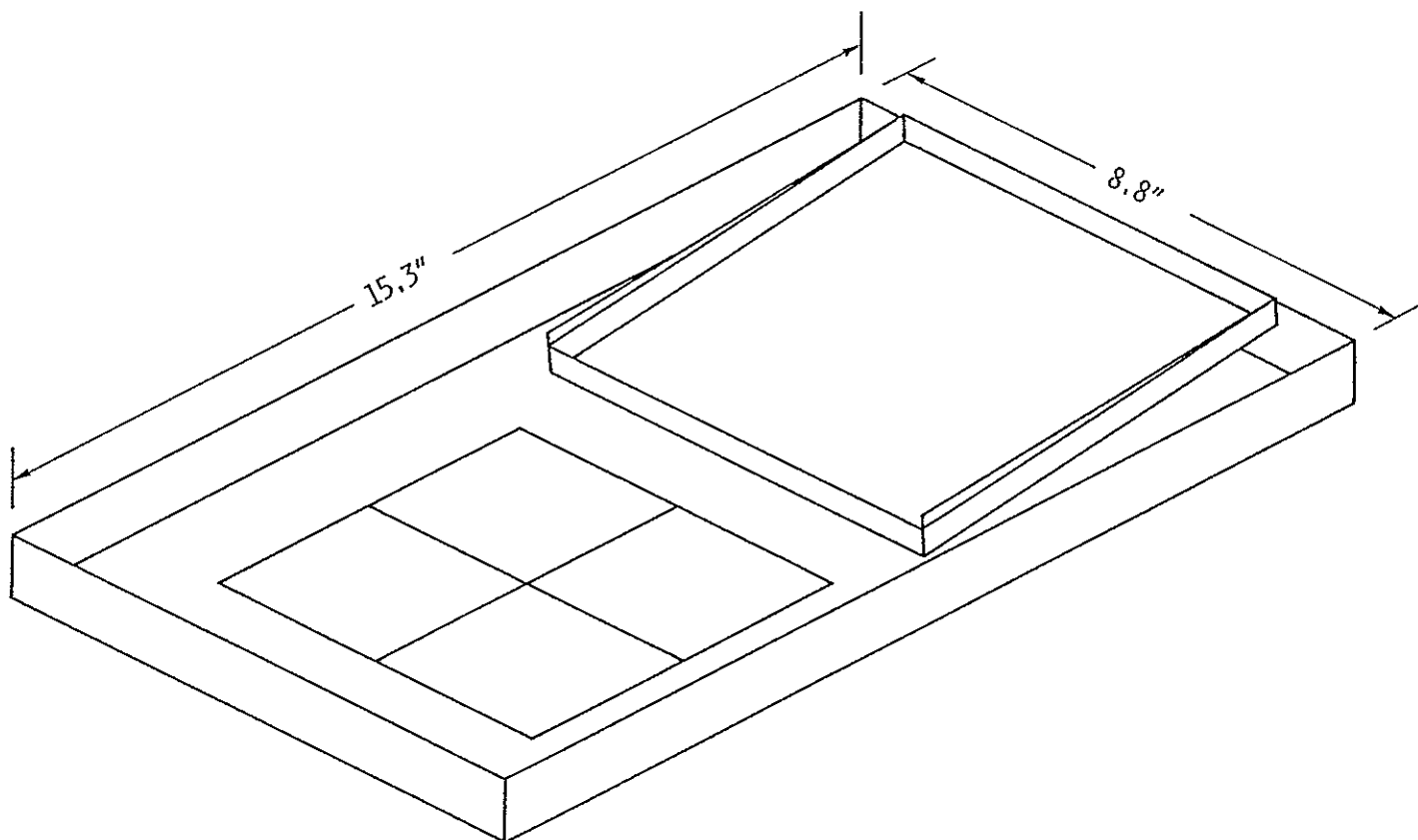


Figure 5. ML12-7 experiment as resolved for the SCATHA shadowing study.

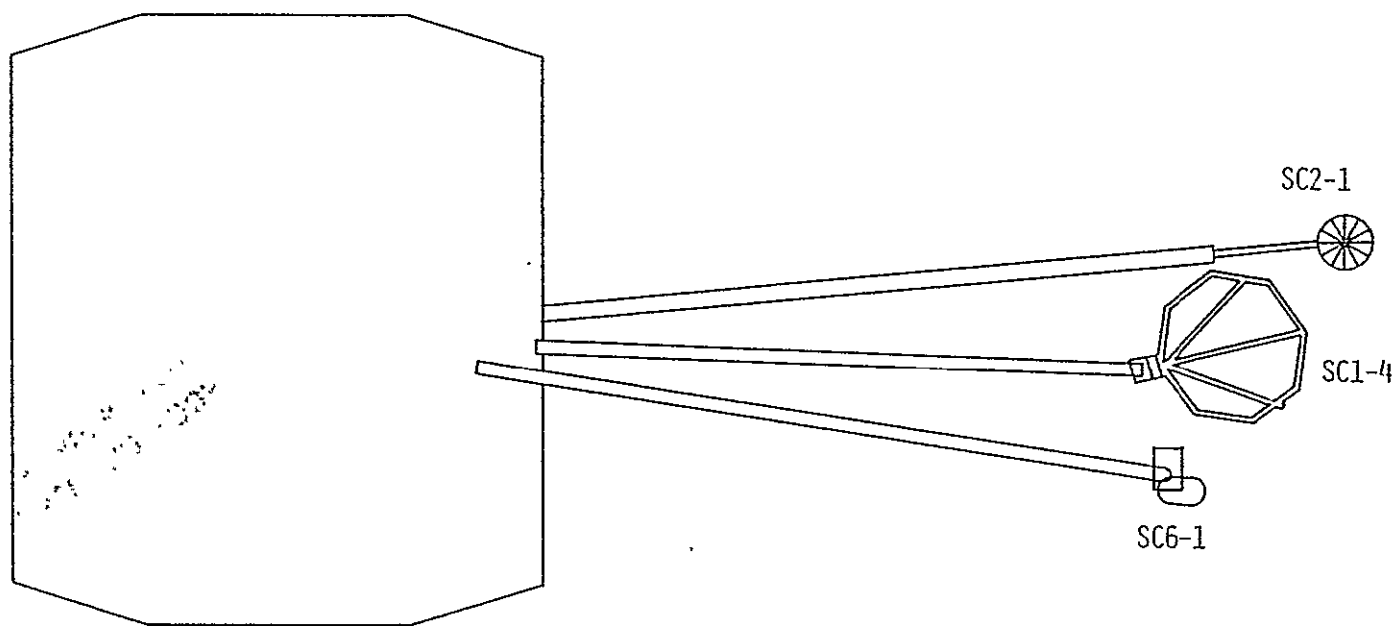
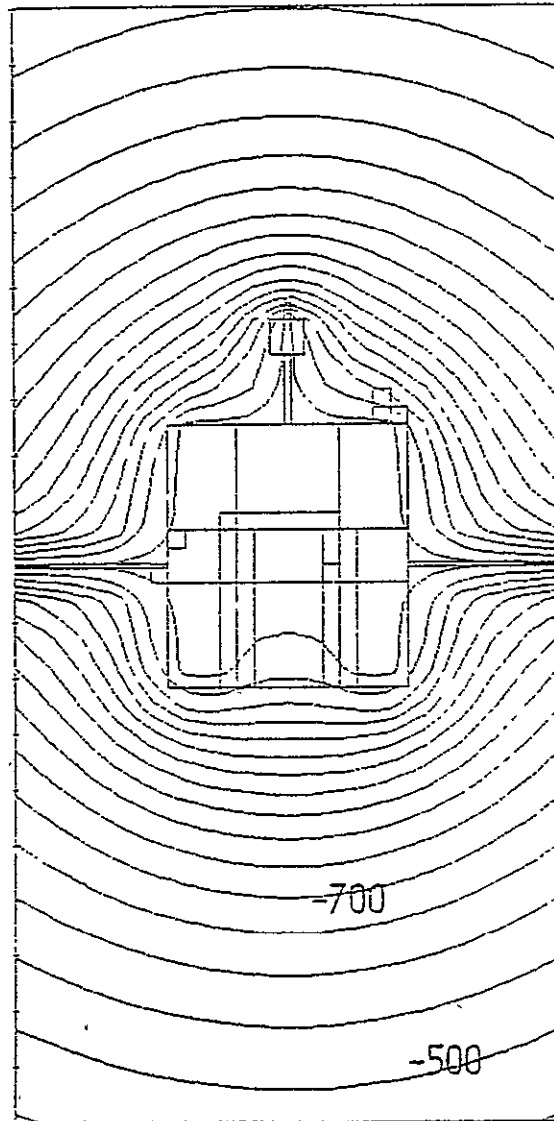


Figure 6. SCATHA booms as resolved in the shadowing study.



ORIGINAL PAGE IS
OF POOR QUALITY

Figure 7. Potential contours in a vertical plane through SCATHA center (only two of the four grids are plotted). Note the contours extending into the aft cavity. Time $\sim 10^{-3}$ seconds. Contours from -450 to -1250 volts in 50 volt steps.

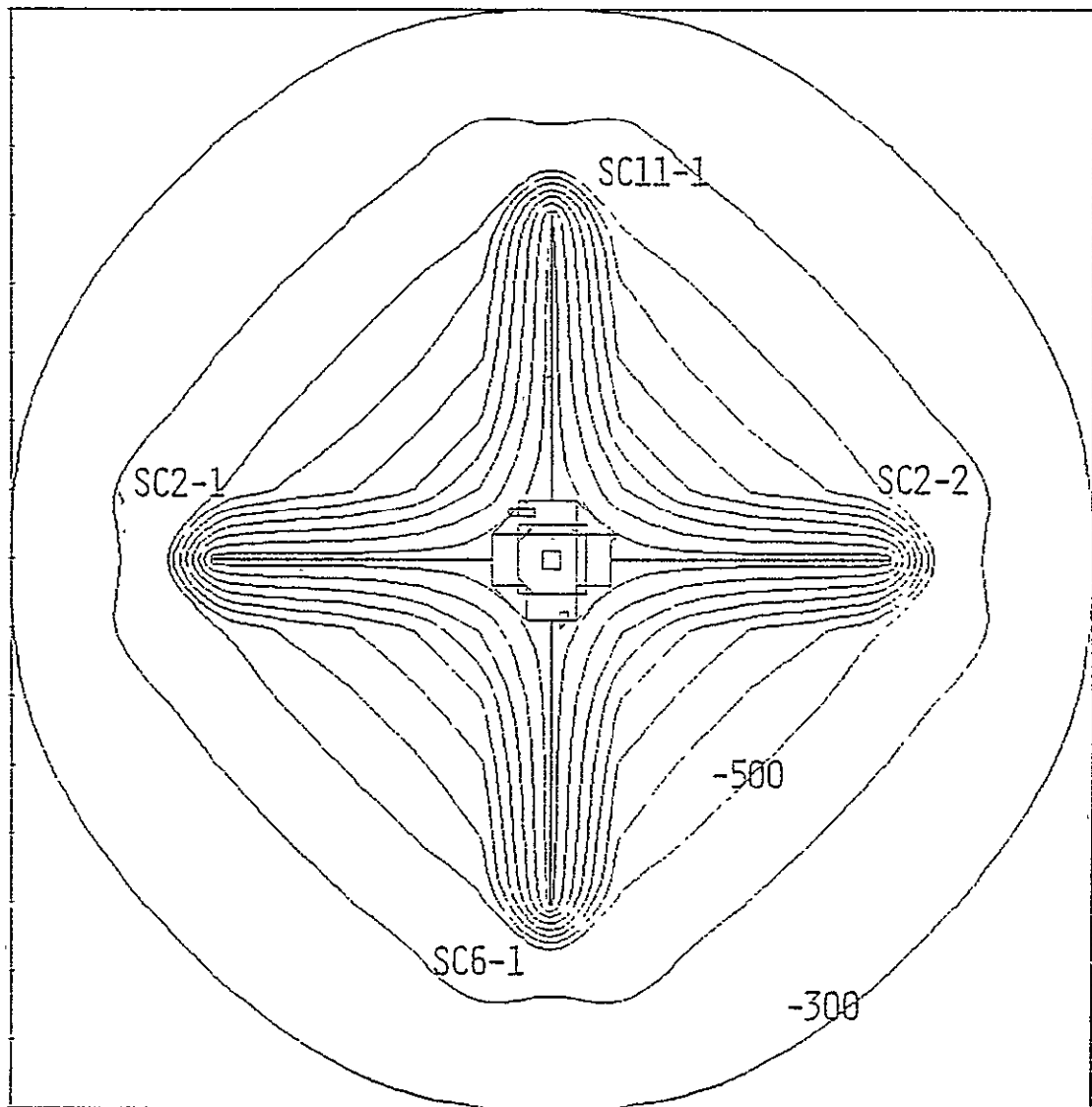


Figure 8. Potential contours in a horizontal plane through SCATHA center. Time $\sim 10^{-3}$ seconds. Contours from -300 to -1200 volts in 100 volt steps. The relative orientations of the booms is the same in later figures. The dimples in the potential contours near the boom ends are artifacts associated with an imperfect match of potential interpolation functions.

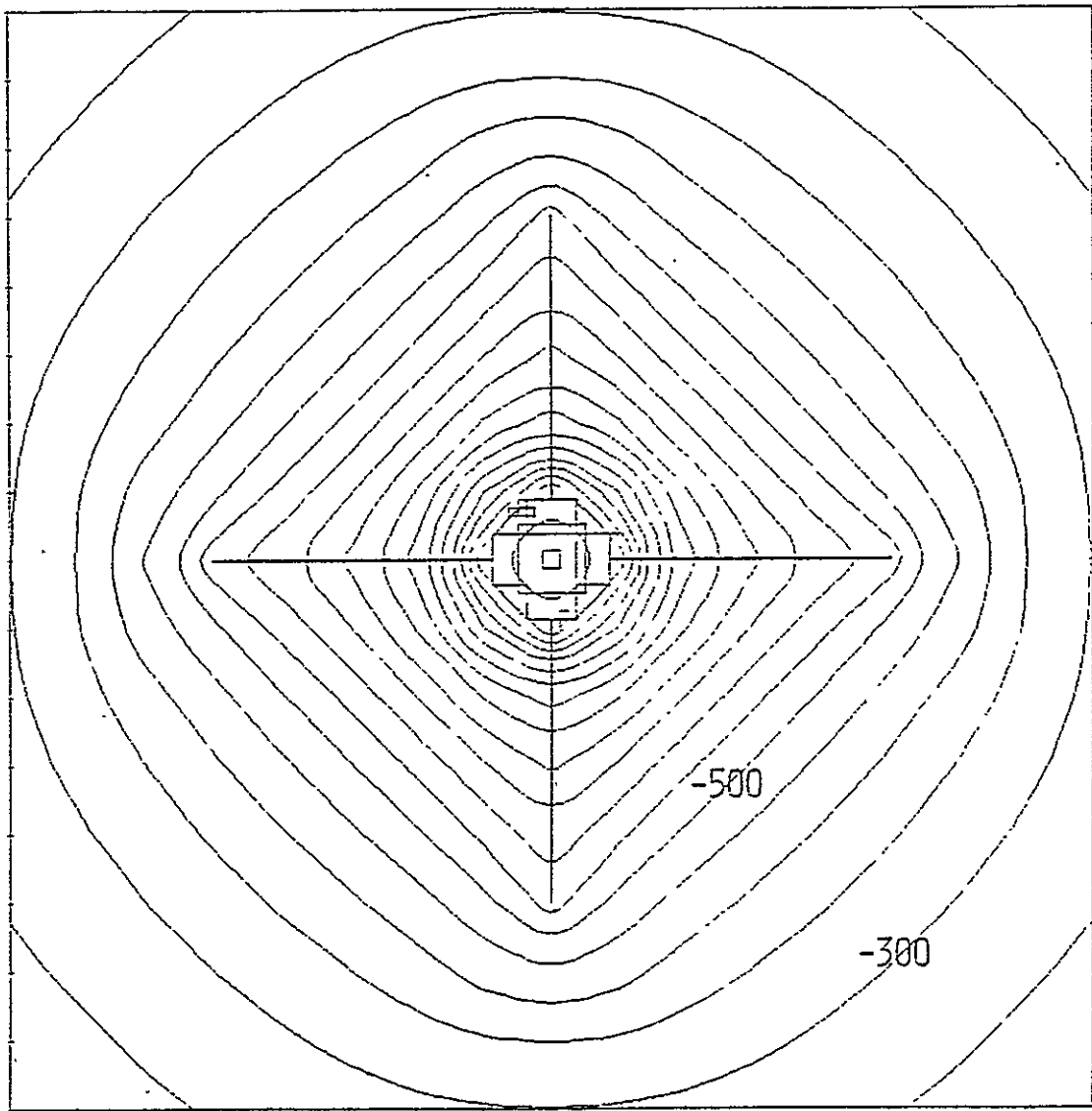


Figure 9. Potential contours in a horizontal plane 1 m below SCATHA center. Time $\sim 10^{-3}$ seconds. Contours from -250 to -1150 volts in 50 volt steps.

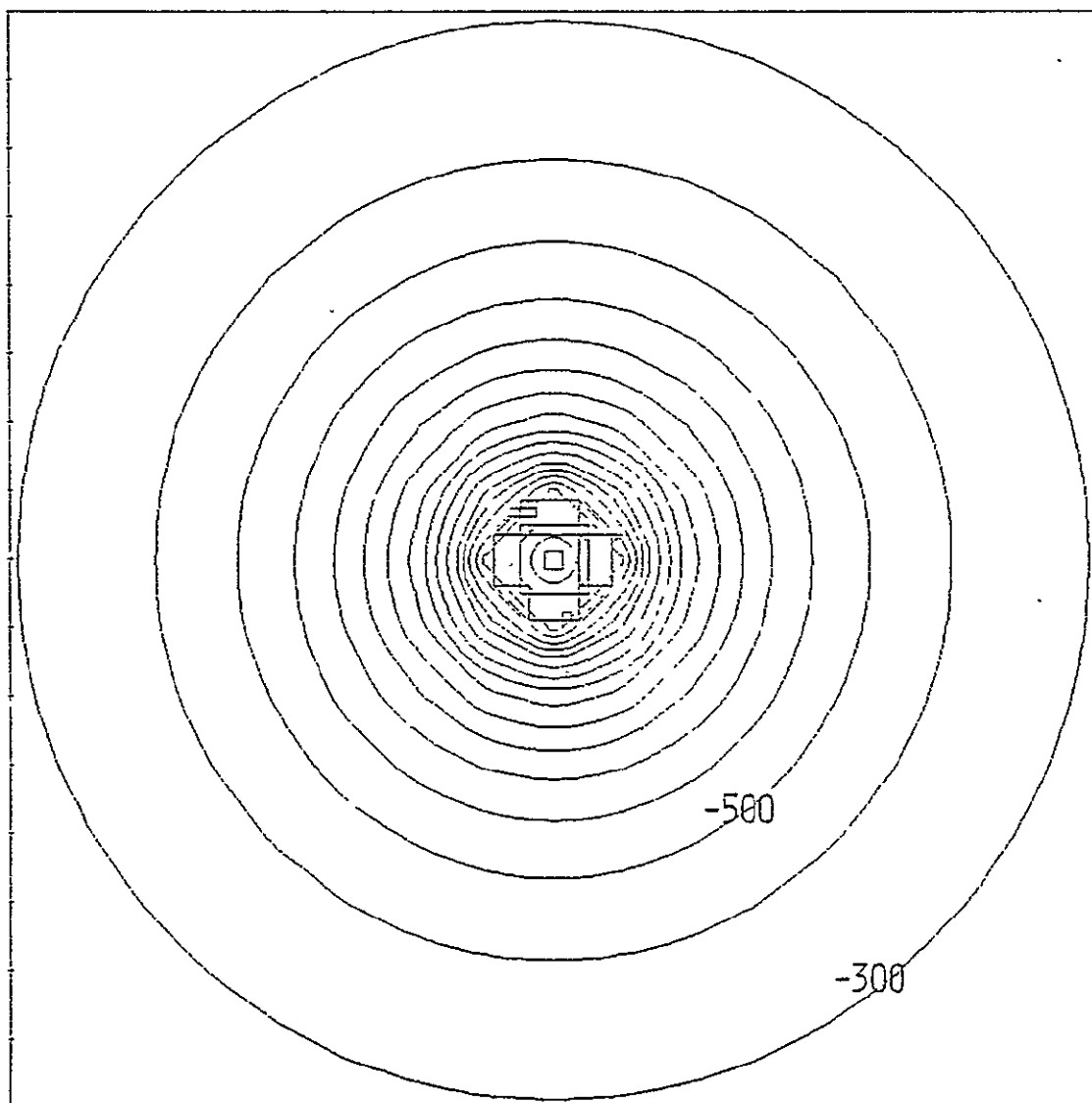


Figure 10. Potential contours in a horizontal plane 1 m below SCATHA center for a model in which the booms have been removed. Time $\sim 10^{-3}$ seconds. Contours from -300 to -1900 volts in 100 volt steps.

ORIGINAL PAGE IS
OF POOR QUALITY

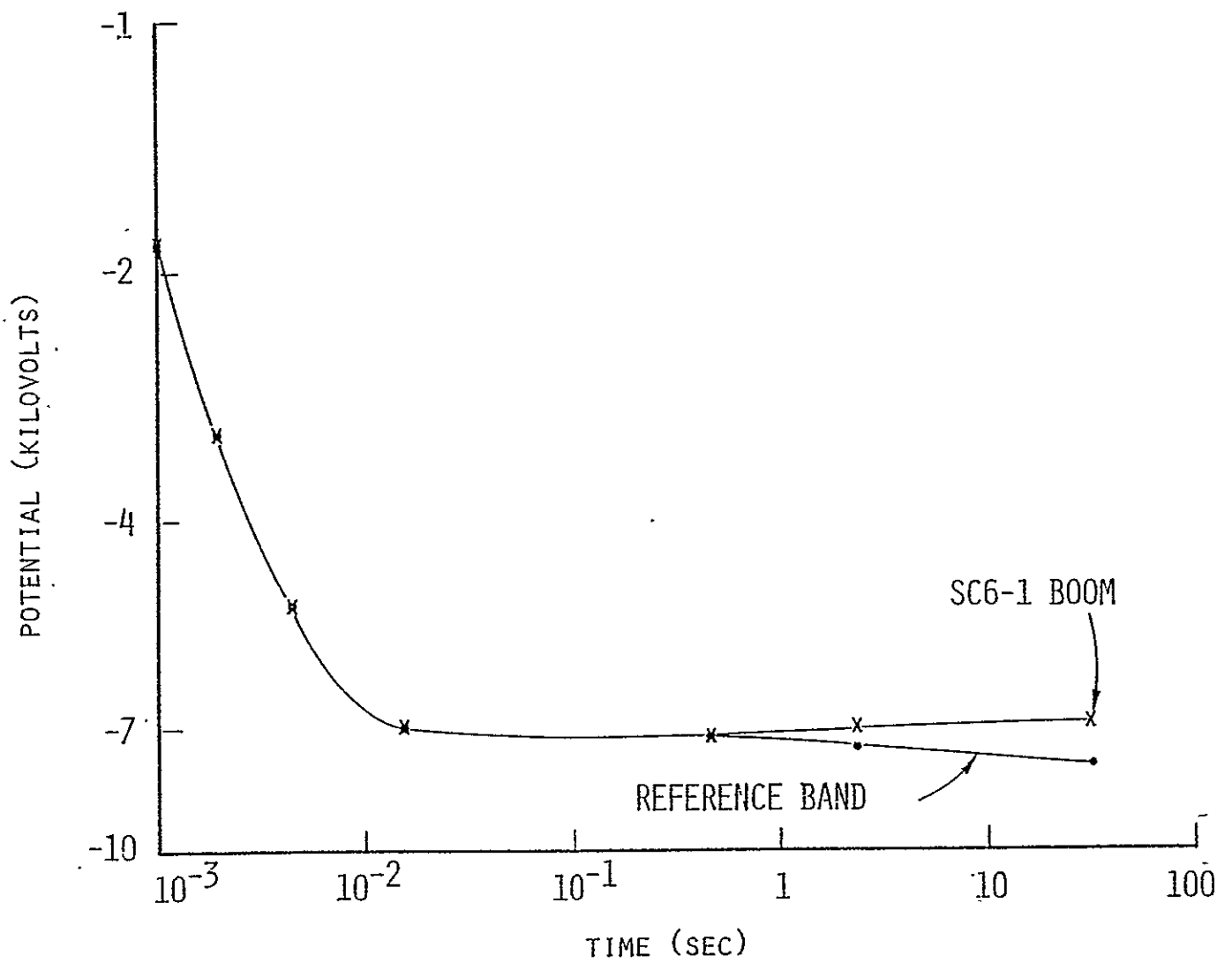


Figure 11. Spacecraft potential versus time for two points on SCATHA satellite.

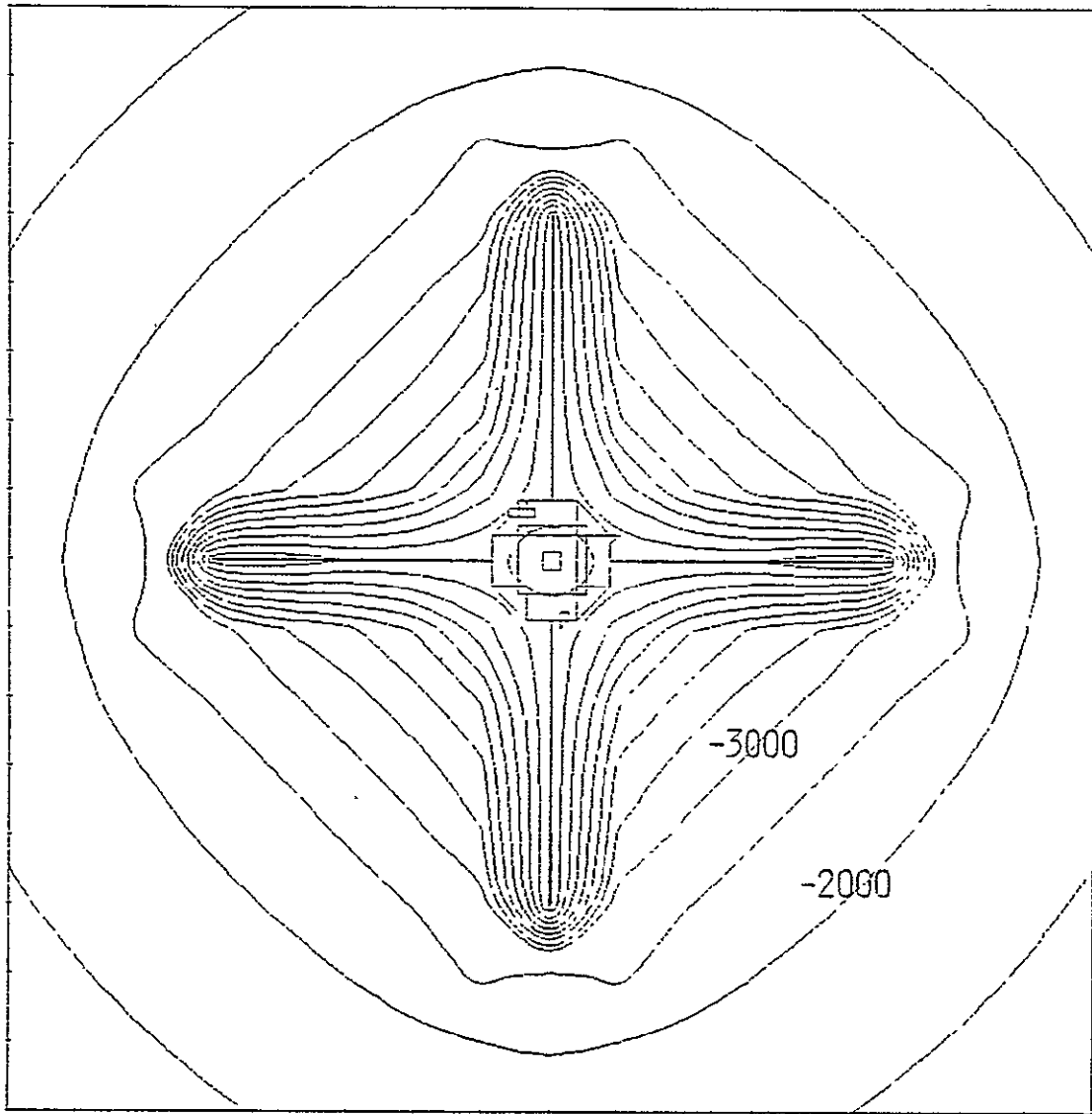


Figure 12. Potential contours in a horizontal plane through SCATHA center, with differential charging along booms. Time ~22 seconds. Contours from -2000 to -7000 volts in 500 volt steps.

ORIGINAL PAGE IS
OF POOR QUALITY

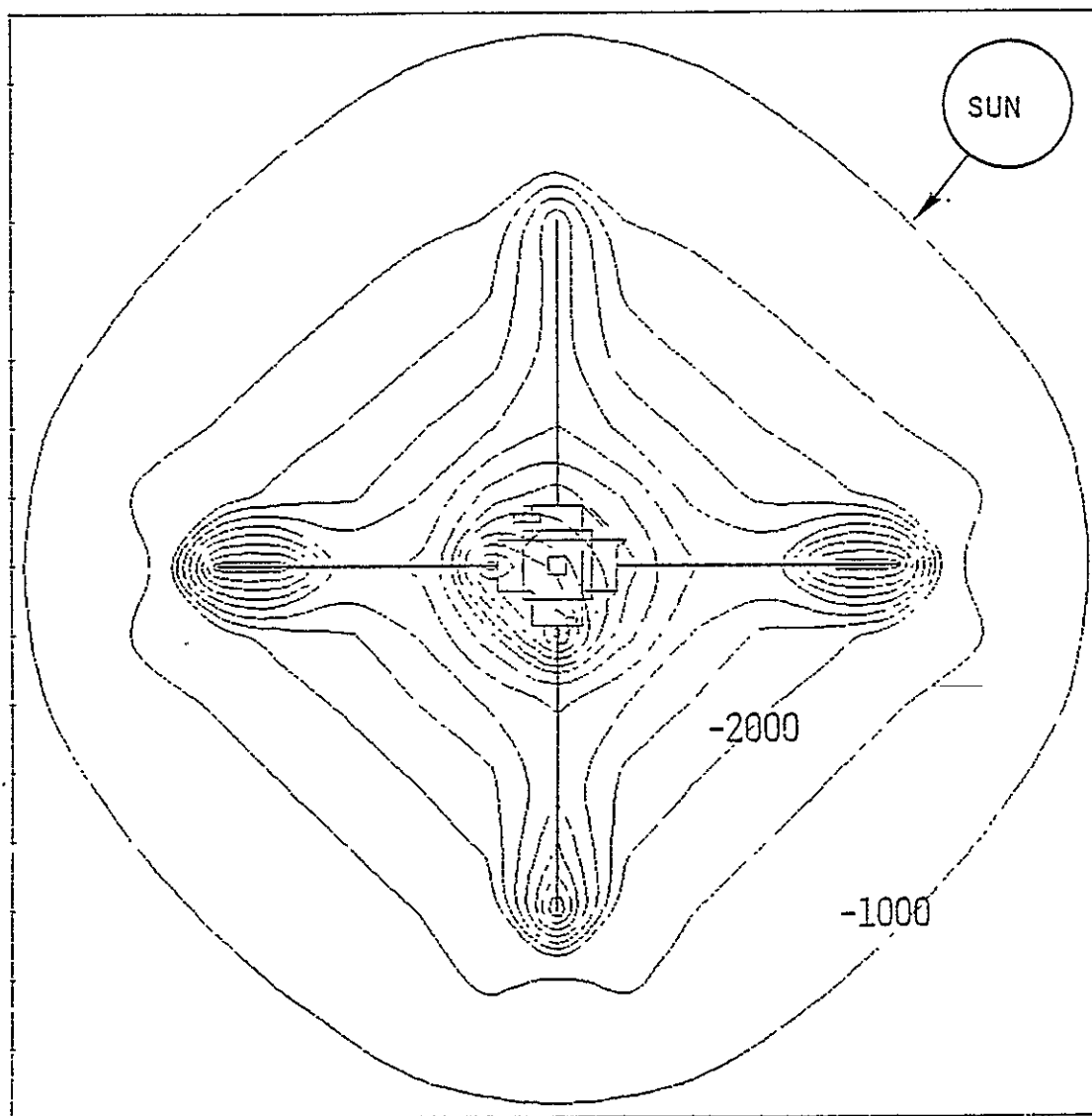


Figure 13. Potential contours for sunlit case in a horizontal plane through SCATHA center. Time ~38 seconds. Contours from -1000 to -7500 volts in 500 volt steps.

17. TWOD — TWO DIMENSIONAL SPACECRAFT CHARGING COMPUTER CODE

17.1 INTRODUCTION

For the purpose of validating the ability of NASCAP to predict the presence of a sheath of photoelectrons and secondary electrons, Systems, Science and Software has constructed a two-dimensional (R- θ) spacecraft charging code capable of predicting equilibrium potentials and space charge densities about an infinitely long, dielectric-coated cylinder. The TWOD code features

1. A flexible finite element formulation of the electrostatic potential problem.
2. A fast ICCG (Incomplete Cholesky Conjugate Gradient) potential solver.^[3]
3. Efficient particle tracking algorithms.
4. Self-consistent formulations for space charge due to low energy emitted electrons.
5. Linear (Debye length) screening for ambient plasma.
6. An approximate effective-surface-conductivity treatment for charge transport in the photosheath; the conductivity value is determined consistent with the emitted current and external field.
7. A first-order-implicit time-stepping treatment to promote stable convergence.

The above features are either based on NASCAP ideas, extensions of techniques used in NASCAP, or formulations which might, at least in principle, be incorporated into NASCAP. In its final form, TWOD will treat material properties and environment characteristics identically with NASCAP.

17.2 CODE STRUCTURE

A block diagram of the preliminary version of TWOD is shown in Figure 17.1. This version does not include input or object definition sections, nor does it calculate currents based on material properties and environment specifications. Implementation of such features will be simple and straightforward, in many cases involving direct transference of NASCAP routines.

TWOD operates on a computational grid consisting of a central conductor surrounded by a ring of surface nodes and successive rings of space nodes. The space nodes are spaced uniformly in angle and are at arbitrary, specified radii, allowing fine resolution near the surface while including a large volume of space.

TWOD operates in a time-stepping fashion, although procedures have been biased in favor of producing stable convergence toward equilibrium at the expense of accuracy in the time history. At each step, the Charge Section calculates incident and low-energy emitted currents to each surface node. The low-energy particles are tracked to find any barriers to their escape and their contribution to space charge. It is known^[6] that tracking of these particles to determine surface currents is an unstable procedure; therefore, following a suggestion of Whipple^[7] an effective photosheath conductivity, calculated as described below, is used. Finally, the net current to each node is calculated, and an estimate is formed for the derivative of each node current with respect to its potential. These current derivatives serve to limit the voltage excursions, and are chosen to ensure stability. (See below.)

Where space charge has an important effect, it is at best marginally convergent. Therefore, we use the ICCG potential solver to calculate the potential change due to

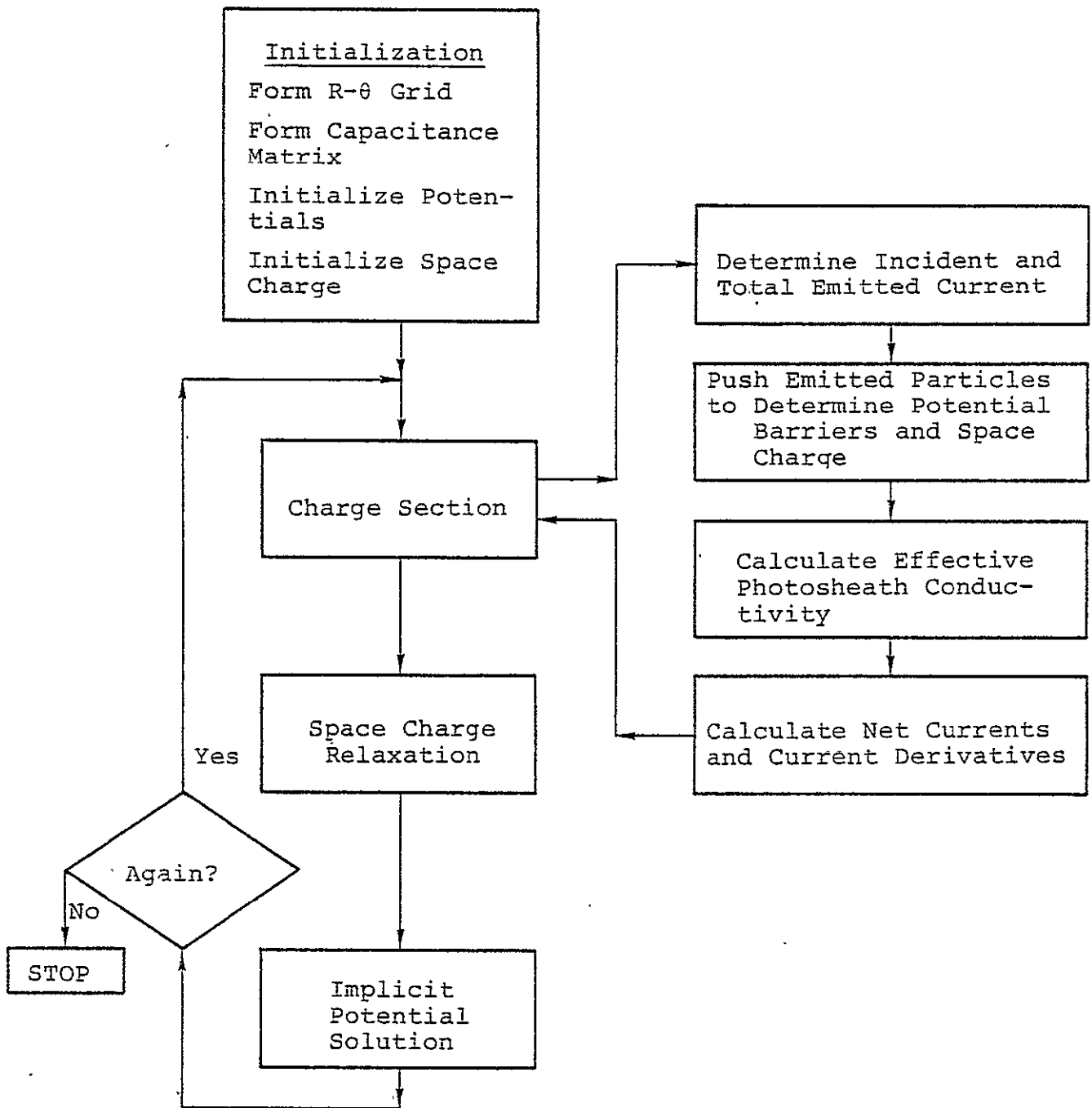


Figure 17.1. Block diagram of TWOD code.

the change in space charge. The old space charge is then averaged with the newly calculated space charge so as to produce a maximum space charge induced potential change of two volts.

To complete the timestep we must solve

$$\tilde{C} \left(\tilde{V}(t_2) - \tilde{V}(t_1) \right) = \int_{t_1}^{t_2} [\tilde{J}(t) + \tilde{\sigma}(t) \tilde{V}(t)] dt + \Delta \rho_s \quad (17.1)$$

TWOD solves Eq. (17.1) "implicitly", i.e., with the integrand on the right hand side evaluated at the advanced time. Since the integrand can be very nonlinear, we approximate

$$\tilde{\sigma}(t) \approx \tilde{\sigma}(t_1) \quad (17.2a)$$

$$\tilde{J}_i(t) \approx \tilde{J}_i(t_1) + \tilde{J}'_{ii}[V_i(t) - V_i(t_1)] \quad (17.2b)$$

where the coefficients of the diagonal matrix coefficients \tilde{J}'_{ii} are estimated so as to ensure stability. (The space charge terms, $\Delta \rho_s$, are calculated as described above. Debye shielding is included in the capacitance matrix \tilde{C} .) Equation (17.1) now becomes

$$\begin{aligned} [\tilde{C} - (\tilde{J}' + \tilde{\sigma})(t_2 - t_1)] [\tilde{V}(t_2) - \tilde{V}(t_1)] \\ = [\tilde{J}(t_1) + \tilde{\sigma}\tilde{V}(t_1)] (t_2 - t_1) + \Delta \rho_s \end{aligned} \quad (17.3)$$

Equation (17.3) is solved using the ICCG potential solver to obtain potentials for use in the next timestep.

17.3 EFFECTIVE PHOTOSHEATH CONDUCTIVITY

In order to handle photosheath currents stably within the implicit potential solution it is necessary, following a suggestion of Whipple,^[7] to express these currents in the form

$$J_{\theta}(\theta) = \sigma_{\theta}(\theta) E_{\theta}(\theta) . \quad (17.4)$$

Equation (17.4) is already a substantial approximation, because it is (a) linear, (b) local and (c) neglects "production gradient" transport. However, it is almost always the case that either $\sigma_{\theta}(\theta)$ is large enough to maintain a nearly uniform potential over a photoemitting area, or there is very little transport in the electron sheath. Therefore, Eq. (17.4) will always give the correct potential and space charge configuration, well within uncertainties in material properties and environment specifications.

Figure 17.2 shows the geometry to be used in calculating photoconductivity. $J_{\theta}(Z)$ represents the current density of those electrons emitted to the right of the plane and landing to the left. We wish to calculate

$$\int_{Z_0}^{\infty} J_{\theta}(Z) dZ = \int_{Z_0}^{\infty} \rho(Z) v_{\theta}(Z) dZ = \rho_s \bar{v}_{\theta} \quad (17.5)$$

where ρ_s has dimensions of surface charge density. Neglecting curvature effects,

$$\rho_s = \int_0^{\epsilon_{\min}} J(\epsilon_z) t(\epsilon_z) d\epsilon_z \quad (17.6)$$

where ϵ_z is the normal electron energy component, ϵ_{\min} is the minimum energy required for escape from the satellite, and

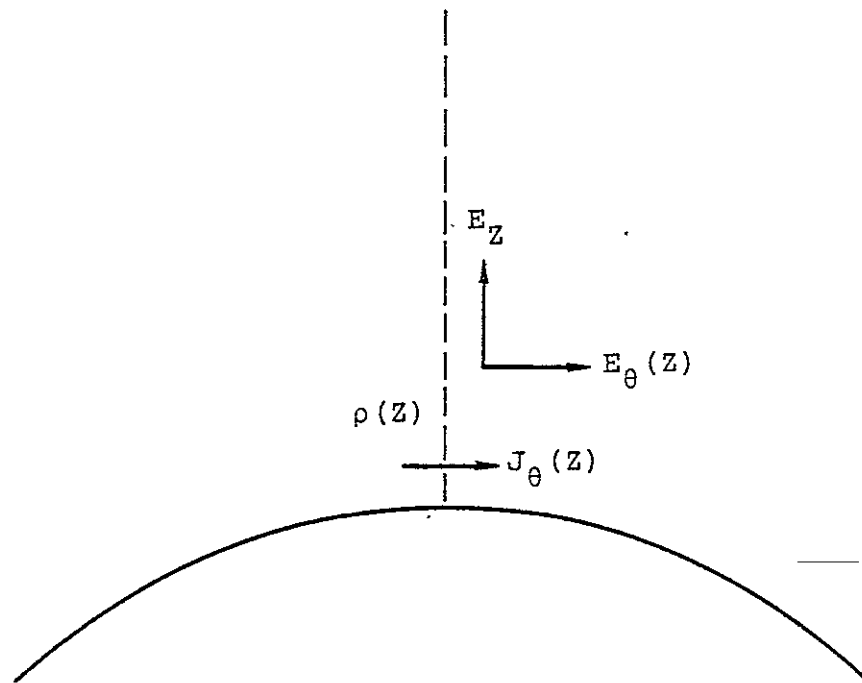


Figure 17.2. Conductivity in photoelectron sheath.

$t(\epsilon_Z)$ is the flight time. The mean transverse velocity of such a particle is

$$\bar{v}_\theta(\epsilon_Z) = \frac{1}{t(\epsilon_Z)} \int_0^t dt_1 \int_0^{t_1} dt_2 \frac{e}{m} E_\theta(Z(t_2)) \quad (17.7)$$

so that

$$\int_0^\infty J_\theta(\epsilon) dZ = \int_0^{\epsilon_{\min}} J(\epsilon_Z) d\epsilon_Z \frac{e}{m} \int_0^t dt_1 \int_0^{t_1} dt_2 E_\theta(Z(t_2)) \quad (17.8)$$

Formula (17.8) can be put into relatively simple form if we assume

$$E_Z = \text{constant } (>0) \quad (17.9a)$$

$$E_\theta(Z) = E_\theta(Z_0) \frac{Z_0}{Z} \quad (17.9b)$$

We then obtain

$$\begin{aligned} \sigma_\theta(E_Z, \epsilon_{\min}, J, Z_0) &= \frac{2}{E_Z^2} \int_0^{\epsilon_{\min}} \epsilon_Z J(\epsilon_Z) d\epsilon_Z \\ &\times \int_0^1 dx_1 g\left(x_1, \frac{4 \epsilon_Z}{Z_0 E_Z}\right) \end{aligned} \quad (17.10a)$$

where

$$g(x, a) = (4a + a^2)^{-1/2} \ln \frac{2 + ax + x \sqrt{4a + a^2}}{4 + 4ax(1 - x)} \quad (17.10b)$$

ϵ_z is in electron volts, E_z is in volts/meter, and $J(\epsilon_z)$ is in $\text{amps/m}^2\text{-eV}$. Under most circumstances E_z^{-2} is the dominant factor in the conductivity. However, when E_z becomes small, the integral also becomes small, so that the conductivity does not diverge.

17.4. EXAMPLE: ISOTROPIC FLUX

As an example of the space charge feature of TWOD, we simulated a case in which the entire surface of a one meter radius cylinder was emitting photoelectrons at a rate of 1.25 nA/cm^2 while receiving high energy incident electrons at a rate of 0.125 nA/cm^2 . Zero potential boundary conditions were set at a 12 meter radius. The equilibrium space charge and potential profiles are shown in Figure 17.3. The potential function clearly indicates formation of a space charge barrier about halfway between the surface and the outer boundary. The details of the potential profile are surely sensitive to the outer boundary condition, and would be modified by Debye screening. (The space charge anomaly near the surface is due to poor statistics for the lowest energy particles.)

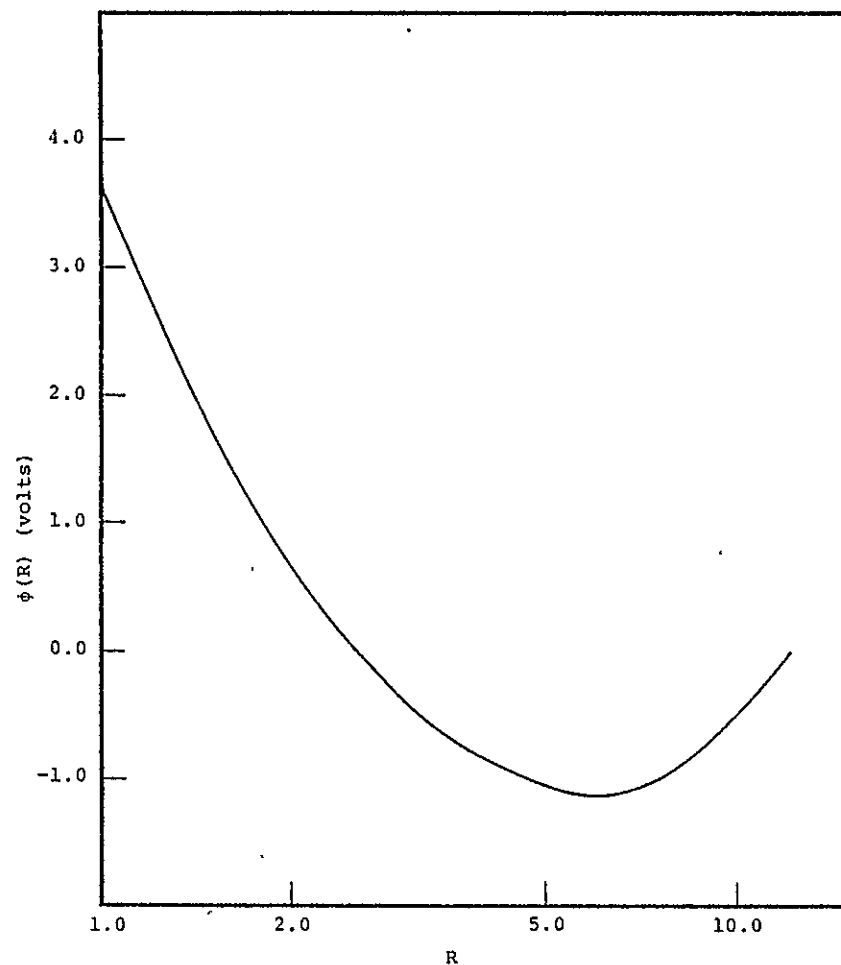


Figure 17.3a. Potential profile outside uniformly sunlit sphere.

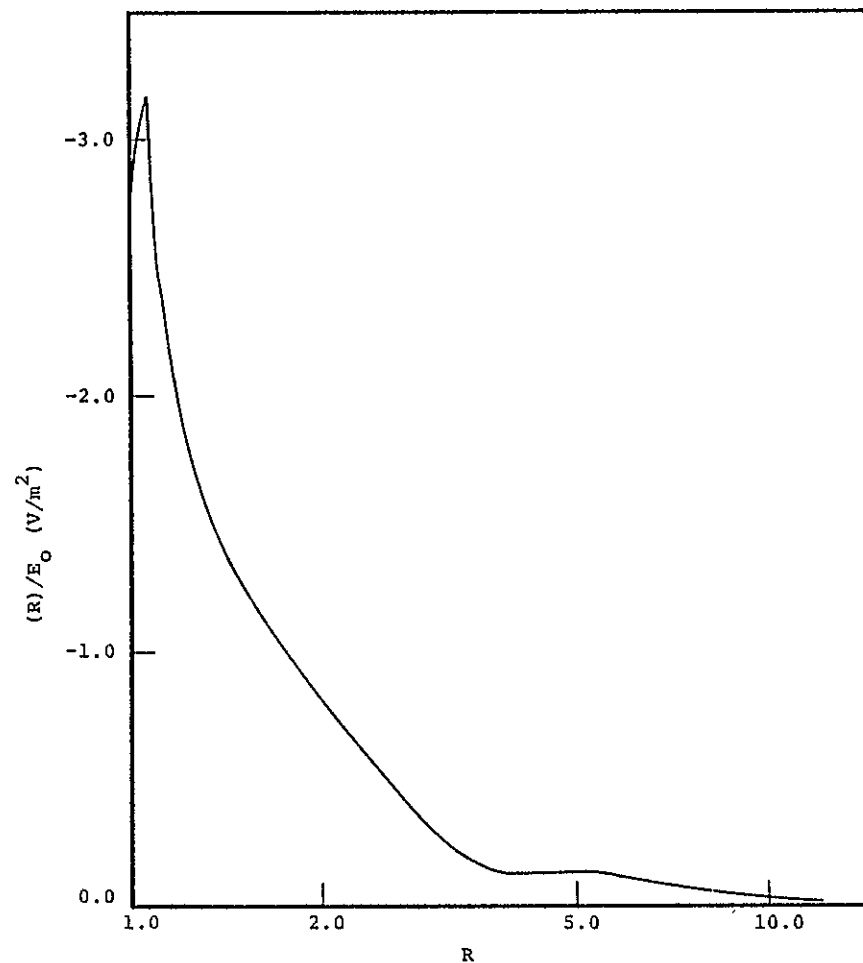


Figure 17.3b. Space charge density profile outside uniformly sunlit sphere.

17.5 COMPARISON OF TWOD AND NASCAP

It is important to recall that TWOD includes a self-consistent treatment of the space charge in the photosheath and an implicit effective surface conductivity arising from charge transport in the photosheath. NASCAP treats the effects of photoemission implicitly by first estimating the maximum possible potential changes about a sunlit surface element and then adjusting the incident flux accordingly. Effective photosheath surface conductivity is not treated in NASCAP. The validity of these approximations is assessed by the comparisons given below.

The TWOD program treats problems in R- θ geometry; we have performed calculations on a one meter radius cylinder with sunlight incident from one side. The cylinder was covered with a 10^{-4} m thick dielectric with $\epsilon = 1$, and zero boundary conditions were forced at a radius of 12 m. The incident current was from a plasma with $n_e = n_i = 3 \text{ cm}^{-3}$ and $T_e = T_i = 1 \text{ keV}$, and the photocurrent was 2 nA/cm^2 for normal incidence. No secondary or backscattered electron currents were included. Figures 17.4 and 17.5 show the equilibrium potential distribution and space charge density. The shaded surface reached a potential of -2926 volts and the most sunlit cell reached -1029 volts. An electrostatic barrier of approximately 1 volt formed about 15 cm above the most sunlit cell, leading to a maximum in the space charge density in the same region.

The corresponding NASCAP calculation was performed on a right octagonal cylinder with an average radius of 1 m and a length of 3.24 m. The cylinder was covered with a dielectric 1 cm thick with $\epsilon = 1$. The zone size was 27 cm, and monopole boundary conditions were forced at the edge of the second nested grid. Material parameters in NASCAP were adjusted to produce no secondary and negligible backscattered electron

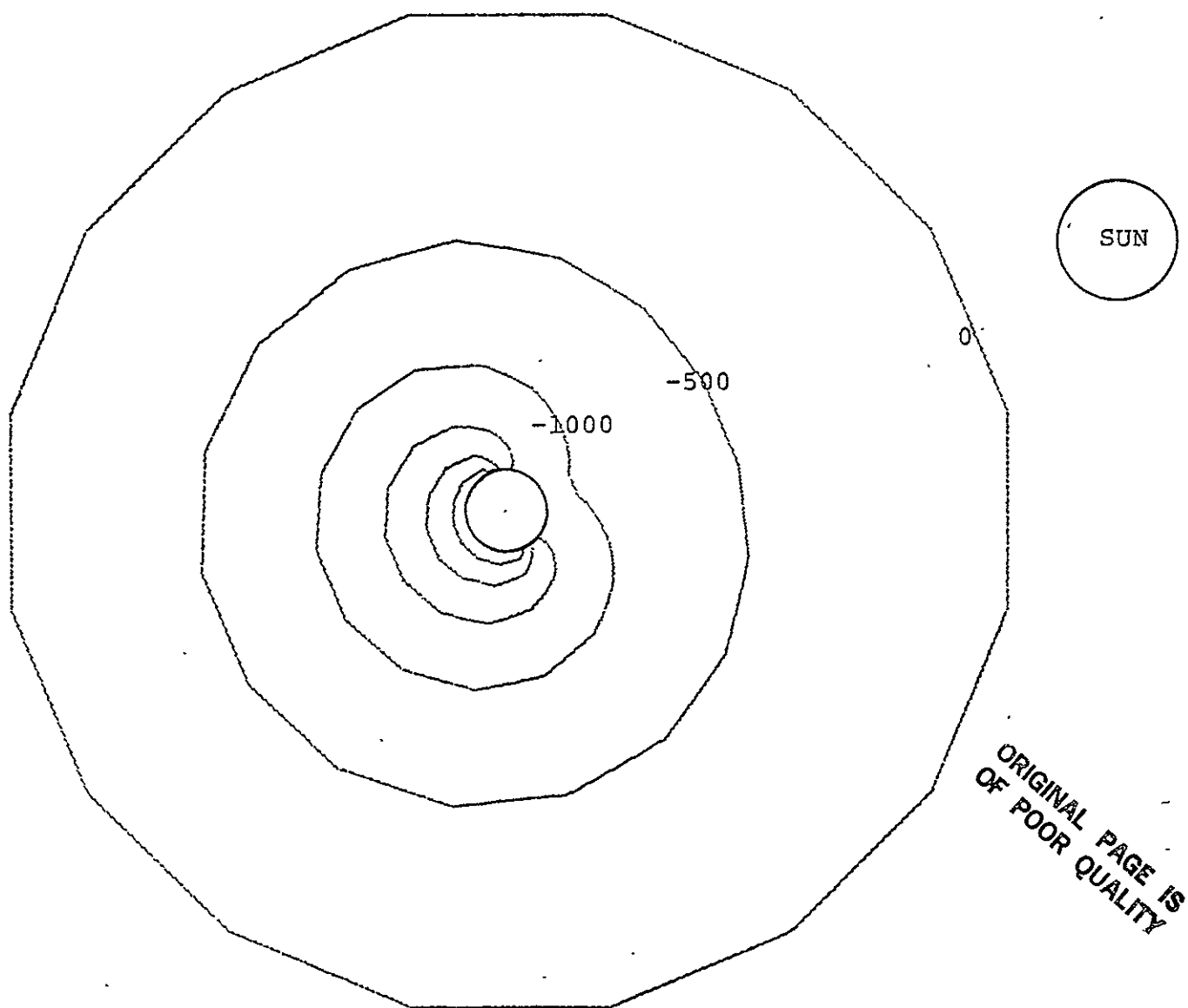


Figure 17.4. Equilibrium potential contours from TWOD code. Contours from 0 to -2500 volts in steps of 500 volts.

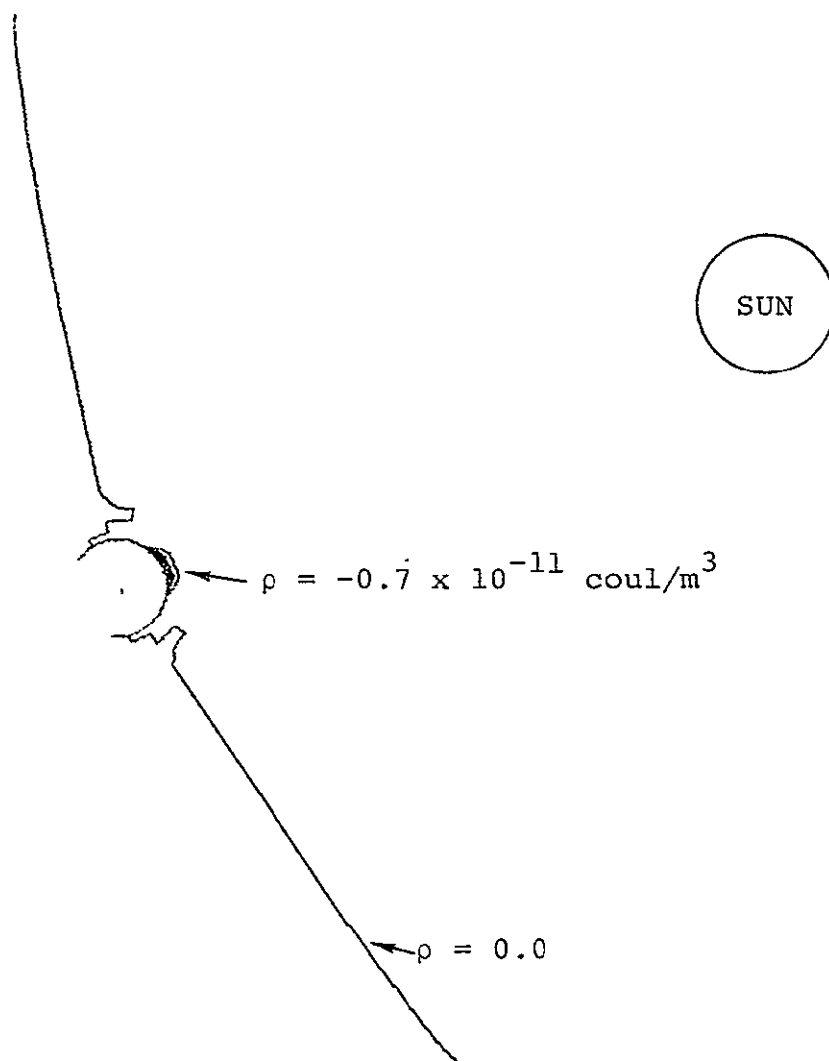


Figure 17.5. Photosheath density from TWOD code. The maximum space charge density is $-5.2 \times 10^{-11} \text{ coul/m}^3$.

current. The ambient plasma density was $n_e = n_i = 1 \text{ cm}^{-3}$, and the plasma temperature was adjusted so that the cylinder would charge to -2930 volts in the dark; this led to $T_e = T_i = 1.26 \text{ keV}$. The calculation was allowed to proceed until the potentials reached equilibrium, and the resulting potential distribution at the midpoint of the cylinder is shown in Figure 17.6. The back surface potential was -2950 volts, and the most sunlit node reached -970 volts. The NASCAP "SHEATH" option was then used to track low energy particles from the cylinder surface using the fixed equilibrium potential fields; plots of the resulting predicted photosheath space charge density are shown in Figure 17.7. Note the appearance of a maximum in the space charge density about one zone, or 27 cm, above the most sunlit cells.

A comparison of Figures 17.4 and 17.5 with Figures 17.6 and 17.7 indicate that the qualitative features of the NASCAP and TWOD predicted potential and space charge distributions agree well. A more detailed comparison is given in this section.

The equilibrium surface potentials are plotted versus angle in Figure 17.8. The predicted differential charging was 1897 volts using TWOD and 1980 volts using NASCAP, an error of 6 percent. This discrepancy is due to the effective photosheath surface conductivity, which was ignored in the NASCAP calculation. The oscillations in the dark side potentials from the NASCAP calculation are an artifact resulting from the procedures used to calculate average cell potentials for the charging algorithm and to share cell currents among nodes. We can eliminate these oscillations by using revised averaging and sharing procedures with the current derivatives, $(\partial J / \partial V)$, as weighting factors.

The radial dependence of the potentials are compared in Figure 17.9. Both calculations show a small potential barrier above the most sunlit cell; the location of the barrier

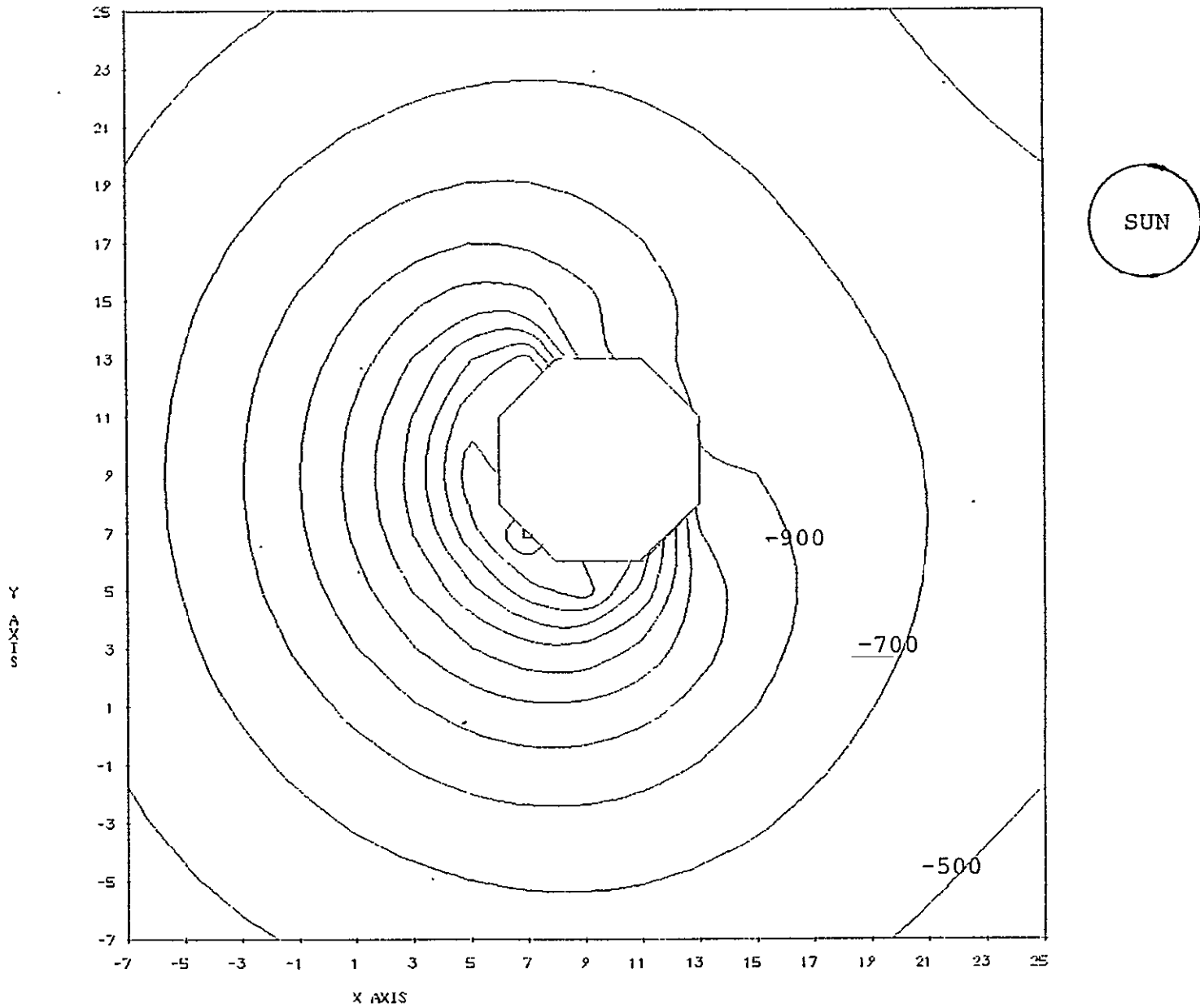


Figure 17.6. Potential contours (two grids) from NASCAP code. Contours from -500 to -2700 volts in 200 volt steps.

ORIGINAL PAGE IS
OF POOR QUALITY

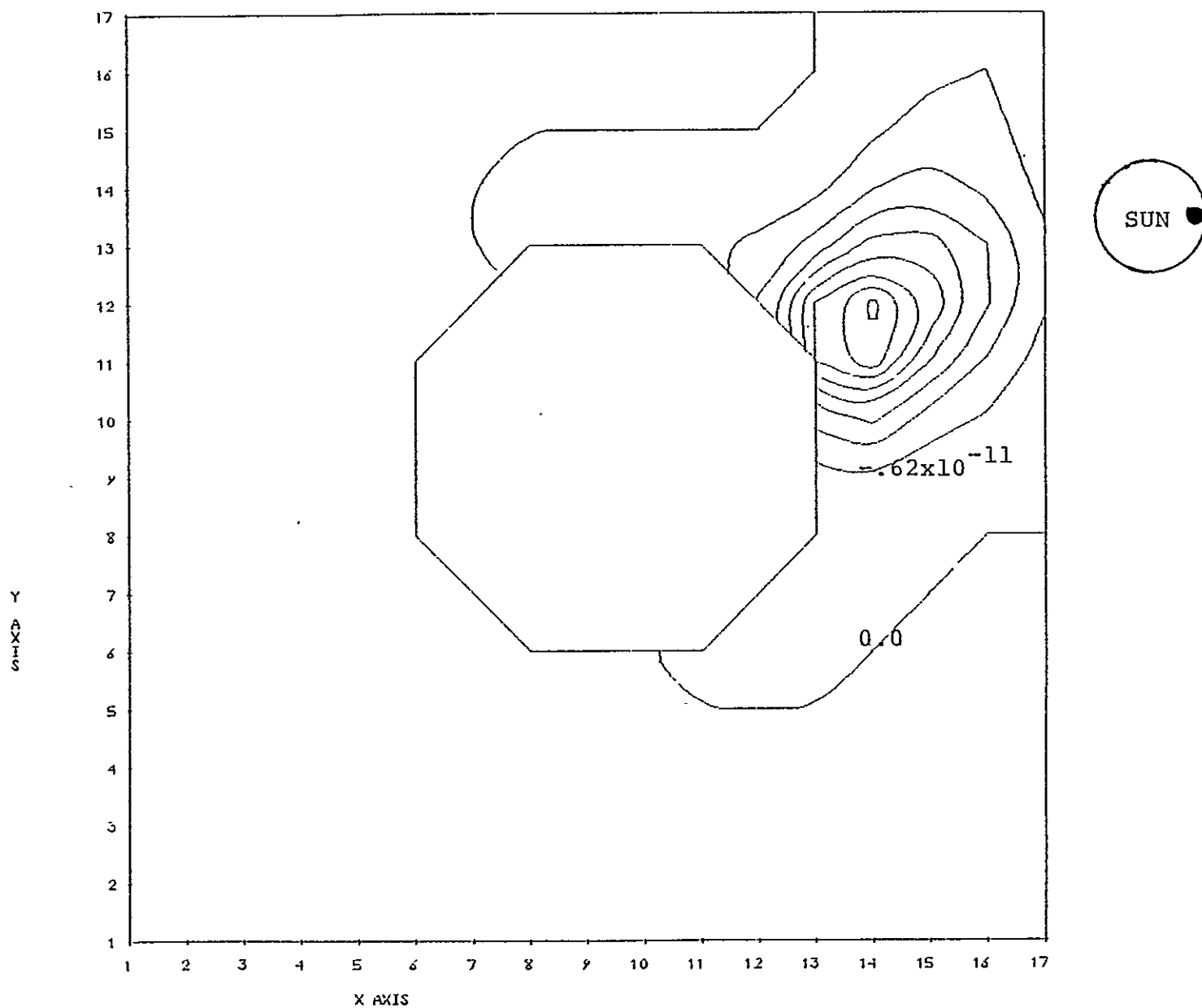


Figure 17.7. Photosheath density for inner grid from NASCAP "SHEATH" routine. Contours from 0.0 to -4.9×10^{-11} coul/m³ in steps of $.62 \times 10^{-11}$ coul/m³.

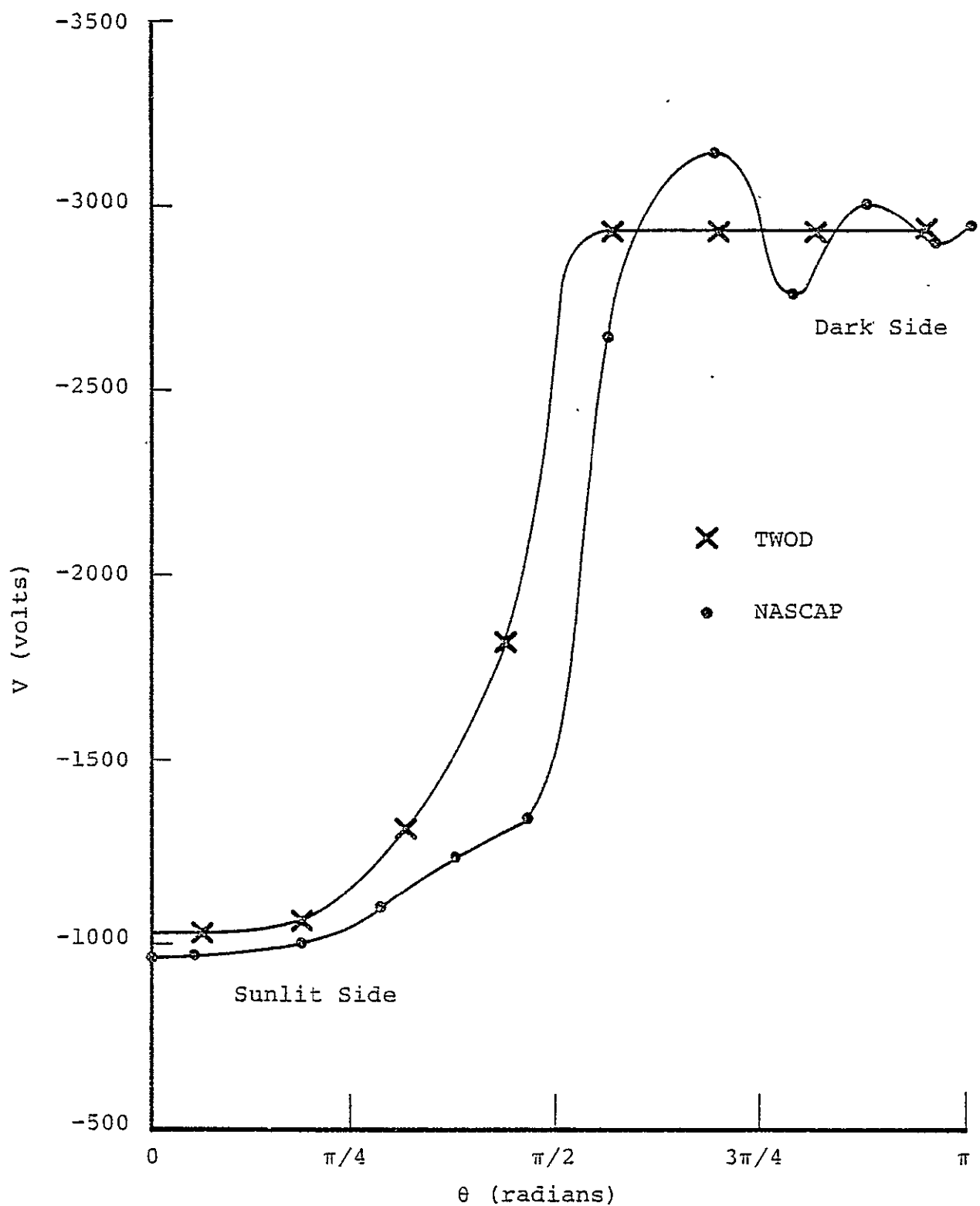


Figure 17.8. Equilibrium surface potential versus angle for a cylinder sunlit from one side.

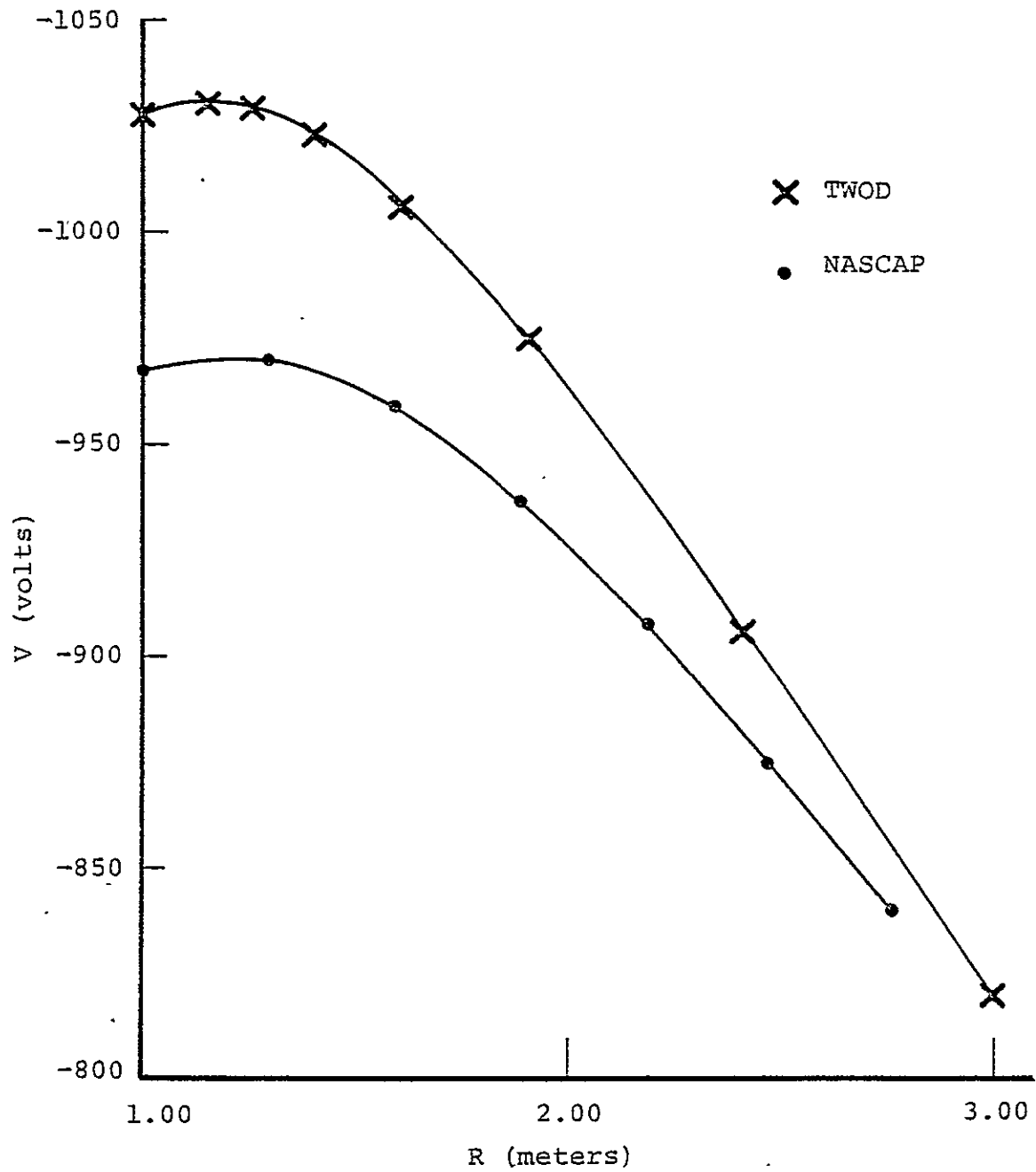


Figure 17.9. Potential versus radial distance for a cylinder sunlit from one side, in direction of incident sunlight. Cylinder radius = 1.00 meter.

is nearer the surface in the TWOD results, at 15 cm, than in the NASCAP results, where it is nearer 30 cm. However, since the zone size in the NASCAP calculation was 27 cm, a barrier nearer than this distance cannot be resolved. The maximum in the space charge density was 5.2×10^{-11} coul/m³ using TWOD, and 5.1×10^{-11} coul/m³ using NASCAP, in good agreement.

The above comparisons demonstrate that in conditions of strong differential charging, the approximations used in NASCAP to treat the effects of a photosheath introduce only small errors.

18. THIN PLATES

The thin plate algorithms were coded and tested in both potential and charging sections of the code. These routines are fully compatible with the LONGTIMESTEP option. Restrictions on the thin plates include that surface cells on the underside not be subdivided. The present potential plotting algorithms do not include the potentials on the bottom of thin plates.

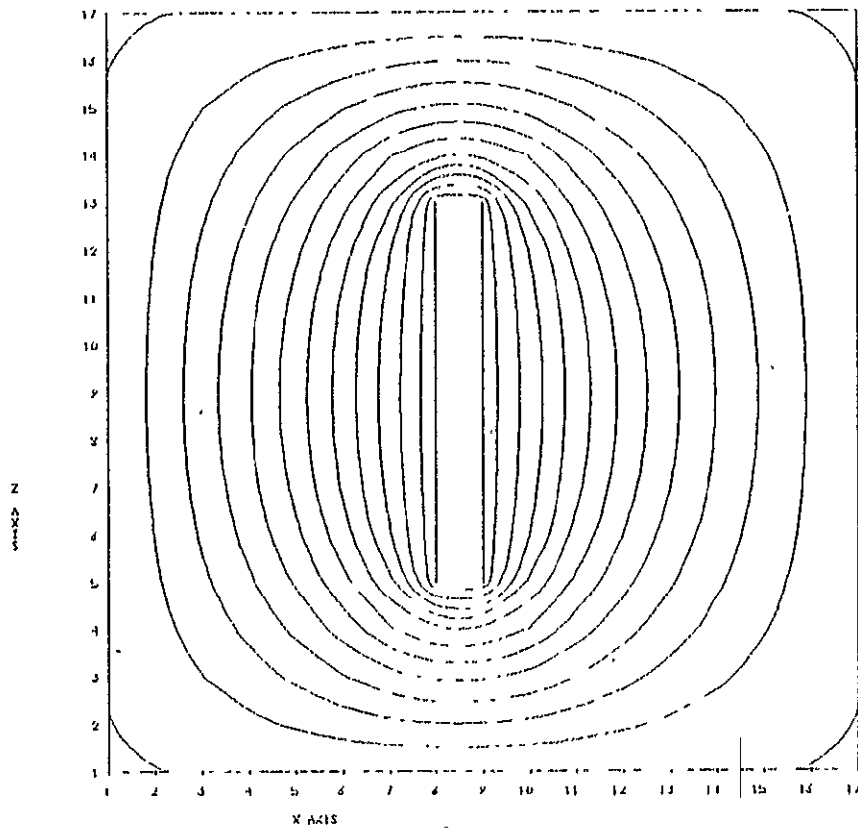
18.1 THIN PLATE EXAMPLES

In order to test the algorithms several plate capacitor configurations were calculated. The results indicate that the accuracy of the representation is consistent with that of the other geometries treatable by NASCAP. For the special case of a parallel plate capacitor with a guard ring to minimize fringing fields, the results were accurate to within a few percent. Figures 18.1 through 18.4 show contours for several different configurations, Figure 18.4 being the parallel plates with a guard ring.

ORIGINAL PAGE IS
OF POOR QUALITY

POTENTIAL CONTOURS ALONG THE X-Z PLANE OF $Y = 0$

$\Delta U = 0.0000$ $\Delta U_0 = 11.0000$ $\Delta Z = 10.0000$



POTENTIAL CONTOURS ALONG THE X-Z PLANE OF $Y = 0$

$\Delta U = 1.0000$ $\Delta U_0 = 11.0000$ $\Delta Z = 10.0000$

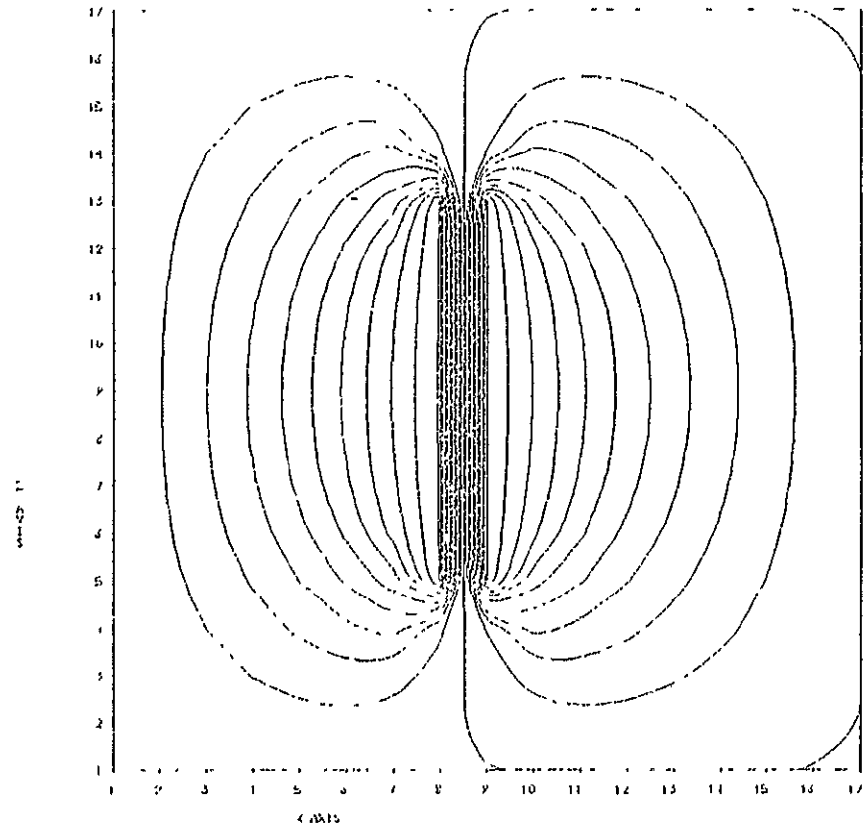
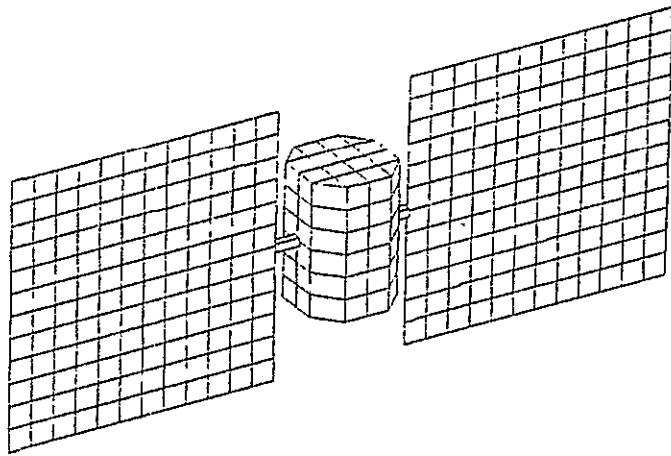


Figure 18.1. Conducting parallel plates in a grounded tank. The left plot shows the two plates at the same potential; the right plot has them biased two hundred volts with respect to each other.



POTENTIAL CONTOURS ALONG THE Y-Z PLANE OF $X = Y$

$Z_{MIN} = 10.21 \times 10^1$ $Z_{MAX} = 00.000$ $\Delta Z = .10600 \times 10^3$

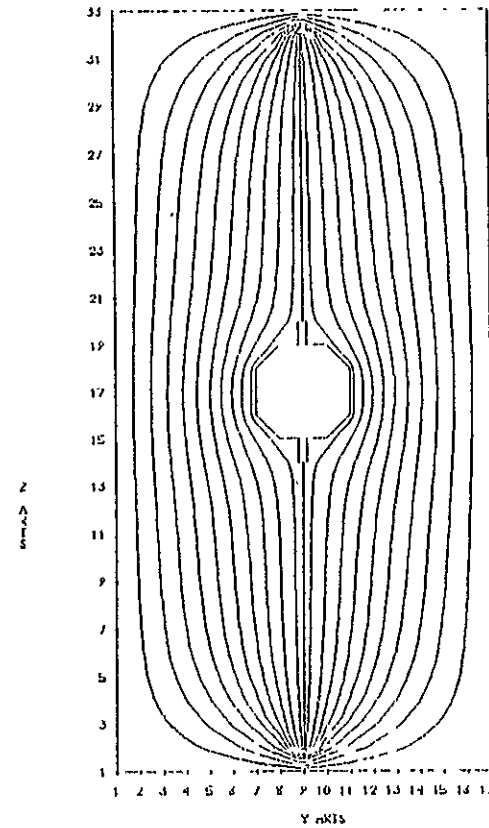


Figure 18.2. Conducting paddle satellite in a test tank. The potential contours are for -1052 volts on spacecraft ground.

POTENTIAL CONTOURS ALONG THE X-Z PLANE OF $Y = 9$

ZMIN = -33677.02 ZMAX = 000000 AZ = 50000.01

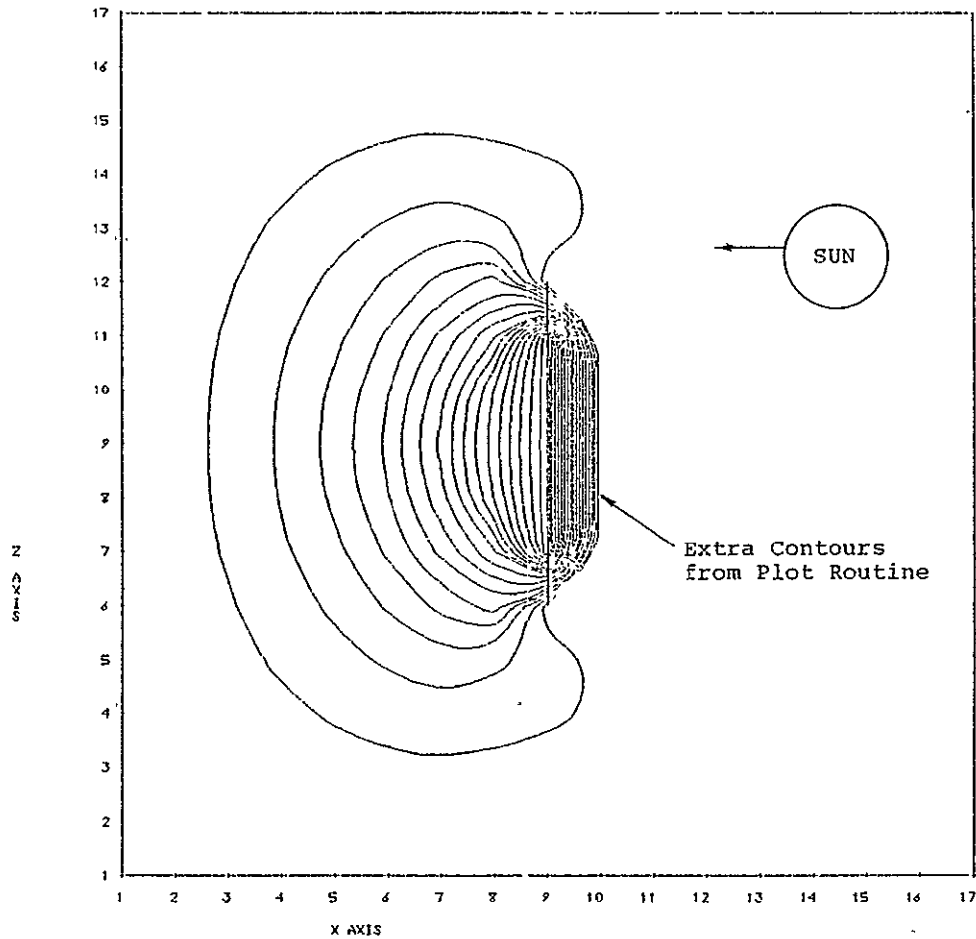
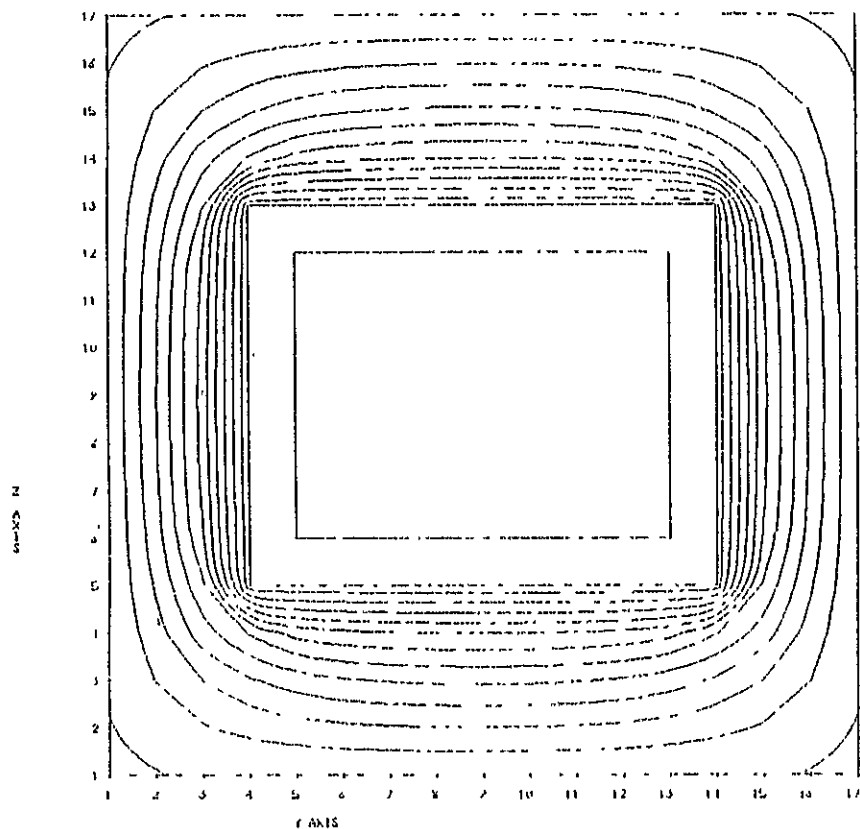


Figure 18.3. A differentially charged dielectric covered plate in sunlight. The extra contours on the photo-emitting surface are an artifact of the potential plot routines which do not presently have the capability to include potentials on the back side of plates.

POTENTIAL CONTOURS ALONG THE Y-Z PLANE OF X = 2

 $Z(III) = .000000$ $Z(IV) = .160000$ $\Delta Z = .160000$


POTENTIAL CONTOURS ALONG THE X-Z PLANE OF Y = 2

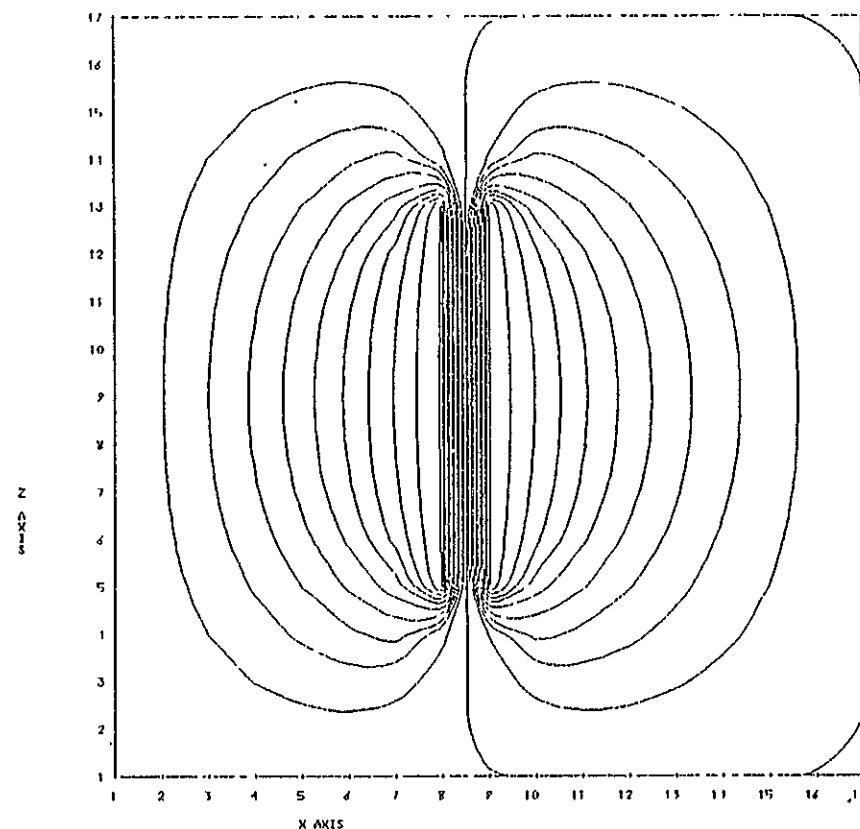
 $Z(III) = .10127+03$ $Z(IV) = .92715+02$ $\Delta Z = .10+00+02$


Figure 18.4. Guard ring parallel plate capacitor. These are the same configuration as Figure 18.1, but the amount of charge on the central plate can be calculated separately. This allows accurate comparison to analytical theory.

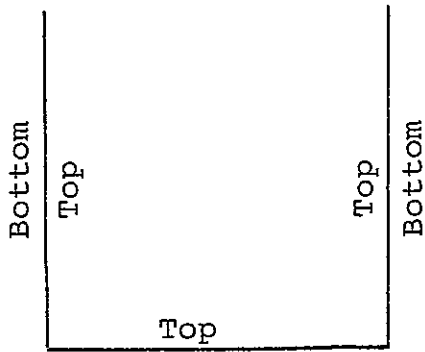
18.2 DEFINITION OF THIN PLATES

The definition of a thin plate is similar to that of a rectangular parallelepiped, with the exception that the 'SURFAC' designation is replaced by 'TOP' or 'BOTTOM'. Example:

```
PLATE
CORNER          3      1      4
DELTAS          2      4      0
TOP             +Z                      TEFLON
BOTTOM          -Z                      KAPTON
ENDOBJ
```

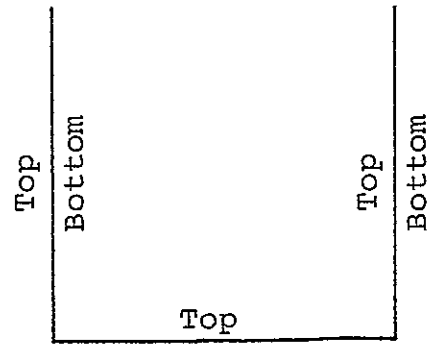
The distinguishing characteristic of a thin plate is that nodes interior to it are doubly defined. Thus, if an object contains more than one thin plate, a consistent specification of "top" and "bottom" must be maintained. Also, because of the way "bottom" points are treated in the potential solver, a volume cell touching the "bottom" of one thin plate may not touch the "top" of another.

EXAMPLES:



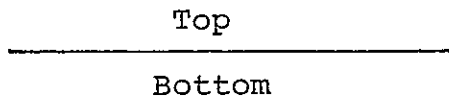
Bottom

VALID



Bottom

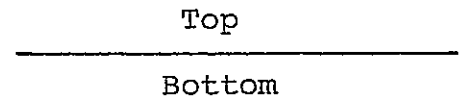
INVALID



Bottom

Top

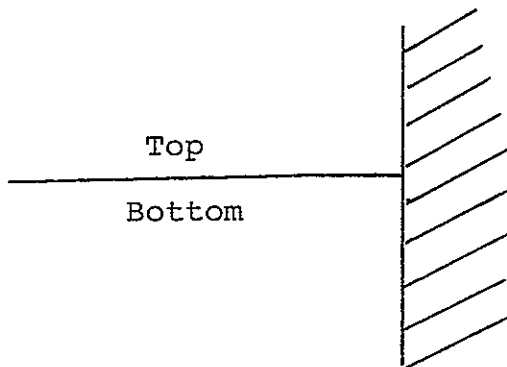
VALID



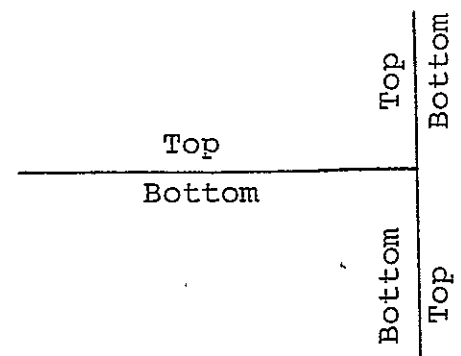
Top

Bottom

INVALID



VALID



INVALID (Contains
triple point)

REFERENCES

1. Cassidy, J. J., "NASCAP User's Manual," Systems, Science and Software Report SSS-R-78-3739 (DRAFT), August 1978.
2. Hestenes, M. R. and E. Stiefel, "Method of Conjugate-Gradients for Solving Linear Systems," J. Res. Nat'l. Bur. Std., 49, pp. 409-436, 1952.
3. Kershaw, D., "The Incomplete Cholesky-Conjugate-Gradient Method for the Iterative Solution of Systems of Linear Equations," J. Comp. Phys., 26, p. 111, 1978.
4. Aarset, B., R. W. Cloud and J. G. Trump, "Electron Emission from Metals Under High-Energy Hydrogen Ion Bombardment," J. Appl. Phys., 25, p. 1365, 1954.
5. Laframboise, J. G. and L. W. Parker, "Probe Design for Orbit-Limited Current Collection," Physics of Fluids, 16, p. 629, 1973.
6. Laframboise, J. G., private communication.
7. Whipple, Jr., Elden C., "Some Preliminary Results on The Charging of Insulators by Photoemission," 1977.

DISTRIBUTION LIST

National Aeronautics and Space Administration	
Washington, D.C. 20546	
ATTN: W. R. Hudson/Code RP	1 copy
D. P. Cauffman/Code ST	1 copy
A. F. Timothy/Code ST	1 copy
National Aeronautics and Space Administration	
Ames Research Center	
Moffett Field, CA 94035	
ATTN: H. Lum, Jr./M.S. 244-7	1 copy
National Aeronautics and Space Administration	
Goddard Space Flight Center	
Greenbelt, MD 20771	
ATTN: R. O. Bartlett/Code 408.0	1 copy
A. Kampinsky/Code 715.0	1 copy
E. G. Stassinopoulos/Code 601.0	1 copy
R. Bever/Code 711.4	1 copy
Jet Propulsion Laboratory	
4800 Oak Grove Drive	
Pasadena, CA 91103	
ATTN: R. Goldstein/M.S. 122-123	1 copy
National Aeronautics and Space Administration	
Lyndon B. Johnson Space Center	
Houston, TX 77058	
ATTN: J. E. McCoy/Code TN2	1 copy
National Aeronautics and Space Administration	
Langley Research Center	
Hampton, VA 23665	
ATTN: J. D. DiBattista/M.C. 158B	1 copy
National Aeronautics and Space Administration	
Lewis Research Center	
21000 Brookpark Road	
Cleveland, OH 44135	
ATTN: Head, Space Systems Section, M.S. 500-213	1 copy
Technical Utilization Office/M.S. 7-3	1 copy
Report Control Office/M.S. 5-5	1 copy
Office of Reliability and Quality Assurance/M.S. 500-211	1 copy
AFSC Liaison Office/M.S. 501-3	2 copies
Library/M.S. 60-3	2 copies
J. C. Roche/M.S. 501-8	20 copies
Patent Counsel/M.S. 500-311	1 copy

DISTRIBUTION LIST (Continued)

National Aeronautics and Space Administration George C. Marshall Space Flight Center Marshall Space Flight Center, AL 35812 ATTN: R. C. Chappell/ES 53	1 copy
National Aeronautics and Space Administration Scientific and Technical Information Facility P. O. Box 8757 Baltimore/Washington International Airport Maryland 21240 ATTN: Accessioning Department	10 copies
Air Force Geophysics Laboratory Hanscom Air Force Base, MA 01731 ATTN: PH/C. P. Pike	1 copy
Air Force Materials Laboratory Wright-Patterson Air Force Base, OH 45433 ATTN: MBE/W. Lehn	1 copy
Air Force Office of Scientific Research Bolling Air Force Base Washington, D.C. 20332 ATTN: H. R. Radoski/NP	1 copy
Air Force Systems Command AFSC/DLCEA Andrews Air Force Base, MD 20331 ATTN: Captain D. L. Beadner	1 copy
Air Force Weapons Laboratory Kirtland Air Force Base, NM 87117 ATTN: Lt. W. G. Kuller	1 copy
Space and Missile Systems Organization Los Angeles AF Station P. O. Box 92960 Worldway Postal Center Los Angeles, CA 90009 ATTN: YATT/Captain M. Bunn	1 copy
Defense Nuclear Agency Headquarters Washington, D.C. 20305 ATTN: RAEV/Major Carl Bloemker	1 copy

DISTRIBUTION LIST (Continued)

Communications Research Centre
Shirley Bay
P. O. Box 490, Station A
Ottawa, Ontario
Canada KIN 8T5
ATTN: V. Gore 1 copy

Department of Electrical Engineering
Pennsylvania State University
121 Electrical Engineering
East Building
University Park, PA 16802
ATTN: J. Robinson 1 copy

Department of Physics
University of California at San Diego
P. O. Box 109
La Jolla, CA 92037
ATTN: C. McIlwain 1 copy

Aerojet Electrosystems Company
1100 West Hollyvale Street
Azusa, CA 91720
ATTN: C. Fischer/Dept. 6751 1 copy

Aerospace Corporation
P. O. Box 92957
Los Angeles, CA 90009
ATTN: J. R. Stevens 1 copy

Boeing Aerospace Company
P. O. Box 3999
Seattle, WA 98124
ATTN: H. Liemohn/M.S. 8C-23 1 copy

Communications Satellite Corporation
Comsat Laboratories
Clarksburg, MD 20734
ATTN: A. Meulenberg, Jr. 1 copy

Ford Aerospace and Communications Corporation
Western Development Laboratories Division
3939 Fabian Way
Palo Alto, CA 94303
ATTN: D. M. Newell/M.S. G-80 1 copy

DISTRIBUTION LIST (Continued)

General Electric Company Valley Forge Space Center P. O. Box 8555 Philadelphia, PA 19101 ATTN: V. Belanger/U-2439	1 copy
Grumman Aerospace Bethpage, NY 11714 ATTN: M. Stauber	1 copy
Hughes Aircraft Company P. O. Box 92919 Los Angeles, CA 90009 ATTN: E. Smith/M.S. A620	1 copy
IRT Corporation P. O. Box 80817 San Diego, CA 92138 ATTN: J. Wilkenfeld	1 copy
JAYCOR 1401 Camino del Mar Del Mar, CA 92014 ATTN: E. P. Wenaas	1 copy
Kaman Science 1500 Garden of the Gods Road Colorado Springs, CO 80907 ATTN: F. Rich	1 copy
Lee W. Parker, Inc. 252 Lexington Road Concord, MA 01742 ATTN: L. Parker	1 copy
Lockheed Palo Alto Research Laboratory 3251 Hanover Street Palo Alto, CA 94303 ATTN: J. B. Reagan/Bldg. 205, Dept. 52-12	1 copy
Martin Marietta Corporation P. O. Box 179 Denver, CO 80201 ATTN: D. E. Hobbs	1 copy

DISTRIBUTION LIST (Continued)

Massachusetts Institute of Technology Lincoln Laboratory P. O. Box 73 Lexington, MA 02173 ATTN: F. G. Walther	1 copy
McDonnell Douglas Astronautics Company 5301 Bolsa Avenue Huntington Beach, CA 92647 ATTN: W. P. Olson	1 copy
Mission Research Corporation 1150 Silverado Street P. O. Box 1209 La Jolla, CA 92038 ATTN: V. van Lint	1 copy
RCA Astroelectronics Division P. O. Box 800 Princeton, NJ 08540 ATTN: H. Strickberger/M.S. 91	1 copy
Science Applications, Inc. 101 Continental Building Suite 310 El Segundo, CA 90245 ATTN: D. McPherson	1 copy
Science Applications, Inc. 2860 S. Circle Drive Colorado Springs, CO 80906 ATTN: E. E. O'Donnell	1 copy
Simulation Physics, Inc. 41 B Street Burlington, MA 01803 ATTN: R. G. Little	1 copy
Stanford Research Institute 333 Ravenswood Avenue Menlo Park, CA 90425 ATTN: J. Nanevicz	1 copy
TRW Systems One Space Park Redondo Beach, CA 90278 ATTN: A. Rosen	1 copy

DISTRIBUTION LIST (Continued)

Science Applications, Inc.
8330 Old Courthouse Road
Suite 510
Vienna, VA 22180
ATTN: B. L. Beers

1 copy

Hughes Research Laboratory
3011 Malibu Canyon Road
Malibu, CA 90265
ATTN: Dr. Jay Hyman

1 copy